Magnetic Phenomena in Interface-Engineered Multilayer Thin films

ARIAM MORA-HERNANDEZ

Magnetic Phenomena in Interface-Engineered Multilayer Thin films

Ariam Mora-Hernández

A Thesis presented for the degree of
Doctor of Philosophy

Magnetism and X-rays group
Department of Physics
University of Durham
England

October 2020

Dedicated to

To my family, in particular to my mother Rocío Hernández Balderas who is my rock.

Magnetic Phenomena in interfacial engineered multilayer thin films

Ariam Mora-Hernández

Submitted for the degree of Doctor of Philosophy

October 2020

Abstract

The effects of spin-orbit coupling and symmetry breaking at the interface between a ferromagnet and non-magnetic material are of particular interest and importance for current and future spintronic applications. Consequently, the effect of proximity induced magnetization (PIM), the interfacial Dzyaloshinskii-Moriya interaction (DMI) and the spin-orbit-torque (SOT) in Pt are studied in this thesis with a detailed investigation of the mechanism and the implications on engineered interfacial multilayers thin films. In this work, Co_2FeAl (CFA) and Co are the ferromagnet material investigated.

PIM is investigated in CFA-based multilayer structures under the influence of annealing for different heavy metals (HMs). In some cases the PIM is presented along with the interfacial DMI. However, interfacial quality plays a crucial role in the strength of PIM and the influence of interfacial quality and thermal processes on DMI and PIM are not understood. Here, it was found that the thermal process increased the PIM in Pt samples. On the other hand, the magnetism was cancelled by the annealing process for the Ir samples.

The DMI determines the type and symmetry of non-uniform magnetic structures and arises at interfaces between a ferromagnet and a nonmagnetic material with strong spin-orbit coupling. As that DMI depends of the symmetry of the system, interfacial roughness further breaks the symmetry at the interface in a heterostructure. A description of how controlled induced interfacial roughness can be used to tailor the DMI in model Pt/Co/Ta(Pt) thin-film multilayer structures. Magneto-optic Kerr effect microscopy is used to quantify the strength of the DMI indirectly via the asymmetric growth of bubble-like domains. Brillouin Light Scattering (BLS) is also used to directly quantify the DMI from the asymmetry induced in the spin-wave dispersion. The influence of engineered interface roughness on DMI as measured by BLS is presented. Fluctuations were found in the DMI when the roughness increases from 0 to 35 Å by both methods of analysis, which suggests that changes in the interfacial characteristics in the multilayer modify the interfacial DMI.

Furthermore, micromagnetic simulations are used to show how a current-driven domain wall motion using SOT is employed to create a bubble-skyrmion on the top of a square pillar using the difference in perpendicular magnetic anisotropy in

the different regions on a strip. High bubble-skyrmion velocity was found once the structure was depinned.

Future spintronic applications rely on the understanding of interfacial engineering devices. Towards this goal, this thesis provide contributions to the advantageously use of thermal processes, interfacial quality in terms of roughness and intermixing in multilayer thin-film stacks and the creation of skyrmion-bubbles to be used as potential information carriers.

Declaration

The work in this thesis is based on research project carried out at the Magnetism and X-ray group, the Department of Physics of Durham University, England. No part of this thesis has been submitted elsewhere for any other degree or qualification and it is all my own work unless referenced to the contrary in the text.

The magnetic thin films presented in this work were prepared by author. The structural characterisation with XRR presented in chapter 5 and 6 were performed by author with assistance from Dr Christy Kinane at the Rutherford Appleton laboratory, R53 material characterisation lab. Analyses were performed by the author. The MOKE microscopy measurements in chapter 6 were made by the author with assistance of Alexandra Huxtable at the University of Leeds. Analysis of experimental data was performed by author using a software provided by Leeds University.

All the polar and transverse MOKE experiment in chapter 6 was performed by the author at the Wolfson Nanotechnology Lab, Department of Physics, Durham University.

Brillouin light scattering experiments were performed at the Galileo Institute in the Université 13 North, Paris, France by Dr Yves Roussigné, Dr Mohamed Belmeguenai and Dr Andrei Stashkevich. Analysis of experimental data was performed by author.

Polarised neutron reflectivity experiments were conducted at the Polref beamline at ISIS neutron facility, Didcot, England along with Dr Christy Kinane, Dr Aidan Hindmarch, Mr Ben Nicholson. Analysis of experimental data was performed by author.

Synchrotron radiation was employed in x-ray resonant magnetic reflectivity experiments conducted at the XMaS beamline, ESRF, France. These were coordinated

by the author with a team which includes Dr Aidan T Hindmarch, Dr Laurence Bouchenoire and Mr Ben Nicholson. Analysis was performed by the author with assistance from Dr Oto-Obong Inyang.

December 14, 2020

Acknowledgements

I like express my thankfulness to the Mexican National Council on Science and Technology (CONACyT) who granted me an scholarship that made this research possible.

There are many people that I offer my thanks and gratitude to. Firstly to my supervisor Dr Aidan Hindmarch for his guidance, patience and understanding during the whole of this project. Also, to Prof Del Atkinson who gave me the academic balance at critical times during my PhD. Their constructive advice, guidance, constant motivation, meticulous scrutiny and scientific approach have help me to a very great extent to a successful completion of each phase of the tasks on this thesis. Also, many thanks to the staff and student of the Physics department for creating a conducive and engaging work and learning environment.

I am deeply thankful to Dr Christy Kinane (Isis neutron facility) and Dr Laurence Bouchenoire (XMaS beamline, ESRF) for their help and technical assistance during Synchrotron experiments. Also, it is important to appreciate the support staff in both facilities. Many thanks to Dr Yves Roussigné, Dr Mohamed Belmeguenai and Dr Andrei Stashkevich for providing me the assistance and opportunity to use their facility as well as the friendly collaboration.

I would also like to thank the other people with whom I have worked alongside in room 142: Sinan Azzawi, Ben Nicholson, Charles Swindells, Sarah Hamilton Liam Stubbington, Kaleel Alsaeed and Joseph Troughton. We've had many fruitful discussions, some with more Physics in than others. I am grateful to my partners in crime and former housemates, Alejandro Galán-Gonzales and Maura Ramirez-Quezada. As well as all the good friends I've made in the Durham Physics department.

Finally I would extend my utmost gratitude to those closest to me, both my

parents and my sister, my family who have provided me with so much support and encouragement throughout my whole PhD.

December 14, 2020

List of Publications

- **A. Mora-Hernández**, A. T. Hindmarch, Del Atkinson. Current-driven domain wall dynamics along a square pillar in a multilayer with PMA.

  In preparation

- **A. Mora-Hernández**, B. Nicholson, O.-O. Inyang, A. T. Hindmarch, M. Belmeguenai, Y. Roussign, H. Bouloussa, S. M. Chrif, A. Stashkevich, M. Nasui, M. S. Gabor. Proximity induced magnetization in Co_2FeAl ultrathin films: effects of the annealing temperature and the heavy metal material.

  In preparation

- **A. Mora-Hernández**, B. Nicholson, A. T. Hindmarch, M. Belmeguenai, Y. Roussign, Alexandra Huxtable and T. A. Moore. Dzyaloshinskii-Moriya interaction in multilayers with engineered interfacial roughness.

  In preparation for submission to Physical Review B.

- M. Belmeguenai, Y. Roussign, H. Bouloussa, S. M. Chrif, A. Stashkevich, M. Nasui, M. S. Gabor, **A. Mora-Hernández**, B. Nicholson, O.-O. Inyang, and A. T. Hindmarch. Thickness Dependence of the Dzyaloshinskii-Moriya Interaction in Co_2FeAl Ultrathin Films: effects of Annealing Temperature and Heavy- Metal Material. Physical Review Applied 9, 044044 (2018)

Contents

List of Figures

List of Tables

Chapter 1

Introduction

The ultimate goal of the field of spintronics is to exploit the spin of the electron for active applications such a spin-transistor [1] or a racetrack memory [2]. With the development of sophisticated thin-film fabrication techniques such as sputtering and molecular beam epitaxy, this has become a reality where synthetic multilayer structures can be fabricated which exhibit magnetic properties dramatically different from their bulk counterparts.

In ultrathin ferromagnetic (FM) films in contact with a nonmagnetic heavy metal (HM), a noticeable interfacial Dzyaloshinskii-Moriya interaction (DMI) can arise due to the large spin-orbit coupling (SOC) in the presence of the broken inversion symmetry at the FM/HM interface [3, 4], leading, for instance, to asymmetric spin-wave dispersion [5]. Interfacial DMI in FM/HM bilayers is usually stronger than bulk DMI in noncentrosymmetric chiral magnets [6, 7], which also has the advantage of room temperature operation using conventional magnetic materials. In such structures, the combination of the interfacial DMI, which stabilises chiral Néel domain walls (DWs), and the spin-Hall effect [8, 9] has been found to enable a surprisingly fast current-driven DW motion [10–14]. It has also been observed that both the velocity and the direction of the DW motion depend on the DMI strength and can be controlled by engineering the interface between the two materials [15–17]. From a technological point of view, these structures are of great importance, due to their enormous potential for current-controlled DW motion for the development of novel memory-storage devices with high density and performance in so-called racetrack

memories [2]. This phenomenology was found in a vast number of different studies that use structures with Pt as the HM due to its attractive properties for spintronic applications [18].

The SOC is the interaction between the electrons spin and its orbital motion around the nucleus. SOC play a crucial role in other phenomena such as the spin Hall effect (SHE) [19–21] that can lead to spin-orbit-torque (SOT) [22], spin pumping [23, 24], magnetic dead layer formation [25], and proximity induced magnetisation [26, 27]. This proximity induced magnetisation (PIM) in the heavy metal is associated with the large Stoner factor of the *d*-transition elements [28–33], such as Pt [10, 34–39] which exhibits some degree of induced moment when placed in direct contact with a ferromagnetic material. The selection of the ferromagnetic material is also crucial looking forward to device applications. Therefore, Heusler alloys are potential candidates because they exhibit extremely small precessional damping, a high Curie temperature, and a relatively high spin-polarisation [40, 41].

Until now, the description of the interactions involved in this kind of structure are theoretically predicted in ideal systems. This implies that there is perfect control in the quality of the thin-film layers and at the interfaces (including both components of the roughness between layer in thin-film stacks, intermixing, lack of impurities, etc). Changing the quality of the interfaces will modify the interfacial DMI just as much to the PIM and in general the dynamics of the system [42]. Characterising the details of potentially asymmetric interface properties, such as the roughness, degree of intermixing, and density of stacking faults, remains an outstanding materials science challenge. Therefore, the consequences of such changes in the magnetic properties and interactions are currently a hot topic in the magnetism community.

Magnetic skyrmions are micron or sub-micron sized particle-like magnetic configurations which have magnetisation antiparallel to magnetic field at their centre and parallel to the field at their periphery [43, 44]. Skyrmions as information carriers are believed to have potential in future high density data storage devices and information processing devices [45–47]. In the same HM/FM bilayer systems, the accumulation of spins at the interface subsequently transfer their spin angular momenta to the adjacent ultra-thin FM layer. Consequently, it gives rise to

current-induced spin-orbit torques (SOTs), including a field like torque and an anti-damping like torque [15, 48–53]. These spin torques, in turn, result in an efficient electrical manipulation of skyrmions [54]. This material system is thus technologically appealing for enabling functional skyrmionic logic or memory devices at room temperature [55]. However, it has been challenging to employ electric currents and its induced SOTs in these asymmetric multilayers to create or manipulate magnetic skyrmions at room temperature [56–58]. Until recently, this has been a bottleneck for realizing electrically reconfigurable skyrmionic logic or memory devices. Furthermore, it is necessary to be able to first drive their motion along nanostructures and also nucleate and annihilate them at will. Though isolated skyrmions and skyrmion lattices have been observed in experiments, controlled and effective creation and/or manipulation of skyrmions is still a challenge [59–61].

This thesis tries to contribute in a deeper comprehension of PIM under an annealing process using an Co_2-based Heusler alloy; how the interfacial DMI is influenced by the roughness; finally, a new method to create a bubble-skyrmion and move it using SOT generated by a current.

1.1 Aims of the thesis

The aim of this work is to understand the underlying mechanism of PIM, DMI and SOT DW motion in interfacial engineered multilayer thin films. Trilayer thin film samples were designed to study the magnetic properties at the interface using different regions of the spectrum of light and neutron as probes, highlighting the implications of the interfacial quality on the PIM and the DMI. A deeper understanding of the influence of the interfacial quality on the spin-Hall effect (SHE), DW velocity and in the dynamic parameter such as the damping may lead to a design of a more efficient non-volatile spintronic devices. Furthermore, micromagnetic simulation using SOT to further understand of a new mechanism to artificially create magnetic bubble-skyrmions in patterned multilayer thin films with PMA is presented.

1.2 Thesis Outline

A theoretical background of the relevant physics behind this work is given in chapter 2. First is a discussion of the origin of ferromagnetism and the interactions involved. Following this, the spin-orbit interaction is introduced followed by the antisymmetric Dzyaloshinskii-Moriya interaction which is the central theme of this thesis. Finally, a description of magnetic domains is presented, providing the foundations required for a better description of the analysis and results in later chapters.

In chapter 3, the experimental techniques used for the sample preparation and structural and magnetic characterisation are described.

A detailed description of the development of the Durham MOKE Microscope and the experimental techniques in microscopy used in this work is provided in chapter 4.

The PIM effect investigation in Pt in contact with a Heusler alloy, Co_2FeAl is then reported as a function of the annealing process in chapter 5. This study was performed with different probes. The results were compared between the structural characterisation by x-ray reflectivity and the magnetic characterisation by polarised neutron reflectometry and x-ray resonant magnetic reflectivity to develop a full understanding of the relationship between structure and functional behaviour. Details of the fitting process can be found in the Appendix at the end of the thesis.

Chapter 6 presents the interfacial DMI study of multilayers with engineered interfacial roughness with different multilayered structures. The roughness was intentionally induced by thermally-evaporating Ag or sputtering SiO_2 prior to the multilayer deposition. The DMI analysis was investigated using BLS and the asymmetric bubble expansion method in order to compare the two approaches.

In chapter 7, the investigation of the current-driven DW motion under SOT using micromagnetics simulations to study the creation of an artificial bubble-skyrmion on the top of a pillar that comes from the different perpendicular magnetic anisotropies in two different regions is described.

In chapter 8, the conclusions of this thesis are presented along with a brief summary of the major findings obtained in the investigations and suggestions for further work.

Chapter 2

Theoretical background

This chapter describes the theoretical framework that is relevant to the phenomena discussed throughout this thesis. It provides the physical concepts behind this research. The chapter is split as follows. The first section is the origin of ferromagnetism through a discussion of the interactions involve. Following this, the spin-orbit interaction is introduced followed by the antisymmetric Dzyaloshinskii-Moriya interaction which is the central theme of this thesis. In the last section, a description of magnetic domains is presented which draws together most of the previous topics.

2.1 Hund's rules

In a local-moment model, Hund's rules are used to determine the magnetic ground state of a multi-electron atom. The three rules are [62]:

- For a given electron configuration, the term with maximum multiplicity has the lowest energy. The multiplicity is equal to $2S + 1$, where S is the total spin angular momentum for all electrons. The multiplicity is also equal to the number of unpaired electrons plus one. Therefore, the term with lowest energy is also the term with maximum S, and maximum number of unpaired electrons.

- For a given multiplicity, the term with the largest value of the total orbital angular momentum quantum number L, has the lowest energy.

- For a given term, in an atom with outermost subshell half-filled or less, the level with the lowest value of the total angular momentum quantum number J, (for the operator $|J = L - S|$ lies lowest in energy. If the outermost shell is more than half-filled, the level with the highest value of $|J = L + S|$, is lowest in energy.

In bulk magnets, the dominant magnetic energy terms derive from the exchange interaction, the interaction between orbital wave functions and the local electric fields from neighbouring ions (referred to as crystal fields), spin-orbit coupling, and the magnetic dipolar interaction. The relative size of these energy terms, as well as the electron kinetic energy (related to band-width), fundamentally determine both the static and dynamic properties of the magnetic state. The exchange interaction, whether intra-atomic or inter-atomic, is the quantum-induced manifestation of the charge-charge interaction between electrons which can be understood just from Coulomb repulsion, it is the competition with kinetic energy that gives itinerant (band) magnetism and the Stoner criterion. Considering two electrons occupying the same atom, the triplet state is generally the lower energy state since this requires an antisymmetric spatial component of the wavefunction, which minimises the Coulomb repulsion. This is the origin of Hund's first rule [63]. It stabilizes the magnetic moments in both isolated atoms and solid materials. In solid materials, s- and p-shell electron wave functions are typically hybridised into bands or covalent or ionic bonds and do not contribute to magnetisation, but the less-spatially extended d- and f-shell wave functions retain a more localised nature, with a degree of hybridisation that depends on the details of the chemical bonding. Depending on this degree of hybridisation (bandwidth), either a local-moment model or a band model of magnetism is more appropriate.

For isolated atoms, with one or more outer shell electrons, the intra-atomic exchange interaction leads to the Hunds rule splitting of electron energies, with resulting spin, orbital, and total angular momentum S, L, and $J = L + S$, respectively (capital letters refer to the combined angular momenta of the one or more outer shell electrons of each atom or ion e.g., $J = \sum j$, $S = \sum s$, $L = \sum \ell$). Spin-orbit coupling (discussed later in the chapter) results in a ground state in which spin

and orbital moments are either parallel or antiparallel. This is captured in Hunds third rule which states that for orbitals that are less than half full (e.g., fewer than seven electrons in the f shell), S and L are antiparallel resulting in total angular momentum $J = |L - S|$, while for orbitals that are more than half full, they are parallel and $J = |L + S|$, and for a half-filled orbital, $L = 0$, hence $J = S$. The magnetic moment per atom is $\mu = gJ\mu_B/\hbar$ with μ_B the Bohr magneton and g, $\hbar$ is the reduced Planck constant and the Landé g-factor is given by

$$g = \frac{3}{2} + \frac{S(S+1) - L(L+1)}{2J(J+1)}.$$

In a local-moment picture of a solid, the isolated atom wave functions are no longer exact solutions due to the non-spherically symmetric electric fields of neighboring ions (called crystal fields, although also important in amorphous materials). The relatively weak effects on f-shell electrons leaves the isolated atom wave functions (with S, L, J, and m_J quantum numbers, where m_J is the projection of the total orbital angular momentum along a specified axis) as a good approximation for rare-earth elements, but lifts the degeneracy of the J manifold of orbitals (even in zero magnetic field) to produce singly or doubly degenerate low-lying energy states, depending on even versus odd numbers of electrons. For even numbers there are a singlet and a series of doublet states ($M_J = 0, \pm 1, \pm 2, ..., \pm J$), whose energy depends on the crystal field interaction, including its symmetry, while for odd numbers ($M_J = \pm 1/2, \pm 3/2, ..., \pm J$), there are only doublets (known as Kramers doublets). The doublet states are then split by magnetic field or by inter-atomic exchange interactions. Depending on the symmetry of the crystal structure, the lowest energy state may have a magnetic moment per atom of $gJ\mu_B$, as for isolated atoms, or it may have small or even no moment but a large magnetic susceptibility [64].

2.2 Ferromagnetism

Magnetism in matter is characterised by the magnetic moment $\vec{\mu}$ which is determined by three factors. The spins of electrons, the angular momentum about the nucleus, and the change or reaction of both the orbital moment and the spin when

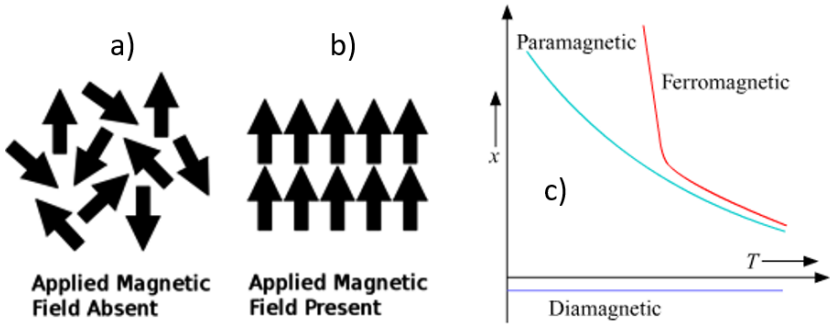

Figure 2.1: Schematic summary of (a) the paramagnetic state without a field and (b) the polarised state in a saturating field, (c) the behavior of ferromagnetic, paramagnetic and diamagnetic materials.

a external field is applied [65]. Ferromagnetic materials present a spontaneous magnetic moment, i.e. a magnetic moment even in zero applied magnetic film. The energy of a magnetic moment in a magnetic field $\vec{B}$ is given by the Hamiltonian,

$$\hat{H} = -\vec{\mu} \cdot \vec{B}. \tag{2.2.1}$$

The magnetic susceptibility is defined as the ratio between the magnetisation and the macroscopic magnetic field, and is dimensionless,

$$\chi = \frac{M}{H}, \tag{2.2.2}$$

where M is the magnetisation and H the magnetic field. Ferromagnetic materials possess a spontaneous magnetisation and below saturation have a large, positive susceptibility to an external magnetic field, and are able to retain their magnetic properties after the external field has been removed. Weiss explained the spontaneous magnetisation of ferromagnets by supposing that, in addition to any externally applied magnetic field H, there is an internal "molecular field" H_{mol}, in a ferromagnet that is proportional to its magnetisation, M, such that

$$H_{mol} = \lambda M, \tag{2.2.3}$$

where λ is the molecular field constant. From the Curie law for paramagnets, it is known that $\chi = \frac{C}{T}$ where C is the Curie constant and T is the temperature.

Now, for the ferromagnetism case, the Curie temperature T_{C} is the temperature above which the spontaneous magnetisation vanishes. In a similar fashion to the case of paramagnetic materials, Curie-Weiss's law [63] describe the susceptibility of ferromagnetic materials as a function of temperature, T, using the relation,

$$\chi = \frac{C}{T - T_{\mathrm{C}}}, \tag{2.2.4}$$

where the Curie temperature, $T_{\mathrm{C}} = \lambda C$. In the presence of an external magnetic field there are two fundamental magnetic states dependent upon temperature (figure 2.1). When the spins of some material are oriented randomly in any directions with no magnetisation, M), is the paramagnetic state (this is the phase above T_{C} of ferromagnetic materials) and when a material is better described by local ordering, this state is called the polarised or ferromagnetic state which is characterised by a magnetisation, $M > 0$. The magnetisation M for spin $J = \frac{1}{2}$ with spin $S = \frac{1}{2}$ and $L = 0$ of a more general case of a ferromagnet can be expressed in terms of the Brillouin expression [62] as

$$M = \frac{Ng\mu_{\mathrm{B}}}{2} \tanh\left(\frac{\mu_0 g\mu_{\mathrm{B}}(H + \lambda M_{\mathrm{S}})}{2k_{\mathrm{B}}T}\right), \tag{2.2.5}$$

where N is the number of atoms, k_{B} the Boltzman constant and T the temperature. Ferromagnetic materials can be described using perturbation theory. By considering quantum mechanically the ferromagnets as paramagnetic materials that uses the exchange interactions as the perturbation [66]. This means, the electrons on the neighboring atoms interact with each other. This approach also converges to the Curie-Weiss law.

2.2.1 Band theory of ferromagnetism

Magnetisation arises due to unpaired electrons spin states in a material, hence completely filled energy bands cannot contribute to the magnetic moment [67]. The spin imbalance in partially filled bands leads to a net magnetic moment in a ferromagnetic material in the absence of external magnetic field and some of the spin-down

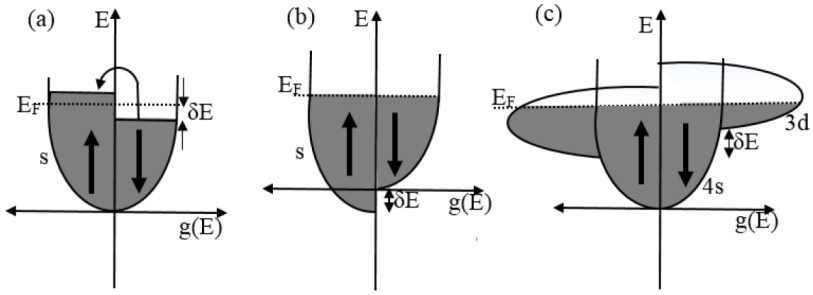

Figure 2.2: Schematic illustration of the electronic density of states showing spontaneous splitting of energy bands in the absence of an applied field (a) shows spin flip (b) resulting band splitting due to spin flip (c) spontaneous magnetisation in 3d transition metals [68].

electrons at the Fermi level are considered to spin flip into the spin-up band as shown in figure 2.2. The number of electrons migrating due to spin flip increases the energy δE in the spin up channel which is considered as the energy required for a spin flip. The band splitting is equal to $2\mu_B$ and we have spin polarisation (i.e $n_\uparrow - n_\downarrow \neq 0$). The magnetisation, M due to promoting electrons from spin-down to spin-up is

$$M = (n_\uparrow - n_\downarrow)\mu_{\mathrm{B}} \approx \mu_{\mathrm{B}} g(E_{\mathrm{F}})\delta E. \tag{2.2.6}$$

where $g(E)$ is the energy dependent density of states. The change of the kinetic and potential energy because of the spin flip are [69]

$$\Delta E_{\mathrm{K}} = \frac{1}{2} g(E_{\mathrm{F}})\delta E^2 \qquad \text{and} \qquad \Delta E_{\mathrm{P}} = \frac{1}{2} U g(E_{\mathrm{F}})^2 \delta E^2, \tag{2.2.7}$$

where U is the Coulomb energy and can be written as $U = \mu_0 \mu_B^2 \lambda$. The state hop from spin-down to spin-up requires a spontaneous increase in the kinetic energy and a decrease in the potential energy. Therefore, the total energy change is

$$\Delta E = \Delta E_{\mathrm{K}} + \Delta E_{\mathrm{P}} = \frac{1}{2} g(E_{\mathrm{F}})(\delta E)^2 (1 - U g(E_{\mathrm{F}})) \tag{2.2.8}$$

When $\Delta E < 0$ spontaneous magnetisation occurs. Hence, $U g(E_{\mathrm{F}}) \geq 1$. This is the Stoner criterion. To satisfy this, the Coulomb repulsion between electrons is large and the density of states at the Fermi-level for a particular spin population is larger; causing spin splitting via the exchange interaction. In $3d$ metals such as Fe, Co and Ni, the ferromagnetism is due to large density of states in the $3d$ band and Coulomb

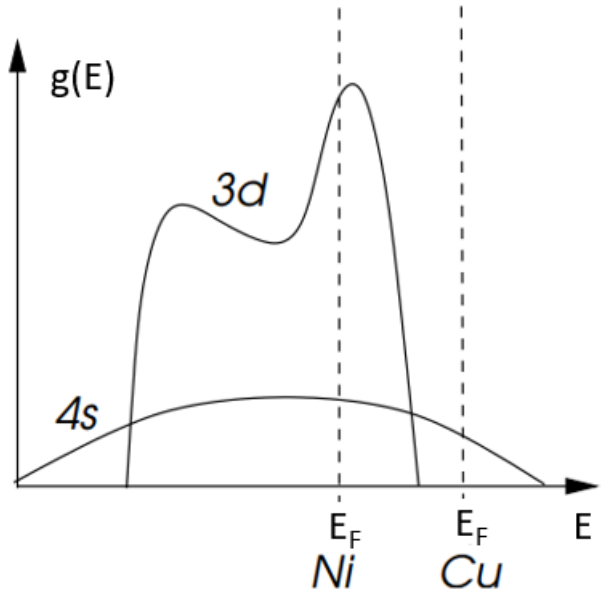

Figure 2.3: Stoner criterion in a band representation. Ni is a ferromagnet due the high density of states (unfilled), $g(E)$, in the $3d$ band. Having as a result the E_{F} within the $3d$ sub-band creating a spin imbalance. Cu in the other hand, is a paramagent because they have a complete filled $3d$ band.

repulsion such that Stoner criterion is met. [70]. The magnetic properties arise from the high density of states in the $3d$ band which can host up to 10 electrons per atom and can be spin-split. Even though these elements have $4s$ electrons, the $4s$ electron band only contains up to two electron per atom and hence g(E_{F}) is small which does not affect the magnetic properties [62]. This is why Cu and Zn as $3d$ elements do not have a magnetic moment because of a completely filled $3d$ band as shown in figure 2.3. Fe, Co and Ni exhibit ferromagnetism because the $3d$ sub-bands shift with respect to each other due to the presence of the exchange interaction creating a spin imbalance as shown in figure 2.2c). Ferromagnetic ordering occurs when the saving in exchange energy is larger than the increase in the kinetic energy. Ferromagnetic metals exhibit finite magnetisation in thermodynamic equilibrium.

2.2.2 Stoner enhancement in platinum

There are some materials that do not satisfy the Stoner criterion but can still present a large susceptibility. In this case, when an external field is applied the total energy

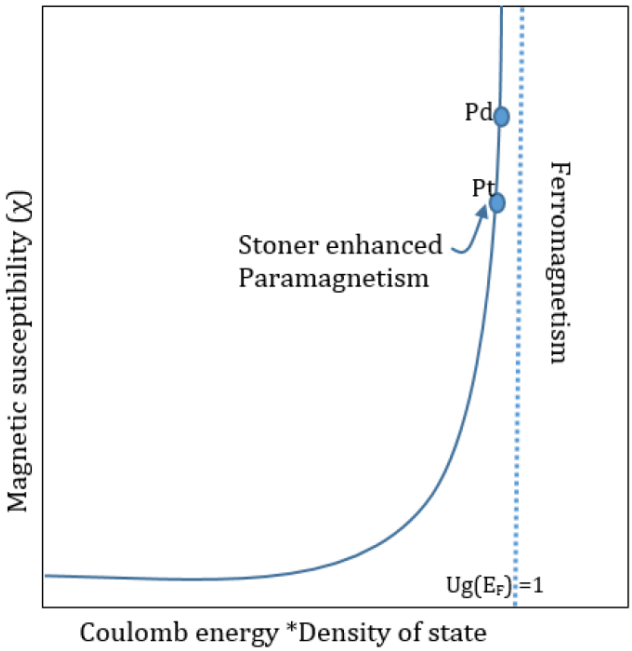

Figure 2.4: Magnetic susceptibility against the density of state g(E_F) showing the enhanced magnetic susceptibility for Pt and Pd.(adapted from [26]).

is expressed as

$$\Delta E = \Delta E_{\mathrm{K}} + \Delta E_{\mathrm{P}} = \frac{M^2}{2\mu_{\mathrm{B}}^2 g(E_{\mathrm{F}})}(1 - Ug(E_{\mathrm{F}})) - \vec{M} \cdot \vec{B}, \tag{2.2.9}$$

where $\vec{M} \cdot \vec{B}$ characterised the effect of the applied magnetic field. The total energy begins to be reduced as a result of field polarisation when

$$\frac{M}{\mu_{\mathrm{B}}^2 g(E_{\mathrm{F}})}(1 - Ug(E_{\mathrm{F}})) - B = 0. \tag{2.2.10}$$

The magnetic susceptibility reduces to

$$\chi = \frac{\mu_0 \mu_{\mathrm{B}}^2 g(E_{\mathrm{F}})}{(1 - Ug(E_{\mathrm{F}}))} = \frac{\chi_{\mathrm{P}}}{(1 - Ug(E_{\mathrm{F}}))}, \tag{2.2.11}$$

where χ_{P} is the Pauli susceptibility. Therefore paramagnetic materials with large densities of state are termed Stoner enhanced paramagnets as shown in figure 2.4 because they have a large enough product of density of states and Coulomb energy to cause a significant enhancement of the magnetic susceptibility, but are unable to cause spontaneous ferromagnetism. This effect is known as Stoner enhancement

and basically explain why if any paramagnets such as Pt and Pd are put next to a ferromagnetic material, the proximity magnetic properties will be enhanced with respect materials that do not satisfy the condition, which may assume some localised ferromagnetic properties. This is as a result of induced transition into a ferromagnetic phase in paramagnet with large $g(E_{\mathrm{F}})$, which can be achieved by placing this paramagnetic material in proximity to a ferromagnet at the interface [71], alloying with a ferromagnetic impurity [72] or by reducing dimensionality in materials [73]. Pt is a paramagnetic material and has been reported to interact with other ferromagnetic material forming alloys with enhanced susceptibility. Platinum is nearly, but not quite, ferromagnetic, suggesting that it might be possible to induce magnetic properties using external stimuli such as an electric field [18].

Pt is an interesting material and popular in the magnetism community because of its rich interfacial phenomena and interesting characteristics for potential spintronics applications. Magnetic thin film multilayers with perpendicular magnetic anisotropy (PMA) are of great interest including in systems with chiral magnetic features that are present at the interface between a heavy metal and the ferromagnet . Moreover, using Pt as a seed layer, the thickness of Pt modulates the strength of the PMA in an adjacent Co layer in a multilayer structure, which in combination with the DMI enables the stabilisation of a particular type of magnetic domain wall called a Néel wall, which can be considered the first step that is the first step towards the skyrmion phase along with the so-called asymmetric exchange interaction Dzyaloshinskii-Moriya interaction (DMI). Furthermore, these magnetic Skyrmions could bring solutions for new data storage technologies [43]. PMA, DMI and magnetic Skyrmions will be described in more detail in the following sections.

2.3 Spin-orbit interaction

A significant number of phenomena within the field of magnetism and spintronics occur as a direct result of the coupling between the electron spin and orbital angular momenta [74]. The spin-orbit interaction (SOI) gives rise to the spin Hall effect, magnetocrystalline anisotropy and provides a mechanism for energy dissipation to

the lattice, as is observed in magnetic damping. This phenomenon was first detectable as a splitting of spectral lines, which can be thought of as a Zeeman-like effect produced by two relativistic effects: the apparent magnetic field seen from the electron perspective and the magnetic moment of the electron associated with its intrinsic spin. Semi-classically, the origin of the SOI can be understood by considering an electron orbiting a nucleus as shown in figure 2.5. In the frame of reference of the electron, the electron is stationary and the nucleus orbits it forming a closed current loop. This orbiting positive charge then produces a magnetic field which interacts with the electron spin. Consequently, the orbital motion of the electron is coupled to its spin. For a single electron orbiting a positively charge nucleus, the SOI Hamiltonian is given by

$$\hat{H}_{\mathrm{SOI}} = \frac{Ze^2}{2m_{\mathrm{e}}c^2r^3}\vec{L}\cdot\vec{S}, \tag{2.3.12}$$

where m_{e} is the electron's mass, Z is the atomic number of the nucleus and r is the radius of the electron orbit. The expectation value is going to be $\langle r^3\rangle \sim \langle Z^3\rangle^{-1}$ hence the atomic SOI scales with Z^4, which explains why the SOI is strong in heavy elements such as Pt, Ta and Ir. However, it is important to note that orbital hybridisation also plays a significant role when considering complete crystals rather than single atoms. The SOI acts as a perturbation to the state which is proportional to $\vec{L}\cdot\vec{S}$, hence energy conservation is involved. Here, the total angular momentum $\vec{J} = \vec{L}+\vec{S}$ is conserved. For example, for an electron bound to a hydrogen-like atom the SOI up to first order in perturbation theory, the shift in energy is

$$\Delta E = \frac{\beta}{2}(j(j+1) - \ell(\ell+1) - s(s+1)) \tag{2.3.13}$$

where

$$\beta = \beta(n,\ell) = Z^4\frac{\mu_0}{4\pi}g_s\mu_B\frac{1}{n^3a_0^3\ell(\ell+1/2)(\ell+1)} \tag{2.3.14}$$

and n is the principal quantum number and a_0 is the Bohr radius.

As the Fermi energy is in the d band, conduction states have $L > 0$ whereas in Au the Fermi energy has s states with $L = 0$.

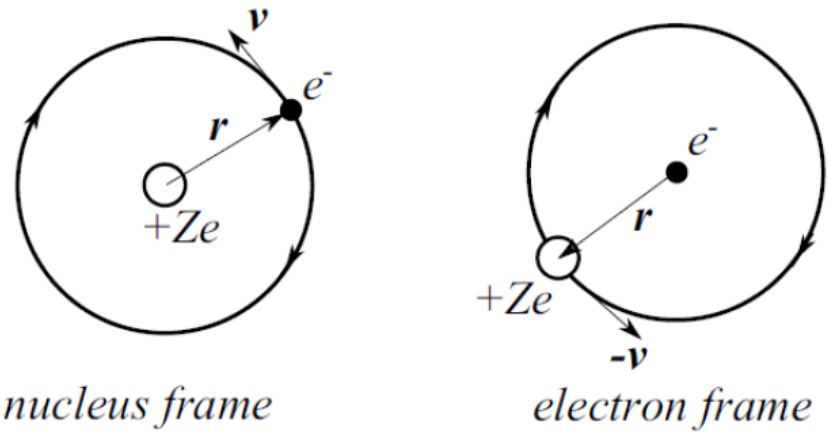

Figure 2.5: Classical schematic of the spin-orbit interaction seeing from two different reference frames.

2.4 Perpendicular magnetic anisotropy

In magnetic films and multilayers, the magnetic anisotropy direction can be changed from the common in-plane direction to the out-of-plane direction by changing the thicknesses of each layer and the material combination. In materials with PMA, the direction of the magnetic moments of the ferromagnetic layer are perpendicular to the plane of the surface. Materials with PMA are important for magnetic information storage applications due to the existence of narrow domain walls which enhance the storage capacity. The effective magnetic anisotropy K_{eff} is the sum of two terms; volume anisotropy K_{v} and a surface anisotropy K_{s} [75]. The K_{v} term is contributed by the total volume of the magnetic moments, and K_{v} is associated with the moments at one or both interfaces. A negative K_{v} indicates the magnetisation is orientated in the plane of the film. The K_{s} term is caused by the interfacial magnetic moments, and positive K_{s} contributes toward the magnetisation direction being perpendicular to the surface. Interface anisotropy was first predicted by Néel in 1954 [76] and then experimentally observed for NiFe films grown on Cu (111) by Gradmann and Müller in 1968 [77]. PMA in multilayers was first observed for Co/Pd in 1985 [78] and later for Co based multilayers of Co/Pt, Co/Pd, Co/Au, Co/Ru, Co/Ir and Co/Ni [79–82]. The effective anisotropy, K_{eff}, of a magnetic structure can be separated into a volume magnetic moment contribution and the

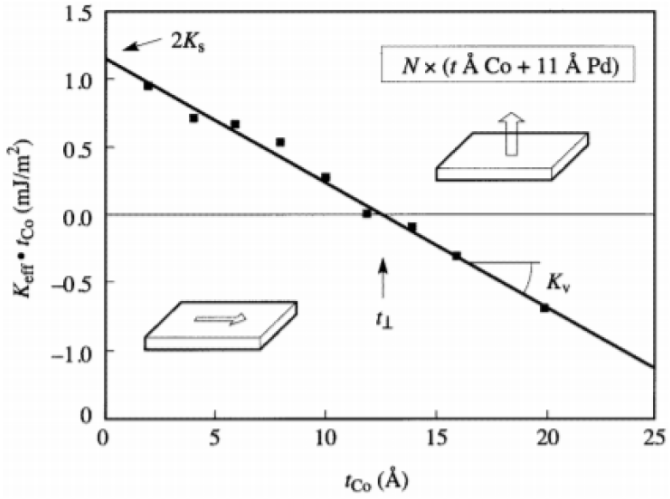

Figure 2.6: Effective anisotropy times Co thickness Vs. Co thickness for Co/Pd multilayers. The gradient indicates the volume anisotropy contribution while the intercept yields the interface anisotropy contribution [83]

surface magnetic moment contribution as [83]

$$K_{\text{eff}} = K_{\text{v}} + 2K_{\text{s}}/t, \tag{2.4.15}$$

where t is the thickness of the magnetic layer. The positive values of $K_{\text{eff}} \cdot t_{\text{Co}}$ shown in Figure 2.6 indicates that at low ferromagnetic film thickness this structure favors the out-of-plane magnetisation direction. The negative gradient indicates that volume anisotropy contribution K_{v} prefers an in-plane magnetisation direction. The intercept denotes that the K_{s} favours out-of-plane magnetisation - this is an interfacial effect. The critical thickness ($t_\perp$) at which the magnetic anisotropy switches from out-of-plane to in-plane magnetisation direction can be calculated from $t_\perp = -2K_{\text{s}}/K_{\text{v}}$. When the ferromagnetic layers are thin, interface effects become more prominent than bulk effects. Anisotropy values for the same material show different values depending on the growth technique used, growth parameters and structural parameters like interface roughness. Using Pt as a buffer layer enhances the PMA with cobalt when deposited with magnetron sputtering due to the Pt buffer layer promoting growth in the fcc (111) orientation [84]. Furthermore, Pt buffer layer from 0-20 nm increases the PMA linearly. The thickness in Co which can provide an out-of-plane magnetisation is typically in the range 0.5-1 nm [85]. These

are the typical film thicknesses used in this research, and hence this can make detecting signals from single ultra-thin layers somewhat more difficult than for thicker films.

2.5 Dzyaloshinskii-Moriya interaction

In 1957, Dzyaloshinskii constructed a model to describe weak ferromagnetism [86]. Based on symmetries he introduced an antisymmetric exchange interactions term which later on was dubbed the Dzyaloshinskii-Moriya interaction. Moriya connected his name to this term when he found how to calculate this asymmetric exchange interaction (AEI) for localised magnetic systems in a microscopic model [87] that complements the theory investigating the role of the SOI, reaching the conclusion that the general exchange interaction has two components

$$\hat{H}_{ij} = \hat{H}_{ij}^{\text{sym}} + \hat{H}_{ij}^{\text{antisym}}.$$

The first term is the strongest interaction and leads to ferromagnetism even at room temperature where thermal fluctuations can overcome weak interactions like the magnetic dipolar interaction. This term is the symmetric and isotropic exchange interaction which is characterised by J the Heisenberg exchange interaction [13],

$$\hat{H}_{ij}^{\text{sym}} = -J_{ij}\vec{S}_i \cdot \vec{S}_j.$$

The exchange interaction between two neighboring spin moments arises as a consequence of the overlap between the magnetic orbitals of two adjacent atoms and favors collinear spin alignment. This so-called direct exchange interaction is strong in particular for 3d metals, because of the comparatively large extent of the 3d-electron charge cloud. The antisymmetric term that is the the so called Dzyaloshinskii-Moriya Interaction (DMI) is

$$\hat{H}_{ij}^{\text{antisym}} = \vec{S}_i \cdot (\vec{S}_j \times \vec{D_{ij}}) = \vec{D_{ij}} \cdot (\vec{S}_i \times \vec{S}_j),$$

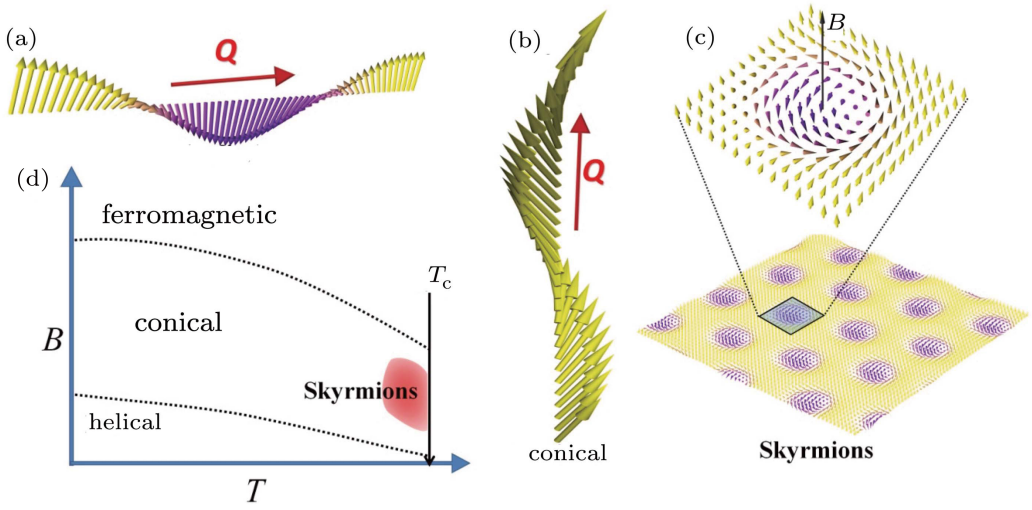

Figure 2.7: Common magnetic phase diagram of bulk helimagnets. Panels (a), (b), and (c) schematically represent the spin configurations of helical, conical, and skyrmion phases, respectively, that develop below the Curie temperature T_c. (d) The phase diagram of magnetic structure in bulk helical magnets [89]

.

where D_{ij} is the Dzyaloshinskii-Moriya (DM) vector, which is perpendicular to both the axis of broken symmetry and the vector connecting two spins. Chirality is a form of asymmetry of the system. When the mirror image of the atomic structure is not identical to the original, it is said that it lacks inversion of symmetry [88]. If the atomic structure of a magnet lacks inversion symmetry we call them chiral magnets. The chirality expresses itself through the phase diagram which shows additional chiral phases which are illustrated in figure 2.7(d). In these phases the magnetisation is "whirled" in some way, e.g. helical as shown in figure 2.7(a). The presence of DMI in a magnetic system favours noncollinear spin alignment — canting the spin alignment — and leads to chiral spin textures. When the DMI is non-negligible, a competition between both exchange and DMI interactions emerges leading to the creation of magnetic phases such helical, conical, bubble, vortex and the so called skyrmion phases (figure 2.7(a-c)). In bulk materials the lack of inversion symmetry in the crystalline structure of these magnets gives rise to weak DMI [90]. For example, in the chiral magnet MnSi the competition of this interaction with the much stronger ferromagnetic exchange results in a twist in the magnetic order, leading to helical order [91]. Since the DM coupling is weak compared to the FM exchange coupling, there are long modulation periods of many lattice constants, e.g.,

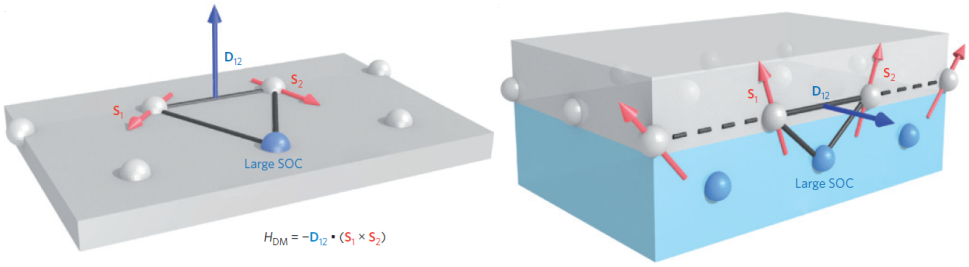

Figure 2.8: Schematic of a DMI generated by indirect exchange for the triangle composed of two atomic spins and an atom with a strong SOC. Sketch of a DMI at the interface between a ferromagnetic metal (grey) and a metal with a strong SOC (blue). The DMI vector D_{12} related to the triangle composed of two magnetic sites and an atom with a large SOC is perpendicular to the plane of the triangle [3].

in the chiral magnet MnSi, the modulation period is about 190 Å, whereas the lattice constant is only 4.6 Å [92]. The competition between these two types of interactions determines the length of the magnetic spirals but not their direction. Consequently, one expects a large ground state degeneracy at zero magnetic field. This degeneracy is, however, lifted by weak magnetocrystalline anisotropy, which provide an easy axis for the ordering wave vector. As a direct consequence, the phase with helical order has a single ordering wave vector. Additionally, if a finite magnetic field is applied, it becomes energetically favorable to have the ordering wave vector point in the direction of the magnetic field. All spins then point in a plane perpendicular to the field, and the system can gain energy by simply tilting all spins continuously out of that plane in the direction of the field, leading to a spiraling umbrella structure. This state is referred to as the conical phase as shown in figure 2.7(c). Depending on the direction of the field, the phase transition between these two phases is either first order or a crossover and occurs at some field value B_{c1} where the energy gain from tilting all spins towards the field [90]. For ultrathin magnetic films, which are the main focus here, interfacial DMIs have been predicted from a 3-site indirect exchange mechanism between two atomic spins S_1 and S_2 with a neighbouring atom having a large SOI [3]. The resulting DMI vector is perpendicular to the plane of the triangle (left-hand side figure 2.8). At the interface between a ferromagnetic thin layer and a metallic layer with a large SOI, this mechanism generates a DMI

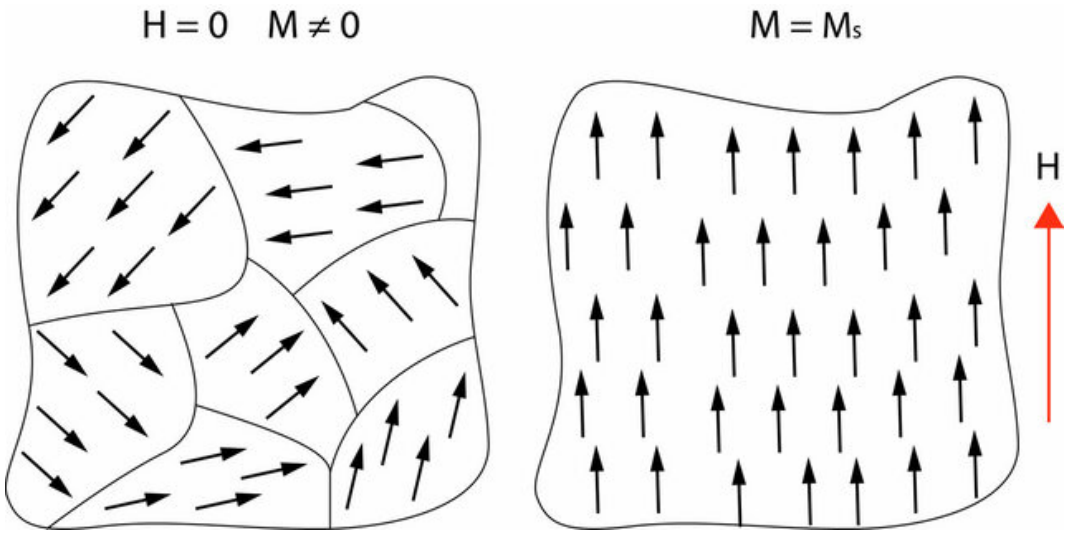

Figure 2.9: Schematic showing the magnetic domains and the spin orientations in zero and externally applied magnetic field H. [93].

for the interface spins S_1 and S_2 with the DMI vector D_{12} shown in the right-hand side figure 2.8. The existence of such an interfacial DMI has also been derived from analytical calculations. The magnitude of the interfacial DMI can be very large, ≈10-20% of the exchange interaction in analytical calculations and up to 30% in ab initio calculations [3].

2.6 Magnetic domains

In the demagnetised state of a ferromagnetic material, its magnetisation breaks into regions with localised collinear alignment of magnetic moments. These are called magnetic domains. The minimum energy comprises of magnetostatic energy, magnetocrystalline energy, magnetostriction energy, Zeeman energy and the exchange interaction defines the characteristic size of the domains as shown in the left-hand side of the figure 2.9 [93]. When a saturating magnetic field is applied to the ferromagnet, the magnetisation points in the direction of the magnetic field as shown in the right-hand side of the figure 2.9. For a ferromagnet in the absence of an external magnetic field, the magnetostatic energy is the magnetic potential generated within the ferromagnet by the interaction of the demagnetising field and the magnetisation. In ferromagnets with uniaxial anisotropy (anisotropy with only one easy magnetisation axis), magnetic moments are expected to be aligned along the easy axis in

the demagnetisation state due to the anisotropy energy. The single domain can be viewed as a magnet that produces a large demagnetizing field. This demagnetisation energy results in a large magnetostatic energy. The large magnetostatic energy can be reduced by splitting the magnetic structure into several regions with antiparallel magnetic moment alignment. Likewise, by introducing small domains in the structure, the magnetostatic energy can be decreased while storing some portion of it in the domain wall. The equilibrium uniaxial domain size d_0 is defined by at the balance between energies as follows:

$$d_0 = L\left(\frac{\sigma_{DW}}{\mu_0 M_S^2 t}\right)$$

where, L is the length and t is the thickness of the single crystal. the domain wall energy density which is described in the next section M_S is the saturation magnetization of the material. The magnetisation energy difference per unit volume between the easy axis and the hard axis is called the magnetic anisotropy energy. Magnetic domains typically form along the easy axis directions [94].

2.6.1 Domain Walls

Domain walls (DW) are the boundaries between the regions of different magnetisation directions called domains. In the simplest case, the width of the DW is defined by the energy balance between the exchange energy and the magnetocrystalline anisotropy energy. In ferromagnetic materials, exchange energy is minimised for parallel alignment of the magnetic moments (eq. 2.4.15). Therefore, a wider domain wall structure is favored by exchange energy. The magnetic moments rotate in small rotation angles (θ) within the domain wall (figure 2.10). In this case, the angle between neighboring magnetic moments is minimised. On the other hand, the anisotropy favors thin domain walls as energetically the magnetic moments prefer to align along the easy axis. The energy trade-off between exchange and anisotropy energies defines the domain wall thickness. In general in DWs, the magnetisation rotates between domains when one travels perpendicularly (direction x) across the DW. Different types of domain walls can be observed in ferromagnetic materials: the

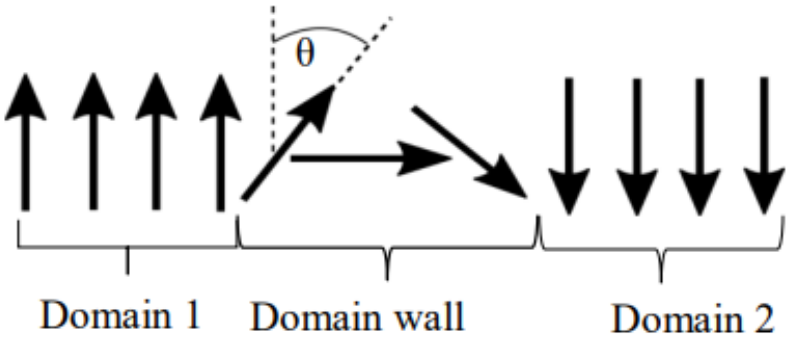

Figure 2.10: Illustration of a 180°DW [75].

simplest magnetic domain wall is the Bloch wall (BW). In this wall, the magnetisation rotates in the plane of the DWs as shown in figure 2.11(a). The DW profile is thus governed by the exchange and the anisotropy energies, the latter being in the ultrathin limit an effective anisotropy incorporating the perpendicular demagnetizing energy. Typical DW widths are of the order of 40 - 100 nm. Alternatively, there are Néel walls (NW). In the NW, the magnetisation rotates orthogonal to the DWs plane as shown in figure 2.11(b), i.e. with the DW normal, x, containing in the magnetisation rotation plane. For perpendicularly magnetised films that are not patterned into nanostrips, the BW does not create volume magnetic charge, whereas the Neel DW does, so that the BW is the lowest energy DW structure [12]. The most energetically favored domain walls are Bloch type of domain walls that can be observed in bulk magnetic materials. In thin films, with in-plane magnetisation, the magnetostatic energy related to the stray field from Bloch walls is comparatively large. Therefore, when the sample thickness is comparable to the domain wall width, Néel type domain wall structure is dominant [12]. The DMI was introduced for low-symmetry crystals. It was shown to favor non-uniform magnetic structures, the so-called skyrmions. In the context of ultrathin films, Fert first mentioned that the symmetry is [3] reduced at the interface. This was confirmed by an extensive analytical study that considered the 2-site and 3-site mechanisms. Quantitative calculations of this interaction by ab initio techniques confirmed its importance for ultrathin films. It has been shown that the DMI changes the nature of the magnetic DW, forcing the existence of Néel walls. Furthermore, another domain wall struc-

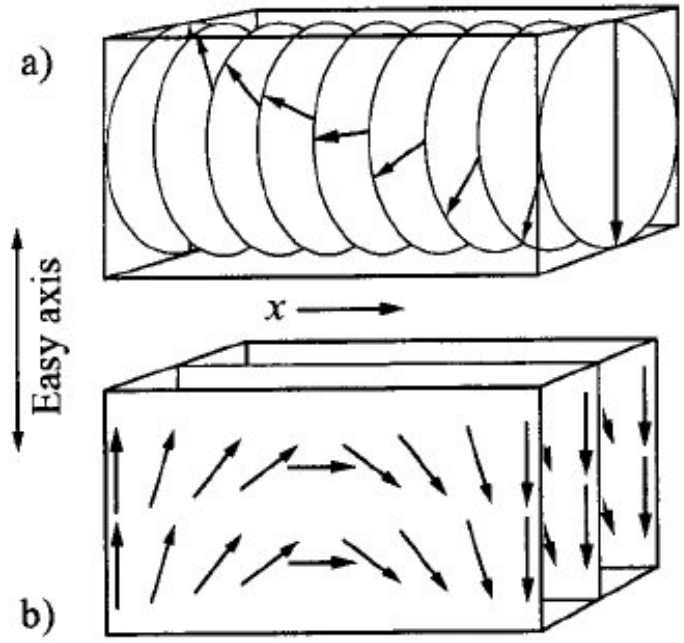

Figure 2.11: Variation of the magnetisation in (a) a Bloch wall or (b) a Néel wall in a planar film where the magnetisation in the domain is parallel to the film plane [95].

ture is possible to find in ultrathin films with perpendicular anisotropy, as a result of uncompensated DMI from the adjacent layers, that Thiaville *et al.* proposed to call Dzyaloshinskii domain wall [12]. Depending on the strength D of this interaction, domain wall magnetisation intermediate between the Bloch and Néel orientation are obtained, turning to Néel at large D.

The DW energy density of a 180° BW can be expressed as the sum of the magnetocrystalline anisotropy energy and the exchange energy as [96]

$$\sigma_{\text{Anisotropy}} + \sigma_{\text{Exchange}} = K_{\text{u}} N a + J s^2 \frac{\pi^2}{N a^2} + \sigma_{\text{DMI}}, \tag{2.6.16}$$

where K_{u} is the uniaxial magnetocrystalline anisotropy, a is the lattice constant, and N is the number of atomic distances within the domain wall. When the DMI strength is negligible the minimized Bloch domain wall thickness Δ_{Bloch} be written as

$$\Delta_{\text{Bloch}} = N_{\text{min}} a \pi \left(\frac{A}{K_{\text{u}}} \right)^{\frac{1}{2}}, \tag{2.6.17}$$

where the exchange stiffness constant $A = \frac{J s^2}{a}$. The 180° Bloch DW energy density

σ_{DW} at the domain wall thickness is

$$\sigma_{\mathrm{Bloch}} = 2\pi(AK_{\mathrm{u}})^{\frac{1}{2}}. \tag{2.6.18}$$

The domain wall energy density of an 180° Néel DW can be written in the same fashion as eq. 2.6.16 however, in this case the DMI is sizeable and favours the Néel DW stabilisation. Furthermore, the magnetostatic energy also contributes in this case as follows [96]

$$\begin{aligned}\sigma_{\mathrm{Anisotropy}} + \sigma_{\mathrm{Exchange}} + \sigma_{\mathrm{Magnetostatic}} = \\ K_{\mathrm{u}}Na + Js^2\frac{\pi^2}{Na^2} + \left(\frac{2\mu_0 M^2}{\pi}\right)Na\arctan\left(\frac{t}{Na}\right) + \sigma_{\mathrm{DMI}}.\end{aligned} \tag{2.6.19}$$

The Néel domain wall thickness $\Delta_{\mathrm{Néel}}$ at the minimum energy density is

$$\Delta_{\mathrm{Néel}} = N_{min}a = \pi\left(\frac{2A}{K_u}\right)^{\frac{1}{2}}; \qquad (t \ll \Delta_{\mathrm{Néel}}) \tag{2.6.20}$$

The NW energy density can be written as

$$\sigma_{\mathrm{Néel}} = \pi t M_{\mathrm{s}}^2 \tag{2.6.21}$$

BW have lower magnetostatic energy than the NW structure. Therefore, the lowest energy domain wall structure in the magnetic films with PMA is achiral BW. In the presence of DMI, the competition between DM energy and the exchange energy defines the minimum energy domain wall configuration. DMI leads to homochiral (right-handed chiral or left-handed chiral) Néel DWs throughout the structure which have been observed [16,17,49,97–99] experimentally. The sign of the DMI determines handedness of chirality. Right-handed chiral domains indicate positive DMI ($D > 0$) and left-handed chirality represents negative DMI ($D < 0$). The chirality can be changed by altering the growth order of the ferromagnetic and the heavy metal layers in the magnetic structure.

2.6.2 Observations of domain walls in thin-film with PMA

The typical size of a domain is in the micron-scale [100]. Microscopy techniques such as transmission electron microscopy, magneto-optical Kerr effect and magnetic force microscopy are used to observe domains and domain walls. In the experiments, the Magneto-optical Kerr effect (MOKE) was used to observe domain structures and their evolution, which is explained in the next chapters. MOKE has many advantages over other methods. It is a non-destructive direct magnetisation observation technique [101, 102]. The observation method does not affect the magnetisation of the sample. It has the capability of observing fast dynamics such as fast domain growth. The same basic experimental setup can be used for domain imaging as well as for characterising material (obtaining hysteresis loops). However, it also has disadvantages such as the spatial resolution limited by the wavelength limit, it is also easy to overcome the Kerr signal by spurious noise and not getting direct information of the electronic structure or magnetic moments [103]. Two different instruments were used in this work (see Chapter 3 and 4). The samples needed to be flat and smooth for the domain observation. Special techniques such as image processing have to be used to enhance the low contrast also, the optical resolution is limited to 3 μm with the apparatus built in this work due to the objective lenses available.

2.6.3 Magnetic field induced domain wall motion

The process of changing the direction of the magnetisation of the magnetic moments gradually without changing the position of the atoms is called DW motion. DWs can be moved either by applying an external magnetic field, H_{ext}, or spin-polarised electric current [104, 105]. Magnetic field-driven domain wall motion arises due to the torque applied to the magnetic moments from the interaction with the external magnetic field. Current induced domain wall motion results from the interaction between the spin angular momenta of the conduction electron and the magnetic moments (spin torque). Experimental implementation of current driven domain walls requires lithographic techniques for contacts needed for injecting current [106, 107].

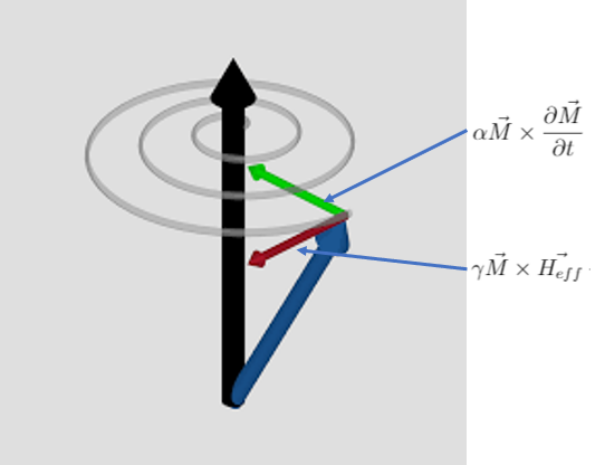

Figure 2.12: Precession of magnetic moments rotation with an external magnetic field. The blue arrow indicates the direction of the magnetic moment and the green and red arrows shows the torques that arises from the external magnetic field. In particular, the damping vector and the precession respectively [108].

Field-driven DW motion to extract DMI and manipulate domains was investigated in this work. The motion of the magnetisation with an external magnetic field can be described by the Landau-Lifshitz-Gilbert (LLG) equation,

$$\frac{\partial \vec{M}}{\partial t} = \gamma \vec{M} \times \vec{H_{\text{eff}}} + \alpha \vec{M} \times \frac{\partial \vec{M}}{\partial t}. \tag{2.6.22}$$

where $\gamma = \frac{ge\mu_0}{2m_e}$ is the gyromagnetic ratio, g is the Landé-like factor, and H_{eff} the effective magnetic field which represents the local field (which is the total effect that comes from all the magnetic energy contributions) felt by the magnetisation. According to Landau-Lifshitz, the magnetisation experience a torque when the applied field is not parallel to the magnetisation direction. That results in magnetisation precession around the field direction. The first term in the eq. 2.6.22 is the torque due to the magnetic field. If the magnetisation experiences only this torque, they will precess endlessly around the external field. Moreover, experiments show that the magnetic moments precession experience damping and relaxation into the effective field direction (figure 2.12 [108]). The Landau-Lifshitz equation was modified by Gilbert adding the damping constant as it is known now [109] and was added the second term in eq. 2.6.22, where α is the damping constant and $\alpha > 0$. Figure 2.13(a) shows when an external magnetic field is applied across the Néel DW, mag-

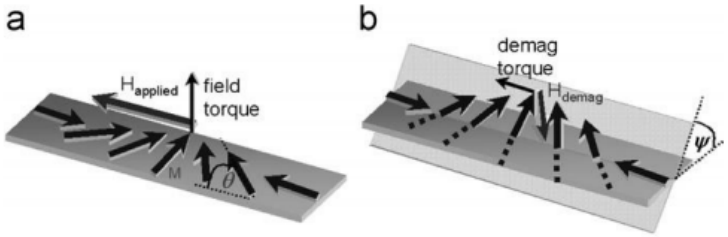

Figure 2.13: DW motion with an external magnetic field [109].

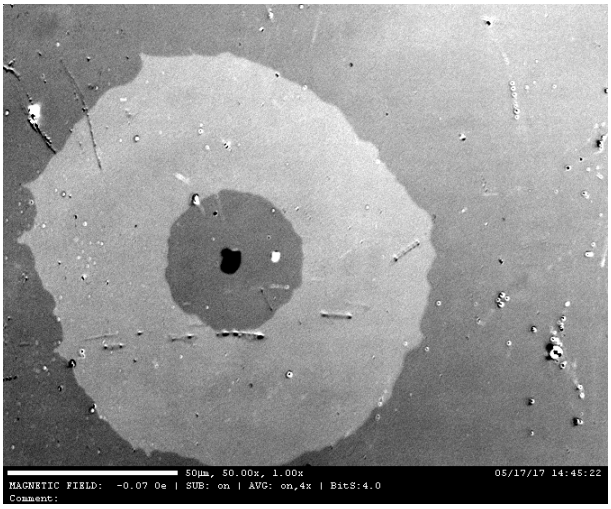

Figure 2.14: Background corrected image taken with a MOKE microscope on a Pt/Co/Pt samples with strong PMA. The dark gray is showing the direction going into the page and the light gray is the one coming out of the page.

netic moments experience a torque which is pointing out of the plane. This torque tilts the magnetisation in the out-of-plane direction and hence produce a demagnetisation field as shown in figure 2.13(b). The interaction between the demagnetisation field and the magnetic moments produces a torque along the external field direction which results in the domain wall motion along the external field direction. Domains in a ferromagnetic material which are parallel to the external magnetic field tend to expand while antiparallel domains shrink due to the interaction between the field and magnetic moments. When the external field is larger than the saturation field H_s, the material becomes a single domain structure with all the magnetic moments aligned along the external field direction creating the saturated state. If the external field strength decreases and slowly increases in the opposite direction, then the magnetic domains nucleate and expand along the reverse direction. The nucleation centres are usually defects or impurities of the structure, and the nucleation

process is a thermally activated process. When the reversed external field becomes larger than the H_s, a single domain can be observed along the reversed field direction. Figure 2.14 shows a MOKE image that demonstrates the different states of the magnetisation. After the nucleation, the domain wall velocity response to the magnetic field can be divided into three main regimes [110], called the creep, depinning and flow regimes and are shown in figure 2.15. At low magnetic fields (creep regime), the behavior of the domain wall motion is defined by the material disorder, defects, and the thermal energy. At zero temperature, domain walls are pinned to the impurities. Impurities are local energy minimum sites. Therefore, domain

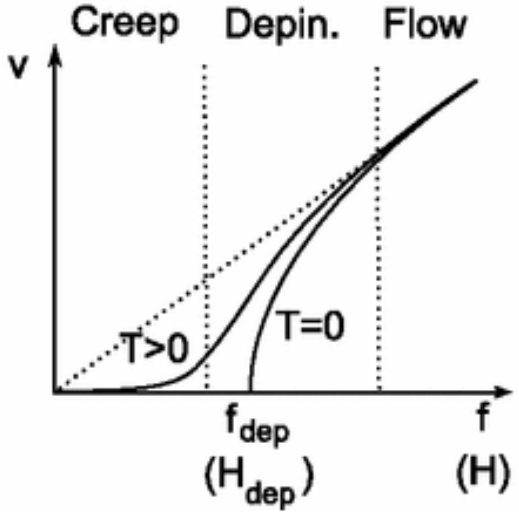

Figure 2.15: The domain wall velocity as a function of external magnetic field, at three different regimes depending the strength of applied magnetic field [111].

walls prefer to stay pinned to impurities, and a low magnetic field which is below the depinning field is not sufficient to unpin the domain walls. However, at finite temperature, thermal energy overcomes the domain wall pinning, and slow domain wall motion can be observed with low magnetic fields. When the magnetic field is greater than the depinning field (in the flow regime), the domain wall motion is independent of the material disorder, and domain wall velocity increases linearly with increasing magnetic field. Domain wall evolution in the creep regime is described in more detail in chapters 4 and 6.

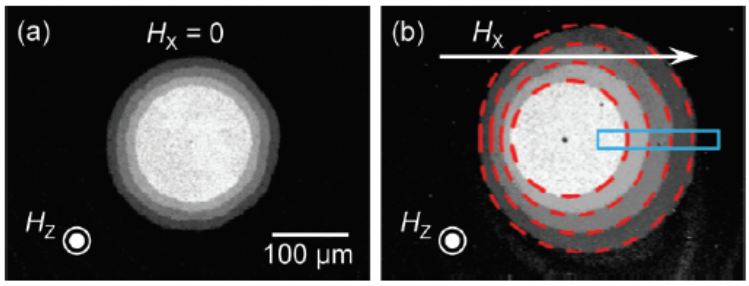

Figure 2.16: Circular DW expansion driven by an out-of-plane magnetic field Hz (3 mT), (a) without an in-plane magnetic field and (b) with an in-plane magnetic field Hx (50 mT). Image were obtained using a MOKE microscope. The white arrow and the symbols indicate the directions of each magnetic field. The blue box in (b) designates where the DW displacement is measured. The dashed red circles in (b) show the calculation results based on eq. 2.6.23 and 2.6.24 with an extension to arbitrary angles [112].

2.6.4 Influence of DMI on DW motion

Domain wall motion equations derived from the LLG equation in the presence of the DMI, in-plane and out-of-plane magnetic fields, and PMA can be written as

$$\frac{\hbar}{\lambda}(1+\alpha^2)\frac{\partial r_{\mathrm{DW}}}{\partial t} = Qg\alpha H_z + \frac{\pi}{2}\left(\frac{H_{\mathrm{DMI}}}{\lambda} - QhH_x\right)\sin\phi_0, \tag{2.6.23}$$

$$\frac{\hbar}{\lambda}(1+\alpha^2)\frac{\partial \phi_0}{\partial t} = -gH_z + \frac{\pi}{2}\alpha\left(Q\frac{H_{\mathrm{DMI}}}{\lambda} - ghH_x\right)\sin\phi_0, \tag{2.6.24}$$

where α is the Gilbert damping constant, r_{DW} is the DW position, Q is the domain wall charge [128], ϕ_0 is the azimuthal DW angle, H_z is the out-of-plane magnetic field, H_x is the in-plane field, λ the magnetostriction constant, $\hbar$ is the reduced Planck constant and H_{DMI} is the DMI field. Figure 2.16 shows of the numerical solutions of eq. 2.6.23 and 2.6.24 in 2D systems show asymmetric domain wall expansion due to the DMI field and in-plane magnetic field.

2.6.5 Creep theory

Creep theory describes very slow motion of interface or boundary between two different regions under very weak driving forces, and it is seen in various systems including superconductors, ferromagnets, ferroelectrics, and soft matter. In particular for ferromagnetic materials, it can be used to describe the thermally activated slow change in the microscopic magnetic domain structure. Interfacial defects and grain disorder

at the surface of actual samples cannot be integrated into the LLG model. However, Creep theory can implement in-plane and DMI fields while describing the motion of the DW. Therefore, creep theory is more appropriate than the LLG model to explain the experimental data. Creep theory is used in this thesis to investigate the DMI field in magnetic multilayers in the presence of in-plane and out-of-plane fields. A detailed description of creep theory with domain wall energy density and the methodology can be found in Chapter 4.

2.7 Summary

This chapter is focused on the background theory of magnetism and magnetic domain walls. It begins with the Hund's rules which help to determine the quantum number for the ground state of atoms. Simple interactions in material such as spin-orbit and the Dzyaloshinskii-Moriya interaction following by theories of ferromagnetism were discussed. Finally, domain wall theories and the effect of the DMI on the propagation of the magnetic domains was introduced.

Chapter 3

Experimental techniques

This chapter discusses the experimental methods used for the realisation of this project, from the fabrication of the thin-films to the characterisation methods to extracting the structural and magnetic properties of thin films. Firstly, the deposition technique is discussed, then the investigation techniques used to probe the structure of thin films. Grazing incidence x-ray reflectivity gives structural information from the layers and interfaces with sensitivity to thickness of layer, interface roughness and interfacial intermixing. Polarised neutron reflectivity provides the magnetic depth profile through the thin-films. X-ray magnetic resonance reflectivity has been used as an element-specific technique that can extract the magnetic moment. Magneto-optical Kerr effect magnetrometry provides information on the magnetisation orientation as a function of applied field. Similarly, Brillouin light scattering and ferromagnetic resonance will provide information about the dynamics of the magnetisation.

3.1 Preparation of thin films

This section explains the procedure and the experimental method to elaborate the thin films on which this thesis is based. Starting with the deposition method - magnetron sputtering was used here. Sputtering is used extensively in the microelectronics industry to deposit thin films of various materials in integrated circuit processing. When lithography was used in this research, this process was completed

in a class 1000 clean room facility at Durham university Engineering department using optical lithography. The photolithography transfers a pattern from a mask to a photosensitive layer. This is done by coating the sample with the photoresist using the spinner and, then, the sample is placed in the Mask Aligner, where a mask is place over the sample to transfer the pattern by illuminating with the ultraviolet light source. Next, the resist is stripped (removed) by placing the sample in the developer that removes the illuminated regions of photoresist on the sample. For the photolithography, the process involved the use of the positive photoresist spinner and the EVG620 Mask Mligner. Following the process, the samples are ready for deposition. Depositions were made onto Si/SiO_2 substrates. Prior to deposition and lithography, the substrates were diced into appropriate sizes using a diamond scribe and then cleaned in acetone and then isopropan-2-ol using ultrasonic agitation for 180 seconds approximately. The chips were then dried with dry nitrogen gas.

In the next section the process of sputtering is presented. Following this a description of the fabrication processing used to make the samples in chapter 7 is given, namely, optical lithography and wire bonding for electrical connections to the samples.

3.1.1 The magnetron sputtering deposition method

Sputtering deposition involves the ejection of atoms or molecules of a material from a target by the bombardment of high-energy particles as shown in figure 3.1. It is a popular deposition technique due to its versatility. In many cases, sputtered films now outperform films deposited by other physical vapour deposition (PVD) processes, and can offer the same functionality as much thicker films produced by other surface coating techniques [113]. Sputtering requires a number of criteria. Firstly, ions of sufficient energy must be created and directed towards the surface of a target to eject atoms from the material. Secondly, ejected atoms must be able to move freely towards the object to be coated with little impedance to their movement. Therefore sputter coating is a vacuum process: low pressures are required to maintain high ion energies and to prevent too many atom-gas collisions after ejection from the target. A magnetron source relies on the fact that primary and

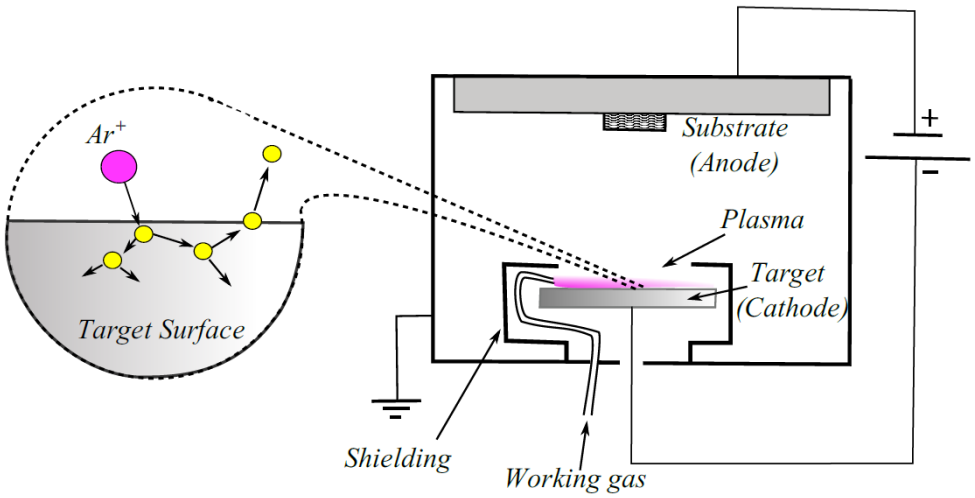

Figure 3.1: Schematic demonstrating the key features of the sputtering system. The voltage can be as large as 600 V in order to ionise the Ar working gas. Collisions between the Ar^+ ions and the target causes the ejection of atoms from the target surface which then condense on the substrate and vacuum chamber walls. [26]

secondary electrons are trapped in a localised region close to the cathode into an continuous "racetrack". This increases the chance of an ionising collision with a gas atom taking place and so the ionisation efficiency is increased. This results in a drop of the impedance of the plasma and the magnetron source operates at much lower voltages than diode systems (500-600 V as compared with several kV).

All cathodic processes require a plasma or glow discharge in order to work. The plasma may be generated by DC or RF power. The substrate onto which the sputtered film will be deposited is placed face down in the main chamber of the sputtering system and the material is deposited onto it.

Technical details of the sputtering system

The model used for this project was Mantis Qprep500 sputtering system as shown in figure 3.2. The sputtering system operates in ultra high vacuum (UHV) with a base pressure of the order 1×10^{-8} Torr. The system consist of two chambers divided by a gate valve: the sample load-lock and the main deposition chamber. The load-lock allows the user to transfer the sample into the system without venting the main chamber. The UHV is reached using a turbo-molecular pump in each chamber. These are connected by backing lines to oil-less scroll pumps (backing pumps). The process of pumping down the system starts with the backing pumps

reaching a pressure of 10 Torr, after which the turbo pumps are switch on. The turbo-molecular pumps are likely to stall if operated at a higher pressure since the mean free path of the gas molecules would be less than the spacing between the rotary blades, which results in a pressure accumulation at the rear of the pump. Performing maintenance on the system or changing the target material requires venting the system to atmosphere. The process consists of switching off the turbo-molecular pumps and once the pumps have stopped rotating, opening the vent valves to introduce dry nitrogen to the chamber. This helps reduce the adsorption of water vapour onto the chamber walls. Having two chambers allows opening the gate valve without significant contamination to the main chamber vacuum once the load-lock has reached a pressure below 7×10^{-6} Torr.

The system has five magnetron sources (targets) which allows a choice from five different materials at the same time. To power these, there are two DC supplies and one RF supply, which are switched between sources using relay circuits. Both the targets and the turbo-molecular pumps are water cooled. Also, each target has an argon gas inlet line, for which the flow rate is controlled using a mass-flow controller. During the deposition process, the sample is rotated to help produce a uniform deposition. The deposition rate from each target is measured in-situ using a quartz crystal monitor that is calibrated with x-ray reflectivity (XRR); discussed in the next section.

3.2 X-ray reflectivity of thin films

Electromagnetic radiation incident on a material is scattered from the electron cloud of an atom, which is driven into oscillation by the absorption of an incident photon energy. This oscillation then acts as a source, instantly re-radiating a photon with the same energy in an elastic process known as non-resonant Thomson scattering. In the case where the incident photon energy is sufficient to promote an electron to an incompletely filled orbital the atom transitions to an excited state in a process known as absorption. Illumination of a material containing many atoms shows both scattering and absorption effects, better described in terms of waves which propagate

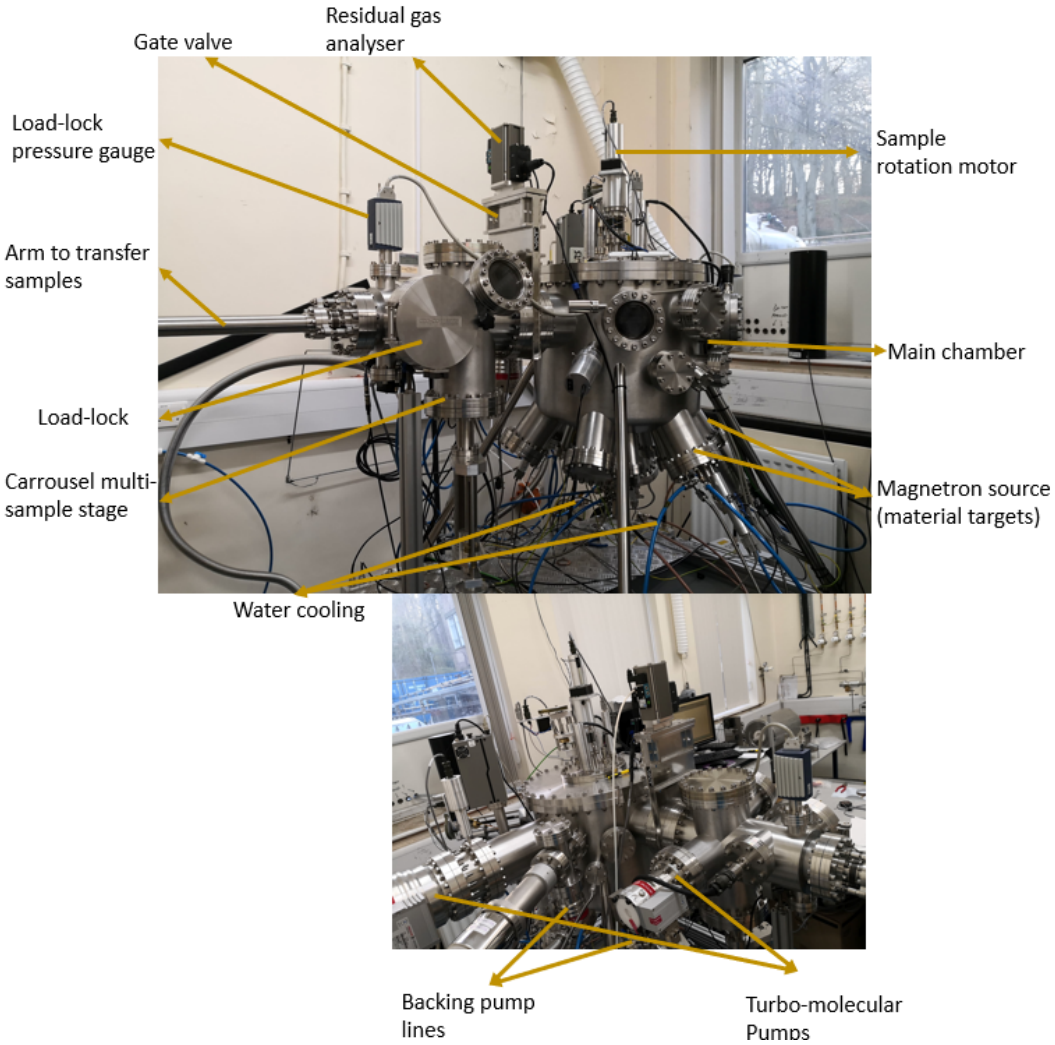

Figure 3.2: Front view and back view of the Mantis Qprep500 sputtering system, where the key features are labelled.

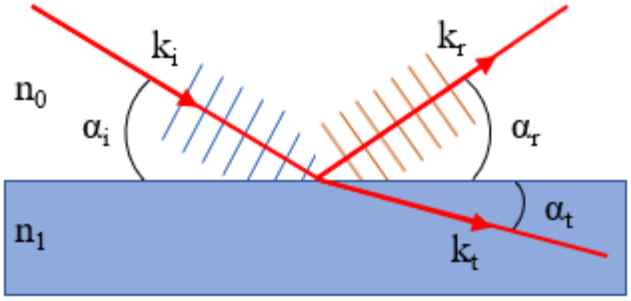

Figure 3.3: Schematic showing the wavefronts and wavevector, k, of an incident x-ray beam at angle α_i that is reflected and transmitted from an interface between materials of refractive index n_0 and n_1.

in all directions. These waves interfere with each other in such a way that it is possible to determine the material structure by measuring the scattered beam from a sample. Grazing incidence x-ray reflectivity (XRR) is a well established scattering technique for determining the layered structure of thin films. The scattering of x-rays from a surface results in both reflection and transmission of the beam, as illustrated schematically in figure 3.3. The angles of the reflected, α_r, and transmitted, α_t, beams depend on both the incident beam angle, α_i, and the refractive indices either side of the surface, n_0 and n_1. Furthermore, the condition for specular reflectivity is such that the incidence angle is equal to the reflected angle, consequently the total wave vector transfer is in the normal direction to the film. The Fresnel equations for reflection and transmission describe how electromagnetic waves travel between layers of different refractive index. However, the derivation of these equations assume that the surfaces and interfaces are perfectly smooth. Real films present two contributions to the interfacial roughness σ: topographical roughness, σ_top, and intermixing, σ_int. Figure 3.4 illustrates that these contributions to the interface width give rise to the same distribution in electron density along the z-direction and are therefore indistinguishable with specular XRR. The interface width is defined as [26]

$$\sigma = \sqrt{\sigma_\mathrm{top}^2 + \sigma_\mathrm{int}^2}.$$

Figure 3.5 shows the quantitative information that can be obtain such as the layer thickness, interface width and layer density. The penetration of x-rays into a

sample allows subsurface layers and interfaces to be characterised non-destructively. The following sections briefly introduce the general theory behind x-ray scattering and the measurement geometry. Derivations are not included since the purpose of this chapter is to introduce the important equations and concepts used in the fitting procedure for the XRR analysis. However, detailed discussions of the XRR technique and analysis can be found in [114].

3.2.1 Principles of specular reflectivity

The refractive index of a substance in the x-ray region of the spectrum is slightly less than one. If an x-ray beam strikes a substance with a flat surface at an incident angle equal to or less than the critical angle, θ_c, then total external reflection will occur. The refractive index n of a material for x-rays can be calculated using:

$$n = 1 - \delta - i\beta. \tag{3.2.1}$$

The real and imaginary components, δ and β, describe the dispersive and absorptive aspects of the wave-matter interaction. Similarly, following Parratt's recursive formalism for the multilayer case [114],

$$\delta = \left(\frac{r_e\lambda^2}{2\pi}\right) N_0\rho \sum_i x_i(Z_i + f_i'(E))/\sum_i x_i M_i \tag{3.2.2}$$

and

$$\beta = \left(\frac{r_e\lambda^2}{2\pi}\right) N_0\rho \sum_i x_i(Z_i + f_i''(E))/\sum_i x_i M_i, \tag{3.2.3}$$

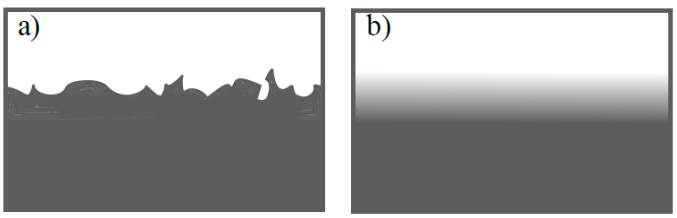

Figure 3.4: Schematic representations comparing a) a topographically rough interface and b) an intermixed interface. If the interface width σ is the same, both the topographically rough and intermixed profiles can give rise to the same electron density profiles.

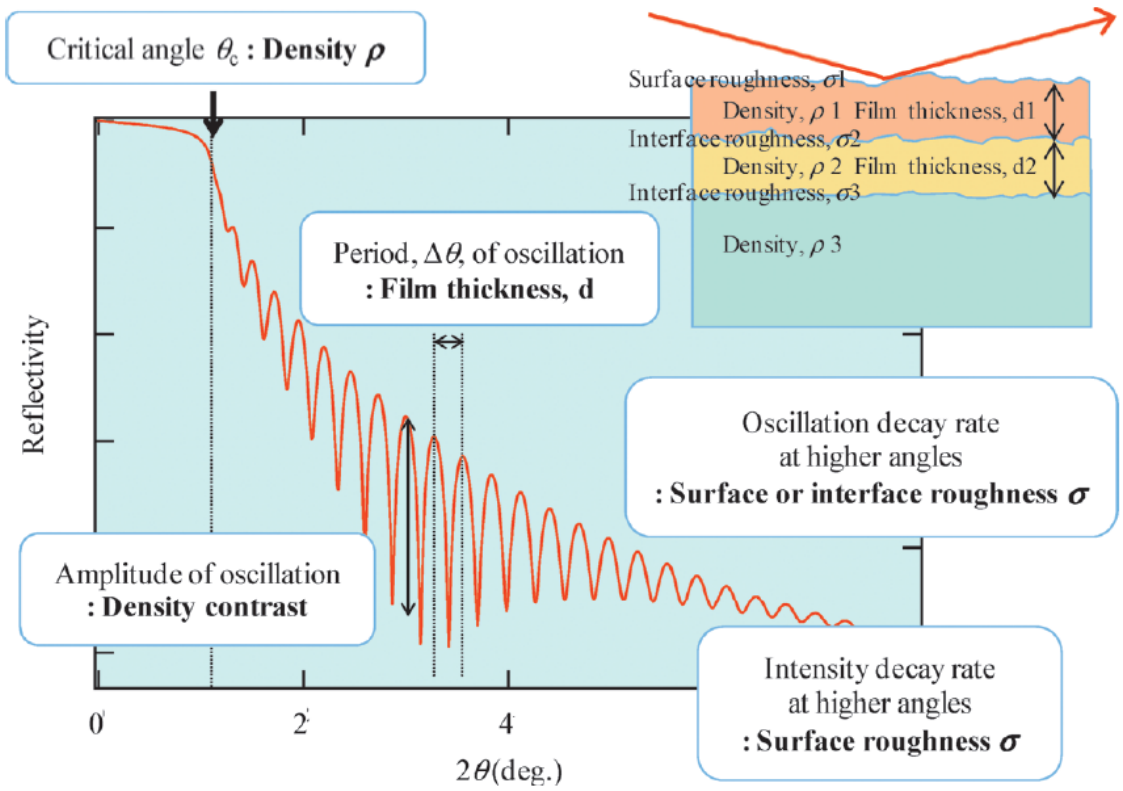

Figure 3.5: Information provided by x-ray reflectivity profile [114]

where r_e is the classical radius of the electron (2.818×10^{-9} m), N_0 is the Avogadro number, λ is the x-ray wavelength, ρ is the density, Z_i is the atomic number of the i-th atom, M_i is the atomic mass of the i-th atom, x_i is the atomic ratio (molar ratio) of the i-th atom and $f'(f'')$ is the atomic scattering factor (anomalous scattering factor) of the i-th atom and has an energy dependence. As shown in eq. 3.2.2 the refractive index is expressed as a complex number. The value of the parameter δ in the formula ranges from 10^{-5} to 10^{-6} for x-rays with energy and wavelength approximately 1 Å and 10 keV respectively. Also, δ depends on the x-ray wavelength and the density and composition of the material. The parameter β is related to the x-ray absorption, expressed by the linear absorption coefficient μ as

$$\beta = \lambda\mu/4\pi.$$

Now, using Snell's law, the critical angle for total external reflection case is given by

$$\alpha_{\mathbf{c}} = \sqrt{2\delta},$$

above $\alpha_{\mathbf{c}}$ x-rays penetrate the surface. Interference of x-rays reflected from the substrate and surface gives rise to Kiessig fringes and the spacing of these fringes is inversely proportional to the total film thickness. They occur when the requirement for constructive interference is satisfied, which is given by

$$d \sin \alpha_{\mathbf{t}} = m\lambda, \tag{3.2.4}$$

where d is the characteristic spacing in the layer structure in thin films and m is a positive integer. Eq. 3.2.4 is analogous to Bragg's law for diffraction from atomic planes but instead for multilayer interfaces. X-ray reflections occur at all interfaces in a multilayer film. The x-ray reflectivity of a multilayer film as a function of θ can be theoretically calculated using equation eq. 3.2.5. In eq. 3.2.5, the vacuum or gas phase on the top of the film with n layers is regarded as the $j = 1^{\text{st}}$ layer. Each layer in the multilayer film is numbered in sequence starting with $j = 2$, and the substrate is considered as the j= n + 1 layer. When the reflection coefficient at the interface between the j^{th} and $(j+1)^{\text{th}}$ layers is defined as $\mathrm{R}_{j,j+1}$, the value of $\mathrm{R}_{j,j+1}$ can be calculated using the recurrence formula [114]

$$R_{j,j+1} = \frac{R_{j+1,j+2} + F_{j,j+1}}{R_{j+1,j+2} \times F_{j,j+1} + 1} a_j^4, \tag{3.2.5}$$

with

$$F_{j,j+1} = \frac{g_j - g_{j+1}}{g_j + g_{j+1}} \left(\frac{-8\pi g_j g_{j+1} \sigma_{j+1}^2}{\lambda^2} \right), \tag{3.2.6}$$

$$a_j = \exp -i\pi g_j d_j / \lambda \tag{3.2.7}$$

and

$$g_j = \sqrt{n_i^2 - \cos^2 \theta}. \tag{3.2.8}$$

The recurrence eq. 3.2.5 together with eqs. 3.2.6 to 3.2.7, can be used to calculate the values of $R_{j,j+1}$ first starting at the interface with the substrate, and then the next upper interface in sequence up to the surface layer. The x-ray reflectivity I/I_0 is calculated last. It is assumed that the substrate is of semi-infinite thickness.

3.3 X-ray resonant magnetic reflectivity

XRR is sensitive to the sample structure and can be used to obtain the cross-sectional profile of the sample. Additionally, x-ray magnetic circular dichroism (XMCD) can be used by tuning the x-rays to a resonant energy of electronic transitions and using circularly polarised light. The name of this combination of these techniques is x-ray resonance magnetic reflectivity (XRMR), which can be used to extract the magnetic cross-sectional profile and it is element-specific because the x-ray energy is tuned to be resonant to an atomic transition. XRMR was used to study the interfacial proximity induced magnetisation in chapter 5.

3.3.1 Resonant magnetic scattering

From the previous section the refractive index in eq. 3.2.1 contains of the absorptive and dispersive terms δ and β, which were described by eq. 3.2.3 and 3.2.4 respectively. These terms are energy dependent. For grazing incidence XRR the first term of the sum was sufficient and $f_0 \approx Z$. The anomalous charge scattering lengths, $f'(E)$ and $f''(E)$, have weak energy dependence, except at the resonant energy where they are associated with strong absorption as shown in figure 3.6 [115].

From eqs. 3.2.1 to 3.2.4, it can be seen that the refractive index, and consequently the reflectivity, depend on the product of the total scattering length and atomic density ρ. This product is referred to as the structural scattering length density (sSLD). The sSLD is specific to each material. It gives quantitative information of the structural cross section of the sample. In analogy to the resonant charge scattering lengths $f'(E)$ and $f''(E)$, resonant magnetic scattering lengths $m'(E)$ and $m''(E)$ can also be included in the description of the refractive index. The complete expression for the total scattering length, within the dipole approximation, becomes

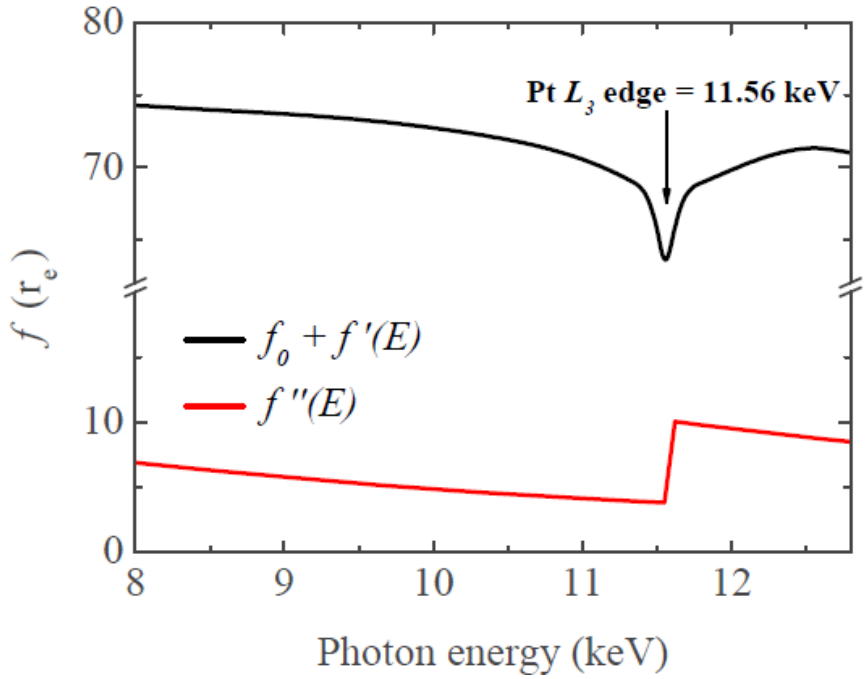

Figure 3.6: Calculated energy dependence of the real and imaginary components of the scattering length for Pt. Data reproduced from the NIST scattering length database [116]and plot was taken from [26].

$$f(E) = (\hat{\epsilon}_s \cdot \hat{\epsilon}_i)F^0(E) - i(\hat{\epsilon}_s \times \hat{\epsilon}_i) \cdot \hat{m}F^1(E). \tag{3.3.9}$$

Here $\hat{\epsilon_i}$ and $\hat{\epsilon_s}$ are unit vectors indicating the polarisation state of the incident and scattered x-rays respectively, F^0 is the total charge scattering length, comprised of both real, $f_0 + f'(E)$, and imaginary, $f''(E)$, parts and F^1 is the equivalent total magnetic scattering length, containing analogous real $m'(E)$ and imaginary $m''(E)$ components. Accordingly, the refractive index is a function of the direction of $\hat{m}$ and the polarisation of the beam. This representation can then be incorporated into Parratt's recursive formalism whereby reversing the magnetisation or the x-ray polarisation helicity results in a change in the XRMR intensity. The magnetic scattering length density (mSLD) is defined as the product of the magnetic density and the magnetic scattering factors, $m'(E)$ and $m''(E)$, where the magnetic density is the product of the magnetic moment μ and the atomic density ρ. In analogy to the sSLD profiles, an mSLD profile is representative of the distribution of magnetised resonant atoms throughout the sample.

Resonant circular dichroic effect

The modern definition of dichroism is the polarisation dependence of the light absorption by a material. Dichroism occurs when the material's symmetry is broken. Circular dichroism is enabled by breaking either the inversion or the time-reversal symmetry. In non-centrosymmetric crystals the parity-odd symmetry permits natural circular dichroism. Here, we will only treat the XMCD originating from time-reversal symmetry breaking by a magnetic ordering.

In a simple picture, XMCD can be described as a two-step process [117]. The $2p$ core state of a $3d$ metal is split in a $j = 3/2$ level (L_3 edge) and $j = 1/2$ level (L_2 edge), where spin and orbit are coupled parallel and antiparallel, respectively as shown in figure 3.7 and the edges refer to excitation between the core state and the Fermi energy. In the first step, the emission with the light helicity vector parallel (antiparallel) to the $2p$ orbital moment results in excited electrons of preferred spin up (down) direction. In the second step the excited electron has to find its place in the unoccupied $3d$ conduction band, and if there are less spin-up than spin-down holes available, the XMCD spectrum has a net negative L_3 and positive L_2 peak. In a more sophisticated picture, the polarisation dependent selection rules give rise to a multiplet structure, which can serve as a fingerprint for the ground state electronic and magnetic structure.

The effect is dependent on the transitions from the spin-split core states to the conduction state above the Fermi energy. Therefore, F^1 in eq. 3.3.9 plays a dominant role only when the x-ray energy is close to the resonant energy. Only the m'' in eq. 3.2.12 contributes to the absorption and is measured directly using the XMCD. On the other hand, when measuring XRMR, the magnetic sensitivity arises through the combination of absorption and re-emission, which then depends on both m' and m'' and hence these factors cannot be isolated independently. For this reason absolute values for magnetic moments cannot be extracted using XRMR alone. The F^1 term is linear in magnetisation, hence by measuring the scattering intensity under positive/negative magnetisation or left circularly polarised (LCP)/right circularly polarised (RCP) helicity, the magnetic contribution to scattering can be isolated [118].

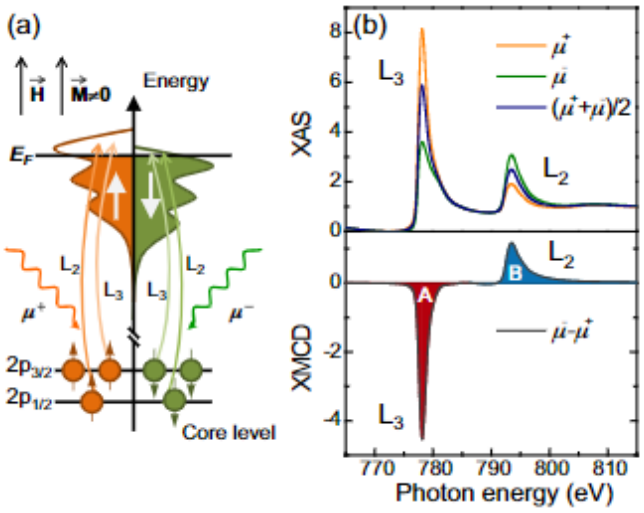

Figure 3.7: (a) Diagram of the two-step picture of XMCD for a single-electron in the resonant excitation process for a magnetic material. In the first step, a circularly polarised photon excites a spin polarised electron from the spin-orbit split $2p$ level (Fano-effect). From the $2p_{3/2}$ level (L_3 edge) x-rays with positive helicity ($q = +1$) excite 62.5 % spin up electrons and those with negative helicity ($q = -1$) excite 37.5 % spin-up electrons, while the $2p_{1/2}$ level (L_2 edge) $q = +1$ gives 25 % spin-up and $q = -1$ gives 75 % spin-up. Note that the minority spin direction (= majority hole spin direction) is the same as that of the sample direction. In the second step the spin polarised electrons have to find a place in the unoccupied $3d$ band (Pt is $5d$), resulting in a difference if the $3d$ electrons are spin polarised. (b) x-ray absorption at the Co $L_{2,3}$ edge for right (μ^+) and left (μ^-) circular polarisation together with the difference spectrum: the XMCD. [117]

3.3.2 Spin-asymmetry measurements

The principle difference between conventional XRR and XRMR is that circularly polarised x-rays were used in the latter, the x-ray energy was tuned to a resonant absorption edge and the difference in scattering intensity under positive/negative magnetic saturation or alternatively RCP/LCP x-rays was determined. The experimental arrangement is otherwise very similar. Here the measurements were made on the XMaS beam line at the European Synchrotron Radiation Facility (ESRF). The reflected intensities $I^{+(-)}$, corresponding to beam helicity parallel (antiparallel) to the saturating in-plane magnetic field applied in the scattering plane, were measured as a function of the scattering angle 2θ. The derived spin asymmetry is

$$\text{Spin asymmetry} = \frac{I^+ - I^-}{I^+ + I^-}.$$

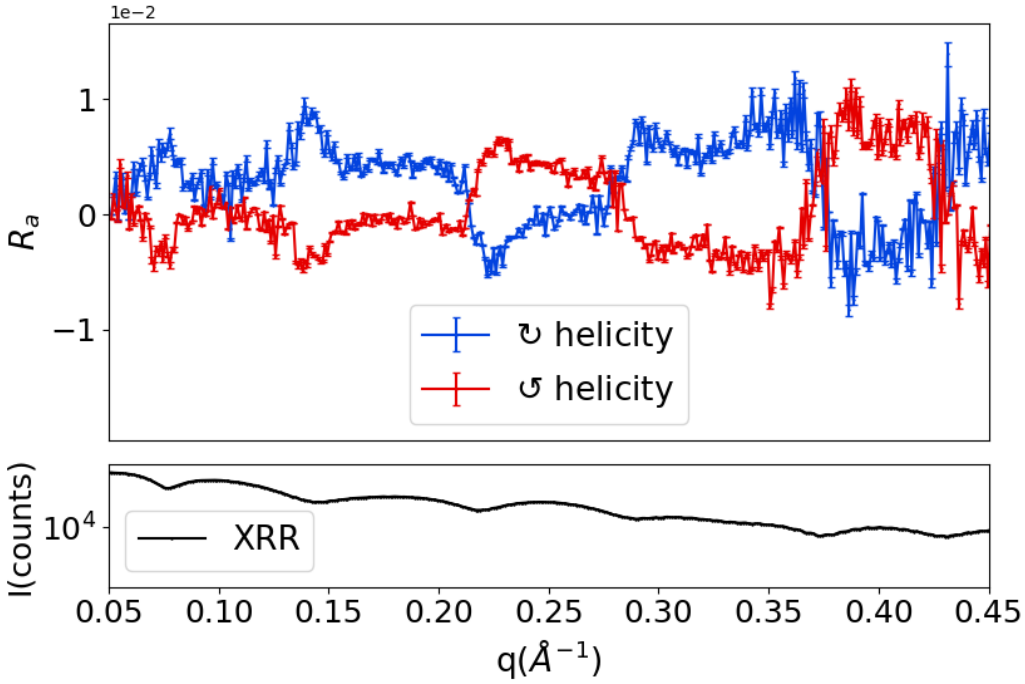

Figure 3.8: A typical measurement of the angular dependence of spin asymmetry. Obtained by reversing the magnetisation at each x-ray incidence angle θ. Reversing the light helicity and repeating the measurement caused a reflection in the x-axis.

Circularly polarised x-rays were obtained using a diamond phase plate. Close to the Bragg condition, a perfect crystal of a birefringent material can behave as a phase retarder and convert linearly polarised light into circularly polarised light and vice versa, when the phase retardation is equal to $\pm\pi/2$. In figure 3.8, there is an example of a measurement for a Ta/Pt/Co_2FeAl/MgO/Ta multilayer structure measured at the Pt L_3-edge. Note that the peaks in the spin asymmetry coincide with the Kiessig minima, this is because the spin asymmetry contains the normalisation to the total scattered intensity. This technique was used to measure the proximity polarisation of Pt in chapter 5.

The interaction of light with magnetism is not restricted to the x-ray region of the electromagnetic spectrum. In the next section the magneto-optical Kerr effect is introduced, which occurs in the visible part of the spectrum.

3.4 Magneto-optical Kerr effect

The microscopic origin of the magneto-optical Kerr effect (MOKE) is the same as XMCD and XRMR effects in the x-ray part of the electromagnetic spectrum. The angular momentum of the light interacts with the orbital moment of the electrons which is coupled to the spin through the spin-orbit interaction [119]. The MOKE occurs in the optical region and the excitations originate from the conduction bands rather than the low lying core states. The rotation of the plane of polarised light passing through magnetic material was first reported by Faraday [120] which was followed by the discovery of a similar effect for the reflection of light by Kerr [121]. For MOKE magnetometry, linearly polarised light is used, which itself can be expressed as the sum of LCP and RCP components. The angle of the polarisation axis of the linear polarisation is dependent on the phase difference between the LCP and RCP contributions. The MOKE arises due to the difference in the effective refractive index experienced by LCP and RCP light within a magnetised medium. This phenomena is referred to as circular birefringence. The consequence of this is that, after reflection from a magnetic surface, a phase difference develops between the LCP and RCP light, which results in a rotation of the linear polarisation axis. This rotation is referred to as the Kerr rotation. Alongside this, it is usual that some degree of ellipticity also develops after reflection as a consequence of the material exhibiting a degree of circular dichroism. The origin of the circular birefringence, and therefore the MOKE, is due to the combination of the exchange interaction and the spin-orbit interaction in ferromagnetic materials. The effective refractive index for LCP and RCP has a dependence on the magnetisation of the film and hence the Kerr rotation can be used to probe the magnetic state of the sample. A more detailed understanding of the origin of MOKE requires a deep discussion of dielectric tensor theory that is not necessary in this thesis, which can be found in [122].

3.4.1 MOKE geometries

Dependent on the choice of measurement geometry the MOKE is sensitive to different components of magnetisation with respect to the plane of the sample. They are

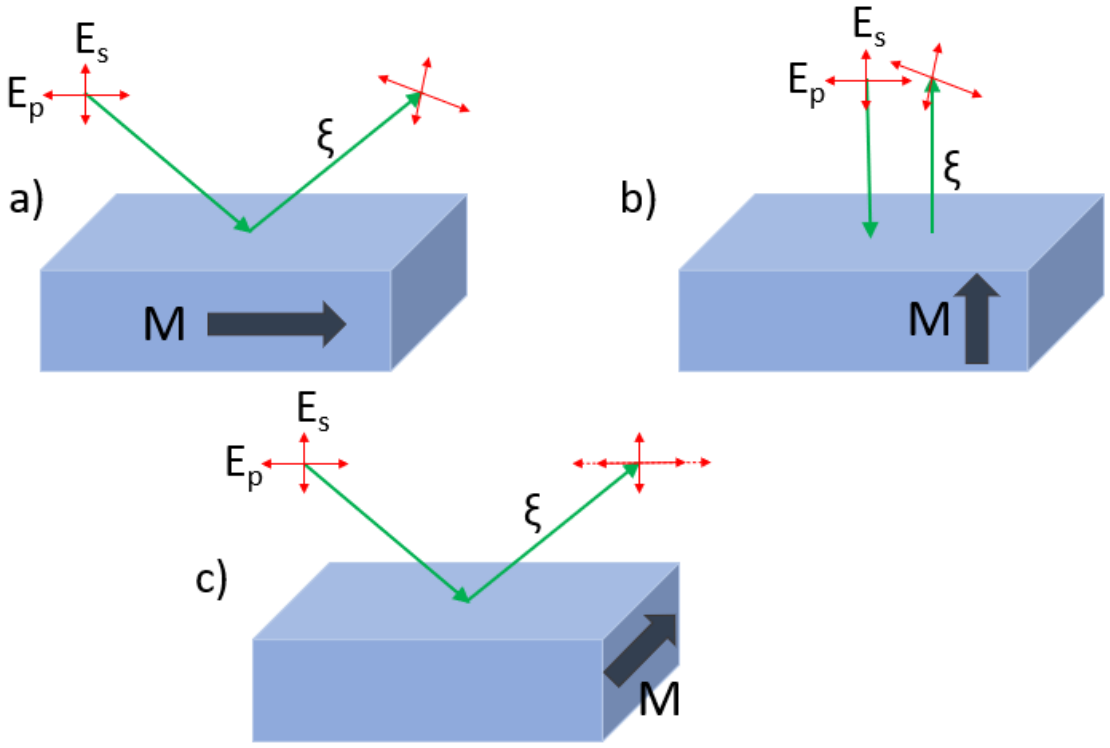

Figure 3.9: MOKE geometries. a) Longitudinal, b) polar and c) transverse which only occurs with *p*-polarised light.

longitudinal, polar and transverse geometries (shown in figure 3.9) and are sensitive to different components of magnetisation. The Kerr rotation only occurs if there is a component of magnetisation along the scattering vector. In-plane magnetisation measurements are possible with longitudinal and transverse MOKE. Out-of-plane magnetisation measurements are done with polar MOKE. The transverse MOKE is unique in that it only occurs with p-polarised light. It does not result in a Kerr rotation, since no component of M lies along the scattering vector ξ, but instead it gives rise to a magnetisation dependent intensity variation as shown in figure 3.9. Most of the measurements performed here used polar MOKE to probe magnetisation perpendicular to the sample plane, however longitudinal MOKE was also used for in-plane magnetised samples.

3.4.2 Penetration depth

In a metallic thin film, the MOKE is sensitive only to the magnetisation within around 20 nm of the sample surface. This is because the effect is limited by the penetration depth of the light into the sample. The penetration depth is given by

$$\lambda_{\mathrm{MOKE}} = \frac{1}{2k\beta} \tag{3.4.10}$$

where k is the wave vector of incident light and β relates to the absorption component of the refractive index. At the depth given by λ_{MOKE} the laser intensity is attenuated to $1/e$ of its original value. For film thicknesses below λ_{MOKE} the Kerr rotation is proportional to the total magnetic moment of the sample, and hence is proportional to the sample thickness. However, extracting absolute magnetic moments from the MOKE is challenging since it is significantly affected by reflections that occur at the ferromagnet/substrate interface. For film thicknesses above λ_{MOKE}, the Kerr rotation is limited by the absorptive component.

3.4.3 Experimental set-up

Figure 3.10 shows the experimental setup for both longitudinal and polar MOKE used in this thesis. For the polar MOKE the laser was incident on the sample at

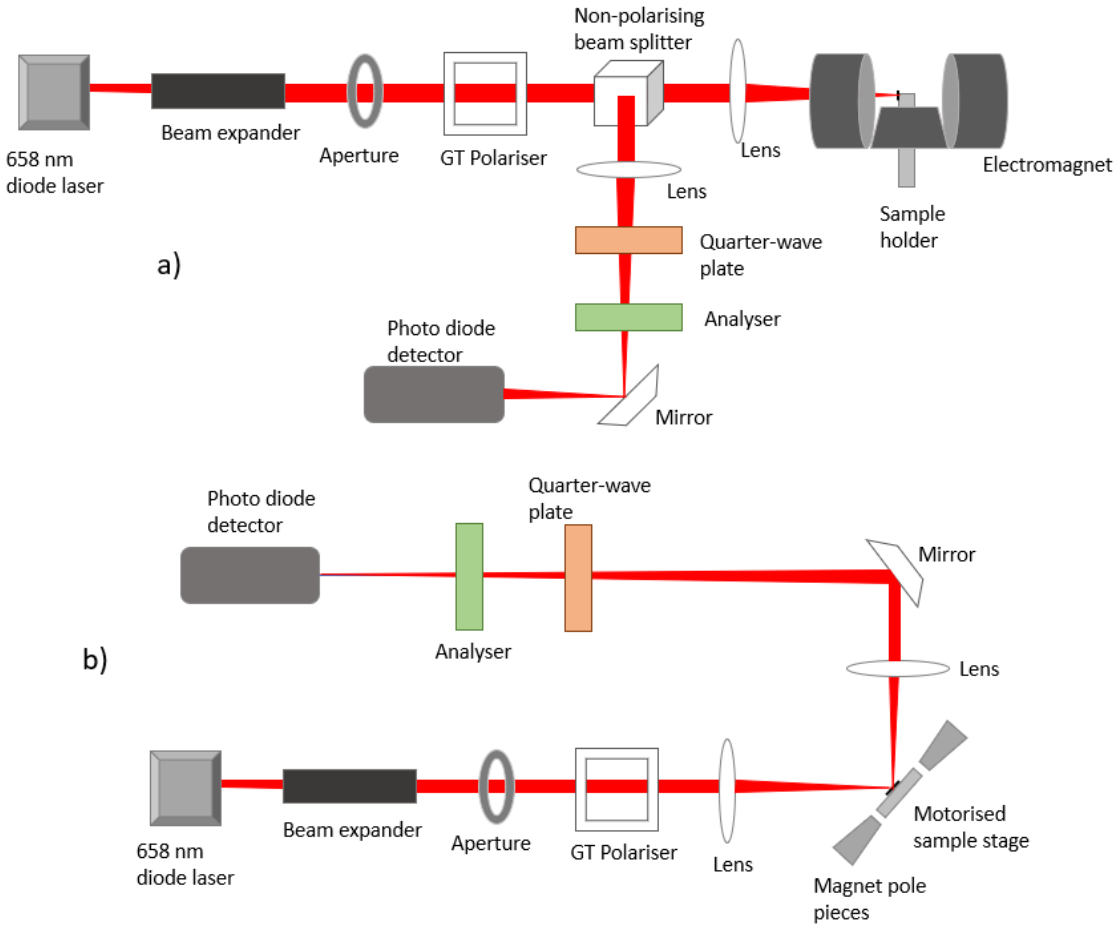

Figure 3.10: Schematic of the MOKE experimental setup where a) shows the longitudinal MOKE trajectory and b) shows the polar MOKE trajectory.

an angle of 90° whereas for the longitudinal MOKE the light was incident at 45°. The polar MOKE measurement requires an additional beam splitter to separate the incident and reflected light from the sample. The following discussion applies to both MOKE setups. A diode laser with a wavelength of 658 nm was used for all MOKE measurement in this thesis. This passed through a beam expander, then a Glan-Taylor polarising prism, which was set to ensure p-polarised light was incident on the sample. The first lens focused the laser spot to a diameter of $\approx$ 10 μm in the case of longitudnal MOKE, and $\approx$ 200 μm in the case of polar MOKE on the sample. The reflected light was then focused onto a photodiode, after passing through a quarter-wave plate and an analyser. The purpose of the quarter-wave plate was to remove any induced ellipticity in the reflected light. The analyser was set to extinction and then offset to between 4-8°, which was variable dependent

on the reflectivity of the sample. The photodiode voltage was passed to a Melles-Griot large dynamic range amplifier that enables the amplification of small signals superimposed onto large offsets, which is typical for the Kerr voltage.

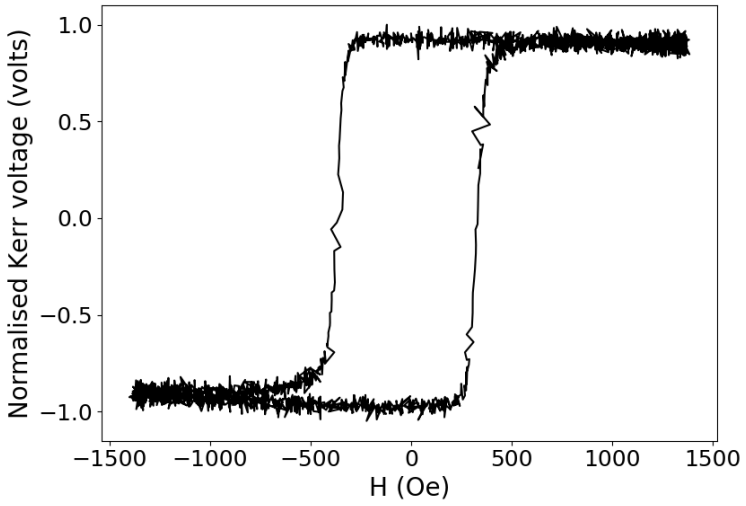

Figure 3.11: Polar MOKE hysteresis loop for a perpendicularly magnetised Pt/Co/ Pt.

The hysteresis loops obtained using these MOKE setups were averaged over many field cycles. Here the magnetic field was driven by a Kepco BOP 50-5M power supply which was in turn driven by a signal generator operating at 1.7 Hz for polar and ≈ 23 Hz for longitudinal MOKE. This oscillating magnetic field would cause the sample to cycle through the hysteresis loop, which would produce an oscillating Kerr voltage, which was measured by an oscilloscope and averaged over many hundreds of field cycles, and therefore provides a very effective way to efficiently enhance the signal to noise ratio. Figure 3.11 shows an example of a hysteresis loop.

It is important to mention that none of the previous techniques are directly quantitative measurements, to get quantitative magnetic information you can use polarised neutron reflectivity and ferromagnetic resonance which are described in the next sections.

3.5 Polarised Neutron Reflectivity

Polarised-neutron specular reflectometry (PNR) was developed in the 1980s as a means of measuring depth-resolved magnetisation in flat magnetic films with characteristic thicknesses from 5 to 5000 Å. PNR has been widely used to study homogeneous and heterogeneous magnetic films. Neutron scattering is analogous to x-ray scattering but neutrons interact with the nucleons providing information on the structure, and the local magnetisation in the sample. These are possible because of the neutron's spin 1/2 property which leads to a coupling between the magnetic moment of the neutron and the magnetisation state of the material. Similar to other reflectivity techniques, neutron reflectivity provides cross-sectional information on the inhomogeneities normal to the sample surface or interface. The depth-dependent scattering potential, V, of the neutron particle is given by

$$V = \frac{2\pi\hbar}{m_n} b_i(r - r_i),$$

with b_i is the scattering length factor of the i-th nucleus at position r_i and m_{N} is the neutron mass. Based on the Born approximation, the reflectivity is

$$R(q) = \frac{16\pi}{q^2}|\rho(q)|^2,$$

where $\rho(q)$ is the average scattering length density profile. This is a one dimensional Fourier transform of $\rho(z)$,

$$\rho(q) = \int_{-\infty}^{\infty} \rho(z) \exp{(iqz)} dz,$$

where $\rho = \sum_i N_i(z) b_i$ is the sum of all the products of the number density of atoms N_i and scattering length b_i. For thicker samples, the reflectivity is approximated as

$$R \approx \frac{16\pi}{q^4}(Nb)^2$$

where N is the number density and b is the neutron scattering length. The product Nb describes the neutron scattering length density (typically given in units of $\mathrm{Å}^{-1}$).

The neutron refractive index, $n(z)$, is given by

$$n(z) = 1 - \sum_i N_i(z) b_i \lambda^2 / 2\pi$$

where λ is the neutron de Broglie wavelength. For most materials the refractive index is close to unity and the scattering length factor is positive and small. The critical wave vector is $q_c = \sqrt{16\pi N b}$. Since neutrons possess an intrinsic magnetic moment and spin this enables the scattering potential to be spin dependent. The neutron spin interacts with the local sample magnetisation as well as strong nuclear interaction between the neutron and the nuclei of the probed material. Therefore, the total scattering factor of neutrons is the sum of the nuclear and magnetic scattering length $b_{\text{tot}} = b_{\text{nuc}} + b_{\text{mag}}$. In the same way, the neutrons incident on a magnetic material experience an additional potential V_{mag}, given by the Zeeman effect, additional to the nuclear potential, V_{nuc}. In the case of polarised neutrons, where the polarisation axis is defined with respect to the magnetisation direction, the total scattering potential is represented as

$$V\mp = V_{\text{nuc}} \pm V_{\text{mag}} = \frac{2\pi\hbar^2}{m_n} N(b_{\text{nuc}} \pm b_{\text{mag}}), \tag{3.5.11}$$

with $+$ and $-$ representing spin-up and spin down neutron polarisation respectively. The scattering potential reflects the difference in the total scattering length for spin-up and spin-down polarised neutrons. An example of the neutron reflectivity of both polarisation states for Ta/Pt/CFA/MgO/Ta multilayer is shown in the upper part of figure 3.12, similarly to the XRMR in the last section. The difference in the spin-up and spin-down polarisation defines the spin asymmetry factor given by

$$\text{Spin asymmetry} = \frac{I^+ - I^-}{I^+ + I^-},$$

where $I^{+(-)}$are the reflectivity of spin-up (spin-down) polarised neutrons respectively. An example spin-asymmetry is shown in lower panel of figure 3.12. The measured reflectivity corresponds to the amplitude of the intensity at the detector, normalised to the incident intensity. The neutron reflectivity intensity approxi-

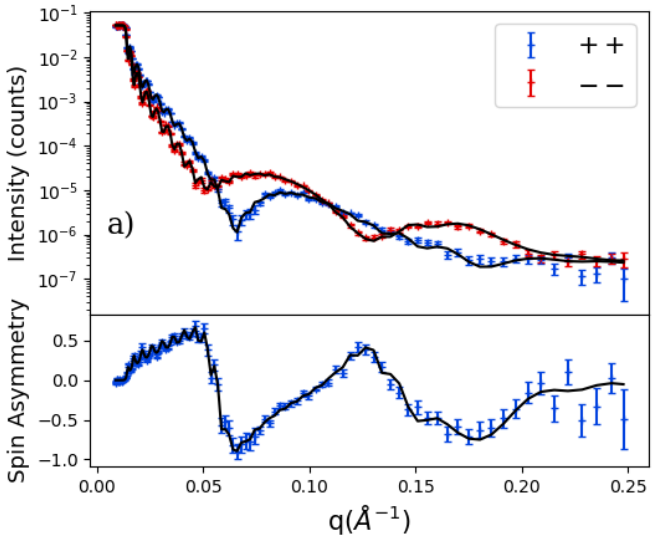

Figure 3.12: Experimental data of polarised neutron reflectivity (upper panel) with the corresponding spin asymmetry (lower panel) for Ta(2 nm)/Pt(3 nm)/CFA(2 nm)/MgO(1 nm)/Ta(2 nm).

mately as q^{-4}, as described in eq. 3.5.11 and the signal-to-noise ratio at high angles is usually limited by background noise from incoherent scattering.

3.5.1 POLREF polarised neutron reflectivity setup

PNR measurements were conducted at the Polref beamline at Rutherford Appleton Laboratory, STFC, UK. Polref is a time of flight reflectometer with an incident neutron beam with a wavelength range of 0.5 - 6.5 Å. The source frequency of the neutron beam is 50 Hz. The neutron beam is at an angle of 2.3 ° from the horizontal to reduce the fast neutrons and background x-rays from the direct line-of-sight with the moderator. The distance between the source and the sample stage is about 23 m and from the sample environment to the detector is 3 m. The neutron beam incident on the sample passes through two synchronous disc choppers, which define the wavelength band, a frame overlap mirror to remove slow neutrons from previous pulses, a polarising mirror, spin flipper, guide field and a beam monitor as shown in figure 3.13. The spin flippers function as spin state polarisers; they are OFF(ON) when +(-) polarisation beam is transmitted. The interaction of the neutrons with the sample is as follows; if the magnetisation of the sample is parallel

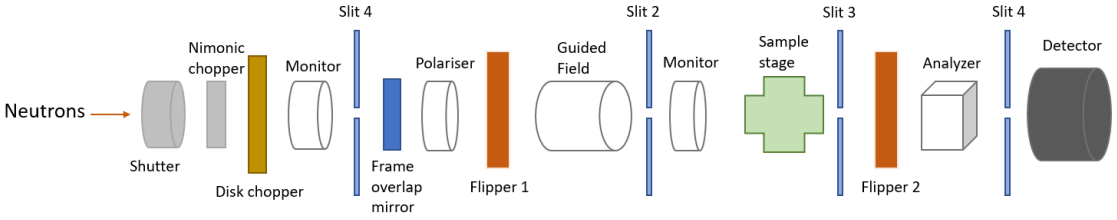

Figure 3.13: Polref schematic, polarised neutron reflectivity setup.

to the applied magnetic field there is no change in the spin state of the neutrons, otherwise, a flip in the spin state in the neutron is going to take place. The scattered polarised states are divided through an analyser before the detector. The neutron polarisation is maintained by a guide field of ≈ 5 Oe. Four possible spin polarisation states can be detected; I^{++}, I^{+-}, I^{-+} and I^{--}, where the first sign represents the polarisation state of the incident neutron and the second the polarisation of the scattered neutron. If the first flipper is OFF, the + polarisation state is incident on the sample and the analyser reflects only neutrons that had not experienced a spin flip, so I^{++} is measured at the detector. I^{-+} is measured when the first flipper is ON, meaning that only $-$ polarised neutrons are allowed through and the analyser only passes the + polarised neutron state. Finally, the I^{--} polarisation state is measured by turning ON both flippers. Generally, I^{++} and I^{--} are known as the non spin flip (NSF) states while I^{+-} and I^{-+} are equivalent and are known as the spin flip (SF) state.

The guide magnetic field is produced by permanent magnets that are designed to minimise the effect of stray fields, thereby sustaining the neutron polarisation. The detected beam is normalised to a monitor located just before the sample. The sample environment is customised to the room temperature regime which uses a magnetic yoke whose field direction matches the controlled incident polarisation, allowing access to the elements of the polarisation matrix. The neutron beam hits the sample and the reflected beam from the sample goes through slits to the detector. Both the perpendicular q_z and parallel q_x components of the neutron wave vector to the surface of the sample can be obtained in each measurement [123]. In this thesis, we only used the q_z component and NSF reflectivity states.

Another approach to directly quantitative probe magnetism and which essentially

relies on the Zeeman effect is the ferromagnetic resonance which is described in the following section.

3.6 Ferromagnetic Resonance

Ferromagnetic Resonance (FMR) is a method to measure magnetic properties by detecting the precessional motion of the magnetisation in a ferromagnetic sample. It is thus related to the electron paramagnetic resonance technique and the nuclear magnetic resonance as well. From a macroscopic point of view, the applied static magnetic field H_{app} causes the total magnetic moment to precess around the direction of the effective field H_{eff}, before relaxation processes damp this precession and the magnetisation aligns with H_{eff}. If the sample is irradiated with a transverse RF field (typically using microwaves in range 4-20 GHz), which in our case is the Oersted field generated from an RF current flow through a coplanar waveguide (CPW). The sample is placed face-down on the CPW. If also the RF frequency coincides with the precessional frequency, the resonance condition is fulfilled and the microwave power is absorbed by the sample. The motion of the magnetisation is described by eq. 2.6.22.

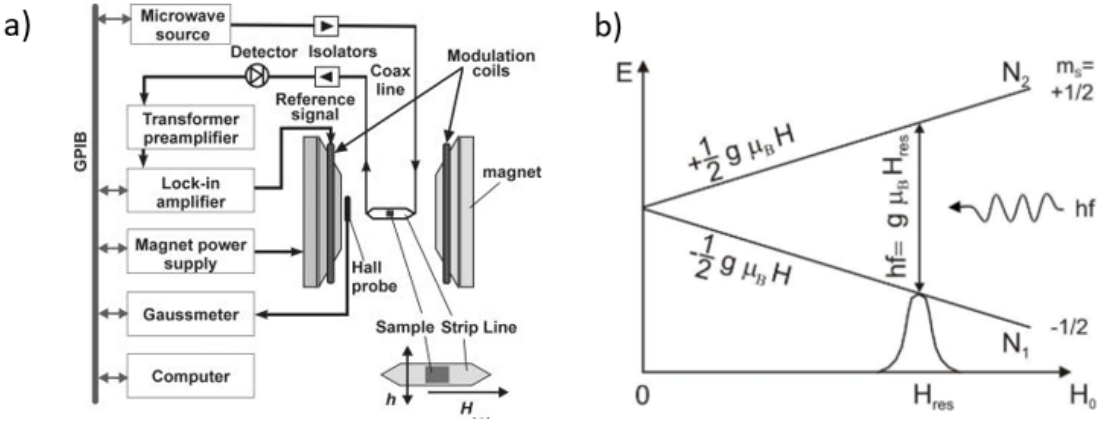

Figure 3.14: a) FMR basic setup and b) Zeeman splitting of the energy levels due to the H field [124].

At a quantum level, the H field creates a Zeeman splitting of the energy levels as shown in figure 3.14b), and the microwave excites magnetic dipole transitions between these split levels. Varying the microwave frequency over larger ranges is

not hard, and the DC magnetic field H_{app} can be varied but produces a smaller background signal. Usually the absorption derivative is measured. The resonance signal resembles a Lorentzian lineshape. The resonance field position H_{res} depends on the anisotropy parameters, g-factor, and magnetisation of the sample. This is described by the Kittel equation

$$f = \frac{\gamma}{2\pi}\sqrt{H_{\mathrm{eff}}(H_{\mathrm{eff}} + \mu_0 M)}, \tag{3.6.12}$$

where M is the magnetisation and γ is the gyromagnetic ratio. The linewidth ΔH is directly connected to the relaxation processes. In ultrathin films, Gilbert damping is commonly used to describe the relaxation. But several other possible relaxation paths are also known, e.g. two-magnon scattering, spin-pumping effect, etc., which can contribute to the linewidth.

The sample is placed on top of the coplanar waveguide in a sample holder. Lock-in detection is used to modulate the amplitude/frequency of the microwave signal to obtain a good signal-to-noise ratio and the entire setup is fully computer controlled. A schematic of the basic setup together with a side view of the sample holder is given in figure 3.14a).

FMR is a uniform precession (stationary) spin-wave mode, and the two-magnon scattering couples this to the thermal spin-wave modes which are probed in Brillouin Light Scattering spectroscopy which is described in the next section.

3.7 Brillouin Light Scattering

Brillouin light scattering (BLS) spectroscopy is a technique by which spin-wave modes can be investigated through their inelastic scattering with photons. This inelastic scattering results in a frequency shift of the reflected light, which can be measured using a tandem Fabry-Pérot interferometer. The backscattering geometry was used for all measurements and is shown in figure 3.15a). Here, the magnetic field was applied in the plane of the film and transverse to the incident light scattering vector. This probes the Damon-Eshbach surface propagation spin-wave mode. Linearly polarised laser light was incident on the sample and the backscattered light

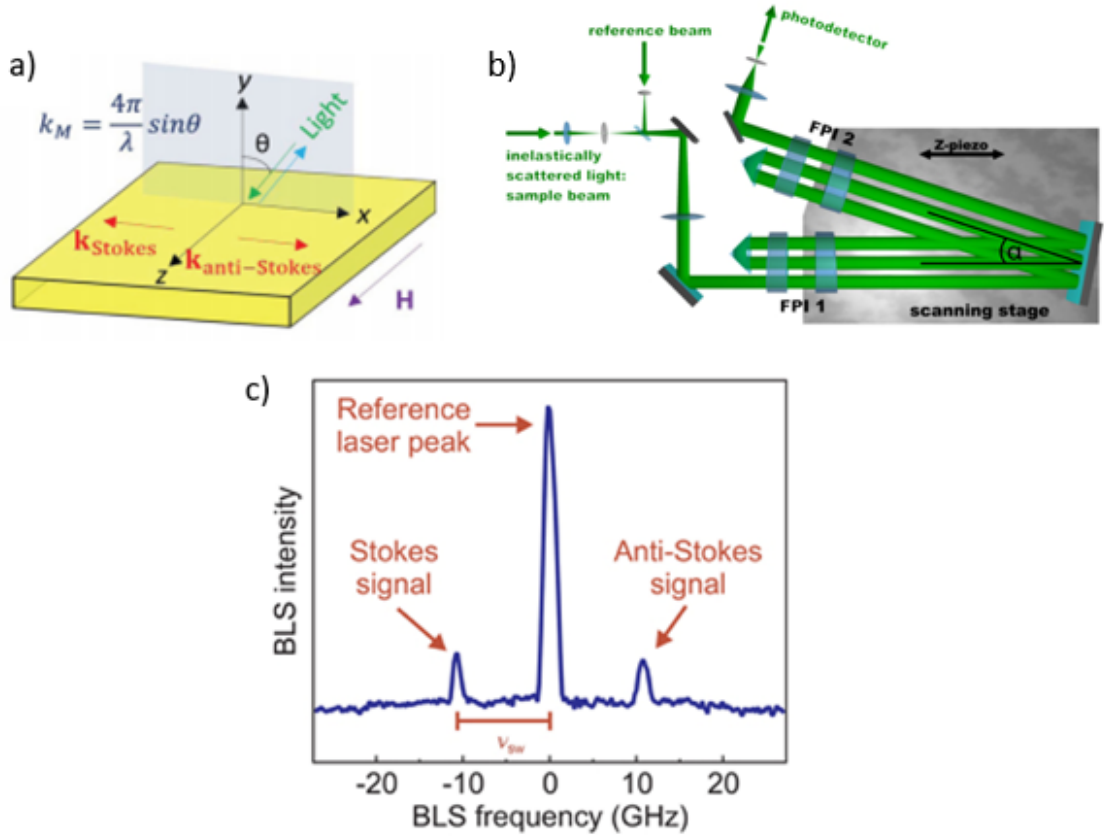

Figure 3.15: a) Schematic of the scattering geometry used to measure the Damon-Eshbach surface spin-wave mode, b) the Fabry-Pérot interferometer and, c) example of a BLS spectrum.

was collected by an objective lens and directed to the Fabry-Pérot interferometer, where it was combined with a reference beam. The interferometer is basically a resonator. The reference beam originates directly from the laser without scattering from the sample and hence provides the reference frequency. The frequency spectrum was then analysed by comparing the interference between the backscattered and reference beams inside the Fabry-Pérot interferometer which is shown in figure 3.15b). An example of a BLS spectrum is shown in figure 3.15c). Most light is scattered elastically through Rayleigh scattering (the reference peak), but at one higher, one lower, Stokes and anti-Stokes lines occur due to phonon and magnon scattering events. The phonon lines can be removed by including a polarisation analyser before the Fabry-Pérot interferometer. From the frequency of the magnon line the energy of the magnon excitation can be calculated. Laser light of wavelength $\lambda =$

532 nm was used. The spin-wave mode probed by the laser is related to the angle of incidence θ by

$$k_{\mathrm{sw}} = \frac{4\pi}{\lambda}\sin\theta, \tag{3.7.13}$$

and hence spin-wave numbers between 0-20 $\mu\mathrm{m}^{-1}$ could be investigated by rotating the sample about the planar axis. From this the spin-wave dispersion relation can be obtained. The BLS data is analysed using an analytical model where the Damon-Eshbach mode frequencies are given by 3.7.14 [125], where for spin-waves traveling along the one direction, the effective field due to the DMI is considered in the LLG equation yielding the following spin wave dispersion relation

$$\begin{aligned} f &= f_0 + f_{\mathrm{DMI}} = \\ &\mu_0\frac{\gamma}{2\pi}\sqrt{[H + Jk^2 + P(k_{\mathrm{sw}}t_{\mathrm{FM}})M_{\mathrm{S}}][H + Jk^2 - P(k_{\mathrm{sw}}t_{\mathrm{FM}})M_{\mathrm{S}}] + M_{\mathrm{eff}}} \\ &\pm\frac{\gamma}{\pi M_{\mathrm{S}}}Dk_{\mathrm{sw}}. \end{aligned} \tag{3.7.14}$$

Here, H represents the in-plane applied field, M_{S} the saturation magnetisation, γ the absolute value of the gyromagnetic ratio, μ_0 the vacuum permeability, $J = 2A/\mu_0 M_s$ the spin-wave stiffness with A the exchange stiffness constant, $P(x) = 1 - (1 - \exp(-|x|))/|x|$, $M_{\mathrm{eff}} = M_{\mathrm{S}} - 2K/(\mu_0 M_{\mathrm{S}})$ with K the anisotropy constant and D the DMI constant.

3.8 Summary

This chapter described the sample preparation and fabrication techniques using sputtering deposition, followed by the structural and magnetic characterisation techniques; XRR, XRMR, PNR, MOKE, FMR and BLS spectroscopy. A brief description of the experimental setup specific to the systems used in taking measurements here was also provided to aid in understanding of the results shown in the later chapters.

MOKE can also be used to image the magnetic domains in magnetic samples using a microscope. In the next chapter, the construction and optimisation of a MOKE microscope to image magnetic domains and domain wall motion is described.

Chapter 4

Development of MOKE microscope and experimental techniques in microscopy of magnetic thin films

There are a variety of techniques to investigate magnetic domain structure of magnetic materials and to gain information on magnetic domain-walls (DWs). One of these techniques is magneto-optical imaging, which has significant advantages of being relatively inexpensive, non-invasive and non-contaminating. Magneto-optical imaging in reflection mode takes advantage of the magneto-optical Kerr effect, while imaging in transmission mode takes advantage of the Faraday effect. The physical principle of both effects is similar, as described in the previous chapter. Light reflected from the surface of a magnetic sample or transmitted through a magnetic sample will interact with the magnetisation within the sample. Through this magneto-optic interaction, the polarisation state of the light will change and the difference between the incident and reflected (transmitted) beams can be used to study the magnetisation within different regions of the sample. In this chapter the construction and designing of Durham MOKE instrument and the asymmetric bubble expansion technique for the estimation of the DMI is presented.

4.1 Magneto-optical Kerr effect microscopy

A magneto-optical Kerr effect (MOKE) microscope is a device in which the magnetic contrast i.e. the magnetic domain structure of the material can be observed using the MOKE. As explained in the previous chapter the MOKE is due to the interaction of polarised light with the surface magnetisation of materials. Similarly, it is possible to detect different components of the magnetisation with respect to the plane of the sample as shown in figure 3.9 in the previous chapter. Figure 4.1 shows an example of magnetic domains in a Pt(4 nm)/Co(0.6 nm)/Pt(4 nm) multilayer structure imaged using a polar MOKE (pMOKE) microscope, developed in this work. Two contrasting grey tones are visible; the light grey corresponds to one magnetisation state up (down) with respect to the sample plane and the dark grey corresponds to the other possible state down (up) respectively. When a sufficiently strong enough magnetic field (saturation field) is applied to the sample, the spins of the entire sample will point in the direction of the field reaching the so called saturation state, as described in section 2.6. A non-contrasting image will be displayed by the microscope in either the light grey or the dark grey. Furthermore, if an opposite magnetic field smaller than the saturation field is applied to the sample some sites will spontaneously reverse their spin state and from those nucleation sites the magnetic domains will expand in a bubble-like structures similar to the ones shown in figure 4.1. If two bubbles expand close to each other they will merge and form one magnetic structure. This type of expansion is usually found in Pt/Co structures with PMA.

This instrument can be used to image both the statics and, depending on the time resolution, the dynamics of magnetic domains in magnetic structures obtain hysteresis loops can be obtained. However, it is also possible to measure in an indirect fashion important quantities, for example, with sufficient resolution, the type of magnetic domain (wall) can be extracted. The perpendicular anisotropy constant and the DMI can also be estimated by a technique called asymmetric bubble expansion which is described in the next section. The magneto-optical Kerr effect is conveniently described by Jones matrix approach [126]. The incident light

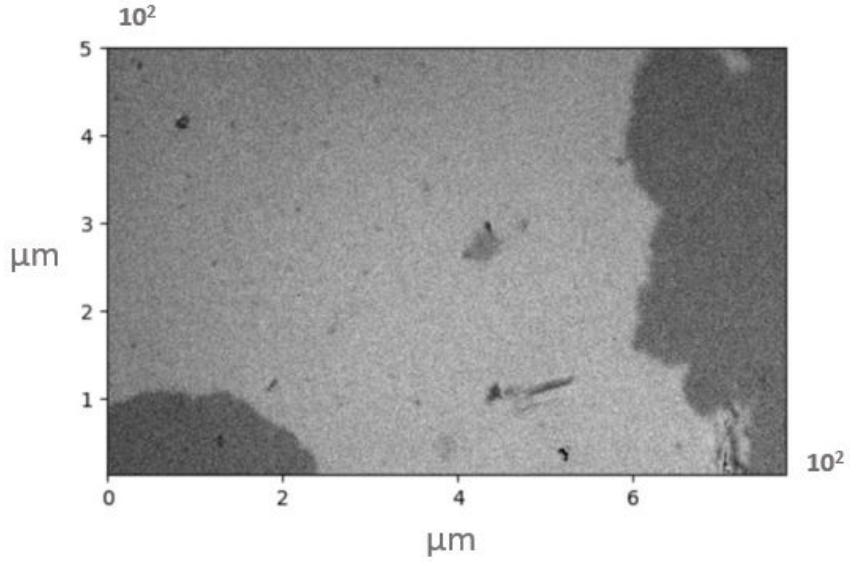

Figure 4.1: Magnetic domains in a Pt(4 nm)/Co(0.6 nm)/Pt(4 nm) structure using a polar setup of a MOKE microscope.

beam is described by the polarisation vector

$$\vec{E} = \begin{bmatrix} E_x \\ E_y \end{bmatrix}. \tag{4.1.1}$$

The effect of the polariser on the incident beam can be represented by the following matrix (assuming an ideal polariser for simplicity)

$$\bar{P} = \begin{bmatrix} 0 & 1 \\ 0 & 0 \end{bmatrix}. \tag{4.1.2}$$

In the instrument, light incident upon the magnetised surface will have linear polarisation in the y-direction. The analysing polariser set to angle Θ from the x-direction (for $\Theta = 0$ the two polarisers will be perfectly crossed) is described by the operator

$$\bar{A} = \begin{bmatrix} \cos^2\Theta & -\cos\Theta\sin\Theta \\ -\cos\Theta\sin\Theta & \sin^2\Theta \end{bmatrix}, \tag{4.1.3}$$

where $\bar{A}$ is the effect of the analysing polariser on the light. The interaction of the light with the magnetised surface can be represented as a summation of the oblique reflection matrix and the magneto-optical effect matrix [126]. The Fresnel reflection

matrix for the sample can be written as

$$\bar{J} = \begin{bmatrix} c_{ss} & c_{sp} \\ c_{ps} & c_{pp} \end{bmatrix} = c_{PP} \begin{bmatrix} c_{ss}/c_{pp} & c_{sp}/c_{pp} \\ c_{ps}/c_{pp} & 1 \end{bmatrix} \tag{4.1.4}$$

where c_{ij} is the ratio of incident j polarised electric vector and the reflected i polarised electric vector. For near normal angle of incidence $r_{ss} \approx r_{pp}$, and this matrix becomes

$$\bar{J} = c_{pp} \begin{bmatrix} 1 & -(\theta_{\mathrm{k}} + i\eta_{\mathrm{k}}) \\ \theta_{\mathrm{k}} + i\eta_{\mathrm{k}} & 1 \end{bmatrix}, \tag{4.1.5}$$

where $c_{sp}/c_{pp} = -c_{ps}/c_{pp} = \theta_{\mathrm{k}} + i\eta_{\mathrm{k}}$ defines the Kerr rotation (θ_{k}) and ellipticity (η_k) parameters for near normal incidence. The Jones vector of the light reaching the detector is obtained from the product of the Jones matrices of the optical components encountered by the light as

$$\vec{E}_{\mathrm{d}} \approx \bar{A}\bar{J}\vec{E}\bar{P} \approx \begin{bmatrix} 0 \\ E_y(\theta_{\mathrm{k}} + i\eta_{\mathrm{k}}) \cos\Theta \sin\Theta \end{bmatrix}. \tag{4.1.6}$$

However, the quantity measured is the intensity which is calculated as $|\vec{E}_{\mathrm{d}}|^2$. Thereafter these terms in eq. 4.1.6 will determine the intensity ratio between the background component of the light and the Kerr effect component of the light. Hence this term is critical in optimizing the contrast when an image of the magnetic domain structures is captured with a digital camera. First, the term will determine the background light intensity and, secondly will determine the intensity of the Kerr effect light. As mentioned before, using the MOKE microscope important quantities can be estimated such as the DMI strength and the sign. Furthermore, it is not trivial to measure the DMI, so sophisticated apparatus is required. However, instead of attempting to measure DMI directly the effect on the system can be used instead in order to estimate the DMI parameter. The asymmetric bubble expansion technique uses this premise to measure the DMI and it will be described in the next section.

4.2 Domain wall creep & the bubble expansion method

The first step towards optimisation of any parameter is to be able to measure it easily and reliably. Several different methods have been used to evaluate the strength of the DMI, D. The most reliable technique to measure D is BLS, which is a direct measurement that uses nonreciprocal propagation of spin waves in materials with DMI as described in the previous chapter. However, the technique's availability is limited, which means that it is not widely available for routine measurements of large numbers of samples [127]. Therefore, a technique where D can be obtained rapidly for a large number of samples is required. Using all the advantages of using non-invasive microscopy with the asymmetric bubble expansion technique promises to be a potential candidate [127, 130–132].

For a circular or bubble domain which is found in multilayers with PMA that contain Pt/Co in the stack as shown in figure 2.14, the DMI imposes an effective magnetic field on the DW in the radial direction and maintains the rotational symmetry with respect to the axis parallel to the out-of-plane magnetic field. It is natural to observe isotropic DW movement, the domain is expanding as shown in figure 4.2(a). However, with the application of an in-plane magnetic field, such rotational symmetry is broken and, thus, it becomes, it becomes possible for the DW to show anisotropic expansion as shown in figure 4.2(b).

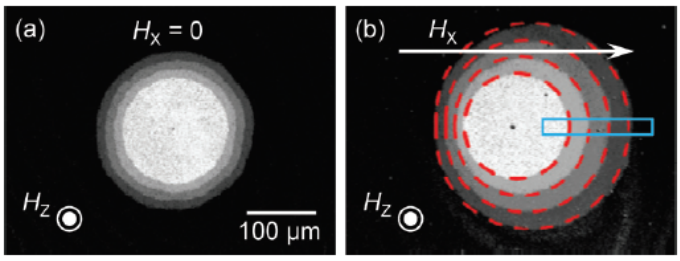

Figure 4.2: Circular DW expansion driven by an out-of-plane magnetic field H_z (3 mT), (a) without an in-plane magnetic field and (b) with an in-plane magnetic field $\mu_0 H_x$ (50 mT). Each image is obtained by adding four sequential images with a fixed time step (0.4 s), which are captured using a magneto-optical Kerr effect microscope. The white arrow and the symbols indicate the directions of each magnetic field. The blue box in (b) designates where the DW displacement is measured. The dashed red circles in (b) show the calculation results [131].

Figure 4.3 shows a two-dimensional contour map $V(\mu_0(H_x,H_z))$ of the DW speed, V, as a function of H_x and H_z. V is measured by detecting the DW displacement at the rightmost point of the reversed domain (indicated by the blue box in figure 4.2b)]), where the DW lies normal to H_x and displacement occurs along the $+x$ axis. The color in the map corresponds to the magnitude of V with the scale shown on the right, each color traces an equi-speed contour. The equi-speed contours are highlighted by the circular symbols, of which the position (H_x, H_z) indicates the value of H_z for each H_x on each equi-speed contour. The contour map shows that all equi-speed contours exhibit an inversion symmetry (or peak) with respect to the horizontal axis at $\mu_0 H_x \approx -26$ mT, which can be called H_0 and is a constant. The peak is shown with the vertical purple dashed line on the map. From the figure, the two types of symbols (crosses and circles) overlap on the same curves manifesting the inversion symmetry with respect to H_0. The non-zero offset H_0 of the symmetry axis can be attributed to the DMI effect, because DMI induces an effective magnetic field H_{DMI} along the x axis in this geometry; thus, the DW experiences a resultant in-plane magnetic field $H_x + H_{\mathrm{DMI}}$. As a result, the experimental value H_0 can

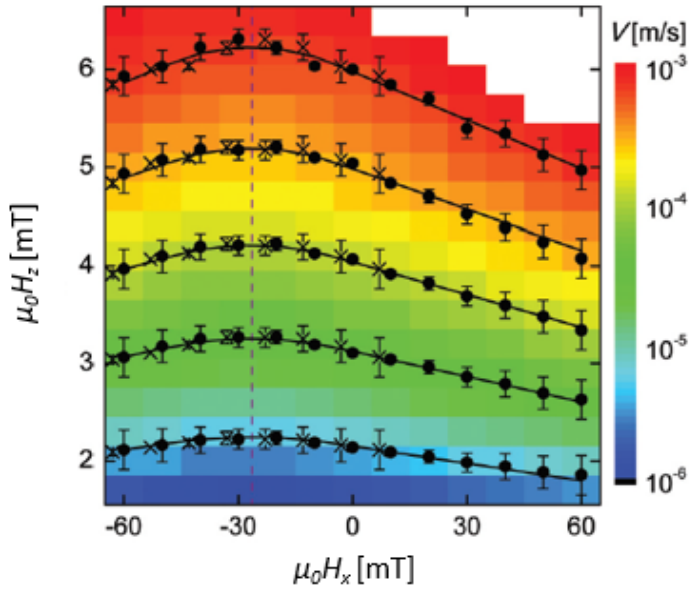

Figure 4.3: Two-dimensional equi-speed contour map of V as a function of H_x and H_z. The color corresponds to the magnitude of V with the scale on the right. The symbols with error bars show the measured positions (H_x,H_z) on several equi-speed contours. The black solid lines show the best fit using eq. 4.1.1. The purple line indicates the symmetric axis $H_x = H_0$ for inversion. Adapted from [131].

be considered an indirect measure of H_{DMI}, and the negative sign indicates that the direction of H_{DMI} at the DW is parallel to the $+x$ axis, which points from the domain that is magnetised along the $+z$ axis to the domain that is magnetised along the $-z$ axis. For the actual measurement, shown in figure 4.6, a typical example of a symmetrically expanding bubble is shown under application of H_z and H_x fields pulses using the following measurement sequence:

1. The sample is saturated with a $H_{z,S}$ field pulse with a duration of t_S, shown in figure 4.4a).

2. A background image is taken and subtracted from all subsequent images.

3. A circular bubble is then nucleated using a nucleation pulse $H_{z,N}$ with a time length of t_N, shown in figure 4.4b).

4. The in-plane H_x field is set.

5. An initial reference image is taken.

6. A propagating pulse field $H_{z,P}$ is applied with a time length of t_P, shown in figure 4.4c).

7. An image is recorded.

   Step 6 is then repeated as many times as need it. H_x is switched off.

8. The obtained images are then processed to extract the bubble nucleation origin and the DW velocity along the bubble circumference.

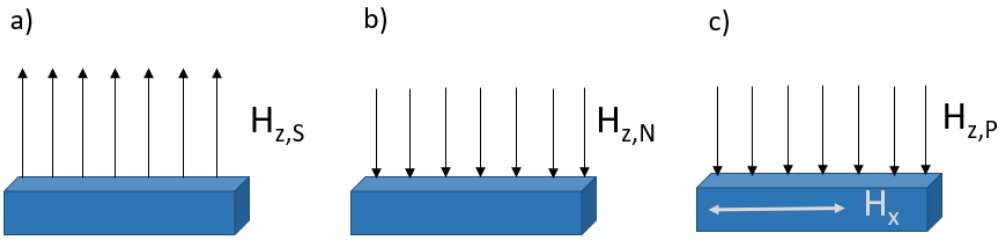

Figure 4.4: Diagram of the procedure. a) Step 1 in the procedure: Saturation of the sample. b) Step 3 in the procedure: Nucleation due to an opposite filed $H_{z,N}$. c) Step 6 in the procedure: A propagating pulse using $H_{z,P}$ field is applied while an in-plane field H_x is also applied.

It is important to note that besides the sequence, special care must be taken to find a nucleation site where a consistent and circular bubble was nucleated for both field polarities (H_z, $-H_z$) during the nucleation pulse. Furthermore, the area around the nucleation site, i.e., the area where the expanding bubble travels through, should be checked for strong pinning sites, which could lead to noncontinuous DW velocities. After mounting every sample, the in-plane field coil angle relative to the sample plane has to be carefully tuned to minimise any leakage into the perpendicular field direction. By fitting and averaging, the expansion of the bubble versus the total applied H_z pulse time, the DW velocity, V, as a function of $\mu_0 H_z$, is extracted. An example is shown in figure 4.5 (black symbols). The data is fitted to the creep law

$$V = V_0 \exp\left(-\xi(\mu_0 H_z)^{-1/4}\right), \tag{4.2.7}$$

where ξ is a scaling constant and in defined as,

$$\xi = U_c H_{crit}^{\mu} / k_B T,$$

with $\mu = 1/4$ [129], where U_c is an energy scaling constant, H_{crit}^{μ} is the critical magnetic depinning field at zero temperature, and $k_B T$ denotes the thermal energy. Variations of the DW energy with the in-plane field affects ξ and this explain the variation of the DW velocity with the in-plane field in the domain expansion method.

In thin films with PMA, BW are preferred due the magnetostatic DW anisotropy field, $H_{K,\mathrm{dw}} = 4K_{\mathrm{dw}}/(\pi\mu_0 M_s)$. Here, $K_{\mathrm{dw}} = N_x \mu_0 M_s^2/2$ is the magnetostatic anisotropy, where $N_x = t_{\mathrm{FM}} \log 2/(\pi\Delta)$ is the demagnetisation coefficient of the DW with t_{FM}, the FM layer thickness and M_s the saturation magnetisation [130]. For magnetic bubbles this leads to the situation in figure 4.6 where the magnetic bubble with its magnetisation along $+z$ (grey area) is shown. Since there is no preferred chirality for Bloch DWs the magnetisation can rotate either clockwise or anticlockwise going through the DW from the inside to the outside of the bubble as indicated by the double arrows.

In a simple description of the effect DMI on DWs, the DMI manifests itself as a

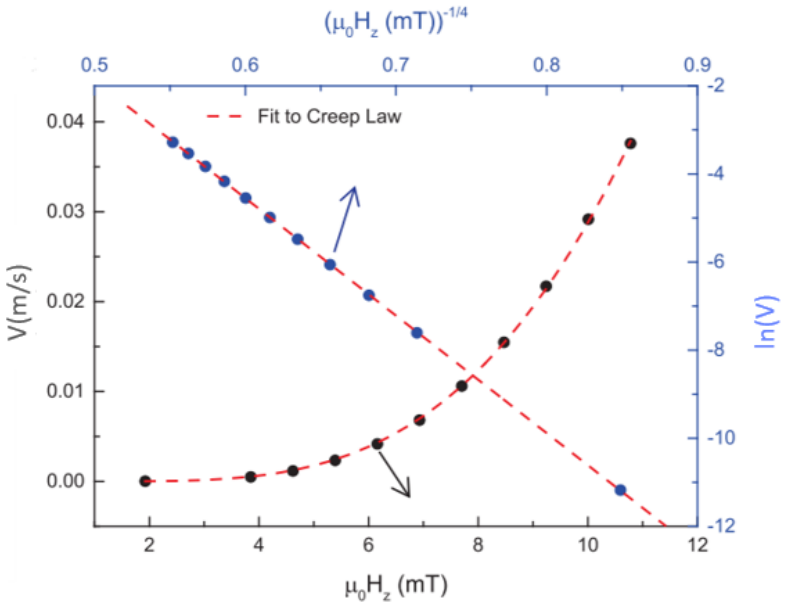

Figure 4.5: Typical velocity V vs $\mu_0 H_z$, black symbols and left-bottom axis and $\ln v$ versus $(\mu_0 H_z)^{1/4}$, blue symbols and right-top axis. The red dashed lines are a fit to the creep law [130].

effective magnetic field, $H_{\mathrm{DMI}} = D/(\mu_0 M_s \Delta)$, pointing in-plane and perpendicular to the DW, where D is the strength of the DMI interaction, and Δ the DW width. Hence, for $H_{\mathrm{DMI}} > H_{K,dw}$ Néel type DWs are preferred as shown in the top right panel of figure 4.6 and depending on the sign of D a clockwise ($D > 0$), or anti-clockwise ($D < 0$) DW chirality is introduced as indicated by the white and purple arrows, respectively [75].

Moreover, for $H_{\mathrm{DMI}} < H_{K,\mathrm{dw}}$, the DW assumes a mixed Bloch-Néel character or the Dzyaloshinskii DW as mentioned in chapter 2. Now, by applying a strong in-plane field along the x axis (H_x), the DWs magnetisation reorients itself along H_x due to the Zeeman energy. This is shown for a bubble with $D > 0$ in figure 4.6c), where it is assumed $H_{\mathrm{DMI}} > H_{K,\mathrm{dw}}$. The DW segments that are parallel to H_x (top and bottom of bubble, orange arrows) become Bloch type DWs with an increase in DW energy density due to the Zeeman energy. The DW segments that are perpendicular to the bubble expansion (left and right of bubble) remain of the Néel type. The Néel DW which has its direction reversed (and thus its chirality), however, undergoes an increase in DW energy density. The same happens when $D > 0$ (figure 4.6d)), albeit here the left and right DW behaviour are reversed. Hence an in-plane

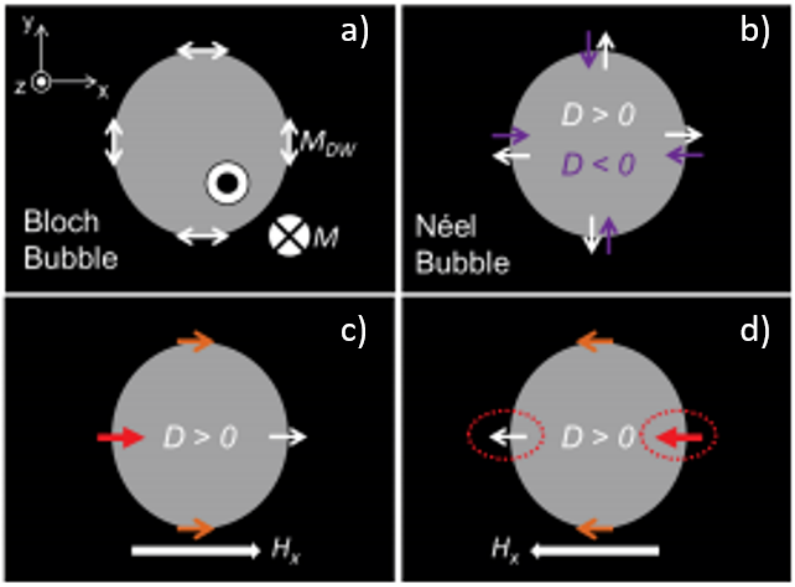

Figure 4.6: a) shows a Bloch bubble where we have indicated the magnetisation angle inside the DW defining the bubble. b) shows a Néel type bubble where the chirality of the DW depends on the sign of the DMI interaction. (c,d) show the orientation when the DWs magnetisation is saturated along the applied in-plane field direction and the thickness of the arrows indicate the increase in energy of the DWs for different D [130].

magnetic field breaks the symmetry of the DW energy profile along the in-plane field direction. This is experimentally shown in figure 4.7 where the bubble expansion is shown with a H_x field applied. A strongly asymmetric expansion is observed where the DW moving in the direction of the applied H_x field moves much faster than the DW moving against the in-plane field. The inset shows the expansion with inverted H_z showing identical asymmetric expansion albeit mirrored in the y-axis because the DMI remains in the same direction. This observation was attributed to a built-in DMI field manifesting itself at the DWs, as explained before. By applying an in-plane field during the expansion the radial symmetry is broken, as the DMI field would prefer Néel type DWs with a certain chirality.

This technique was performed using the MOKE Microscope at the University of Leeds in collaboration with Dr Thomas Moore and his student Alexandra Huxtable. The microscope was commissioned from Evico Magnetics and was used to study samples in a in-plane magnetic field up to 1.3 T and an out-of-plane magnetic field up to 0.9 T, with the capacity of simultaneous measurements of electrical transport properties. The microscope can spatially resolve features that are approximately 1

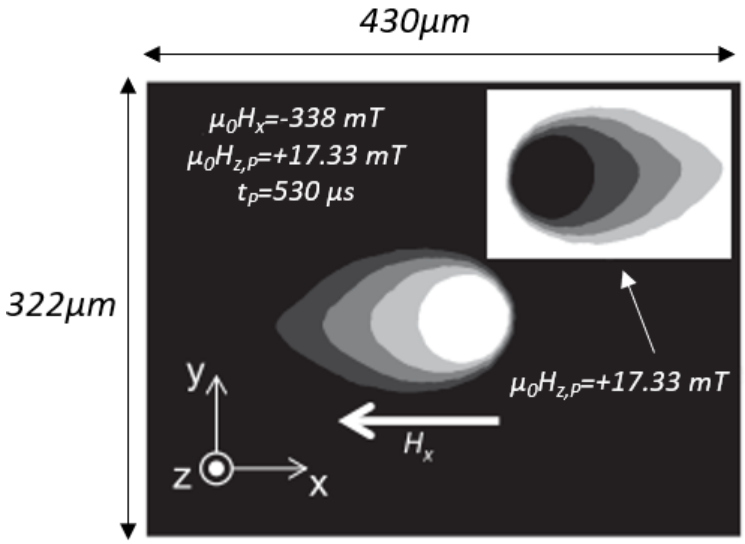

Figure 4.7: Bubble expansion while applying an in-plane field, the inset shows the expansion with inverted H_z showing identical, but mirrored in the y axis, expansion. Adapted from [130].

μm. The illuminating light is a white LED so there is a spectrum of wavelengths. The camera is a 12 bit high-resolution and high sensitivity digital CCD camera made by Hamamatsu, model C8484.

4.3 Construction of the Durham MOKE instrument

Part of this PhD project was to design and construct a MOKE microscope that was low cost and versatility. In order to design the MOKE microscope it was planned to integrate components from an existing Nikon microscope similar to that in figure 4.8. The microscope does not have infinity corrected optics and it was not designed to allow the users to incorporate additional optical components into the frame of the microscope. Therefore, the first task was the expansion of the infinity space needed for the addition of new optical components. The measurements are sensitive to vibrations making it necessary to mount the microscope onto an optical table using custom manufactured clamps. An aluminium cage was fabricated that consists of two plates supported by two posts that provided support to the structure as shown in figure 4.9a). The internal optics that provide the Köhler illumination

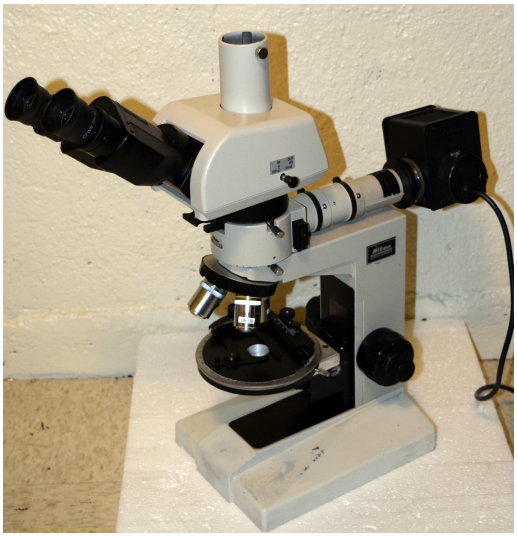

Figure 4.8: Original Nikon microscope similar to the one used as a base for the homemade MOKE Microscope.

similar to the original microscope were implemented within an aluminium box with a homemade setup of optical components mounted on an optical breadboard, as shown in figure 4.9b), minimising the number of parts and screws needed to assemble and disassemble it. Inside this area the lenses, apertures, polariser, analyser, and beam splitter were mounted. The optical breadboard also acted as a structural support at the rear of the cage. In order to detect changes in the polarisation state of the light due to the reflection from a magnetised surface, a pair of nearly crossed polariser were located in the optical path as shown in figure 4.9a). The polarising beam-splitter on the incident beam restricts the polarisation to one direction (for example, x direction). Thereafter, the interaction of the light with the magnetised surface induces a perpendicular component to the polarisation (y direction). The reflected beam is analysed when it passes through a quarter wave-plate, which removes any Kerr ellipticity leaving polarised light with a small rotation of the polarisation and a second analysing polariser, which is oriented nearly crossed with the incident light polariser, as shown in figure 4.9a. As a result, the component of the light that maintained its original polarisation state after the interaction with the magnetised surface is attenuated while the component generated through the MOKE interaction is allowed to pass to the detector [133]. Maximum attenuation of the incident light is achieved when the polariser and analyser are perfectly crossed, however the

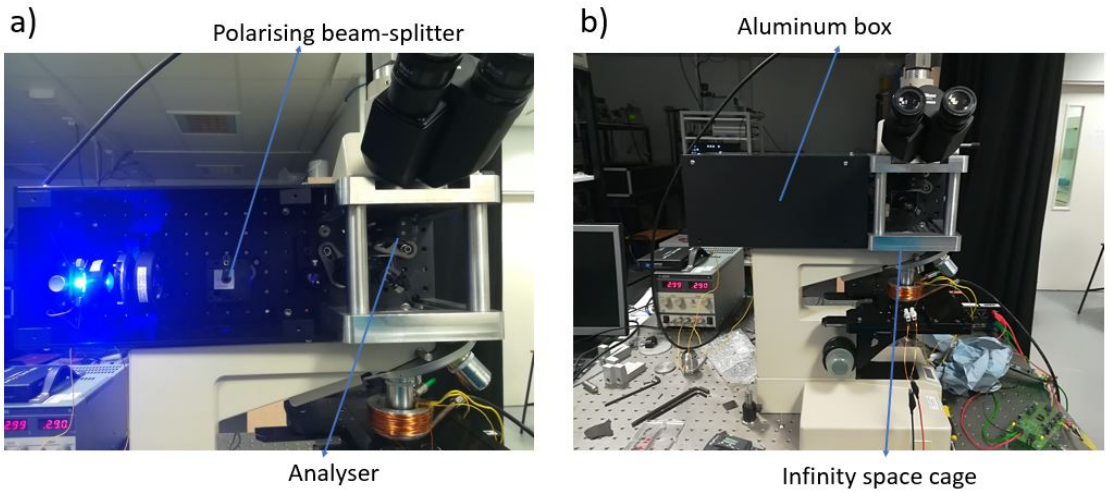

Figure 4.9: Photographs showing details of the MOKE microscope. a) Showing the internal optics. b) The first working version of the microscope.

Kerr component of the light is very weak and would require an extremely sensitive detector. By allowing some of the incident light to reach the detector the Kerr signal and the background (incident) signal are allowed to add coherently, contributing to a higher signal which is easily registered by conventional detectors.

Figure 4.10 shows a diagram of the setup of the microscope. The illumination source chosen was a hexagonal blue singlet chip high power LED (20-40 lumens, $\approx$ 25 mW) which is positioned next to the collector lens. Following that, the beam passes through the intensity controller-field diaphragm and then through the polarising beam-splitter. The beam goes then through the collimator lens and into the condenser's aperture diaphragm that controls the field of view of the microscope. The condenser lens is used to focus before the objective lens. The reflected light, after interacting with the sample goes through a dual rotating carriage with a quarter wave-plate on one side and a polariser on the other side and then to the detector; in this case a CMOS camera. After initial alignment, precise alignment of the optical path was require to optimise the illumination.

4.3.1 Köhler illumination

The first step after the initial alignment is to establish an optimal illumination, which is called Köhler illumination with both the polariser and analyser removed

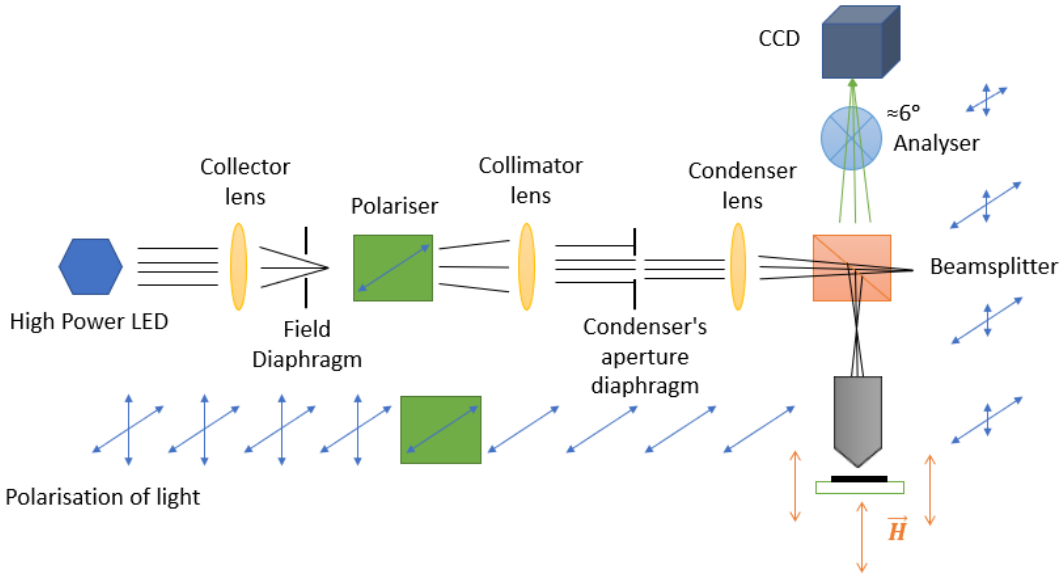

Figure 4.10: Schematic illustration of the MOKE Microscope set-up. Arrows represent the polarisation state at each stage in the optical path.

from the optical pathway. In Köhler illumination, four separate planes combine to form conjugate planes in both the illumination and image-forming light pathways as shown in figure 4.11. The illumination source, aperture diaphragm, back focal plane of the objective lens, and the eye point which is approximately one centimeter above the top lens of the ocular, form the illumination conjugate planes. The conjugate planes are located in the Durham setup shown in figure 4.10 at the high power LED, the field diaphragm, the back focal plane of the objective lens which is the rays convergence point in between the beamsplitter and the objective lens and the camera. In Köhler illumination the collector lens or field diaphragm collects light from the illumination source and focuses it onto the front focal plane of the condenser's aperture diaphragm which, in essence, projects an image of the illumination source, in this case the high power LED, onto the condenser lens. The condenser transmits the light to illuminate the sample. Often, the condenser must be adjusted to guarantee that the filament image appears in the focal plane and fills the aperture. The image of the filament must fill the aperture diaphragm and the field diaphragm and they must share the same conjugate image plane as the sample. This results in extremely even illumination because the filament in the specimen image plane is completely defocused and forms a clear image of the specimen. Closing the field diaphragm

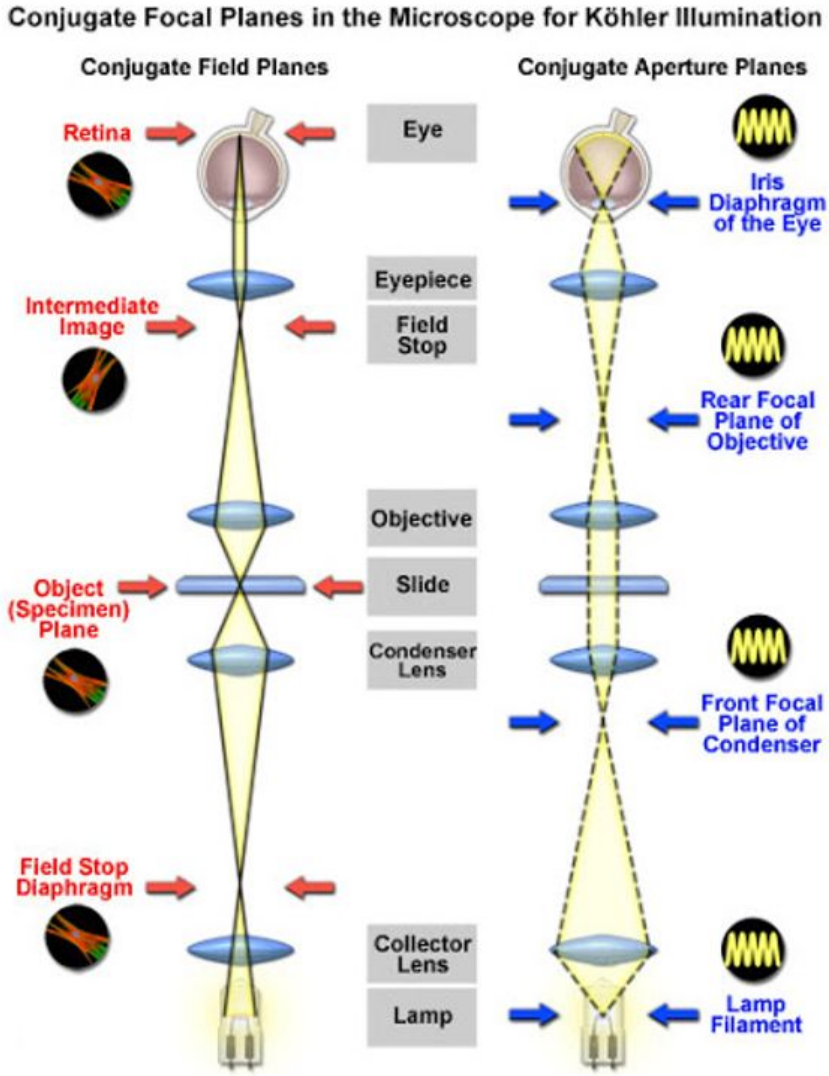

Figure 4.11: Conjugate focal planes in the microscope for Köhler illumination. In the left hand-side, the conjugate field planes and in the right hand-side, the conjugate aperture planes taken from [134].

does not reduce the brightness of the image but merely controls the width of the light beam being transmitted to the condenser and restricts the light to the part of the specimen which is actually being observed. Adjusting the condenser aperture affects the angle of the light being transmitted to the sample. Setting this diaphragm and the aperture of the objective determines the actual working numerical aperture (figure 4.12) of the microscope.

Resolution and contrast increase as the condenser diaphragm is opened. The microscope is now properly configured for observation of specimens in Köhler illumination, but only for the objective that was used to set the instrument. When

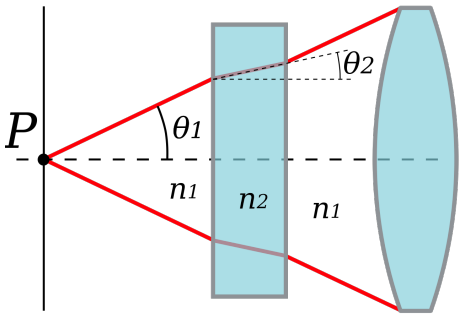

Figure 4.12: Schematic for the numerical aperture [135]. The numerical aperture with respect to a point P depends on the half-angle, θ_1, of the maximum cone of light that can enter or exit the lens and the ambient index of refraction and can be calculated $NA = n_1 \sin\theta_1 = n_2 \sin\theta_2$ [135]

another objective is rotated into the optical path, the condenser aperture and field diaphragm should always be adjusted for optimum illumination.

The procedure to properly set up Köhler illumination in the Durham microscope is:

- Turn on the LED and ensure that light is coming through the field diaphragm. Also, ascertain that the sample is being illuminated.
- Using the coarse focus and then the fine focus, bring the sample into focus.
- Begin closing the field diaphragm and begin adjusting the condenser height to bring the edges of the diaphragm into focus. At this point the field diaphragm and the sample should be in focus.
- Next, center the image of the field diaphragm. Open the diaphragm until its edges are barely outside the field of view of the microscope.
- Adjust the contrast by adjusting the condenser diaphragm and adjust the illumination intensity.

With Köhler illumination optimised, the microscope can then be used for magnetic domain imaging.

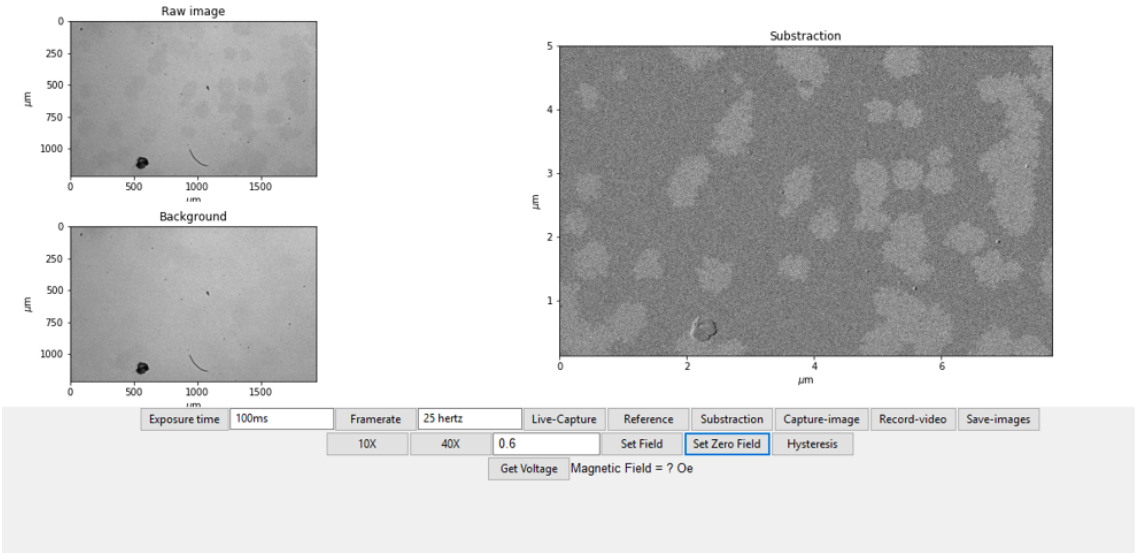

Figure 4.13: Interface to control the microscope, The first image in the top left is the raw image, the one below is background and the large image in the right is the subtraction of the background to the raw image.

4.4 Capabilities of the Durham MOKE microscope

Imaging of magnetic domains using the MOKE microscope is not an intuitive task. The end user of the microscope will need some background knowledge of magnetism, optics, and image processing; therefore the user interface must be flexible to allow the user to change parameters based on individual experiments. On the other hand, the user may not have great knowledge about the system components (camera, power supply, etc); therefore the magnet control and image acquisition must be automated. This was the challenge of creating a user interface for the microscope. Python was chosen as the code language to write the interface because of the vast use of Python in state of the art facilities around the world and in our group. The main feature used within Python was wxPython which enables the window creation, and also allows the inclusion of image spaces and the input controls. Figure 4.13 shows the interface windows software that controls the microscope. Multiple controls are present; the exposure time for the camera to take each frame, the framerate, a button that stops the live-capture, a button that saves an image as the reference or background, the subtraction button shows a processed image that consist of a subtraction of the raw image with the reference or background, a button that saves processed images and

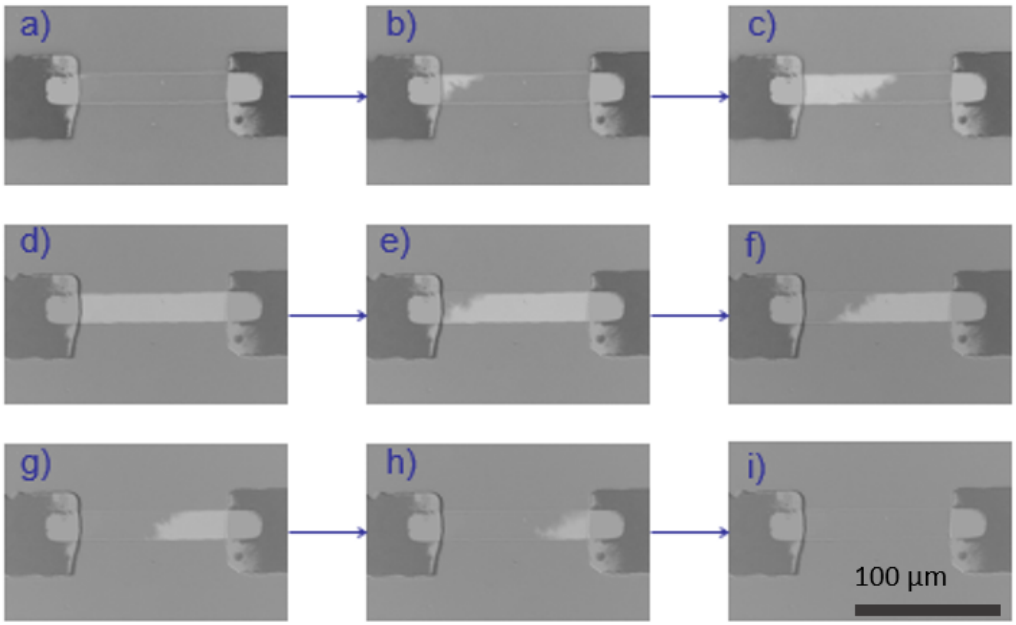

Figure 4.14: Background corrected polar MOKE microscope images taken of a strip of 20 μm width and 100 μm length made by photolithography on Pt(1nm)/Co(0.5nm)/Pt(5nm) growth by magnetron sputtering on Si substrate with native oxide layer. After saturation at $H = 180$ Oe a) $H = 0$ Oe, b) d) $H = 8$ Oe showing the magnetic domains changing direction until forward saturation e) i) $H = 8$ Oe showing the magnetic domains changing direction until reverse saturation.

two buttons to save a series of images to create a video or animation. In the second line of buttons in figure 4.13 shows 10× and 40×, which changes the scale in the images according to the magnification of the objective lens being used. The next button allows setting the magnetic field of the out-of-plane electromagnet, and a button that removes the active magnetic field. Also hysteresis loops are possible in the system. The last button measures the current applied magnetic field sensed by a Hall probe. As shown in the figure 4.13, the first image in the top left is the raw image, the one below is the background image that is currently set, and the large image on the right is the result of subtraction of the background from the raw image. The magnet is a homemade coil electromagnet that provides an out-of-plane magnetic field up to 400 Oe ($\mu_0 H$=40 mT) at the center of the magnet where the sample stages is. The magnet is powered by a Kepco BOP 50-5M power supply which is controlled by the computer through a National Instruments analog output box. The camera is a Thorlabs high-resolution CMOS camera, 1936 x 1216 pixels. Simple operating instructions in order to get an optimum contrast image from the

microscope are:

1. Turn on the LED and magnet power supplies and connect the camera to the computer.

2. Open the software interface.

3. Depending on the size of the features that want to be observed select the 10× or 40× objective lens.

4. Focus the sample, which is going to be shown at the right upper panel of the interface screen, as shown in figure 4.13.

5. Rotate the analyser until you get as low light into the camera as possible then, rotate the quarter-wave plate in the same fashion. Keep alternating until you get a black image.

6. Rotate in the opposite direction the analyser $\approx 6°$.

7. Once in the area of interest on the sample and with the right amount of light, apply an H_S and get a background image.

8. Use the subtraction controller at the interface and start applying an H_N (H_{app}).

9. If images or video (set of images) are to be saved use the corresponding controllers at the interface. In the case of video, first, use the Record-video controller when starting to save images and finally use the Save-images to stop saving images.

An example of the capabilities of the microscope is shown in figure 4.14. This shows is a series of background corrected MOKE images current-induced switching of a 20 μm width and 100 μm length Pt(1 nm)/Co(0.5 nm)/Pt(5 nm) strip patterned on Si/SiO_2 using photolithography. After saturating the magnetic structure with an out-of-plane magnetic field of $H = 180$ Oe in figure 4.14a) setting an applied field of $H = 0$ Oe after a saturation background subtracted image, no change of contrast is presented in the strip. However, in figure 4.14b)-d) a constant out-of-plane magnetic field of $H = -8$ Oe is applied showing a growing white contrast - the magnetic

domains changing direction until saturation is achieved in the opposite direction. Figure 4.14e)-i) then shows an applied magnetic field with the same magnitude but opposite direction of $H = 8$ Oe showing the magnetic domains changing back direction until reverse saturation. This measurement was done using a $40\times$ magnification objective lens.

In conclusion, the microscope has great capability to do imaging on structures with strong PMA. The microscope gives us the possibility to perform quick and reliable measurements and do research in magnetic domains using different patterns on samples.

Chapter 5

Proximity induced magnetisation in heavy metal/Co_2FeAl based multilayers

5.1 Introduction

It is well established that SOI is linked to effects related to spin current generation and detection at interfaces between ferromagnets (FM) and heavy metals (HM) such as spin pumping [136], spin Hall effect [137], anisotropic magnetoresistance [138] and the Rashba effect [139]. Interfacial DMI (iDMI) [86,87,140,141] is the antisymmetric exchange interaction that favours chiral textures in magnetic heterostructures and is responsible for favouring the Néel-type domain wall, which is one of the requirements for potential new spintronics applications based on magnetic skyrmions [3]. Furthermore, It is also expected that extremely fast and efficient spin-orbit-torque-driven (SOT) domain-wall or skyrmion motion should arise in perpendicularly magnetised films.

There also arises another phenomenon: A spontaneous magnetic polarisation on the non-magnetic elements in the interfacial region. This proximity induced magnetisation (PIM) in the heavy metal is associated with the large Stoner factor of the *d*-transition elements [28–33], for example Pd, Ir, W and of course Pt [34] all having been shown to exhibit some degree of induced moment when placed in direct

contact with a ferromagnetic material.

Thermal annealing is a common process used for relief of intrinsic stress [142], structural improvements [143], and surface roughness control in thin films materials [142]. In a qualitative way, annealing modifies the surface morphology of materials depending on both the annealing temperature and time. For metallic thin films, annealing influences the grain size and interfacial roughness [144]. For example, it was found for FePt epitaxial thin films that the in magnetic squareness of the hysteresis increases up to 0.9 (the squareness factor is a measure of how square the loop is and is a dimensionless quantity between 0 and 1, defined by the ratio of the reverse field required to reduce polarisation by 10% from the remanence to zero magnetisation) and increase in the ratio between anisotropy and coercivity where there was an increase in both the anisotropy and the coercivity as the grain size decreased due to a annealed process was applied [145]. As a result, the continuity of the thin film improved. For alloys with the Heusler compositions Cu_2MnIn, Cu_2MnAl and Cu_2MnSn the as-deposited state of thin-films is amorphous. This structural disorder results in as-deposited films that are not ferromagnetic and, in fact, exhibit spin-glass behaviour due to the distribution of Mn-Mn distances and the co-existence of positive and negative exchange interactions. Annealing of the In and Al alloys can create a single ordered phase Heusler structures that are ferromagnetic, with Curie temperatures typical of bulk alloys [146]. In particular, for device applications, thermal processes are important. For example, CMOS processing [147, 148] requires high temperature steps in power electronics or sensor signal conditioning [149] so, if we want to use a ferromagnet in a real spintronic device it needs to survive any thermal processing steps, including e.g. an annealing process to enhance the MgO barrier in a magnetic tunnel junction device [150].

5.1.1 Heusler alloys

Heusler compounds are magnetic intermetallics with face-centered cubic crystal structure and a composition of XYZ (half-Heuslers) or XY_2Z (full-Heuslers) [151] as shown in figure 5.1, where X and Y are transition metals and Z is in the *p*-block such as Al, Si or P. Heusler compounds crystallise in the $L2_1$ structure. Cobalt-

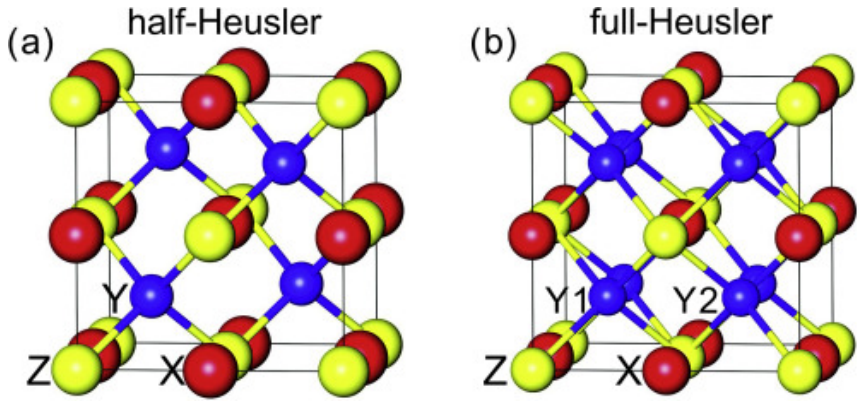

Figure 5.1: Crystal structure of a) half-Heusler compose of XYZ and b) full-Heusler alloy compose of XY_2Z following [154].

based full-Heusler compounds with composition Co_2XZ are attracting attention due to their predicted half-metallic behaviour [152]. For these compounds, the last occupied down-spin band is filled and contains an integer number of electrons, n. Hence $n_\uparrow - n_\downarrow$ is also an integer and the magnetisation M is an integer multiple of the Bohr magneton [153].

The work in this chapter uses the ferromagnetic Heusler alloy Co_2FeAl (CFA). This material is particularly interesting because this compounds exhibit extremely small precessional damping, a high Curie temperature, and a relatively high spin-polarisation that are very attractive properties for spintronics [40, 41]. The $L2_1$ structure represents the most ordered phase of the Co_2-based Heusler compounds. It is important to mention that the Co_2-based Heusler compounds used here is ferromagnetic regardless of the annealing process. However, various degrees of disorder can exist for a given chemical composition, in the form of the interchange of atoms between the different sublattices. The presence of these anti-site defects has a detrimental effect on the material properties, such as the half-metallicity and the damping. In order to obtain Heusler films with the well-ordered $L2_1$ structure, high temperature annealing is usually required since the $B2/L2_1$ phase transition in the bulk occurs at about 1000 K in most of the Co_2-based Heusler compounds [155].

On a set of samples with the same structure, BLS measurements were performed to evaluate the iDMI as a function of the annealing temperature [141] as shown in figure 5.2. Three different temperatures were compared: RT, 250 °C and 400 °C. The results shows that the iDMI decreases when the annealing temperature

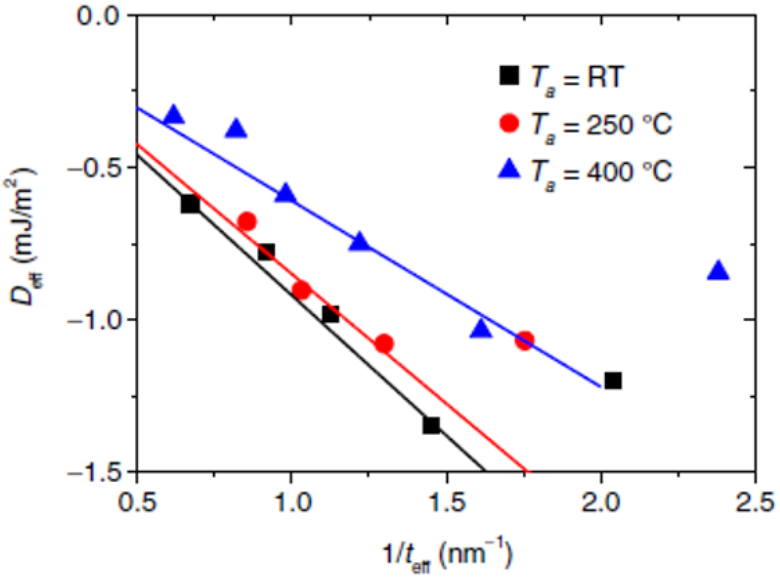

Figure 5.2: Variation of the effective iDMI constant (D_{eff}) versus the reciprocal effective thickness of Co_2FeAl films in Pt(3 nm)/Co_2FeAl/MgO(2 nm) stacks annealed at various temperatures (T_a) 5.2.

increases, which suggests that the DMI at the interfaces is affected by structural changes induced by the thermal process. With this in mind, in the next chapter a study of iDMI in multilayers with engineered interfacial roughness is presented. The results in this chapter are part of a collaboration with the Université Paris 13. The structure studied here was set by the collaboration.

In this chapter, PIM is investigated in CFA-based multilayer structures under the influence of annealing for different HMs. In some cases the PIM is presented along with the iDMI [42]. However, interfacial quality plays a crucial role in the strength of PIM and the influence of interfacial quality and thermal processes on DMI and PIM are not understood.

5.2 Samples and experimental techniques

The sample growth and all measurements in this study were performed at room temperature. CFA thin films were grown on a thermally oxidised Si substrate using a magnetron sputtering system with a base pressure lower than 2×10^{-8} Torr. Prior to the deposition of the CFA film, a 2 nm Ta seed layer and a HM layer (the HM was

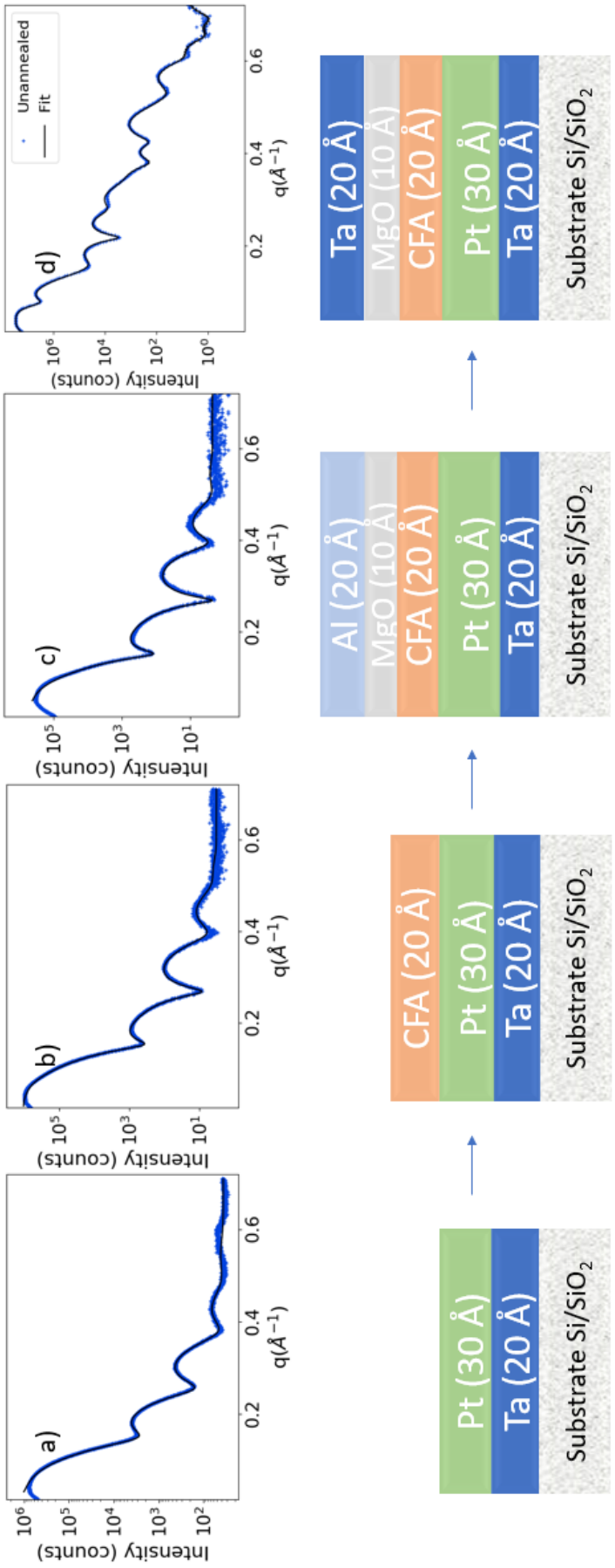

Figure 5.3: Systematic procedure to obtain robust fits by building up layer-by layer to a complex sample structure. a) Step 1: XRR on Si/SiO_2/Ta/Pt sample with its fit. b) Step 2: XRR on Si/SiO_2/Ta/Pt/CFA sample with its fit based on that in a). c) Step 3: XRR on Si/SiO_2/Ta/Pt/CFA/MgO/Al sample with its fit based on that in c), d) Step 4: XRR on Si/SiO_2/Ta/Pt/CFA/MgO/Ta original sample with its fits.

either 3 nm Pt or 3 nm Ir) were deposited onto the substrate [140, 141, 156]. Next, the CFA films, with thicknesses of 2 nm, were deposited at room temperature by dc sputtering under an argon pressure of 1 mTorr and a deposition rate of 0.1 nm/s. MgO was deposited onto the CFA to mimic the interface used in a magnetic tunnel junction device, which is usually used as a key layer in the device readout. In order to protect the structure from air exposure, the CFA-based multilayers were capped. Three sets of sample structures were studied here: Pt-buffered samples capped with MgO(1 nm)/ Ta(2 nm), Ir-buffered samples capped with MgO(1 nm)/ Ta(2 nm) and Pt-buffered samples capped with MgO(1 nm)/ Al(2 nm) for the reference set of samples. Pieces cut from the same wafer were annealed. As mentioned earlier, the Heusler alloys were amorphous in the as deposited state. Therefore, an annealing process was required to initiate the crystallisation and introduce the atomic ordering. Therefore, the CFA-based multilayers were annealed at 400 °C for one hour [141]. The Ir and Pt layers have the expected (111) texture [85]. The nominal layer thicknesses were confirmed using x-ray reflectivity measurements using a Rigaku smartlab with Cu-kα radiation with wavelength of 1.54 Å. Layer thicknesses, roughnesses and densities were extracted from fitting the data using GenX software [157]. GenX uses a differential evolution algorithm for fitting, primarily, x-ray and neutron reflectivity data. More detail about the fitting software is given in the Appendix. In particular, information about the fitting procedure of the XRR curves can be found in the Appendix (section A.6.1).

The CFA films grown on Si substrates have polycrystalline structure and do not display any preferential growth direction [141]. In the heterostructures investigated here, the combination of strong SOI from the HM and inversion asymmetry due to the MgO overlayer induces significant net DMI. This makes the Ta layer not critically important for the DMI however, Ta imposes structural complexity.

In order to overcome the complexity of the XRR curve and to generate robust structural models of the multiple layers and interfaces in the pristine sample, a set of reference samples were made. The final structure was broken down by building up the whole stack in a 4-step process which is displayed in figure 5.3. This set consists four samples: the initial sample was deposited Ta/Pt, the next was

Ta/Pt/CFA and the final one was Ta/Pt/CFA/MgO/Al. The final sample structure is Ta(2 nm)/Pt(3 nm)/CFA(2 nm)/MgO(2 nm)/Ta(2 nm) approximately as shown in the figure 5.3 d). Figure 5.3 a)-d) shows the XRR curves from the 4-step process to systematically fit the final sample. Figure 5.3a) shows the XRR curve and sample schematic for a simple Ta/Pt bilayer on Si/SiO_2, allowing layer thicknesses and interface widths for these initial layers to be more easily determined. The addition of the CFA layer does not bring substantial differences to the XRR, as shown in figure 5.3b). Adding the MgO with a capping layer of Al produces Kiessing fringes with larger amplitude, figure 5.3c). The Al capping layer is needed because if the MgO is left uncapped it will absorb water and this will cause the CFA also to oxidise [158]. The Al layer prevents this from happening by forming an oxide layer itself (the thickness is self-limiting). Aluminium is light and so has only low interaction with x-rays, as does AlO_x as the interaction depends on the electron density in the material; these capping layers then should be essentially invisible. It is also shown in the figure that there are no big changes between the x-ray data in 5.3a), b) and c) and this is due to the fact that the element that plays a major role is the heavy metal which is the same in all those samples. The Al layer makes negligible difference to the measured x-ray reflectivity, as anticipated. The layer thicknesses and interface roughnesses for the Ta, Pt, CFA and MgO layers obtained from modelling the data from this sample set are then used in the fitting of the original sample.

Polarised neutron reflectivity (PNR) measurements for the CFA samples were made on the beamline Polref at Isis Neutron Source. Details of the technique are provided in chapter 3. The measurements were made using an in-plane external magnetic field of 0.3 Tesla to ensure magnetic saturation of the sample along the beam, the neutron beam was polarised parallel (I^+) and antiparallel (I^-) to the field. The derived spin asymmetry $I^+ - I^-/I^+ + I^-$ provides information on the depth configuration of the magnetisation through the multilayer structure.

XRMR measurements were made on the XMaS beam line at the European Synchrotron Radiation Facility (ESRF). The x-ray energy is tuned to the L_3 absorption edge of the element of interest, in this case Pt (≈ 11.5 keV) and Ir (≈ 11.2 keV). The

reflected intensity $I^{+(-)}$, corresponding to beam helicity parallel (antiparallel) to the saturating in-plane magnetic field applied in the scattering plane, is measured as a function of the scattering angle 2θ. The derived asymmetry $R_a = I^+ - I^-/I^+ + I^-$ is sensitive to PIM in the heavy-metal layer and is expected to reverse sign when the magnetic field is reversed. The asymmetry is uniformly zero in the absence of PIM. Care must be taken as asymmetry will also be uniformly zero if the energy is not on resonance. The fit of the spin asymmetry was made on an average of both helicities spin asymmetries, $\frac{(I^+ - I^-)}{2}$, (or the orientation of the external magnetic field). Similarly to the XRR data, both PNR and XRMR data were modelled using GenX. Similarly, more details about the fitting process can be found in the appendix. In the next section the structural and magnetic information provided by this fitting is described.

5.3 Multilayer structural analysis

From figure 5.3c) and d) there is a clear difference in the XRR curves when the only difference is the Al capping instead of the Ta capping layer. Ta as a capping layer increased the complexity of the reflectivity as it tends to diffuse vertically downwards in the structure [27] and also it oxidises, creating a layer of TaO_x (modelled as Ta_2O_5) with a thickness of approximately of 35 Å. Unlike Al, Ta has a more significant impact on the reflectivity due to the higher electron density, also with the diffusive behaviour the structure with Ta is significantly more complex as can be observed in figure 5.3d).

Furthermore, it is of great interest and importance for device applications to investigate how thermal processes can affect the devices on a structural level. Figure 5.4a) shows the XRR curves for both the non-annealed and the annealed samples with their respective fits for the Pt samples. The XRR for the annealed sample exhibits important changes in the middle part of the figure 5.4a). Sharper Kiessig fringes around q =0.3 $Å^{-1}$ and the opposite effect just after q =0.4 $Å^{-1}$ indicate changes in thicknesses, roughness and interfacial quality and also possible intermixing.

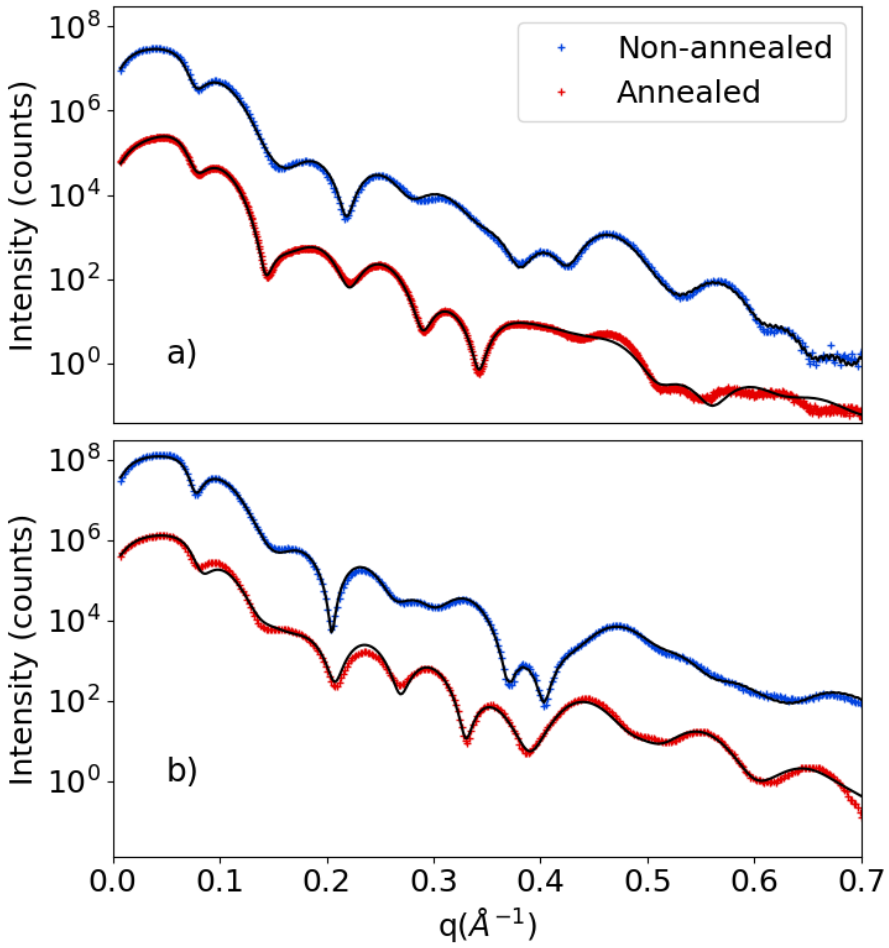

Figure 5.4: Comparison between the non-annealed and the annealed XRR curves samples with their respective fits made using GenX [157]. a) For the Ta(2 nm)/Pt(3 nm)/CFA(2 nm)/MgO(2 nm)/Ta(2 nm) samples and b) for the Ta(2 nm)/Ir(3 nm)/CFA(2 nm)/MgO(2 nm)/Ta(2 nm) samples.

Figure 5.4b) shows both the Ir non-annealed and annealed samples in which a similar effect is observed. The annealed Ir sample presented more difficulty in obtaining a best fitting model due to greater intermixing and/or diffusion. One possible explanation is that when a thermal process is applied to structures with an Ir layer the Ir tends to diffuse or intermix with the adjacent layers [159]. A more detailed discussion will be given along with the PNR results in the next section.

5.4 Depth resolved magnetism analysis

As informed in chapter 3, PNR is sensitive to the depth dependence of magnetisation in multilayered structure. Two reflectivity curves per sample are obtained, corresponding to spin states I^+ and I^-, and the spin asymmetry $R_a = I^+ - I^-/I^+ + I^-$ for both are shown in figure 5.5. The first feature to notice in all the plots in figure 5.5 is the small fringes on the range in q (0-0.06 $Å^{-1}$) which corresponds to interference fringes due to the 100 nm of the thermally oxidised Si/SiO_2 layer on the silicon substrate. These high frequency oscillations do not not give any directly useful information about the magnetic thin-film layers of interest in the samples. Figure 5.5 a) and b) show the PNR and spin asymmetry for the Pt samples, both the non-annealed sample and the annealed sample exhibit splitting between the two reflectivity profiles corresponding to the two neutron spin states. The splitting of the reflectivity curves in q is the result of the interaction of the neutron spin moment with the local magnetic induction, and the presence of such splitting demonstrates that ferromagnetism is present in the samples. The Pt annealed sample, figure 5.5b), presents a larger splitting than its non-annealed analogue. Accordingly, also the spin asymmetry is larger due to the thermal process which corresponds with what was found by Knut *et al.* [160], who observed that the thermal process in Co_2MnGe thin films deposited by magnetron sputtering induces diffusion processes within the Heusler alloy that are responsible for an increase in the magnetic moment in Co, this was measured with PNR and XRMR. Figure 5.5c) shows the Ir non-annealed sample where there is a clear splitting, *ergo* it also presents ferromagnetism. Nevertheless, it is interesting to notice that there is less splitting than in the Pt samples which can suggest that Pt enhances, or Ir decreases, the magnetisation of CFA. Also, it is important to point out that PNR is not sensitive to PIM as the moment is too small in comparison with the ferromangetic layer and localised within the sample as the PIM is only present within a nm from the interface [161]. In contrast, the Ir annealed sample is no longer magnetic which can be immediately seen from the fact that it does not present splitting in the reflectivity curves. This loss of the room temperature magnetic signal from the sample is consistent with the intermixing of the ferromagnetic layer with the Ir or MgO layer owing to the annealing process,

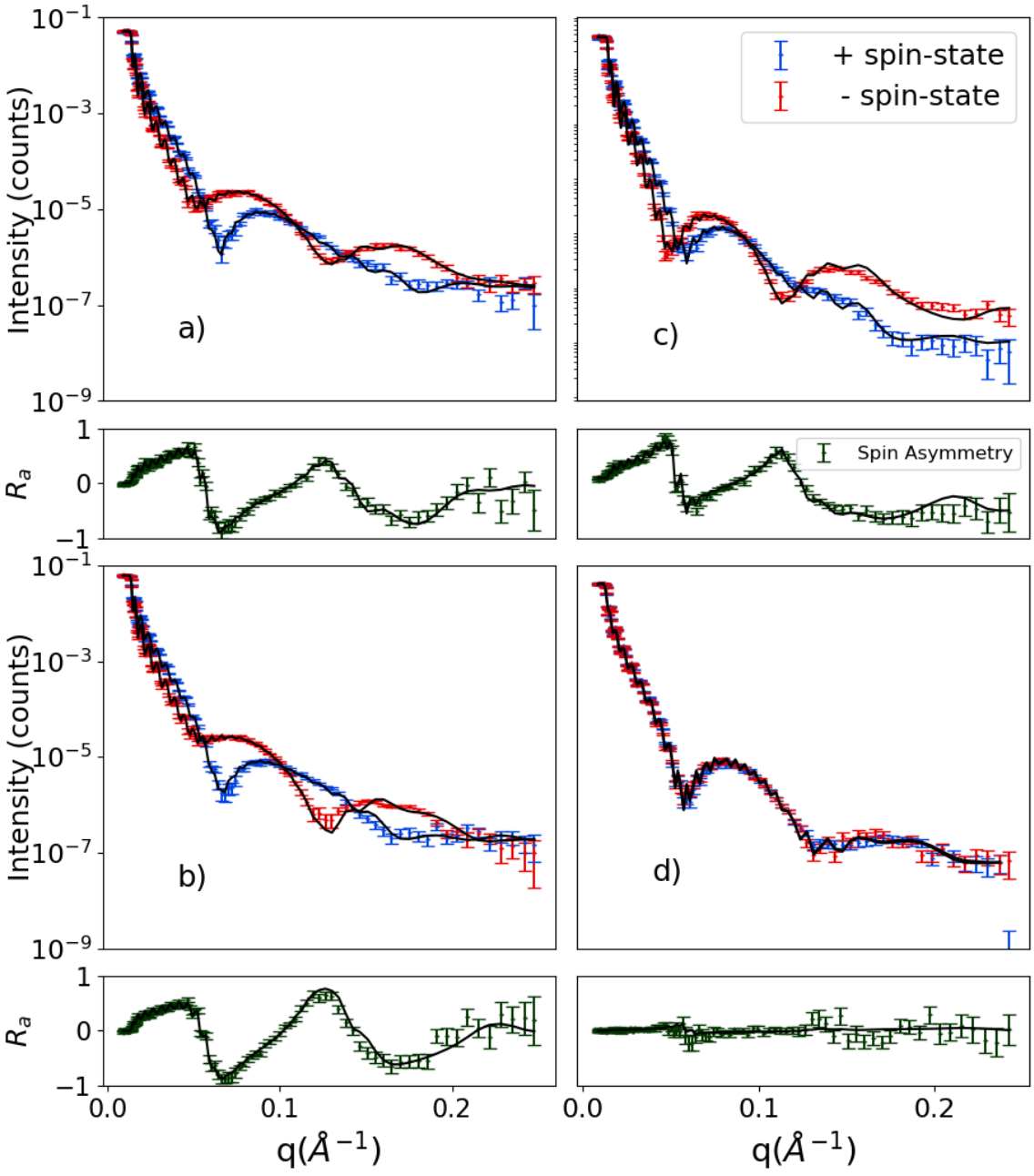

Figure 5.5: Spin-up and spin-down neutron reflectivities and spin asymmetries R_a. a) Non annealed Ta(2 nm)/Pt(3 nm)/CFA(2 nm)/MgO(2 nm)/Ta(2 nm) sample. b). Annealed Ta(2 nm)/Pt(3 nm)/CFA(2 nm)/MgO(2 nm)/Ta(2 nm) sample. c) Non annealed Ta(2 nm)/Ir(3 nm)/CFA(2 nm)/MgO(2 nm)/Ta(2 nm) sample. d) Annealed Ta(2 nm)/Ir(3 nm)/CFA(2 nm)/MgO(2 nm)/Ta(2 nm) sample. The annealed Ir sample does not present spin asymmetry, in which case we can conclude the sample is no longer magnetic at room temperature. The fits to the data were made using GenX software [157].

also seen in XRR (and MOKE). The fitting shows that this is the case; it appears that instead of of having three well-defined layers Ir, CFA and MgO after annealing at 400 °C there are two intermixed layer, Ir-CFA and CFA-MgO, neither of which are magnetic. We have observed similar intermixing between Ir and other FM metals and different temperatures of annealing [159]. Information about the fitting procedure of the PNR data can be found in the Appendix (section A.6.2).

In order to get a more accurate description of how the proximity induced magnetism in HM/CFA is modified due to the annealing process an element-specific measurement is require to give a full picture of the phenomenon. In the next section XRMR is described to analyse what contribution is coming from the HM.

5.5 Proximity induced magnetisation analysis

From the PNR analysis we learned that the there was splitting on the spin states reflectivity curves that confirmed magnetism in the sample, which may or may not contain contributions from the HMs. In order to measure the induce magnetic moment in the heavy metal XRMR was used. XRMR is an element-specific technique, in which the x-ray energy is tuned to the L_3 absorption edge of the target element, in this case either Pt or Ir. A reversible polarisation x-ray beam with, approximately 90% circularly polarisation was introduced using a diamond phase plate. Note that the peaks in the spin asymmetry coincide with the Kiessig minima, which occurs because the spin asymmetry contains the normalisation to the total scattered intensity. Figure 5.6a) shows the Pt non-annealed magnetic reflectivity and spin asymmetry, where the non-zero asymmetry shows that there is a proximity induced magnetisation (PIM) in the Pt. The reflectivity profile is very similar to the non-resonant XRR, shown in figure 5.3d), but not identical due to the different energy of the x-rays. The energy was tuned in the resonant edge of Pt enhancing the absorption and thus, the information will be centred on the Pt modifying the sSLD and as result the reflectivity curves. As the spin-asymmetry is larger at larger q this suggests that the PIM is localised in real space – close to the interface. For the Pt annealed sample, figure 5.6b), the data are very different, with larger

asymmetry at lower q suggesting the magnetism is less localised in real space. Also, there are several processes going on at once; the interface profile may become more complicated than the error-function approximation that GenX uses, which creates difficulty in fitting the higher q part (localised at the interface) or it may be that further slicing the structure is required, as the density varies with the position due to intermixing. This is computationally intensive in GenX to solve this problem. This might support our argument about the intermixing. Therefore, the fitting at high q was challenging.

For the Ir samples, figure 5.6c) shows the non-annealed sample which also has non-zero spin asymmetry with higher spin asymmetry for small angles and shows PIM; there is an induced magnetic moment also in Ir. It is important to notice that the measurement on the Ir samples cannot be compared with the one of Pt because the measurements were done at different energies as indicated in section 5.2.

Based on the PNR measurements, which show that the Ir sample annealed at 400 °C is not magnetic at room temperature, it was thought that the high temperature induces intermixing and/or diffusion into the magnetic layer therefore, only a limited XRMR measurement was conducted to confirm an absence of magnetic signal. In order to evaluate if the annealing temperature affects the result, a piece of the unannealed samples was taken and annealed at 200 °C for an hour and then similarly, the measurement was performed. The result can be found in figure 5.7 which shows, for the Ir samples, the comparison of the spin asymmetry, R_a, for the non-annealed and the 200 °C annealed. From the data available it appears that the thermal process makes a detrimental impact on the quality of the Ir-CFA interface and decreases the PIM apparent in Ir; R_a does decrease as we increase the temperature although doubling the temperature does not make a proportional detriment – this is the evidence for PIM decreasing (rather than the other way around as this was expected). More information about the fitting procedure of the XRMR data can be found in the Appendix (section A.6.3).

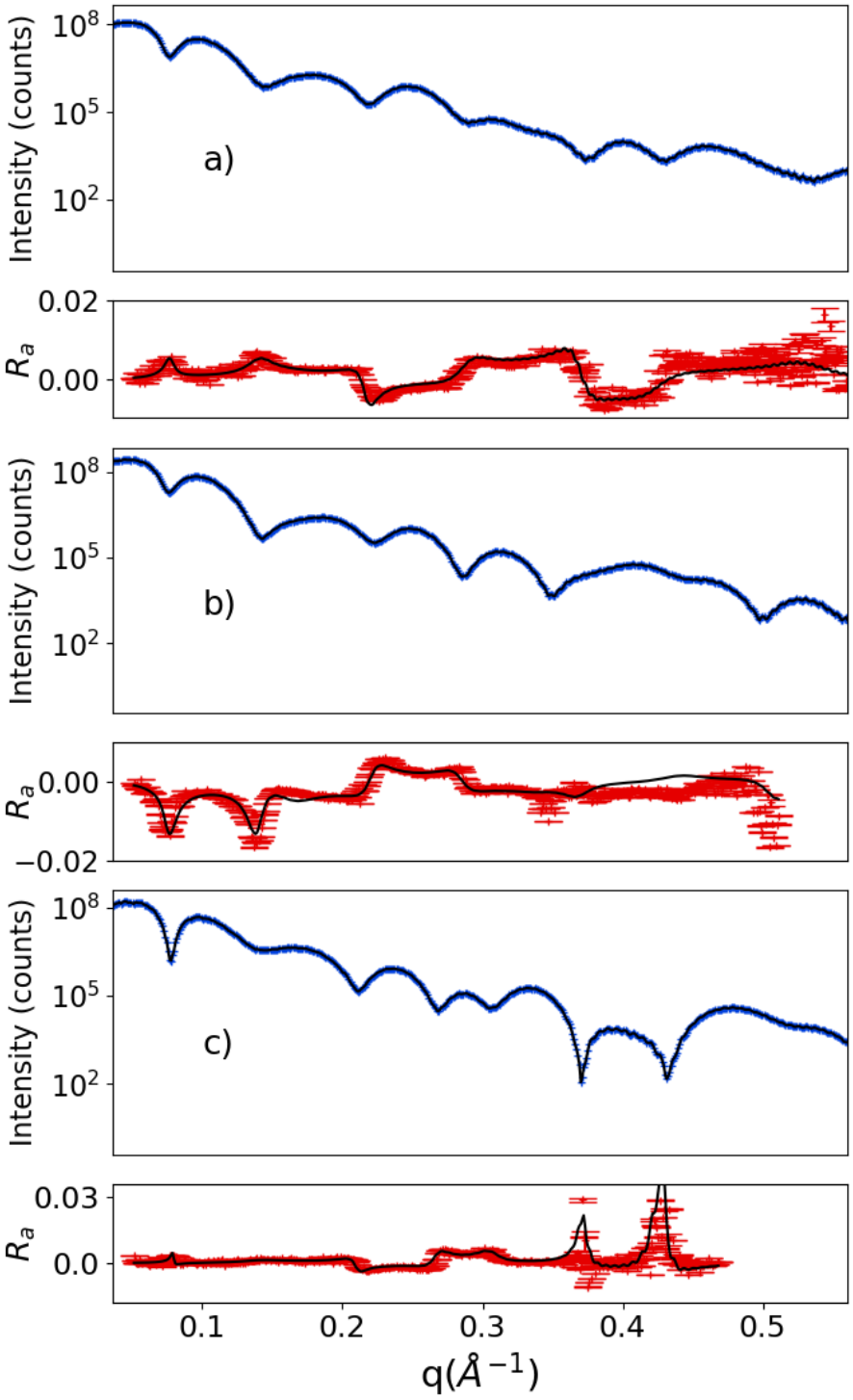

Figure 5.6: XRMR reflectivity and spin asymmetry. a) Unannealed Ta(2 nm)/Pt(3 nm)/CFA(2 nm)/MgO(2 nm)/Ta(2 nm) sample. b) Annealed Ta(2 nm)/Pt(3 nm)/CFA(2 nm)/MgO(2 nm)/Ta(2 nm) sample. c) Unannealed Ta(2 nm)/Ir(3 nm)/CFA(2 nm)/MgO(2 nm)/Ta(2 nm) sample. Fits to the reflectivity and spin asymmetry were made using GenX software [157].

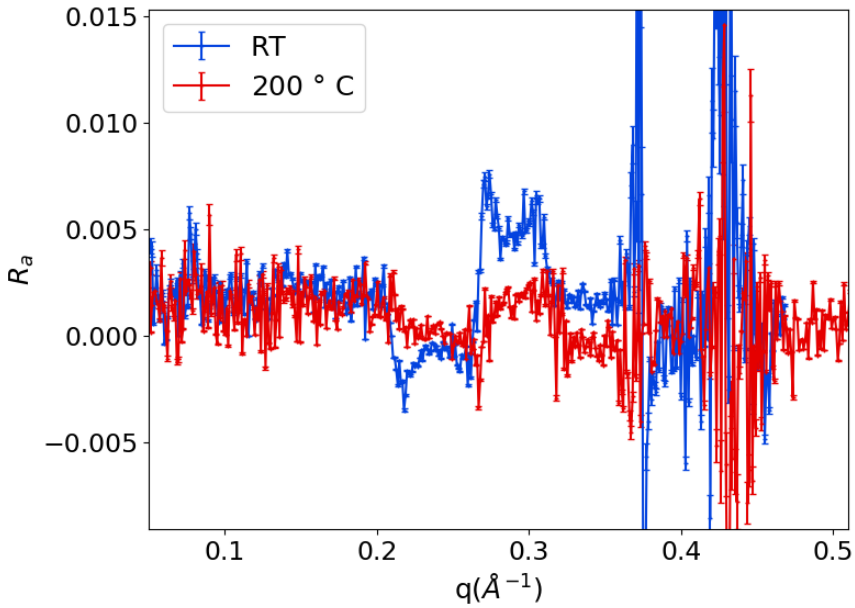

Figure 5.7: XRMR spin asymmetry for the non-annealed and the 200 °C annealed Ir samples.

5.6 Scattering length density and general discussion

Although the measurements that are used here use different type of probes, either light or neutrons, there is a quantity that can be extracted that allows for a comparison of the results and enables a fuller analysis of the samples; this is the scattering length density (SLD). From fitting of the XRR data a structural scattering length density (sSLD) is obtained. The sSLD informs on the scattering power, or the refractive index of a material, and it depends on the electronic density (atomic number) of the material. Therefore, the heavy metals contributes most strongly to the sSLD landscape. The upper row of figure 5.8 shows the sSLDs from XRR for Pt non-annealed (left) where the coloured background represents the different layers in the sample according to the fitting and figure 5.8 (middle) for the Pt annealed sample. There is a clear decrease in the amplitude of the sSLD in the Pt layer after annealing, and a broadening of the interface between Pt and CFA. This suggests diffusion of some component of CFA into Pt as a result of annealing at 400 °C. Figure 5.8 (top

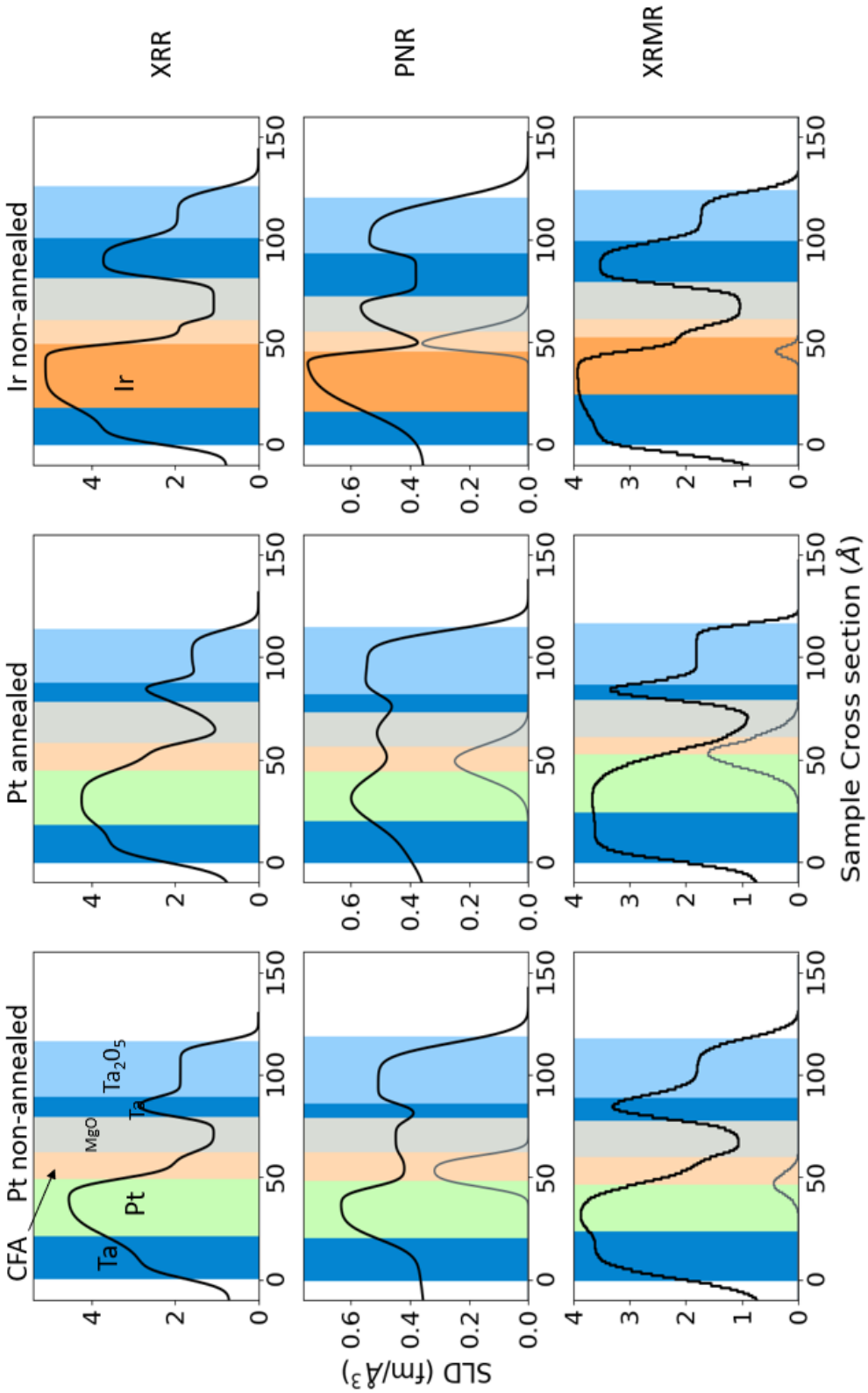

Figure 5.8: Structural and magnetic scattering length density for the Ta(2 nm)/Pt(3 nm)/CFA(2 nm)/MgO(2 nm)/Ta(2 nm) unannealed, Ta(2 nm)/Pt(3 nm)/CFA(2 nm)/MgO(2 nm)/Ta(2 nm) annealed and Ta(2 nm)/Ir(3 nm)/CFA(2 nm)/MgO(2 nm)/Ta(2 nm) unannealed samples. First row is the XRR for the 3 samples. Then, the second row is the PNR and finally, in the thrid row is the XRMR, in which we can see that the annealing process in the Pt sample created an increase in the PIM. Each colour will identify one material as shown in the first image (top left). The colours will remain the same for all the plot except for the Ir ones which is indicated.

right) shows the sSLD for the Ir non-annealed sample. A comparison between the non-annealed and the annealed Ir samples is shown in figure 5.9. The sSLD profile for the Ir sample after annealing shows the complete disappearance of a distinct CFA layer as a result of thermally induced intermixing of Ir into CFA and CFA into MgO as shown in figure 5.9b), in which the intermixed layers are highlighted in different colours from the non-annealed sample. The annealed Ir sample no longer exhibits room-temperature ferromagnetism. This result is interesting as in the non-annealed case the Ir interface is sharp, and a sharp interface usually occurs when materials do not mix easily [162], yet it mixes readily at high temperature. In order to investigate further the depth resolved magnetism in the CFA layers the same set of samples the magnetic SLD (mSLD) were obtained from PNR and XRMR.

The PNR SLD profiles are shown in the middle row of figure 5.8, and show both the structural depth profile and how the magnetisation is distributed within the samples. In the case of unannealed Pt (left) the mSLD is mainly concentrated in the ferromagnetic layer as expected. A small magnetisation contribution is present also apparently in the Pt layer; which may be due to roughness and/or intermixing of the Pt/CFA interface inherited from the sSLD, but may also be a result of PIM in Pt. The Pt annealed sample (middle) presents a broader distribution of the mSLD which, suggests that both the Pt/CFA and CFA/MgO interfaces become more strongly intermixed as the sSLD shows, with broader gradient in between the CFA and Pt/MgO, which then explains why the magnetic signal extends further into the Pt and MgO layers – due to the intermixing.

Note that, on the other hand, the sharp Ir/CFA interface in XRR shows up in both the structural and magnetic SLDs for the unannealed Ir sample in figure 5.8 (right); the sharp die-off of magnetism into nominal Ir layer is most likely due to the roughness and/or intermixing rather than PNR being sensitive to PIM in Ir. In contrast, for the Ir annealed sample, figure 5.5d), the sample presents no ferromagnetism as there is no splitting in the reflectivity curves. Further, a comparison between the sSLD and mSLD of both the non-annealed and annealed Ir is shown in figure 5.10. For the Ir annealed sample in figure 5.10b) it can be observed that the mSLD is basically null while the sSLD presents significant differences compared to

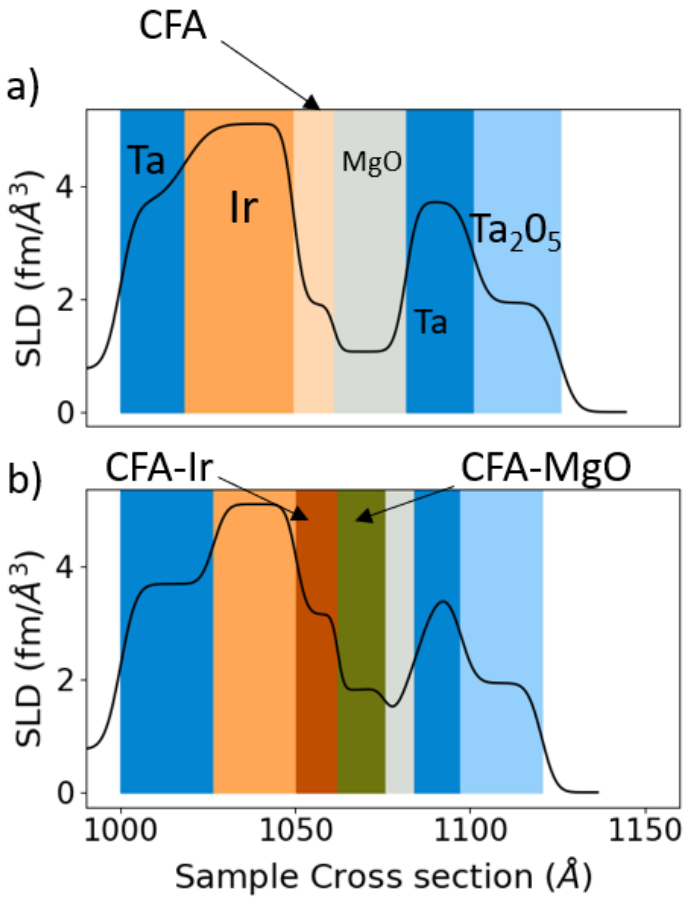

Figure 5.9: XRR sSLD for both a) the non-annealed and b) the annealed Ir samples which shows the intermixing of the CFA layer with its adjacent layers.

the non-annealed analogue.

As the main contribution to the mSLD arises from the neutron's interaction with the total magnetic moment of the atomic electrons of the material. The mSLD is directly proportional to the magnetisation by

$$\text{mSLD}(z) = -\frac{m}{2\pi\hbar^2}\mu_n M \approx 2.853 \times 10^{-9} M, \tag{5.6.1}$$

in cgs units, from which the magnetisation can be extracted [163] in order to compare with the equivalent to what it is being measured by VSM or SQUID. The raw mSLD data is given in units of $1/\text{Å}^2$ and represents the depth resolved distribution of the magnetisation of the film. Within the magnetic layer, the mSLD is maximum close to the centre of the CFA layer. This can be modelled and interpreted as the magnetisation being uniform across the layer (ideally mSLD should be a rectangle)

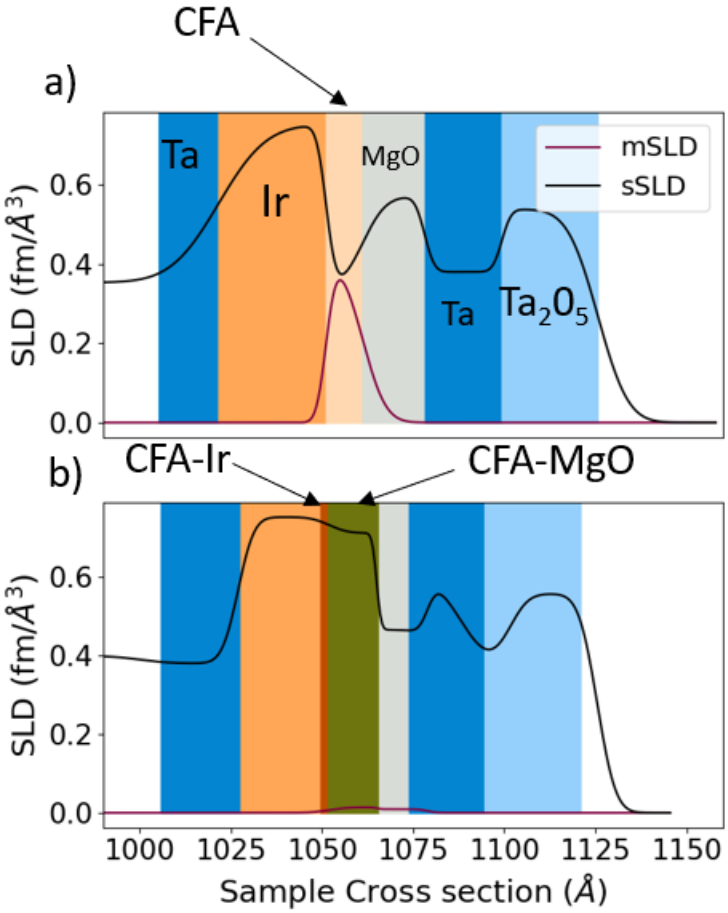

Figure 5.10: sSLD and mSLD for both a) the non-annealed and b) the annealed Ir samples.

but this is convoluted with the structural interfaces to give a 'peak'; so the magnetisation is uniform but there is 'less' CFA at the edges and more of other materials contributing to the reduced signal and therefore, this approach will overestimate the magnetisation. Now, if considering just the peak in the mSLD as representing the uniform magnetisation in the layer the Pt non-annealed and annealed M is 1110 ± 50 emu/cm^3, and 870 ± 40 emu/cm^3 respectively. Similarly, for the Ir non-annealed M = 1255 ± 60 emu/cm^3. The error is set to 5% for the magnetisation calculation inherited from the mSLD. The reported value for the CFA thin films deposited by magnetron sputtering at room temperature and the annealed analogue at 400°C for one hour by Belmeguenai *et al.* are 1200 ± 50 emu/cm^3 and 1170 ± 50 emu/cm^3 [140] for films grown using the same deposition system and processes as used for the samples reported here. On the other hand, the theoretical mag-

Magnetisation (emu/cm^3)			
Peak values			
Pt		Ir	
Unannealed	Annealed	Unannealed	Annealed
1110 ± 50	870 ± 50	1255 ± 60	20 ± 5
Integrated values			
Pt		Ir	
Unannealed	Annealed	Unannealed	Annealed
570 ± 30	580 ± 30	520 ± 30	10 ± 5

Table 5.1: Summary of the magnetisation calculated from the neutron mSLD for both Ta(2 nm)/Pt(3 nm)/CFA(2 nm)/MgO(2 nm)/Ta(2 nm) and Ta(2 nm)/Ir(3 nm)/CFA(2 nm)/MgO(2 nm)/Ta(2 nm) unannealed and annealed.

netisation for the bulk CFA is 880 emu/cm^3 which corresponds to a half-metallic material [164–166]. The value for the Pt annealed found by PNR is close to the reported value.

Alternatively, there is another option in which it is assumed that the magnetisation is not uniform across the layer and is actually represented by the mSLD; this is usually done for thicker layers, but less accurate for thinner layers. Comparatively with the first approach (taking the peak), this approach underestimate the magnetisation as the magnetic layer is rather thin. The layer quality (vertical and lateral roughness and intermixing) plays a bigger role in this approach, thus is also possible to estimate the magnetisation integrated over all the magnetic layer. For the Pt non-annealed sample, this approach gives a net magnetisation of 570 ± 30 emu/cm^3 and 580 ± 30 emu/cm^3 for the Pt annealed. Similarly, for the Ir non-annealed gives a net magnetisation of 520 ± 30 emu/cm^3. All the magnetisation values can be found in table 5.1

From the results of the first approach it is found that the Pt annealed sample presents a smaller magnetisation even with the annealed process. This was unexpected because improvement in the crystal order from the CFA was expected. However, at the same time it is found a broadening of the mSLD that goes beyond the magnetic layer which can be coming from the HM in the integrated magnetisation calculation and is also than is the case in the unannealed sample. In order to complete the picture, the mSLD from the XRMR will give a more in-depth description of the magnetisation that comes from the HM. The sSLD for the annealed

sample also shows that the interface is much broader (the layers do not have flat tops) which suggests wider alloying.

The XRMR SLD profiles are shown in the lower row of figure 5.8. Figure 5.8 (left) shows the sSLD and mSLD for the non-annealed Pt and it shows a similar behaviour to the sSLD obtained from the XRR. As XRMR is an element-specific technique the mSLD is entirely coming from the Pt which is purely PIM. The mSLD shows a small induced magnetisation in Pt, which decays away from the interface with CFA over a lengthscale of 1.2 ± 0.1 nm. This suggests that the contribution to the mSLD observed by PNR in figure 5.8 (middle, left), which decays over a larger lengthscale 2.5 ± 0.1 nm, is not specifically the result of PIM. On the other hand, figure 5.8 (middle) also shows the SLD for the annealed sample. The sSLD is again consistent with those from both XRR and PNR, with the structural profile, parameterised by the layer thicknesses and interface roughnesses, in agreement within experimental error. The mSLD shows an enhanced PIM which is both of larger amplitude, and greater spatial extend suggests intermixing.

We have two very different counterintuitive set of results: the sample annealed at 400 °C is supposed to enhance the CFA crystallisation, but in the case of Ir it has the opposite effect; this suggests that Ir/CFA is not a good material combination for devices. For Pt there is an intermixing between Pt and CFA; the anneal procedure that is 'needed' to order the CFA actually has an effect of disordering the interface, which likely is not ideal.

This demonstrates that thermal annealing causes a diminution of the quality of the structure which affects the magnetic properties of the sample that contrarily improve the PIM in Pt, which can be due to alloying with Co that creates more polarisation. This is the primary result presented in the chapter, which is opposite to what was expected. Even if the structure of the CFA layer improved with the anneal process, the same process induced other structural changes that worsen the overall quality and thus also worsen the magnetic properties. This may be a result of the complexity of the multilayer structure. In the case of the unannealed Ir sample, figure 5.8 lower left, this shows the SLD and mSLD similarly to the Pt samples, the SLD is similar to the one obtained in the XRR and the mSLD shows the PIM in

the Ir layer. In contrast, the annealing process in the Ir samples caused the CFA layer to disappear, which is attributed to intermixing with the adjacent layer, which destroys the magnetism in the sample. It important to note that it is possible to compare the magnetic signal between Pt samples as they are measured at the same beam energy, but not with Ir.

5.6.1 FMR analysis

At this point, there were several values for the magnetisation obtained according to different analysis approaches. Alternatively, FMR measurements were performed to compare with the magnetisation estimates obtained from the mSLD. Figure 5.11a) shows the linewidth, ΔH, which is directly connected to the relaxation processes, and in figure 5.11b) the Kittel curves for both the non-annealed and annealed Pt samples [65]. As described in chapter 3, after fitting both curves, the Gilbert damping, α, the magnetisation, the anisotropy, H_a and the linewidth were extracted and presented in table 5.2. The linewidth informs about the structural defects within the ferromagnetic layer and, it is found that the linewidth for the Pt annealed is double than the unannealed case confirming that the thermal process produces more defects – Pt diffusing into the CFA layer. With Pt in the CFA layer would increase the SOI in the layer which will increase the g-factor as it was found here. Moreover, α doubled up with the thermal process and knowing that α is affected by the spin pumping. This increase suggests after the thermal treatment the interface became less transparent and this also could come from detriments at the interface found in the XRR, PNR and XRMR results. The magnetisation values obtained from FMR were 321 $\pm$ 11 emu/cm^3 for the unannealed Pt and 288 $\pm$ 60 emu/cm^3 which is substantially lower than the values obtained from PNR. Before the measurements, calibration of the system was performed with reference samples.

The magnetisation calculated from FMR gives a smaller value (almost half) in comparison with the one calculated from the PNR. It is important to mention that both measurement are believed to be reliable as calibration was performed with reference samples to reproduce known values. Also, is important to note that the experiments were performed at separate times, the FMR being performed more than

FMR results		
	Non-annealed Pt	Annealed Pt
Magnetisation (emu/cm^3)	320 ± 10	290 ± 60
α	0.0191 ± 0.0002	0.0411 ± 0.0009
ΔH (Oe)	38.97 ± 8.19	79.53 ± 26.88

Table 5.2: Summary of the magnetic parameters calculated with FMR.

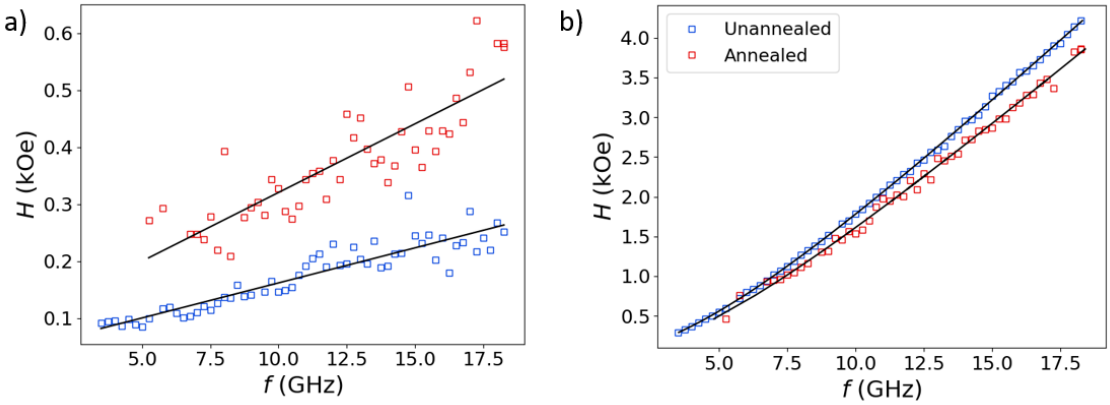

Figure 5.11: FMR measurements for both the non-annealed and the annealed Ta(2 nm)/Pt(3 nm)/CFA(2 nm)/MgO(2 nm)/Ta(2 nm) samples with fits. a) the linewidth curve and b) the Kittel curve. Errors on the frequency and field are smaller than the marker size.

a year after the PNR. Thus, it is possible the magnetic properties of the structures somehow degraded over time.

Analysing the magnetisation obtained by different experiments suggest that the magnetisation is degrading over time. This decay of the magnetisation might be rather due to structural changes over time that increases disorder at room temperature. If this is the case it would make the structure used here not ideal for devices applications because they will stop functioning just from staying on a shelf. Furthermore, when a device is being used heat is produced which will elevate the temperature, which will worsen following this line of thought. For example, CMOS devices operate from 100 up to 350 °C of temperature which is slightly lower that the thermal process applied here. In the case of Ir, if a computer is built out of CFA/Ir it will break itself within a couple of hours of being switched on.

5.7 Summary

Co_2FeAl films were prepared by sputtering on Si/SiO_2 substrates using different buffer and capping layers. There is a consistent story told by all three techniques XRR, PNR and XRMR shown in the SLDs (fig 5.8). As expected the annealing process changes the structure of the samples and also modified the magnetic properties both in the layer and the interfaces. The structural configuration after the thermal process cause a detrimental on the magnetism on the Ir samples due to a possible intermixing with the adjacent layers. Moreover, it also induced a decreased in the magnetic moment of the CFA which contrarily creates an increase in the PIM in the Pt sample. Even though CFA seem to be a promising material for domain-wall devices, but careful control of growth, and optimisation of thermal treatments is required for devices containing CFA in order to work. Finally, we noticed that the magnetisation decreased over time suggesting that this whole structure will not be able to sustain the properties require to create devices.

Chapter 6

Dzyaloshinskii-Moriya interaction in multilayers with engineered interfacial roughness

The previous chapter focused on the proximity induced magnetisation that arises in heavy metals such as Pt and Ir and how it can be modified when a thermal process is applied. Furthermore, what the thermal process effectively modifies is the interface quality between the heavy metal and the ferromagnetic layer which does not just modify the PIM, but also also a change the DMI induced in asymmetric multilayers [141]. The structural changes modify the magnetic properties of the system.

Magnetic materials with PMA have great impact on current and future high-density information storage applications as higher bit densities with large thermal stability may be achieved. In particular, in PMA materials having very narrow domain walls, high spin-torque efficiencies and fast domain wall velocities might be expected. A domain wall is chiral if two domain walls separated by a domain are distinguishable from its mirror image, as shown in figure 6.1a) [172]. On the other hand, an achiral domain wall would not be distinguishable from its mirror image as displayed in figure 6.1b). Formation of achiral Bloch domain walls is favored during magnetisation reversal in PMA materials. Magnetic and non-magnetic heavy metal systems like Pt/Co exhibit PMA. However, due to strong spin-orbit coupling in

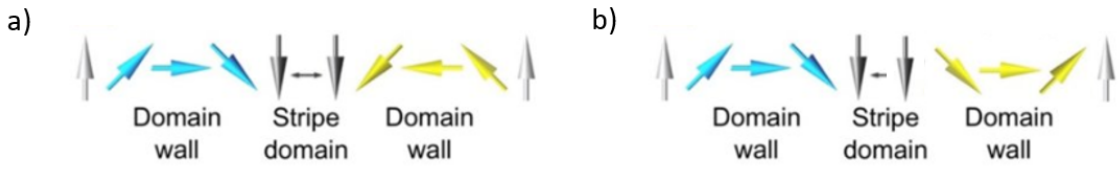

Figure 6.1: a) Schematic of a chiral domain wall [172] in which the DW1 (blue arrows) and DW2 (yellow arrows) are distinguishable from its mirror image. b) Schematic of an achiral domain wall, adapted from [172].

these materials, the antisymmetric exchange interaction at the interface between a ferromagnet and heavy metal that is termed the Dzyaloshinskii-Moriya interaction (DMI) results in the formation chiral Néel rather than Bloch domain wall structures as described in chapter 2. The symmetry breaking associated with the DMI is required for the formation of atomic scale topologically protected chiral magnetic textures such as skyrmions. Skyrmions have typical dimensions of 10 - 100 nm, which is about one order of magnitude smaller than the stable domain size in ferromagnetic materials with PMA. So skyrmions opens the possibilities of significantly increasing information storage density and novel logic device applications [3, 173–175].

Interfacial DMI material systems with opposite growth order exhibit the opposite sign of DMI [10, 37, 38]. Therefore, to obtain a sizeable DMI, it is essential to form an asymmetric layer structure. Furthermore, it was reported that even with symmetric layer structures like Pt/Co/Pt, DMI may exist, because the two interfaces are not be symmetric in terms of different growth sequence, roughness, thicknesses, the degree of layer intermixing that is the result of different growth parameters [36] such as gas pressure. The DMI depends on the geometry of the structure and the quality of the interfaces between the the ferromagnetic layer and the adjacent layer. Numerous studies changing parameters have been performed in order to investigate the true behaviour of the DMI. Cho *et al.* showed the proportional dependence of the DMI on the inverse thickness of the magnetic layer for Pt/Co/AlO_x and Pt/CoFeB/AlO_x [35]. Moreover, it was confirmed that the DMI is a purely interfacial effect for Co with Pt underlayer. Additionally, Tacchi *et al.* explored how changing the Pt thickness enhances the DMI for CoFeB/Pt(d_{Pt})/Cu. where d_{Pt} was changed in the range between 0 and 6 nm [39]. Wells *et al.* investigated the role

of intermixing on the interfacial DMI. It was found that deposition temperature increases the intermixing of the top and the bottom interfaces and, subsequently, also increased a non-zero net interfacial DMI for Pt/Co/Pt [36].

A deeper understanding of the interfacial DMI mechanism in such structures and a precise estimation of its magnitude are therefore crucial for tailoring efficient spintronic devices.

In this chapter, the influence of interfacial roughness, σ, on DMI in Pt/Co/Pt and Pt/Co/Ta systems with broken inversion symmetry was studied. BLS and the asymmetric bubble expansion technique were used to determine the DMI as a function of the roughness in the multilayers.

6.1 Structural characterisation of multilayers

The road towards having a controlled induced-roughness method into the multilayer thin-films was not straightforward and it took almost 8 months to find a suitable seed material and deposition method for it.

Pt(11 nm)/Co(0.6 nm)/Pt(4 nm) [Pt/$Co_{\perp}$/Pt], Pt(7 nm)/Co(3 nm)/Ta(4 nm) [Pt/$Co_{\parallel}$/Ta] and Pt(4 nm)/Co(1.1 nm)/Ta(4 nm) [Pt/$Co_{\perp}$/Ta] thin film structures were grown at room temperature using the magnetron sputtering system described in chapter 3, with a base pressure lower that 2×10^{-7} Torr.

It is not an easy task to control the roughness at individual interfaces in a multilayer thin film stack. However, there are methods to systematically control the overall roughness at all interfaces. A simple process to engineer the surface roughness was developed; depositing a seed layer that in this context will change the roughnesses of all the interfaces. SiO_2 was the ideal material because the substrates used in this work already has a SiO_2 layer, which is convenient as it does not oxidise and makes the fitting process easier. Similarly, silver provides a rough surface when deposited by thermal evaporation. Prior to deposition of the multilayer structures Pt/$Co_{\perp}$/Pt and Pt/$Co_{\parallel}$/Ta, Ag layers of different thickness were deposited by thermal evaporation, whereas sample set Pt/$Co_{\perp}$/Ta had SiO_2 layers deposited by sputtering. Deposition of the multilayer onto sets of these seed layers allows other-

wise identical, high quality, multilayer deposition of films with engineered roughness onto thermally oxidised Si wafer. The Ag layer nominal thickness varied from 0.5 nm to 4 nm and the SiO_2 from 0.1 nm to 1.4 nm. Each thin film set was deposited at the same time after the roughness induction to make them identical.

Figure 6.2a) shows the Pt/$Co_\perp$/Pt, Pt/$Co_\parallel$/Ta and Pt/$Co_\perp$/Ta multilayer stacks studied here. The XRR measurements for both set of samples with the Ag buffer confirmed the nominal layer thicknesses, roughnesses and densities from fitting the measured reflectivity profiles that are shown in figure 6.2c) and d) by using `GenX` software [157].

Pt as a buffer layer enhances the PMA with cobalt when deposited by magnetron sputtering due to the Pt layer promoting the growth of the fcc (111) orientation [85]. Figure 6.2c) shows the XRR for the Ag(d_{Ag})/Pt/$Co_\perp$/Pt where there is a clear increase of the roughness in the samples. A more dramatic change is found for 1.5 nm of Ag, which is observed in the fading away of the Kiessig fringes gradually as the Ag thickness increases. On the other hand, figure 6.2d) shows XRR for the Ag($\mathrm{d_{Ag}}$)/Pt(11 nm)/Co(0.6 nm)/Ta(4 nm), which is more complex due to the presence of Ta. Ta as a capping layer increased the complexity of the reflectivity as it can diffuse vertically downwards through the layers [27] and also it oxidizes, creating a layer of TaO_x (modelled as Ta_2O_5) with a thickness of approximately 4.5 nm . The effect of the Ag presence is similar to the previous structure. However, the roughness is larger due to the thinner Pt bottom layer. The roughness at the lower Pt/Co interface as a function of the Ag thickness for the Pt/$Co_\perp$/Pt shows a growing non-linear behaviour until d_{Ag}=25 Å, which is presented in figure 6.2b). The Pt/$Co_\perp$/Pt set presented a simpler structure which made fitting the structure from x-rays possible using GenX. This is because the structure has a thinner ferromagnetic layer and in order to preserve the integrity of the ferromagnetic layer a thicker Pt layer was deposited to reduce the roughness in the structure. On the other hand, it was not possible to fit the Pt/$Co_\parallel$/Ta due to the larger roughness in comparison to the layer thickness in the system Pt/$Co_\parallel$/Pt. More information about the roughness estimation using GenX can be found in the Appendix (section A.7).

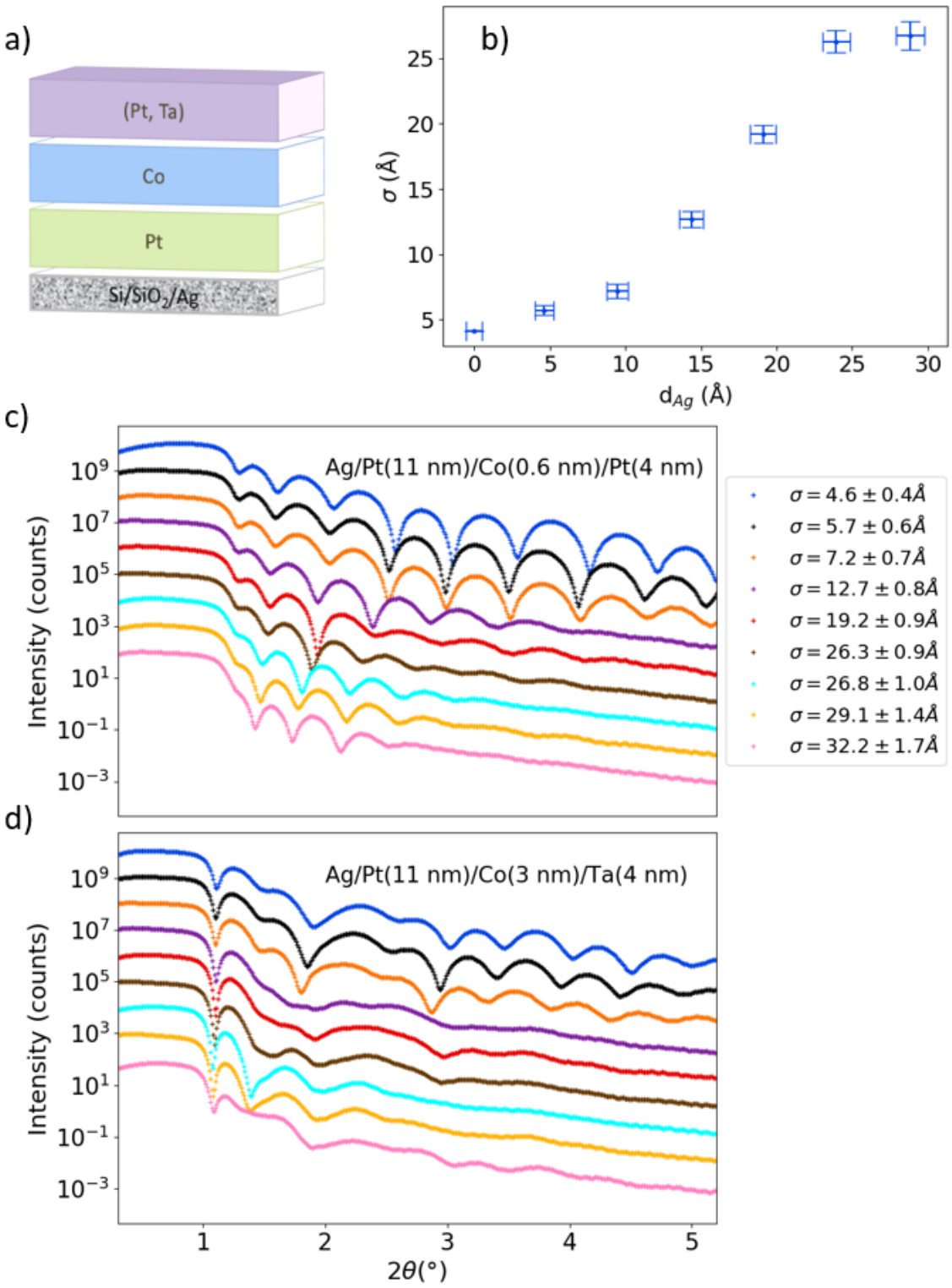

Figure 6.2: a) Multilayer stack schematic. b) Relation between the roughness at the Pt/Co interface and the Ag thickness, extracted from GenX fits. XRR for the roughness induced multilayer stack with thermally-evaporated Ag from 0–4 nm. c) Ag(d_{Ag})/Pt(11 nm)/Co(0.6 nm)/Pt(4 nm), d) Ag(d_{Ag})/Pt(7 nm)/Co(3 nm)/Ta(4 nm).

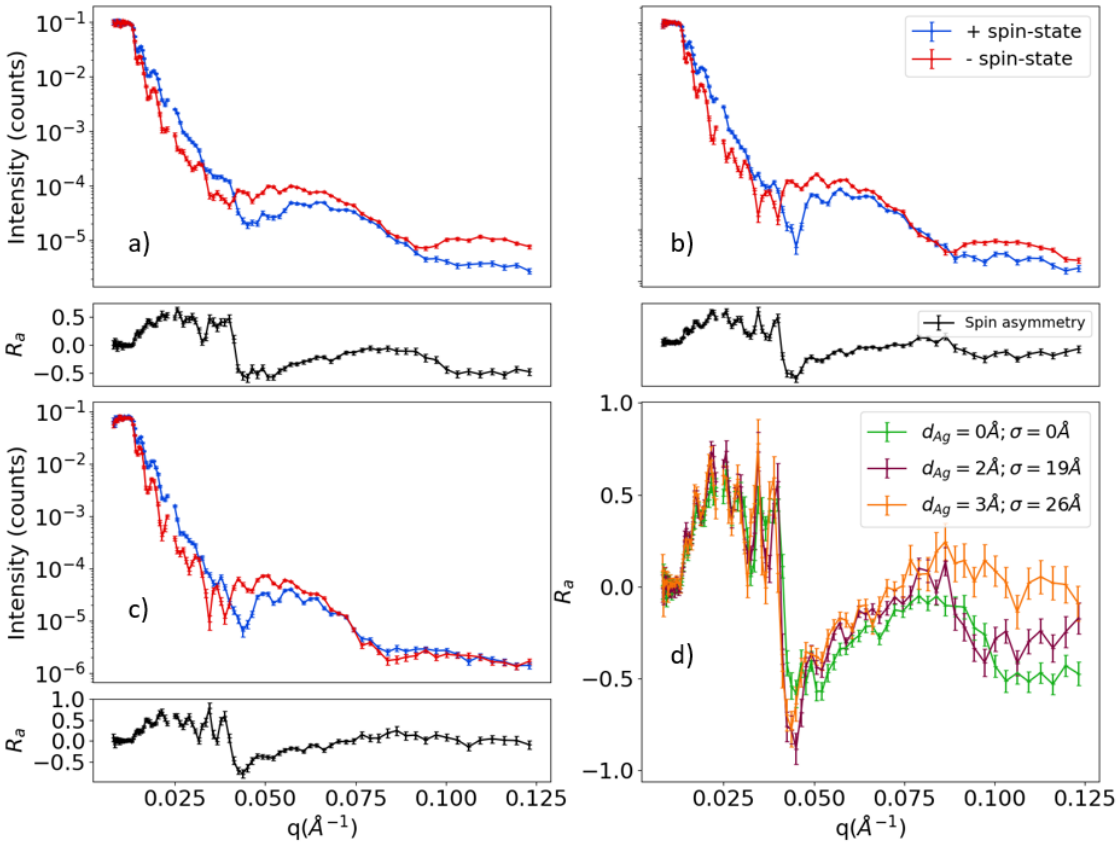

Figure 6.3: Spin states reflectivity and spin asymmetry for Ag (0–4 nm)/Pt(7 nm)/Co(3 nm)/Ta(4 nm) as function of σ. a) For $\sigma = 0$ Å, b) $\sigma = 19$ Å, c) $\sigma = 26$ Å and d) the comparison of the all spin asymmetry.

6.2 Magnetic characterisation of multilayers

From chapters 3 and 5 it was learned that PNR is sensitive to the depth dependence of magnetisation in the multilayer structure. With two reflectivity curves per sample, corresponding to spin states I^+ and I^- and the spin asymmetry $R_a = I^+ - I^- / I^+ + I^-$ are shown in figure 6.3 for Ag(d_{Ag})/ Pt(7 nm)/Co(3 nm)/Ta(4 nm). This stack was the only one measured as it is the only one that presents in-plane magnetisation and PNR in only sensitive to in-plane magnetisation samples. The first feature to notice in all of the plots in figure 6.3 is the small fringes on the range in q (0-0.045 Å^{-1}), which correspond to interference fringes due to the 100 nm of thermally oxidised SiO_2 layer on the silicon substrate. These high frequency oscillations do not give any directly useful information about the magnetic thin-film layers of interest in the samples. Figure 6.3a) shows both the spin state reflectivity curves and the

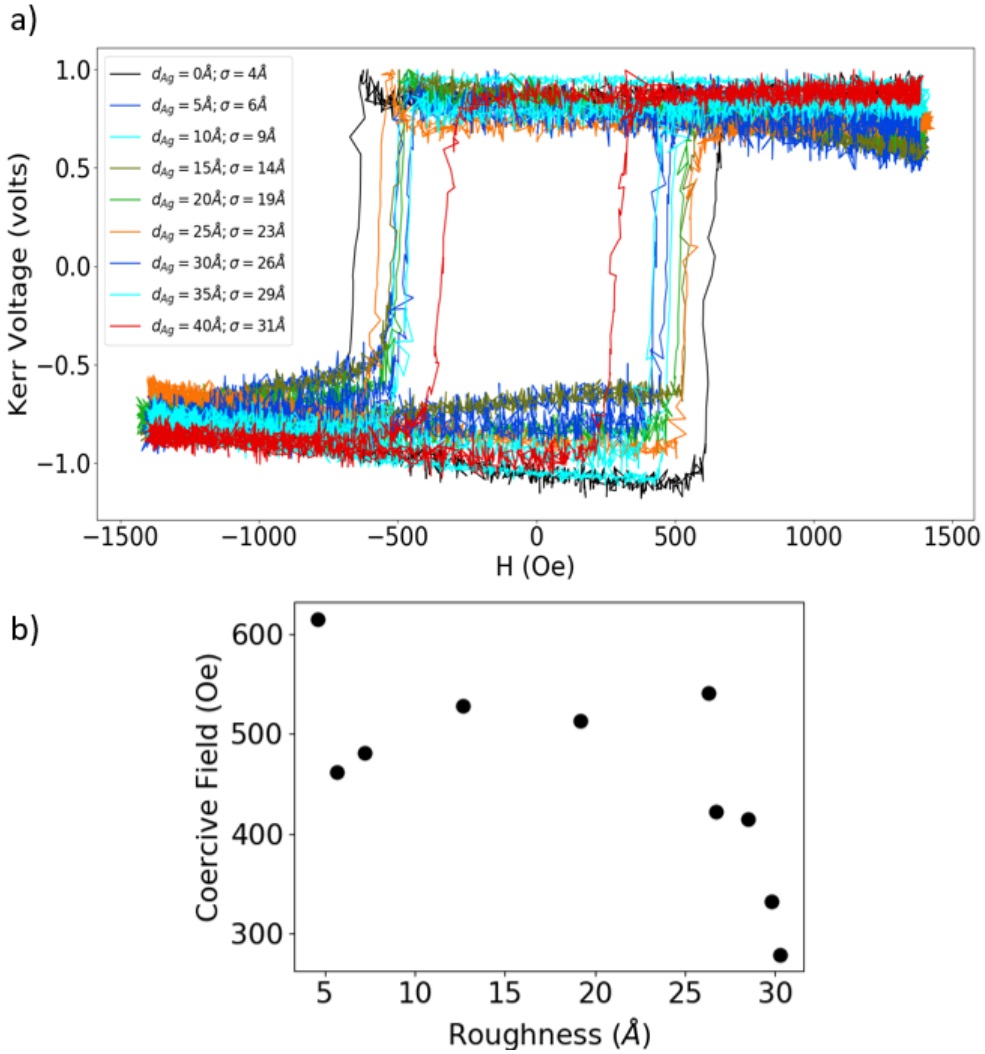

Figure 6.4: a) Out-of-plane MOKE measurements for the roughness induced multilayer stack with Ag (0–4 nm)/Pt(11 nm)/Co(0.6 nm)/Pt(4 nm). b) The coercive field decreases with increasing roughness.

spin asymmetry for $\sigma = 0$ Å($d_{\mathrm{Ag}} = 0$ Å) which shows a splitting in the different spin states reflectivity curves. The splitting of the reflectivity curves in q is the result of the interaction of the neutron spin with the local magnetic induction, and the presence of such splitting demonstrates that ferromagnetism is present in the samples. This is also observed for the other two samples, $\sigma = 19$ Å($d_{\mathrm{Ag}} = 20$ Å) and $\sigma = 26$ Å($d_{\mathrm{Ag}} = 30$ Å) shown in figure 6.3b) and c) respectively. The nominal multilayer structures are identical so that the changes present in the curves are entirely due to the interfacial roughness induced. This is expected to change the structural quality of the multilayers and thus, also change the magnetic properties that are

shown by subtle changes in the spin asymmetry in figure 6.3d). The increase in the spin-asymmetry at large q suggests that the roughness slightly enhances the magnetisation. The highest (negative) signal in the spin asymmetry in all the samples is around $q \approx 0.042$ Å^{-1}, which is also where the changes are more visible in figure 6.3d). Also in the q range ≈ 0.100–0.125 Å^{-1}, the splitting changes for the different samples. This shows that the roughness affects the magnetism of the ferromagnetic layer. Along with the roughness, the Ta layer in the structure might be inducing some intermixing into the ferromagnetic layer which makes the process of fitting the reflectivity curves a more complex task using GenX, similar to that discussed in chapter 5.

Figure 6.4a) shows the polar MOKE measurements for Pt/Co$_\perp$/Pt. The coercive field dependence is not simple, but decreases as the roughness increases above 25 Å as shown in figure 6.4b). The square hysteresis loops suggests PMA in all cases and that the domain wall nucleation energy changes with roughness. Furthermore, the coercive field and the saturation field decreased to less than half of the value comparing with the samples without Ag.

These results supports the idea that roughness creates a variety of grains with different shapes and dimensions on the samples surface, which act as reversal nucleation points enabling lower field nucleation [176]. Having more, lower energy, nucleation sites creates a lower field magnetisation reversal mechanism for switching of the magnetic moment throughout the sample.

Figure 6.5a) shows Kerr microscopy images showing the shape of the reversed domain in the presence of both an in-plane field, $H_x = 500$ Oe, the perpendicular reversal field, which in this case is $H_z = -100$ Oe. The DW presents an ellipse-like shape, which will be discussed in more detail in in terms of the bubble expansion method in chapter 4. Depositing 1 nm and 2 nm of Ag underneath the Pt/Co structure induces approximately 0.7 nm and 1.8 nm of roughness respectively at the Pt/Co interface with provokes a less smooth DW shape as shown in figure 6.5b) and c). When d_{Ag} reaches a critical value of ≈ 2.5 nm it suddenly increases the density of nucleation points when applying a reverse field, as shown in figure 6.5d).

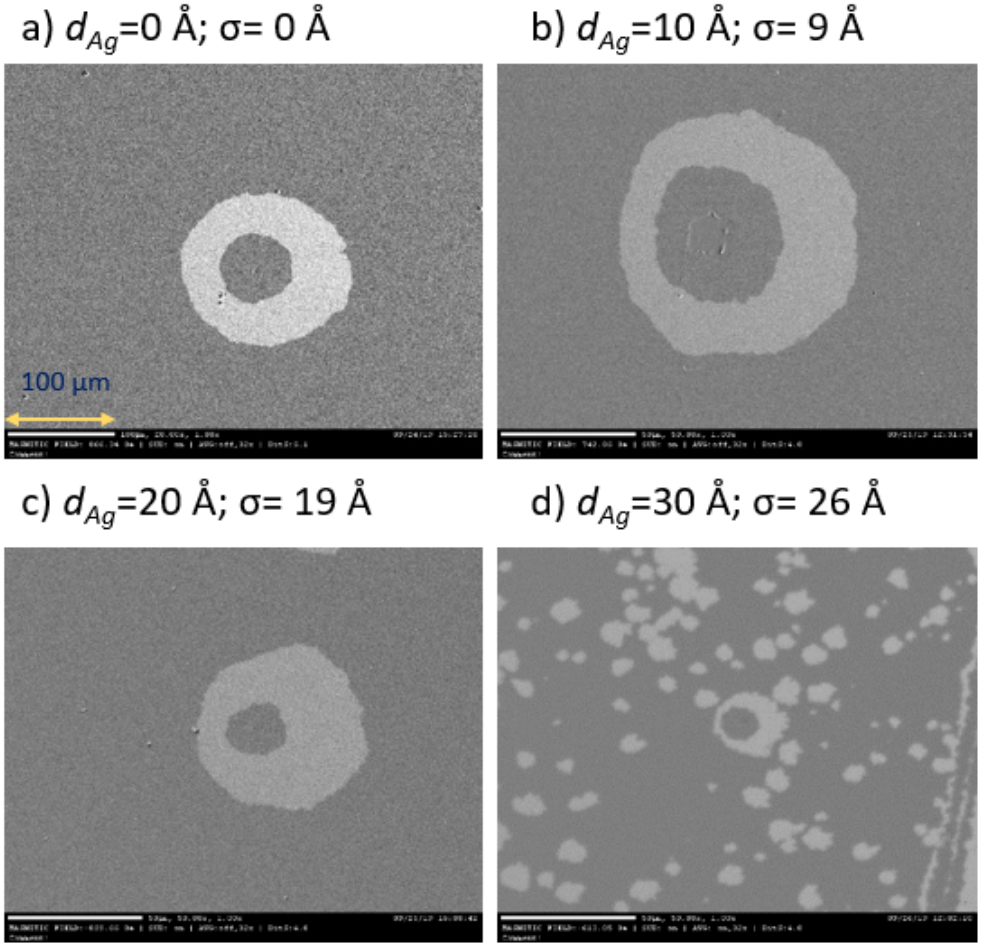

Figure 6.5: Polar Kerr microscopy images measurements for the roughness induced multilayer stack with Ag (0-3 nm)/Pt(11 nm)/Co(0.6 nm)/Pt(4 nm).

6.3 Brillouin light scattering technique to measure DMI

As was discussed in chapter 2, the DMI is an antisymmetric exchange interaction that favours orthogonal alignment of spins and the Hamiltonian takes the form

$$\hat{H}_{\mathrm{DMI}} = \vec{D}_{ij} \cdot (\vec{S}_i \times \vec{S}_j), \tag{6.3.1}$$

where $\vec{D}_{ij}$ is the Dzyaloshinskii-Moriya vector, which is non-zero only in the presence of inversion asymmetry and couples the spins S_i and S_j. The DMI stabilises Néel magnetic domain walls by acting as an effective internal magnetic field and also induces a specific chirality which depends on the sign of this effective DMI field

[13, 15, 74].

The central quantity in this chapter is the DMI and therefore, the effective DMI constant D_{eff} was determined using Brillouin light scattering (BLS) as a function of SiO_2 and Ag thickness in the two different Pt/Co/Ta sample series. The DMI introduces non-reciprocity for spin-wave propagation dependent on the sign of the spin-wave number. This manifests itself as a frequency shift for spin-wave modes travelling in opposite directions. The BLS technique was discussed in more detail in chapter 3.

The BLS measurement geometry was such that the Damon-Eshbach surface spin-wave mode was probed. The frequency of the Stokes (f_{S}) and anti-Stokes (f_{aS}) inelastic magnon lines were compared, where any difference in the shift in frequency was due to the interfacial DMI.

Two examples of BLS spectra for the roughness induced SiO_2(8 Å)/Pt/$Co_\perp$/Ta and SiO_2(11 Å)/Pt/$Co_\perp$/Ta are shown in figure 6.6 a) and b) respectively. The blue points show the Stokes magnon line, and the black points show the anti-Stokes magnon line. The shift in the frequency is calculated as $\Delta f = f_{\text{S}} - f_{\text{aS}}$. For SiO_2(8 Å)/Pt/$Co_\perp$/Ta a frequency shift of $\Delta f = 1.78$ GHz was extracted. The frequency shift for SiO_2(11 Å)/Pt/$Co_\perp$/Ta sample presents a smaller $\Delta f = 1.56$ GHz and both can be clearly observed as a difference in peak position between the Stokes and anti-Stokes lines. In order to extract Δf, a Lorenztian fit has to be made to each magnon peak. If the DMI is purely an interfacial effect, then the expected thickness dependence would follow $D_{\text{eff}} = D_{\text{s}}/t$ where D_{s} is the interfacial DMI constant, which is the more fundamental parameter depending only on the materials on either side of the interface. Given that the FM layer thickness is constant, the only variable that can modify the DMI is the interface roughness. The frequency shift can be converted to the interfacial DMI term using

$$D_{\text{s}} = D_{\text{eff}} t_{\text{FM}} = \frac{\pi}{2\gamma} \frac{M_{\text{s}} t_{\text{FM}} \Delta f}{k_{\text{sw}}},$$

where the gyromagnetic ratio $\gamma = g\mu_{\text{B}}/\hbar$, $t_{\text{FM}} = 11$ Å is the ferromagnetic layer

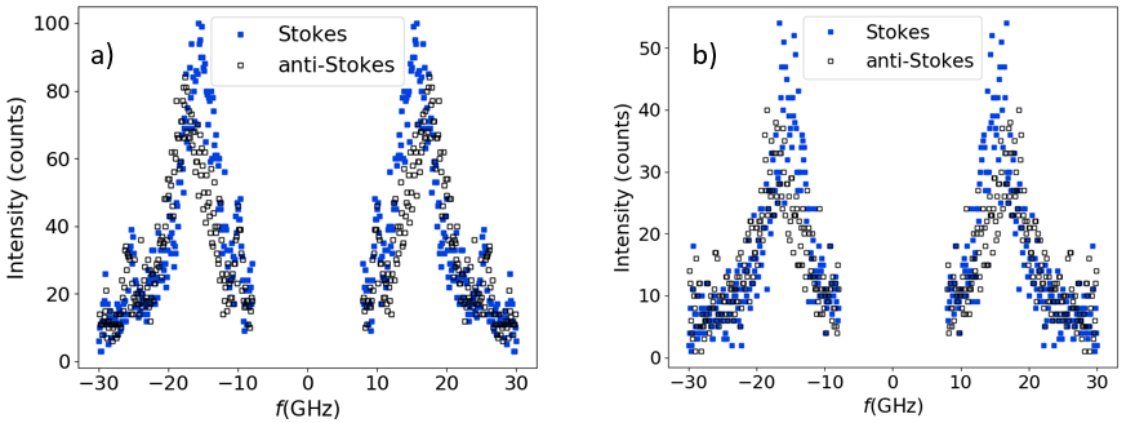

Figure 6.6: Stokes and anti-Stokes magnon lines for a) SiO_2(8 Å)Pt/Co/Ta and b) SiO_2(11 Å)Pt/Co/Ta samples with and incident angle of 30° under a +6 kOe magnetic field .

thickness and k_{sw} is the spin-wave number given by

$$k_{\mathrm{sw}} = \frac{4\pi}{\lambda_{\mathrm{opt}}} \sin\theta.$$

Here, $\lambda_{\mathrm{opt}} = 532$ nm is the laser wavelength and $\theta = 30°$ and $45°$ are the angles of incidence of the laser beam with respect to the surface normal. These were kept constant between measurements.

6.3.1 BLS measurements in Pt/Co⊥/Pt

Figure 6.7 shows BLS signal for Ag/Pt/Co(0.6 nm)/Pt. As the ferromagnetic layer is very thin, the magnon signal is not sufficiently large to extract. The other peaks are due to phonons, and have positions that are independent of applied field. For this reason BLS measurements concentrate on in-plane magnetised films where the ferromagnetic layer is thicker and the signal more easily detected.

6.3.2 BLS measurements in Pt/Co$_{\parallel}$/Ta

In order to obtain a stronger DMI the asymmetry was increased by changing the upper Pt to Ta where Co/Ta has a DMI vector in the opposite direction to Co/Pt, and so the net DMI is no longer close to cancellation. Also, these samples have an in-plane magnetisation because the thickness of the ferromagnetic layer is larger,

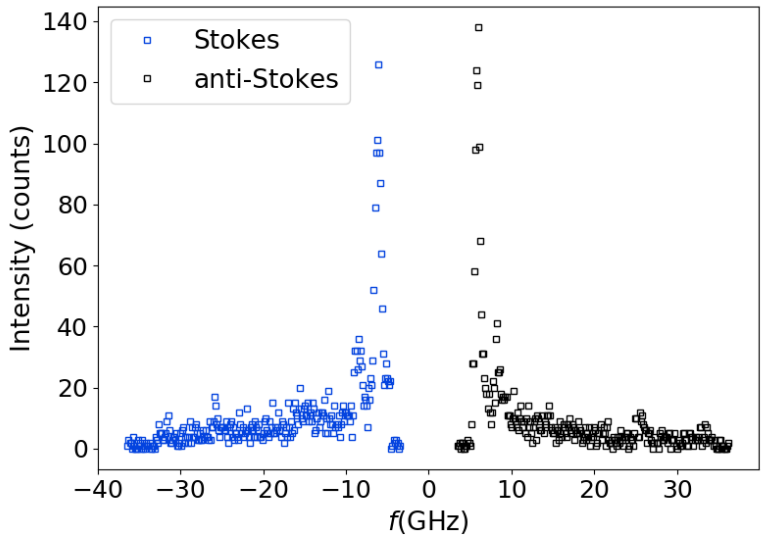

Figure 6.7: Stokes and anti-Stokes phonon lines with and incident angle of 30° under a +6 kOe magnetic field for Ag(d_{Ag})/Pt(11 nm)/Co(0.6 nm)/Pt(4 nm) samples.

which makes the signal BLS stronger and therefore easier to detect. In this case, the samples are Ag(d_{Ag})/Pt(7 nm)/Co(3 nm)/Ta(4 nm). Figure 6.8a) shows the BLS spectrum for the sample without Ag in the structure, in which both the magnon and phonon peaks are visible. The phonon peaks in principle should not present an asymmetry and they are used to check the alignment of the setup, when the alignment is not properly made the phonon peaks present are asymmetric in the spectra. Furthermore, in the ferromagnetic layer the same stimulus creates two magnon peaks. The Stokes peak (blue squares) circled in orange and anti-Stokes (black squares) circled in green are the magnon peaks seen in figure 6.8a). When DMI in present in the system, an asymmetry in both the frequency and the signal amplitude are induced in the Stokes and anti-Stokes signals from the magnon processes. A zoomed-in version of the magnon peaks of the previous image with the fitted Lorentzians are shown in figure 6.8b). Furthermore, figure 6.8c)-f) show the reduced spectra (spectra with only the magnon peaks) for $d_{Ag} = 1, 2, 3$ and 4 nm respectively. The Lorentzian fit helps to extract the peak position and quantifiable uncertainty. In the general discussion in section 1.5, the DMI estimation are presented.

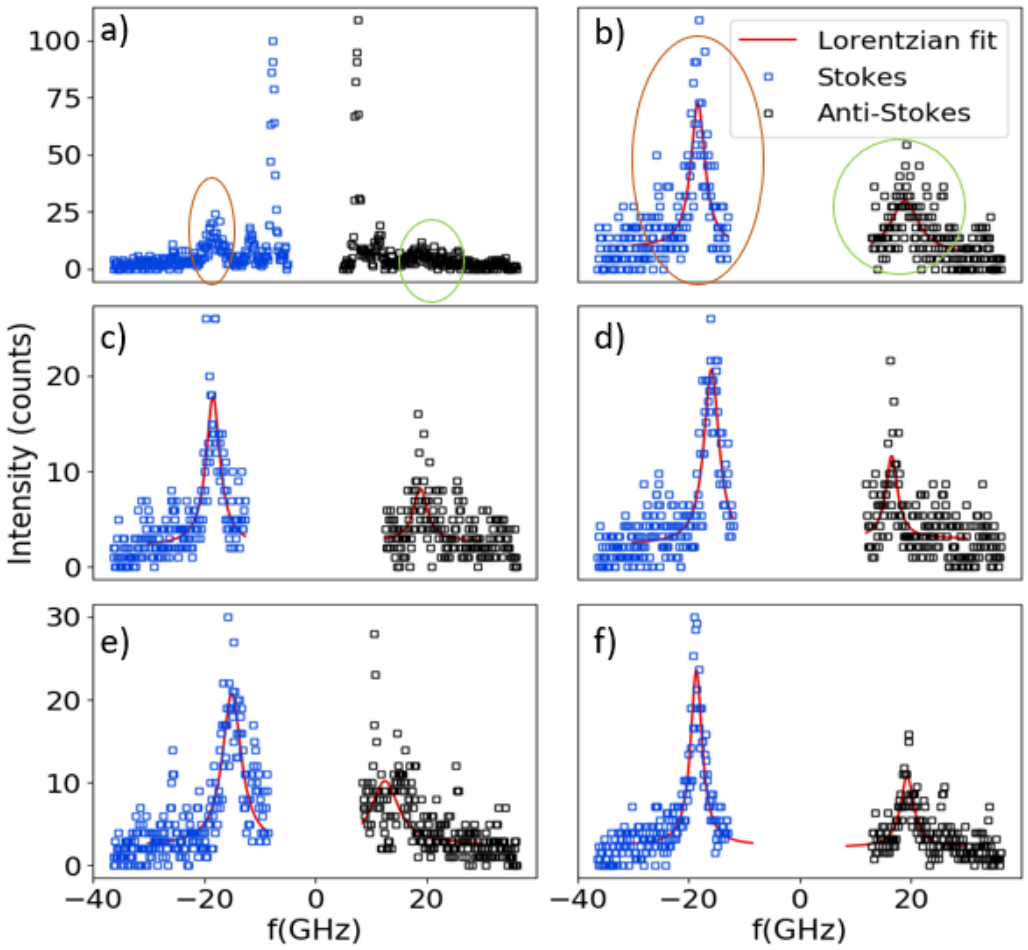

Figure 6.8: BLS spectra for Ag(d_{Ag})/Pt(11 nm)/Co(0.6 nm)/Ta(4 nm) samples with 45° incident angle under +3 kOe magnetic field. a) Whole BLS spectrum for the sample without Ag showing both the phonon and magnon peaks. Zoomed-in plot of the magnon peaks (Stokes peak in blue squares and anti-Stokes peak in black squares) and their fits, b) for the sample without Ag. c) d_{Ag} = 1 nm, d) d_{Ag} = 2 nm, e) d_{Ag} = 3 nm and f) d_{Ag} = 4 nm

6.3.3 BLS measurements in Pt/Co⊥/Ta

In the previous subsection it was described how the roughness induced by depositing Ag underneath the structure modified the Δf in the BLS spectra. As mentioned before, another material could also be used to induce the roughness. For this, the process of deposition is more convenient because SiO_2 does not oxidise and also in the fitting process presents one less layer making the process easier. This set of samples composed of $SiO_2(d_{SiO_2})$/Pt(4 nm)/Co(1.1 nm)/Ta(4 nm) was also analysed by BLS, as described above for in-plane magnetised samples. However, this set is

perpendicularly magnetised, because of the thickness of the ferromagnetic layer, but it is sufficiently thick to present a detectable BLS signal. The same procedure was used to obtained the BLS spectra and results are discussed in section 6.5.

6.4 Asymmetric bubble expansion method for DMI estimation

The field-induced DW evolution of Pt(11 nm)/Co(0.6 nm)/Pt(4 nm) was investigated using a MOKE microscope in polar mode. The measurement were performed using two magnets, an in-plane magnet which applies the magnetic filed in x direction and an out-of-plane magnet which applies a magnetic field in the z direction. See chapter 4 for a more detailed measurement set-up description. The samples were first saturated in the $+z$ direction by the application of a large magnetic field. Once the samples were saturated, a reverse field slightly larger than the coercive field of the sample was applied in the form of field pulses in the $-z$ direction to nucleate magnetic domains. After nucleating domains, the alignment of the in-plane magnet has to be checked to avoid field leakage to the out-of-plane direction. Figure 6.9 shows the process of checking the alignment for each sample. Figure 6.9a) shows a symmetric bubble-like domain after applying a 1 second reverse field pulse of $H_z = -150$ Oe. In figure 6.9b) and c) the same process was followed. However, along with the reverse field a positive in-plane field $H_x = 515$ Oe was applied, this causes the shape of the reverse domain to form an ellipse (creating an asymmetry along the in-plane field direction) with the center shifted from that of the original bubble in direction of the in-plane field. This gives the impression that one of the vertices of the ellipse moves towards the in-plane field direction. The opposite process occurs when applying the opposite direction of the in-plane field as shown in figure 6.9c). The yellow arrows in figure 6.9b) and c) must be similar in length. If this is not the case, the in-plane magnet would be tilted and rotation of the in-plane magnet will be required in order to obtain the proper alignment.

The structure analysed here was Pt/Co/Pt. Since both Pt layers have the same thicknesses and roughness at the interfaces, in principle, the structure should not

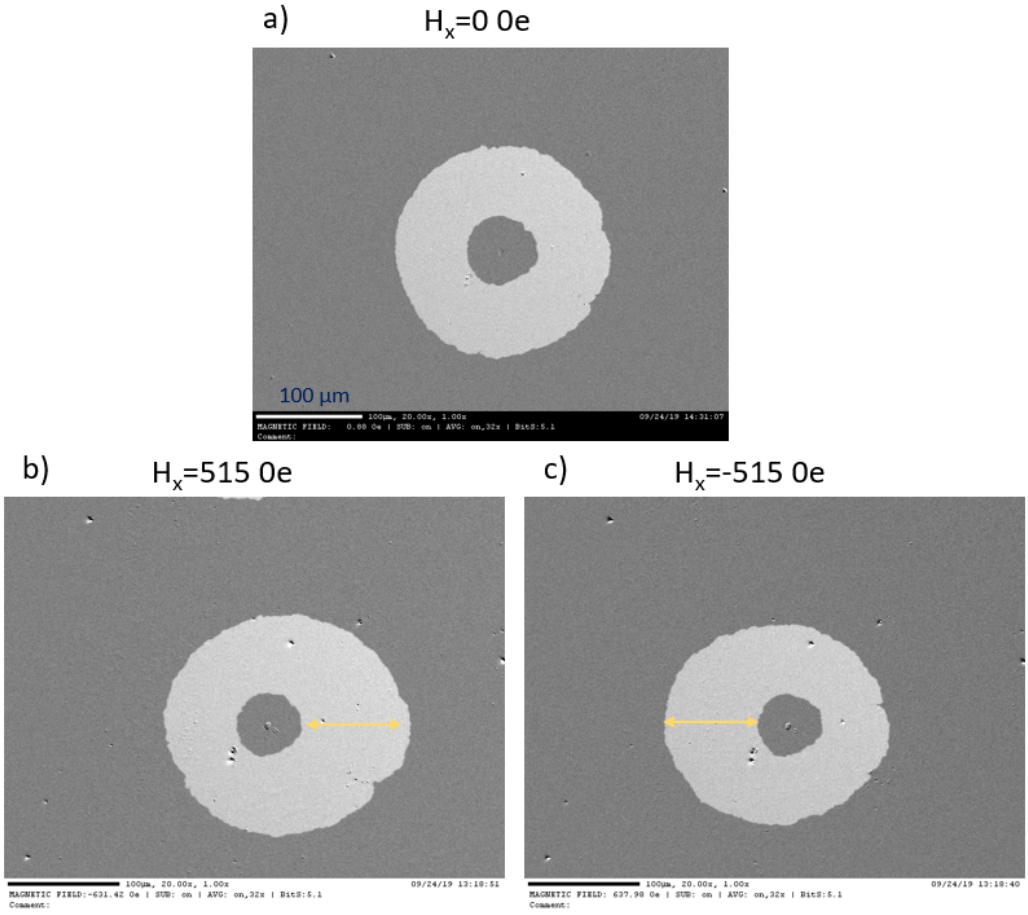

Figure 6.9: One second out-of-plane field pulse H_z=150 Oe in presence of in-plane magnet alignment process on Pt/Co/Pt. a) Positive in-plane field H_x=515 Oe modifies the bubble-like nucleation into an ellipse with larger domain growth to the left. b) Negative in-plane field H_x=515 Oe modifies the bubble-like nucleation into an ellipse with larger domain growth to the right.

present DMI at all. Nevertheless, in practice the structure has different thicknesses of the non-magnetic layer and different roughnesses and/or intermixing at the interfaces. For that reason, a non-negligible but small interfacial DMI in the structure was expected.

Once the in-plane field alignment has been confirmed, the next step in the bubble expansion measurement procedure is to check that the reverse field induces DW propagation in the creep regime, because the theory used to model only applies to domain wall motion in this regime.

Je *et al.* argued that if the DW motion occurs in the creep regime then the DW

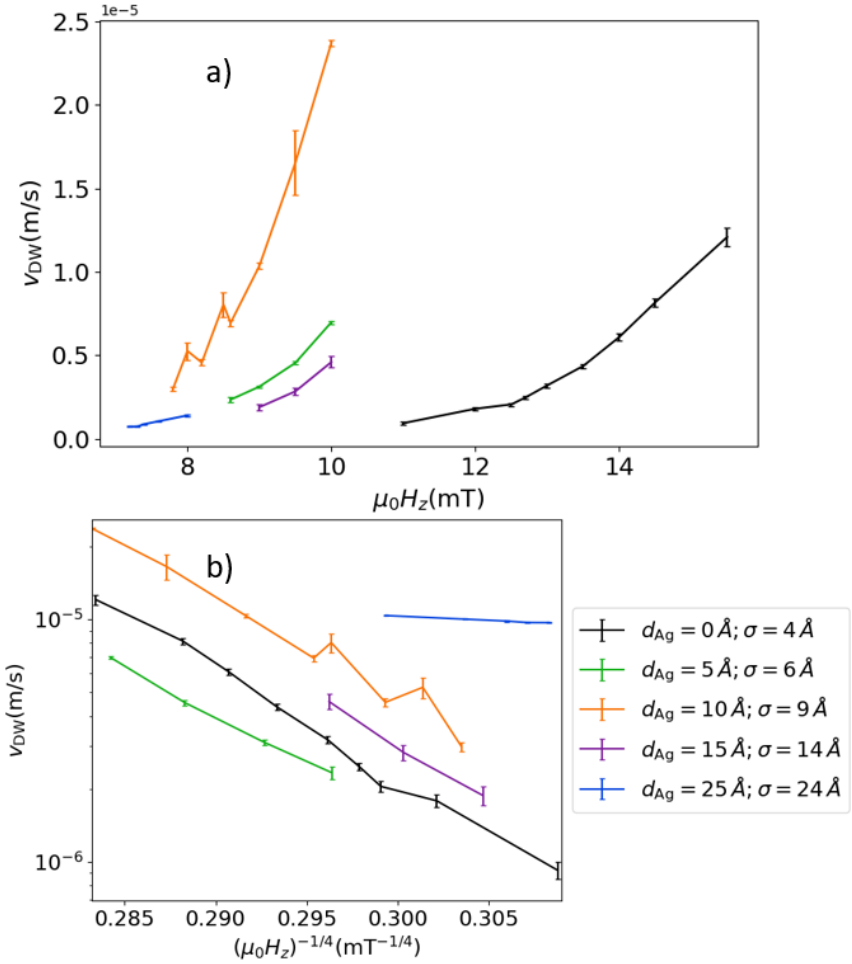

Figure 6.10: Field-induced domain wall motion. (a) DW velocity v_{DW} as a function of H_z applied field for multilayers with increasing σ along with the fits to creep (solid lines). b) v_{DW}, plotted on a logarithmic scale, as a function of scaled driving field to highlight the compatibility of experimental data to the universal creep law. Each set of data is horizontally shifted for a clearer presentation.

velocity is [131]

$$v_{DW} = v_0 \exp\left(-\xi H_z^{-1/4}\right) \tag{6.4.2}$$

where v_0 is the characteristic speed, the 1/4 is the creep scaling exponent [177], and ξ is a scaling constant that is dependent on H_x. Figure 6.10a) and b) shows the changes of DW velocity v_{DW} with increasing applied H_z field for multilayers with different σ. DW dynamics are classified into different regimes of motion including the creep, depinning, and flow regimes [178]. In very low fields, like in this case, the applied field is not enough to overcome the pinning barrier and move the DW. When T $\neq$ 0, thermal excitations can assist the field and cause very slow motion

of DWs known as creep. The linear change of ln (v_{DW}) vs $H_z^{1/4}$ confirms the creep motion of the DWs in this field range [179] as shown in figure 6.10b).

The method requires bubble-like domains as large as possible with no in-plane field as shown in figure 6.9a). This enables more accurate measurements of the speed of the DW, as it depends on the radius of the domain, and so that this domain will fit in the image space. The speed is calculated by dividing the radius of the domain after applying the reverse field by the field pulse duration, $v_{\mathrm{DW}} = d_{\mathrm{DW}}/\mathrm{t_p}$.

After the alignment is performed and creep DW motion confirmed, the measurements are performed by measuring v_{DW} for as many different combinations of in-plane field, out-of-plane field and $\mathrm{t_p}$ as possible. In a structure with a sizable DMI it is expected to obtain larger bubble-like DWs when the in-plane field increases [127]. This is shown in figure 6.11a). However, in the case of our Pt/$\mathrm{Co}_\perp$/Pt with engineered interface roughness, a somewhat different behaviour was obtained. Figure 6.11b) shows the domain expansion for a reverse field pulse of H_z=140 Oe for one second with an in-plane field going from 200 Oe up to 800 Oe in 100 Oe steps. Normally, when the in-plane field is present, the size of the domains is conserved or it can be bigger, and the center shifts further away in the direction of the field as shown in figure 6.11a. Now, in the deliberately roughened set of Pt/$\mathrm{Co}_\perp$/Pt samples studied here, the bubbles were gradually decreasing in size, suggesting that the in-plane field *slows down* the DW propagation speed, as can be observed in figure 6.11b). This behaviour is common across the range of roughnesses, and between multilayer samples deposited in different growth runs. This effect is observed when applying the in-plane field in both directions, and also when saturating in the opposite direction.

Figure 6.12 shows the DW speed, v_{DW}, as a function of the in-plane field, H_x, for different roughness, σ, when the DW is moving under an in-plane field toward the right-hand side (RHS) or towards the left-hand side (LHS). According to the theory when there is a negligible DMI in the structure both RHS and LHS curves would overlap and the global minimum should coincide. Such a behaviour is observed for $\sigma = 0$ Å, but with the exception that the DW velocity decreases as the in-plane field increases. Also, there is an increases by a factor ≈ 3 in the v_{DW} around zero with

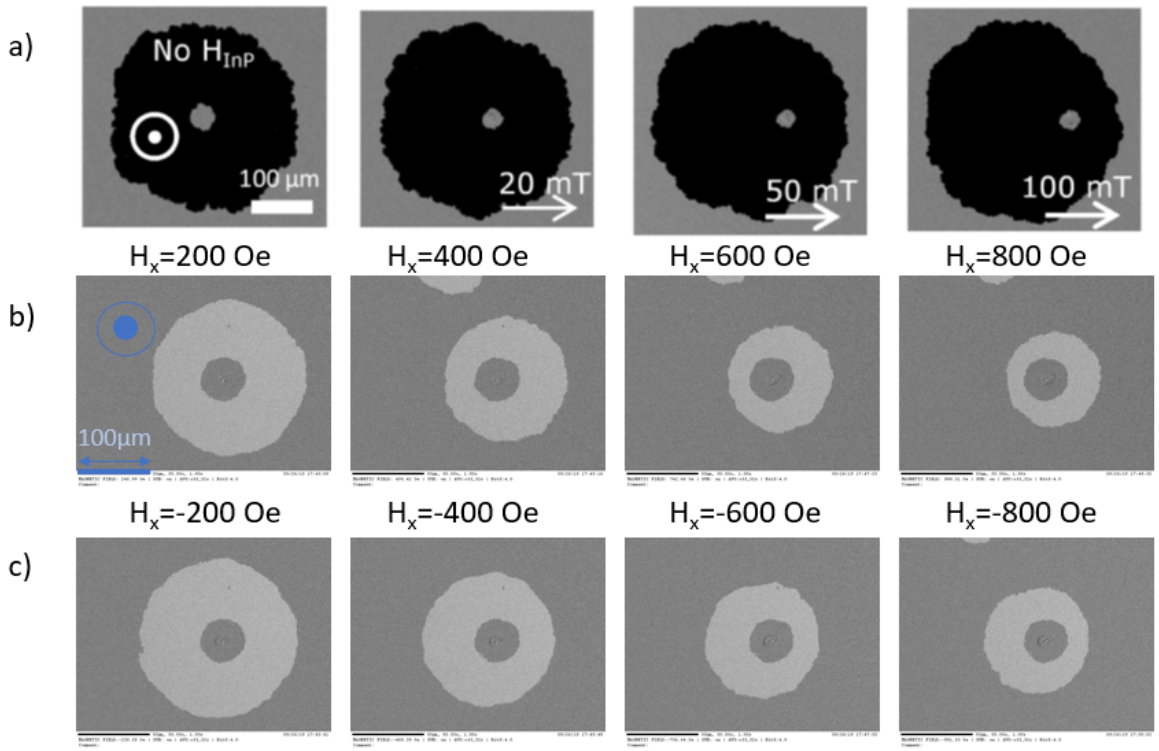

Figure 6.11: Domain expansion in presence of both a reverse field pulse and an in-plane field. a) Expected shape when the in-plane field increases, the size of the DW is basically conserved however, the center shift further away in direction of the field [127]. b) In the set studied here, the bubble was gradually decreasing in size suggesting, that in-plane field slows down the DW. c) Same procedure with the opposite direction of the in-plane field.

respect to high $|H_x|$. On the other hand, from $\sigma = 5$ Å up to $\sigma = 19$ Å in figure 6.12 shows a smooth decrease rather than there being a jump. The data also presents an offset from zero that depends on the field direction and roughness. Nonetheless, RHS and LHS curves for these thicknesses have a shift in the maxima suggesting there is some effect that changes the behaviour of the DW when applying the in-plane field towards different directions. In the next section the procedure to obtain the D_{eff} is described and a comparison between both techniques is presented.

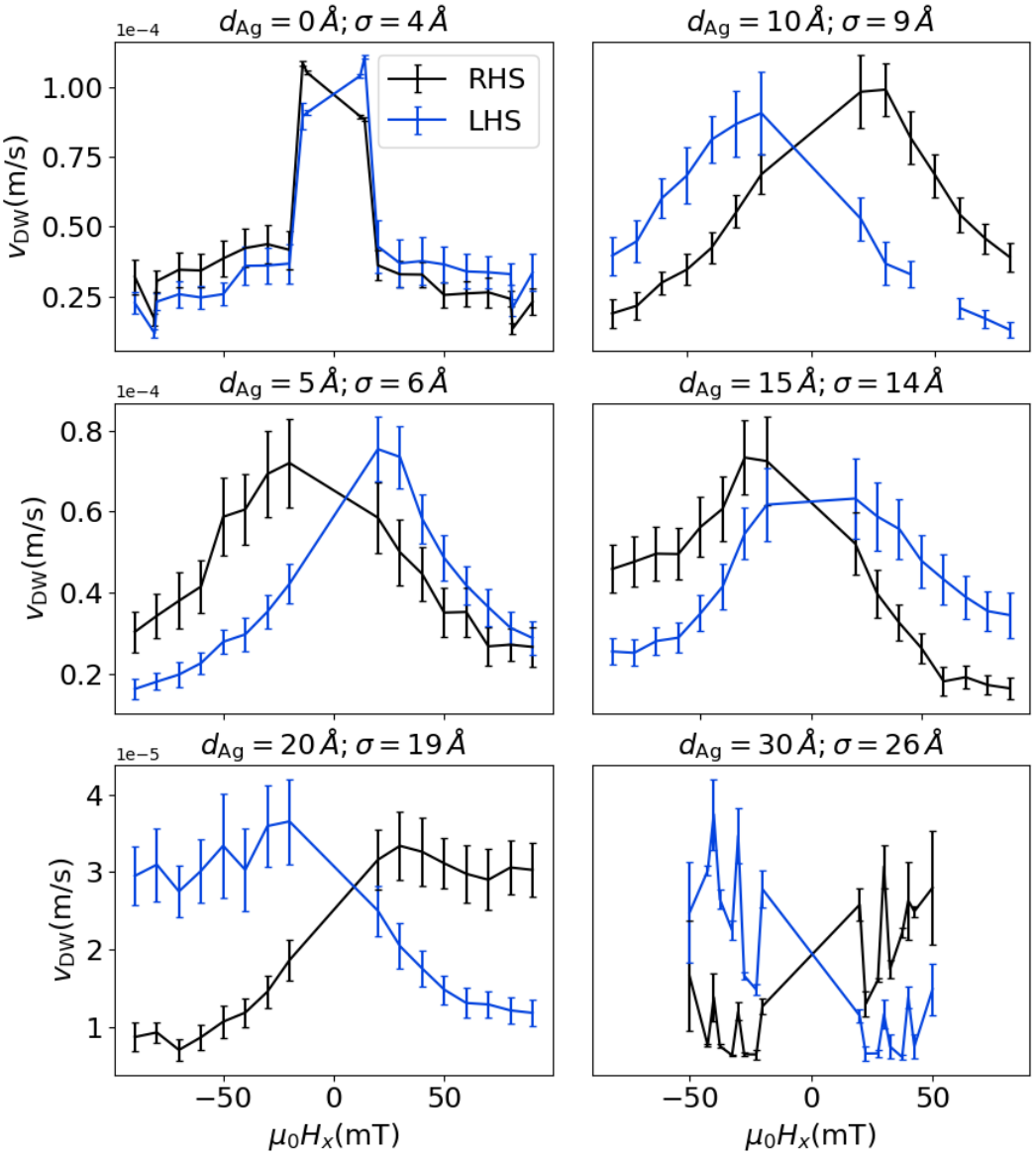

Figure 6.12: DW speed, v_{DW}, as a function of the in-plane field, H_x. Two curves are presented per thickness is presented, when the DW is under an in-plane field toward the right-hand side, RHS curve, or towards the left-hand side, LHS curve. The thicknesses presented are d_{Ag}=0 Å, 5 Å, 10 Å, 15 Å, 20 Åand 30 Å.

6.5 Comparison of the Dzyaloshinskii-Moriya interaction by BLS and the asymmetric bubble expansion method

First, the BLS measurements as the more direct method to estimate the effective DMI is presented. From fitting the reduced BLS curves in figure 6.8 the peaks

positions the frequency shift between the Stokes and anti-Stokes asymmetry are obtained at 3 kOe and angle of incidence of 45°; $\Delta f(\sigma = 19$ Å$)= 0.56$ GHz, $\Delta f(\sigma = 31$ Å$)= 0.86$ GHz, $\Delta f(\sigma = 0$ Å$)= 0.94$ GHz, $\Delta f(\sigma = 19$ Å$)= 0.80$ GHz, $\Delta f(\sigma = 26$ Å$)= 0.64$ GHz. These values were obtained by fitting the positions of the magnon lines and the positions of the phonon lines; the phonon lines should not have a frequency asymmetry but the set-up can introduce such asymmetry; for that reason, the phonon line positions to evaluate the asymmetry due to the set-up was used. To correct the data the following was performed, taking for instance the spectrum for the sample $d_{\mathrm{Ag}} = 1$ nm, the fitted positions for the phonon lines are $f_{\mathrm{pS}} = -7.58$ GHz, $f_{\mathrm{paS}} = 7.36$ GHz. The fitted positions for the magnon lines are $f_{\mathrm{mS}} = -18.40$ GHz, $f_{\mathrm{maS}} = 18.74$ GHz. The real phonon positions are calculated as half the difference of the original peak positions ($f_{\mathrm{paS}} - f_{\mathrm{pS}}/2$ thus, $f'_{\mathrm{pS}} = -7.47$ GHz, $f'_{\mathrm{paS}} = 7.47$ GHz and the real magnon positions were calculated with the difference of the value found using the fitting and thus $f'_{\mathrm{mS}} = f_{\mathrm{mS}} - (f_{\mathrm{paS}} + f_{\mathrm{pS}})/2 = -18.29$ GHz and $f'_{\mathrm{maS}} = f_{\mathrm{mS}} + (f_{\mathrm{paS}} + f_{\mathrm{pS}})/2 = 18.85$ GHz. The asymmetry depends on the effective DMI constant D_{eff} through the relation

$$\Delta f = -\frac{\gamma}{2\pi}\frac{D_{\mathrm{eff}}}{M_{\mathrm{s}}}4k \tag{6.5.3}$$

where $\frac{\gamma}{2\pi} = 3$ GHz/kOe using $g = 2.14$ [180], $M_{\mathrm{s}} = 1400$ emu/cm^3 for a 30 Å thick Co layer [180] and $k = 16.7\ \mu$ m^{-1}. The measurement using 3 kOe external magnetic field for the sample with $d_{\mathrm{Ag}} = 0$ Å, the $D_{\mathrm{eff}}(\sigma = 4$ Å$) = -0.67$erg/cm^2. The rest of the values can be found in table 6.1.

Figure 6.13a) shows D_{eff} as a function of roughness, where there is a fluctuating behaviour in the DMI. However, the associated errors are large which display a constant trend of the DMI within error. Even though, the DMI in this type of trilayer is going to be the addition of the DMI vector from both the lower and the upper interfaces within the structure. Varying the roughness creates an effect on both interfaces. In the case of symmetric structures, the net DMI may be expected to increase from zero to positive values when the quality of the top interface decreases relative to that of the bottom and decreases from zero to negative values when the

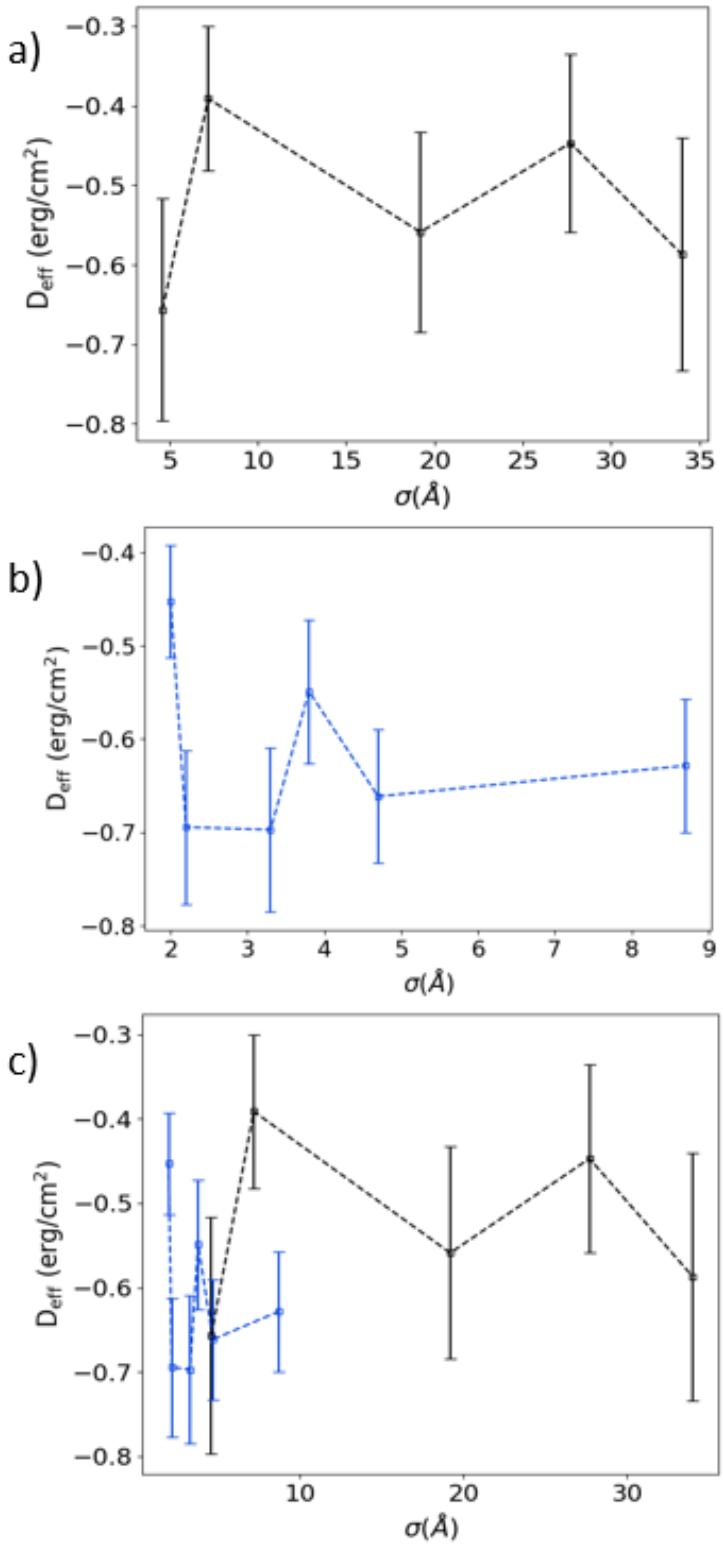

Figure 6.13: Effective DMI as a function of the Ag roughness. a)Pt/Co∥/Ta, b) Pt/Co⊥/Ta and c) comparison of the effective DMI as a function of the induced roughness in both set of samples.

quality of the bottom interface decreases relative to that of the top [36]. In this case, all of the net DMI values are negative because the structure is asymmetric. The direction of the DMI vector in the Pt/Co is the same as the Co/Ta which sets the negative value of the DMI however, the analysis could still be applicable to understand the DMI changes due to roughen interfaces. Changes in the DMI coming from both the bottom and upper interface quality. The seed layer (Ag) impacts more directly the bottom interface and thus decreases relatively to the upper interface. Recalling that the roughness contains both lateral and vertical components, when the roughness increases this does not necessarily mean that the quality of the interface decreases. Therefore, the behaviour in figure 6.13a) could come from the the competition of the roughness contributions which detriment or enhance the quality of the interface as a function of the Ag thickness deposited. However, due to the large uncertainty in the measurements this is not statistically conclusive.

Additionally, figure 6.13b) shows the relation between the effective DMI and the SiO_2 roughness and it can be observed that initially the DMI decreases in magnitude with increasing SiO_2 coverage for the first two samples, then reaches a minimum (largest negative) value which eventually increases again. The behaviour is similar to the previous set even though the thickness axis is smaller in this case. The same description in terms of the competition between the roughness contributions could describe this set. Also in this case, for the first two data points the change is real however, for the rest, the value of the DMI is statistically constant within error.

The comparison of both sets of samples, $\sigma(d_{\mathrm{Ag}})$ (black marker and line) and $\sigma(d_{\mathrm{SiO_2}})$ (blue marker and line), is presented in figure 6.13c). Although the rough seed layer material and procedures were different at around $\sigma = 5$ Å the effective DMI has the same value within error and the phenomenological behaviour is consistent. The results found here are consistent with the study of the impact of interfacial intermixing (3.3×10^{-7} Torr set) made by Wells *et al.* using the asymmetric bubble expansion to estimate the effective DMI field [36]. They found that both the intermixing and roughness affects the effective DMI field by changing both interfaces in sputtered Pt/Co/Pt trilayer by varying the deposition temperature. Recalling that

σ(Ag) (Å)	D_{eff} (erg/cm^2)	σ(SiO_2) (Å)	D_{eff} (erg/cm^2)
4	-0.66 ± 0.14	2	-0.45 ± 0.06
9	-0.40 ± 0.09	2	-0.70 ± 0.08
19	-0.56 ± 0.13	3	-0.70 ± 0.09
26	-0.45 ± 0.11	5	-0.55 ± 0.08
32	-0.59 ± 0.15	9	-0.66 ± 0.07

Table 6.1: Summary of the D_{eff} for Pt/$Co_{\parallel}$/Ta and Pt/$Co_{\perp}$/Ta calculated from the BLS spectra.

Pt/Co/Pt trilayers with strong PMA usually have a very thin ferromagnetic layer, making it challenging to get sufficiently strong magnon signal during BLS measurements, this is the reason why the asymmetric bubble expansion is used for this type of structures. A description of how the effective DMI field is extracted using the asymmetric bubble expansion is given in the next subsection for our Pt/$Co_{\perp}$/Pt set.

6.5.1 DMI with the asymmetric bubble expansion method

Once v_{DW} as function of H_x curves were obtained, as shown in figure 6.12, then it was proceed to extract the location of the maxima by fitting a Gaussian function. The asymmetric bubble expansion method relies on the energy density, ρ_{DW}. When a DW has a Néel structure ρ_{DW} is given by [127]

$$\rho_{\text{DW}} = \rho_0 + 2\Delta K_{\text{D}} - \pi\Delta M_{\text{S}}|H_x + H_{\text{DMI}}|, \tag{6.5.4}$$

where ρ_0 is the Bloch DW energy, K_{D} is the DW anisotropy energy density and Δ is the DW width. In this way, when H_x is equal and opposite to H_{DMI} the DW energy is maximum. Hence there will be a minimum in the velocity of the DW at that particular value of applied field, H_{offset}. On the basis of this simple model, $H_{\text{offset}} = -H_{\text{DMI}}$. In contrast, a maximum instead of a minimum in the v_{DW} as function of H_x was obtained.

Figure 6.14a) shows the v_{DW} as function of H_x for a subset of the data (d_{Ag} = 5 Å; σ = 4 Å, d_{Ag} = 10 Å; σ = 9 Å, d_{Ag} = 20 Å; σ = 19 Å and d_{Ag} = 30 Å; σ = 26 Å) with their fit. This behaviour is not yet well understood, but in order to compare it to previous DMI studies, here it is going to be referred to the shift of the

maxima between the RHS and LHS curves as representative of the DMI, following eq. 6.5.5.

In order to get an estimate of the DMI, first, the effective DMI field was estimated, H_{DMI}. Following the relation $\mu_0 H_{\mathrm{DMI}} = D_{\mathrm{eff}}/M_{\mathrm{s}}\Delta$, where Δ is the DW width and is given by $\Delta = \sqrt{A/K_{\mathrm{eff}}}$ with A the exchange stiffness and K_{eff} the effective anisotropy constant, finally, D_{eff} is calculated by

$$D_{\mathrm{eff}} = \mu_0 H_{\mathrm{DMI}} M_{\mathrm{s}} \Delta. \tag{6.5.5}$$

Using A = 18 pJ/m and K_{eff} = 0.5 MJ/m^3, $\Delta = 2.02 \times 10^{-7}$ m and $\mathrm{M_S}$ = 1.19 MJ/m^3 using from simulations data [127], we find D(σ = 4 Å)=0.57 mJ/m^2 (0.57 erg/cm^2). The rest of the values are displayed in table 6.2. Figure 6.14b) displays the relation between the effective DMI and the interfacial roughness. Changes in the sign of the effective DMI were observed for different roughnesses.

The behavior obtained here is similar to that observed in $[\mathrm{Co/Ni}]_n$ multilayer stacks grown on Pt(111) epitaxially films and confirmed with Monte Carlo simulations by Chen *et al.* [182], where the effective DMI constant reverses sign upon insertion of a thin Ir interlayer. Later Hrabec *et al.* also demonstrated that the sign of the DMI can change when the DW structure goes from Bloch to Néel in sputtered Pt/Co/Pt multilayer structures by introducing Ir at the upper interface between Co/Pt [181]. Thereafter, this suggests that roughness is modifying the DMI which subsequently changes the chirality of the DW similarly to what Ir does in the Hrabec *et al.* studies. Also, it is important to note that the strong DMI in the sample with no roughness comes from the polycrystalline nature of the multilayer and when the roughness is added important changes at the interfaces induces complex process that modify the DMI.

σ(Ag) (Å)	$\mathrm{D_{eff}}$ (erg/cm^2)
4	-0.58 ± 0.06
9	0.56 ± 0.06
19	-1.47 ± 0.14
26	0.87 ± 0.09

Table 6.2: Summary of the D_{eff} calculated from the asymmetric bubble expansion.

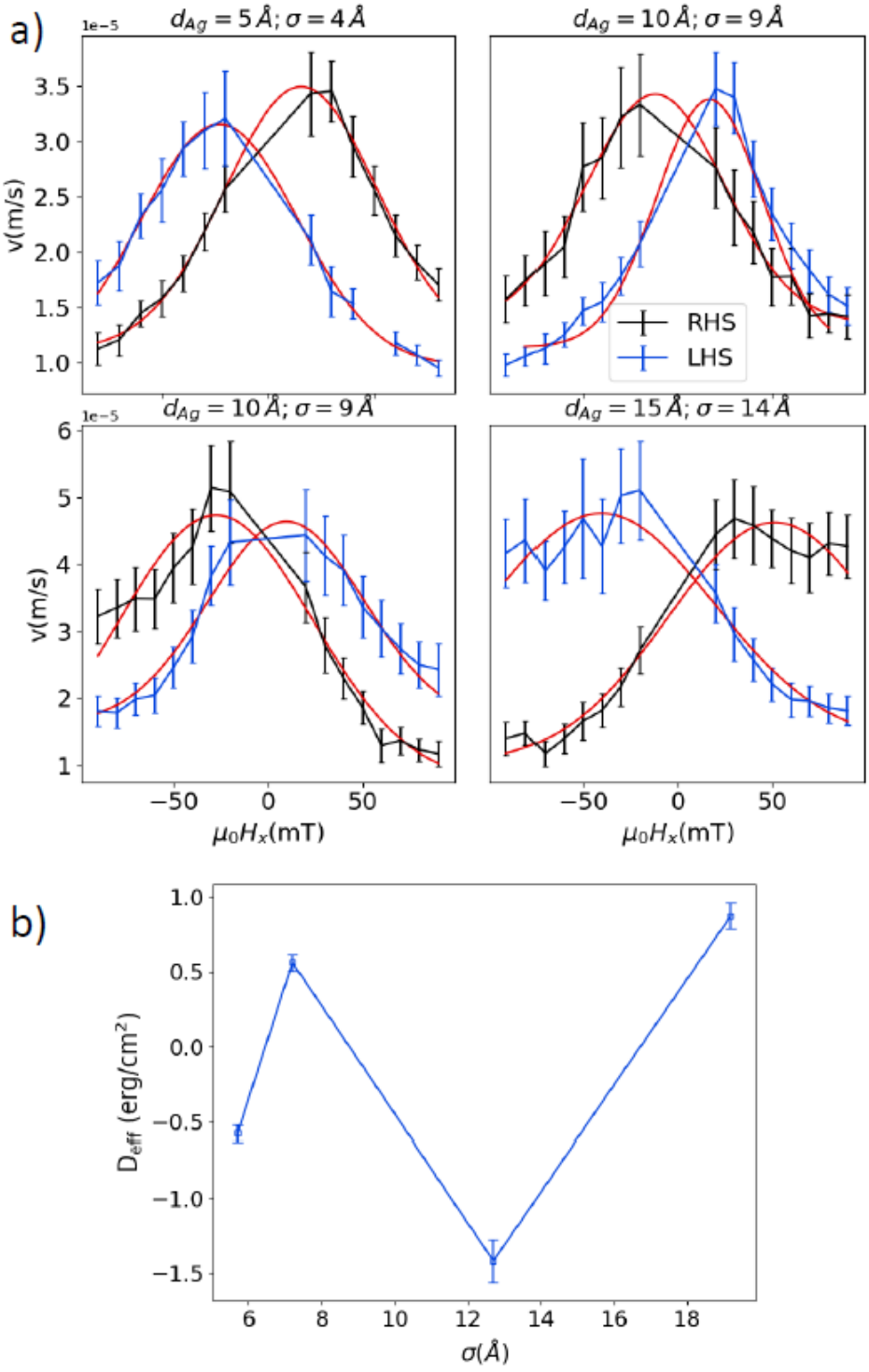

Figure 6.14: a) v_{DW} as a function of H_x along with the reverse field, H_z, for $d_{\mathrm{Ag}} = 5$ Å; $\sigma = 4$ Å, $d_{\mathrm{Ag}} = 10$ Å; $\sigma = 9$ Å, $d_{\mathrm{Ag}} = 20$ Å; $\sigma = 19$ Å and $d_{\mathrm{Ag}} = 30$ Å; $\sigma = 26$ Å. b) Effective DMI as a function of interfacial roughness.

The model used by Je *et al.* [131] and Wells *et al.* [127] relied on the fact that the magnetic domain expansion is in the creep regime. Another explanation for the

behaviour found here is that the magnetic domain expansion could be in other regime such as the depinning or flow regime. However, the creep check was performed and that idea was discarded. Also, the measurements were performed on several separate occasions to verify the results; they were consistent every time.

6.6 Summary

It was demonstrated and quantified the role of the interfacial roughness introduced in sputtered Pt(11 nm)/Co(0.6 nm)/Pt(4 nm), Pt(7 nm)/Co(3 nm)/Ta(4 nm) and Pt(4 nm)/Co(3 nm)/Ta(4 nm) multilayers deposited onto thermally evaporated Ag layers or sputtered discontinuous SiO_2 layers in order to create an engineered interface roughness in the multilayers.

The asymmetric bubble expansion method was used to estimate the DMI in a Pt/Co/Pt stack, which shows that the DWs travels more slowly with increasing in-plane applied magnetic field, in contrast to the conventional behaviour, where it increases.

BLS spectroscopy for the $Pt/Co_{\parallel}/Ta$ stack shows magnon peaks and thus it was possible to estimate the DMI. The DMI measurements suggest that the relation of the DMI with the roughness follows a non-linear behaviour which does not vary depending on whether the magnetisation is in-plane or out of plane.

Finally, even though the results from the asymmetric bubble expansion are yet to be completely understood the behaviour has similar phenomenological features to the DMI results found by BLS, where the DMI fluctuates when the roughness increases, which tell us that changes in the quality of the interfaces in multilayer modify the interfacial DMI. Nevertheless, characterising the details of potentially asymmetric interface properties, such as the roughness, degree of intermixing, and density of stacking faults, remains an outstanding materials science challenge.

Chapter 7

Current-driven domain wall dynamics along a square pillar in a multilayer with PMA

In the previous chapters interfacial phenomena were investigated with scattering techniques using different sources such as light (XRR, XRMR and MOKE) and neutrons (PNR). Both the proximity induced magnetisation (PIM) and the Dzyaloshinskii-Moriya interaction (DMI) were investigated in sputtered Pt/Co multilayers stacks. The influence of the interfacial quality on both phenomena was studied in order to evaluate the suitability of the structures and materials for potential applications. The dynamics of the magnetic domains were analysed using the asymmetric bubble expansion which relies on the field-driven switching of magnetic domains as the magnetisation reversal process which most current magnetic devices are based on. However, there are more switching mechanisms.

A major spintronics application lies in the electrical manipulation of the magnetic moment of a ferromagnet which became popular with the discovery of spin-transfer torque (STT) [183, 184], in which a spin-polarised charge current was utilised to change the magnetic orientation of a ferromagnet. The major advantage of such an electrical technique is device scalability and reduced power consumption over conventional magnetic field based devices. Consequently, STT was used to build magnetic memories such as STT-magnetoresistive random access memory (MRAM) [185]. As

illustrated in figure 7.1a), the basic component of a STT device is the magnetic tunnel junction (MTJ) which consists of an oxide tunnel barrier sandwiched between two ferromagnetic layers. During the device operation, when a charge current is passed through the MTJ, the electrons are spin polarised in one of the FM and are subsequently used to manipulate the magnetic state of the other FM using STT. However, as the charge current tunnels through the insulating oxide barrier, a large write current density can lead to the breakdown of the oxide [186, 187]. Thus, substantial efforts are still being devoted to reducing current required for the manipulation of the magnetisation using STT. Moreover, the magnetic state of the MTJ is sensed using the TMR by passing a smaller read current through the MTJ. As a result of the coupling of the read and write current paths, the read current can lead to accident switching of the magnetic states (read disturbance) [187].

Alternatively, another current-driven technique of magnetisation manipulation, namely, the spin-orbit torque (SOT) [22, 188, 189], was discovered to electrically switch a FM which overcomes the afore-mentioned shortcomings of the STT technique. The technique of SOT utilizes the spin-orbit interaction to generate a spin current and possesses added advantages over STT in terms of reduced power consumption [190] and faster device operation [191]. As illustrated in figure 7.1b), a typical SOT device is composed of a bilayer consisting of a FM and a non-magnetic material (NM) capped by an oxide. When an in-plane charge current is injected into the NM layer, a transverse spin current is generated at the bilayer interface due to the spin-orbit coupling (SOC) effects in the bulk of the NM and/or the interface of NM/FM. This spin accumulation at the interface exerts a torque on the magnetisation of the FM and subsequently has been shown to switch the magnetisation of a FM layer, moving domain walls inside the FM and generating oscillations in an effective manner compared with conventional STT. As shown in figure 7.1c), the SOT writing scheme can be combined with the TMR based reading scheme to construct a SOT-MRAM cell. The magnetisation of the FM1 is controlled by SOT from the in-plane write current, while the magnetic state is sensed by passing a smaller read current through the MTJ. In contrast to the STT-MRAM scheme illustrated in figure 7.1a), the read and write current paths are decoupled in the SOT-MRAM

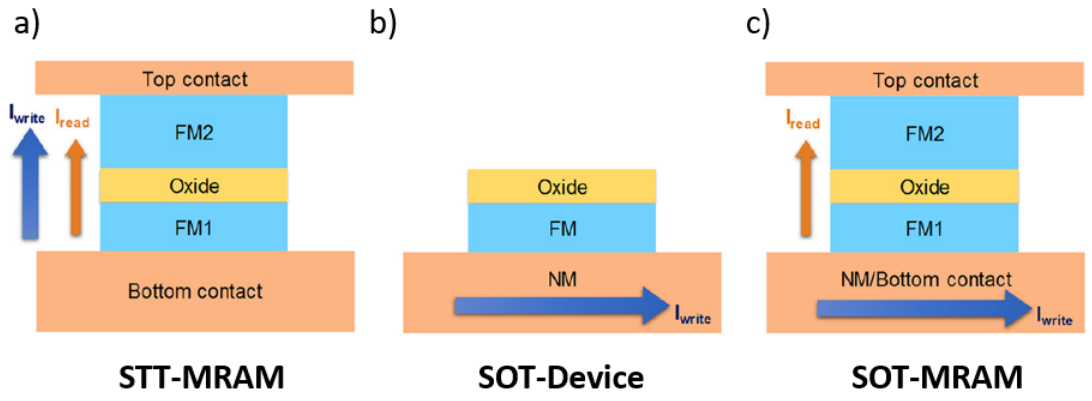

Figure 7.1: a) Schematic of a magnetic tunnel junction in conventional STT-MRAM. The read and write current paths are coupled in the STT-MRAM cell. (b) Schematic of a SOT device illustrating the write current path in the SOT scheme. (c) Schematic of a SOT-MRAM cell utilizing SOT scheme for writing and TMR scheme for readout. Adapted from [192].

in figure 7.1c), which allows for better design margins. Furthermore, as the large write current does not flow through the MTJ, the SOT-MRAM scheme allows for a better device stability.

Although the SOT is attributed to spin accumulation at the FM/NM interface, the detailed microscopic origins of the spin current generation are under debate and research. The two main SOC phenomena that are attributed to generating the spin accumulation are spin Hall effect (SHE) and interface Rashba-Edelstein effect.

First, the phenomenon of SHE exploits the bulk SOC in the NM to convert an unpolarised charge current into a transverse pure spin current. The bulk SOC in the NM arises from either the band structure (intrinsic) and/or addition of high SOC impurities (extrinsic) and gives rise to spin dependent asymmetric scattering of the conduction electrons. This asymmetric scattering leads to deflections of spin-up and spin-down electrons in opposite directions creating a transverse spin current when an unpolarised charge current is injected into the NM [19–21]. Figure 7.2a) illustrates a spin accumulation generated at the FM/NM interface due to the bulk SHE in a NM. Note that the polarisation $\vec{\sigma}$ of the accumulated spins is orthogonal to directions of both the injected charge current ($\vec{J}_C$) as well the generated spin

current ($\vec{J_{\rm S}}$). Accordingly, the SHE is represented using the equation

$$\vec{J_{\rm S}} = \frac{\hbar}{2e}\theta_{\rm SH}(\vec{J_{\rm C}} \times \vec{\sigma}). \tag{7.0.1}$$

Here, $\theta_{\rm SH}$ is the intrinsic property of the NM that quantifies its spin current generation efficiency and is called the spin-Hall angle of the NM. The magnitude of $\theta_{\rm SH}$ determines the amount of the spin current density a NM can generate for a given charge current density, and the sign of $\theta_{\rm SH}$ determines the direction of the spin accumulation at the NM/FM interface. While the process of SHE generates a pure spin current from an unpolarised charge current; conversely, a charge current can be generated due to a pure spin current in the NM by a reverse process.

Second, the Rashba-Edelstein effect originates from an interfacial SOC phenomenon [139, 193, 194] that arises in structures with broken inversion symmetry such as NM/FM/oxide in figure 7.2b), where an internal electric field, $\vec{E}$, is generated along the direction of symmetry breaking [see figure 7.2b)]. The conduction electrons with momentum, $\vec{p}$, moving near this interface with $\vec{E}$, experience an effective magnetic field in the direction $\vec{E} \times \vec{p}$. This magnetic field couples to spin magnetic moments of the conduction electrons and polarises their spin magnetic moment along $\vec{E} \times \vec{p}$. Accordingly, this interfacial SOC (Rashba SOC) is modelled using the Hamiltonian,

$$H_R = \frac{\alpha_{\rm R}}{\hbar}(\vec{E} \times \vec{p}) \cdot \vec{\sigma}, \tag{7.0.2}$$

where α_R is the Rashba parameter. The Rashba-Edelstein effect to generate spin currents originates from this interfacial SOC which is originated in NM/ FM bilayers has been reported and discussed over the last decade [195, 196]. The Rashba effect at the NM/FM interface is illustrated in figure 7.2b).

It should be noticed that a spin-orbit-induced torque is fundamentally different from STT, although its ultimate effects might be similar. Contrary to STT, there is no transfer of spin angular momentum from one ferromagnetic layer to another. Rather, orbital angular momentum is transferred to the electron spins through the spin-orbit interaction intrinsic to the band structure of the ferromagnet. Thus, the application of a spin torque does not rely on two non-collinear, independently

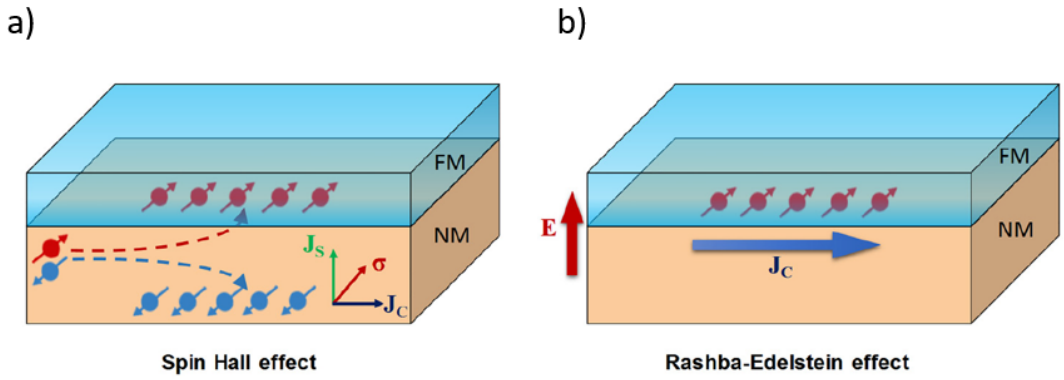

Figure 7.2: a) Illustration of the bulk spin Hall effect in a NM. (b) Illustration of Rashba-Edelstein effect at the FM/NM interface [192].

controlled ferromagnet electrodes and can be realized in a single uniformly magnetised ferromagnetic layer. Moreover, the direction of the spin-orbit torque may be changed by reversing the current, thereby enabling reversible control of the magnetisation [22].

As discussed previously, magnetic skyrmions are micron or sub-micron sized particle-like magnetic configurations which have magnetisation antiparallel to magnetic field at their centre and parallel to the field at their periphery [43,44]. Attention is focused on the ferromagnetic/non-magnetic interfaces having a broken inversion symmetry, which can induce strong Dzyaloshinskii-Moriya interaction (DMI). Even though the formation of Néel-type skyrmions was achieved at interfaces exhibiting strong DMI, the challenges in the creation of skyrmions remained, i.e., low temperature conditions and high external magnetic field are still required. Finally, Pt/Co/Ta and Co/Pd multilayers with perpendicular magnetic anisotropy (PMA) allowed the first observation of room temperature zero field skyrmions [197, 198]. Further, these systems are considered to be the most suitable candidates for industrial applications since they allow large spin currents resulting in faster skyrmion motions.

To use skyrmions as information carriers we must be able to drive their motion along nanostructures and also nucleate and annihilate them at will. However, knowledge about their motion in constricted geometries is lacking, and generating skyrmions is recognized to be very difficult because of their topological stability; that is, they cannot be created or annihilated by a continuous variation in spin

configuration from a uniform ferromagnetic state [199].

It is important to mention that the initial plan was to study SOT in magnetic multilayers experimentally for potential device applications. Similar to what was discussed in chapter 5, the ultimate goal is to contribute towards the future of nanoelectronics. Also, motivated by the study in chapter 6, another way to introduce roughness artificially is by means of patterning a lattice of micro-pillars with different shapes and sizes. With this in mind, a grid of different sized squares were patterned onto a SiO_2 substrate using photolithography with positive photoresist. After the light exposure, platinum pillars with different heights were deposited using a magnetron sputtering system. Afterwards, the photoresist was removed using acetone which thereafter a structure of Pt(2 nm)/Co(0.6 nm)/Pt(4 nm) with PMA was sputtered. Figure 7.3a) shows an optical microscope image of a 20 μm-side square grid and in figure 7.3b) shows the 50 μm-side square grid analogue. Unfortunately, finishing this study was not possible due the global COVID-19 pandemic. The next step toward completion of this study was to use again photolithography however, in this case with negative photoresist to create a strip of material with one line of squares or if possible just one square in the middle of the strip. After the creation of the strip, the deposition of electrical contacts is required in order to inject a current through the structure in the x direction (along the longer side of the strip) similar to one in figure 7.4b). On the top of the pillar the PMA is expected to be larger that in the rest of the strip because of the thicker Pt. This makes the pillar and the rest of the strip have different saturation and reversal fields. For instance, figure 7.3c) shows a MOKE microscope image when applying a magnetic field, $\mu_0 H = 0.005$ mT. The pillars are in the opposite magnetisation state to the rest of the film because the field is not sufficiently strong to reverse the magnetisation of the regions on top of the pillars. The objective is to test whether the pillar can be used to nucleate skyrmions, and whether these can be manipulated and depinned using spin-orbit torques.

Instead, in this chapter micromagnetic simulations were used to study the current-driven DW motion using SOT to investigate the potential creation of an artificial skyrmion-bubble in the top magnetic layer of a pillar structure using the difference

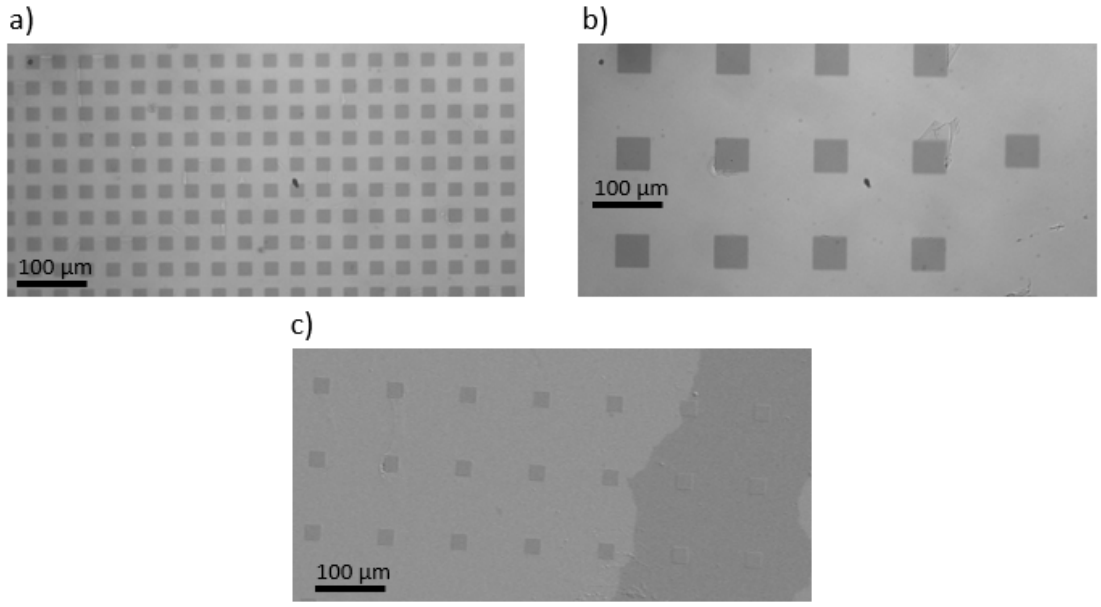

Figure 7.3: Optical microscope images. a) Pattern of 20 μm-side square grid with Pt/Co/Pt structure deposited on top and b) pattern of 50 μm-side square grid with Pt/Co/Pt structure deposited on top. c) Pattern 20 μm-side square grid when applying a reverse magnetic field of $\mu_0 H = 0.005$ mT which shows the square-pillars with the opposite magnetisation state from the rest strip.

in perpendicular magnetic anisotropy in the different regions.

7.1 Current-driven DW motion micromagnetic simulation by spin-orbit-torque

A micromagnetic simulations was conducted to better understand the influence of the spin-orbit-torque driven magnetisation reversals for ns duration current pulses. The software used here to perform the simulations was MuMax^3 [200].

MuMax^3 is a graphics-processing-unit (GPU)-accelerated micromagnetic simulation software [200] that was used in this chapter to simulate magnetic textures and their evolution when subjected to various excitations. The program is written in the Go programming language, using Nvidia's CUDA platform as a compiler to enable the use of the GPU for computation. MuMax^3 allows for the computation of magnetisation dynamics as well as the magnetisation response to an applied magnetic field and various other excitations. To do that, the software uses the GPU, due to

its excellent capability for parallelisation, a quality which is required for optimally resolving 2-dimensional magnetic textures. The software employs a finite-difference spatial discretisation, thus dividing the simulation space into equal sized cells. Due to the many interactions present when solving the LLG equation, which is in the form [200]

$$\vec{\tau}_{LL} = \gamma \frac{1}{1+\alpha^2}\left(\vec{m} \times \vec{H}_{\text{eff}} + \alpha\left(\vec{m} \times \left(\vec{m} \times \vec{H}_{\text{eff}}\right)\right)\right), \tag{7.1.3}$$

where $\vec{\tau}_{LL} = \frac{d\vec{m}}{dt}$ is the total torque similar to eq. 2.6.22 in chapter 2. The quantities of interest can be divided into two categories, based on the whether they are defined in the cell volume or at the boundaries. Volumetric quantities, such as the magnetisation and the effective field are treated at the center of each cell, while coupling quantities which represent relative interactions are considered at the faces of each cell. Due to memory saving considerations, these former quantities are not saved for each cell, rather material regions are defined that encompass more than one cell, and the specific material parameters are saved per each region instead. For the same reason, coupling quantities are saved in a triangular matrix (A triangular matrix is a square matrix with all the entries above/below the main diagonal equal to zero). The effective field collects all the various magnetic interactions in their magnetic field form, into a single vector field as discussed in chapter 2. In order to include a magnetic interaction into the numerical scheme employed by MuMax^3, the description of the interactions in the system must be condensed into a field term as well as an energy density term.

As mentioned in earlier sections, MuMax^3 employs a finite difference method. The premise of this method is that a differential equation of the form of eq. 7.1.3 can locally be approximated as a sum of finite difference quotients [201]. Starting from the Taylor expansion

$$u(x+\Delta x, y, z, t) = u(x, y, z, t) + \Delta x \frac{\partial u(x, y, z, t)}{\partial x} + \frac{(\Delta x)^2}{2}\frac{\partial^2 u(x, y, z, t)}{\partial^2 x} + ... \tag{7.1.4}$$

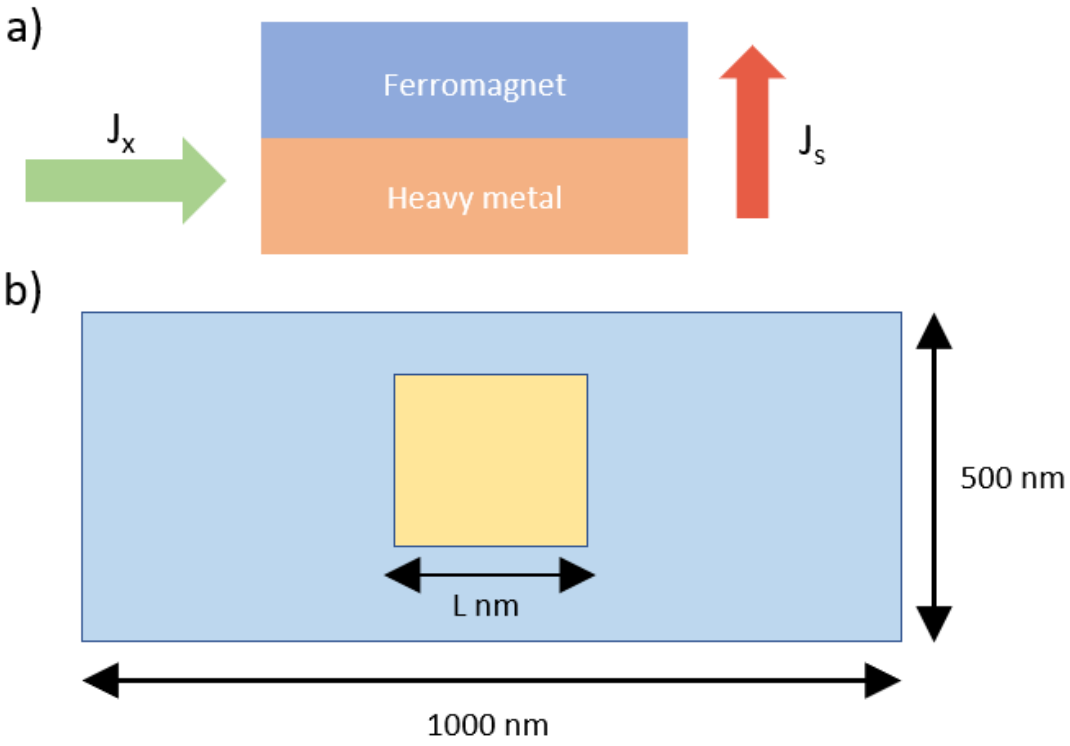

Figure 7.4: Illustration of the layout of the system to be simulated. a) Profile of the system consisting of a heavy metal and a ferromagnet in which a charge current is injected in the x direction. (b) Top-view of the system which shows the pillar of length L.

and ignoring higher order terms one can obtain

$$\frac{\partial u(x,y,z,t)}{\partial x} = \frac{u(x+\Delta x,y,z,t) - u(x,y,z,t)}{\Delta x} \tag{7.1.5}$$

In addition to spatial discretisation, the simulation software uses a collection of solvers which advance the LLG equation. These algorithms follow the Runge-Kutta iterative method, each providing a different order of convergence and error estimate.

7.1.1 Model of the strip thin-film with the square pillar

The system to model was composed of a non-magnetic heavy metal layer next to a ferromagnet, as shown in figure 7.4a). Then, a charge current is injected in the x direction of the heavy metal and because of both the interfacial and bulk components of the SOI the spin Hall effect takes place which produces a spin current

across the sample also shown in figure 7.4a). This spin-current will exert a torque (SOT), which will manipulate the magnetisation. For the micromagnetic simulations it was considered a rectangular sample of dimension (1000× 500× 5) nm^3 that is discretised using 1024 × 256 × 1 finite difference cells. At the center of the sample a square pillar is patterned with dimension of either $L = (250 \times 250)$ nm^2 or (100× 100) nm^2 as shown in figure 7.4b). This type of simulation requires a fixed layer with set polarisation, $\vec{\sigma}$, (in the software, `pol`=spin-Hall angle for SOT Slonczewski-like torques), in the y direction and a spacer layer that the properties are modeled by setting $\Lambda = 1$, the Slonczewski parameter, which is a measure of the deviation from the symmetric behaviour. For the simplest case, we set $\Lambda = 1$ in order not to have any angular dependence [200]. Moreover, the out-of-plane spin-torque parameter ϵ' = spin Hall angle for SOT field-like torque. The pillar was modelled as Pt and the height of the pillar changed the PMA of the structure in the pillar region. Thereafter, on top of the pillar we used micromagnetic parameters consistent to build a perpendicular magnetised multilayer stack with either Pt(2 nm)/Co(0.6 nm)/Pt(4 nm) or Pt(2 nm)/Co(0.6 nm)/Ir(4 nm) system. The saturation magnetisation used was $M_S = 1.2$ MA/m, the exchange stiffness, $A = 20$ pJ/m [127] and, the perpendicular anisotropy constant, $K_{u_{strip}} = 1$ MJ/m^3 for the strip and, $K_{u_{pillar}} = 1.8$ MJ/m^3 for the pillar region. Also, a DMI constant was set of $D_{strip} = 0.45$ mJ/m^2 for the strip and $D_{pillar} = 0.6$ mJ/m^2 for the pillar region. These parameters model the typical thin-films with PMA that were used throughout all this thesis, which also present bubble-like domain expansion under out-of-plane magnetic field [127].

7.2 Spin-orbit-torque current-induced reversal

Figure 7.5 shows the field-driven domain wall motion colour representation of m of all the region surrounding the pillar, where black represents the magnetic moment state pointing down and white the magnetic moment state pointing up, by applying a magnetic field pulse of $\mu_0 H = 70$ mT during 10 ns to the (1000× 500) nm^2 strip with uniform DMI constant of $D_{strip} = 0.45$ mJ/m^2. The 100 × 100 nm^2

pillar, figure 7.5a) has a higher DMI of $D_{\text{pillar}} = 0.6$ mJ/m^2. Also, the pillar region has almost double the PMA than the strip region, which is why the pillar region requires a higher field in order to switch. Alternatively, figure 7.5b) shows the 250×250 nm^2 pillar which, was set using the same. This demonstrates the realism of this modelling as the outputs can be directly compared with what was found experimentally in the MOKE microscope images displayed in figure 7.5c). The field-driven measurements were performed in a patterned 1.5 nm height Pt square pillars grid with Pt(1 nm)/Co(0.6 nm)/Pt(4 nm) multilayer stack sputtered on top. The size of the square pillars are 20 μm and 50 μm respectively. The experiment consisted in applying a magnetic field of 90 Oe during 10 s. The time between images was 1 sec. Although the time and length scales are different between simulation and experiment, the behaviour is qualitatively similar.

The central result of this work is shown in figure 7.6a) and b), where the field-induced and current-induced reversal of m_z was compared. First, a standard magnetisation reversal simulation in the absence of current pulses was performed, recording the normalised z component of the magnetic moment, m_z, during a single sweep of $\mu_0 H$ applied perpendicular to the current injection line. The field was intentionally tilted off-orthogonal by less than $1°(\theta \approx 91°)$ to prevent the formation of magnetic domains. This was done because if the field is applied at precisely 90° to the plane there is no torque to initiate the switching. In this situation, the only remaining torque is the floor of numerical accuracy. The system remains in an unstable stationary point but it is unable to switch to the other energy valley. This can be demonstrated from the fact that repeating the same simulation will result in switching at arbitrarily different field values. One solution to this problem is applying the magnetic field at some angle smaller than one degree deflected from 90° in order to help the nucleation but that is sufficiently small not to bias the simulations.

Magnetisation reversal occurs at the coercive field $\mu_0 H_c = 300$ mT, owing to the dominant component, $\mu_0 H_z$, parallel to the out-of-plane easy axis of the film. Then, the magnetic field sweep was repeated, but was stopped at each value of $\mu_0 H$ to inject a positive (set) current pulse and negative (reset) current pulse and

Figure 7.5: Colour representation of m, measured after 2 ns field pulse of $\mu mH = 70mT$. Time scale in the left-hand side. Field-driven domain wall motion a) for 100×100 nm^2 pillar b) for 250×2500 nm^2 pillar. Colour wheel at the center representing the magnetic moment direction. c) Field-driven MOKE microscopy images on a patterned thin-film with 1.5 nm height Pt square pillars grid with Pt(1 nm)/Co(0.6 nm)/Pt(4 nm) multilayer stack sputtered on top. A magnetic field of $H = 90$ Oe was applied constantly, the time between images is 1 sec.

measuring M_z after each pulse. The blue and red points [figure 7.6b)] indicate the orientation of m_z after the alternating injection of set and reset pulses of amplitude $J = 5 \times 10^{12}$A/m^2. This plot shows two striking effects, illustrated in figure 7.6c). First, blue and red points that represent magnetisation of opposite sign indicate switching of M_z from up to down and vice versa following every pulse of current. Second, the sense of switching reverses as $\mu_0 H$ goes through zero. Positive and negative sweeps of $\mu_0 H$ give identical results to confirm the consistency and the effect is entirely from the spin-current and not the field.

Figure 7.7 shows the SOT current-driven domain wall motion within the strip with non-zero DMI as stated in the model section. The DW motion can be de-

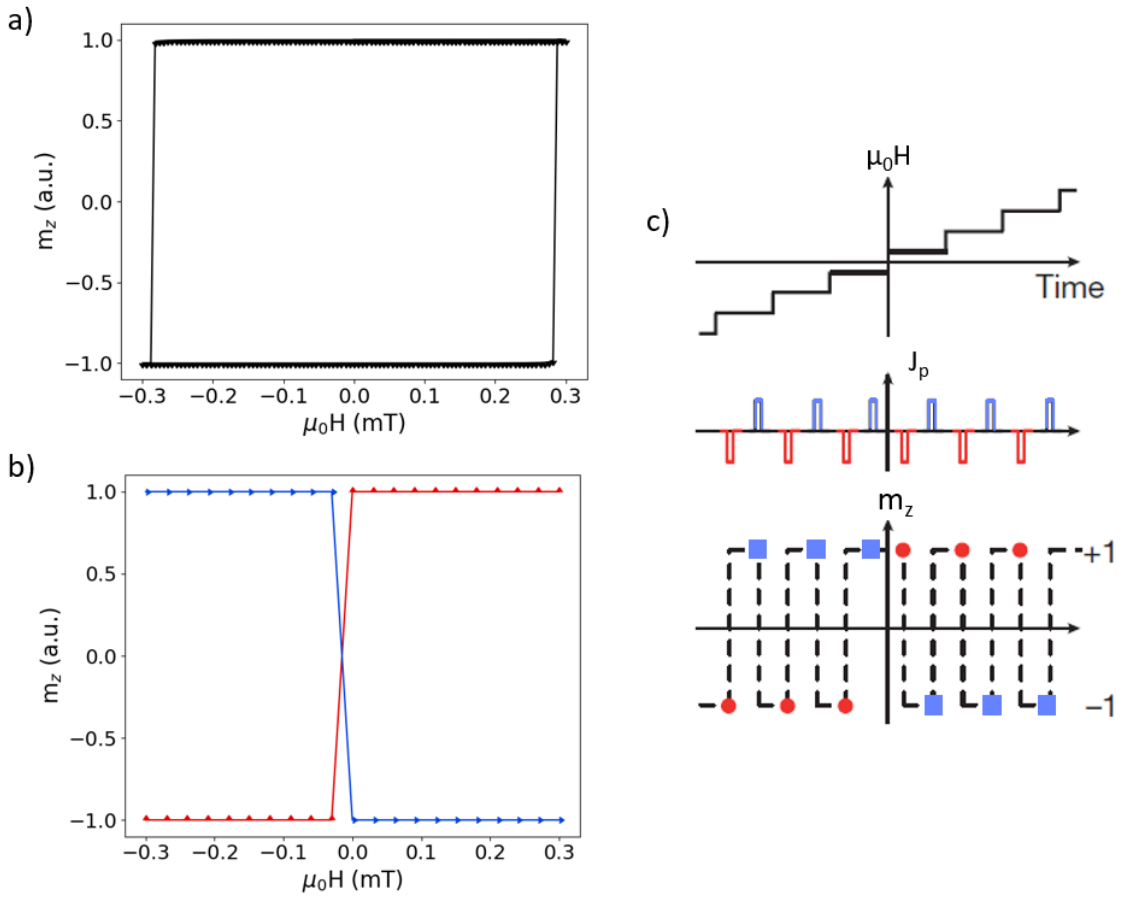

Figure 7.6: Hysteresis loops. a) Field switching and b)current-induced switching, M_z measured after the injection of positive (blue squares) and negative (red circles) current pulses of amplitude $J = 5 \times 10^{12}\mathrm{A/m^2}$. c) Schematic of the pulse sequence and magnetisation measurements. In both a) and b), $\mu_0 H$ applied at $\theta \approx 91°$. The 1° offset with respect to the ideal in-plane direction is used to define the residual component $\mu_0 H_z$ unambiguously.

scribed by the presence of the Slonczewski torque and, it is important to consider the internal structure of the domain wall [202]. For Pt/Co/Pt thin films with zero DMI, the domain walls will be of the Bloch-type [figure 7.8a)]. For this wall type, the Slonczewski torque cannot lead to domain wall motion because of symmetry considerations: the 180° rotational symmetry around the y axis of this wall type prohibits a well-defined direction of movement, because a hypothetical direction of motion would reverse under this symmetry operation while the system and the resulting Slonczewski torque remain unchanged [202]. However, the Bloch wall can easily be perturbed, so that this symmetry is broken. With the DMI in the system it forces the stabilisation of Néel-type domain wall [figure 7.8b)] and therefore, have motion.

Figure 7.7: Colour representation of m_z, measured after the injection positive current pulses. Time scale in the left-hand side. SOT current-driven domain wall motion a) $J = 5 \times 10^{12}$ A/m^2 complete switching of the strip b) $J = 3.8 \times 10^{12}$ A/m^2, the current could not overcome the PMA of pillar. c) $J = 3.8 \times 10^{12}$ A/m^2 making the pillar smaller and applying a small current in the opposite direction enables to just have the pillar. Colour wheel at the bottom representing the magnetic moment direction.

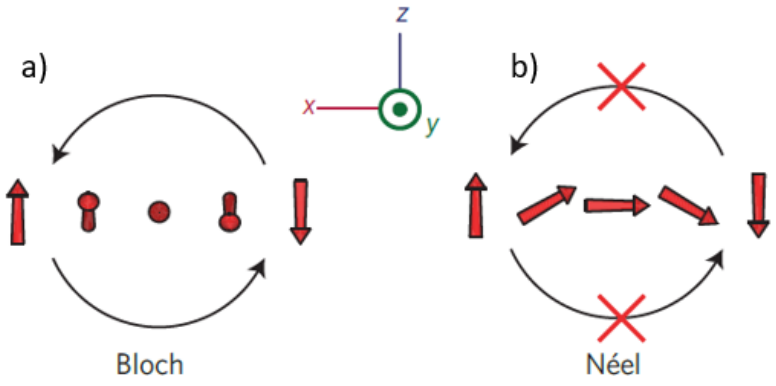

Figure 7.8: a)Bloch domain wall, the magnetisation rotates about the normal of the domain wall. b) Néel domain wall, the magnetisation rotates about a line that is orthogonal to the normal of the domain wall.

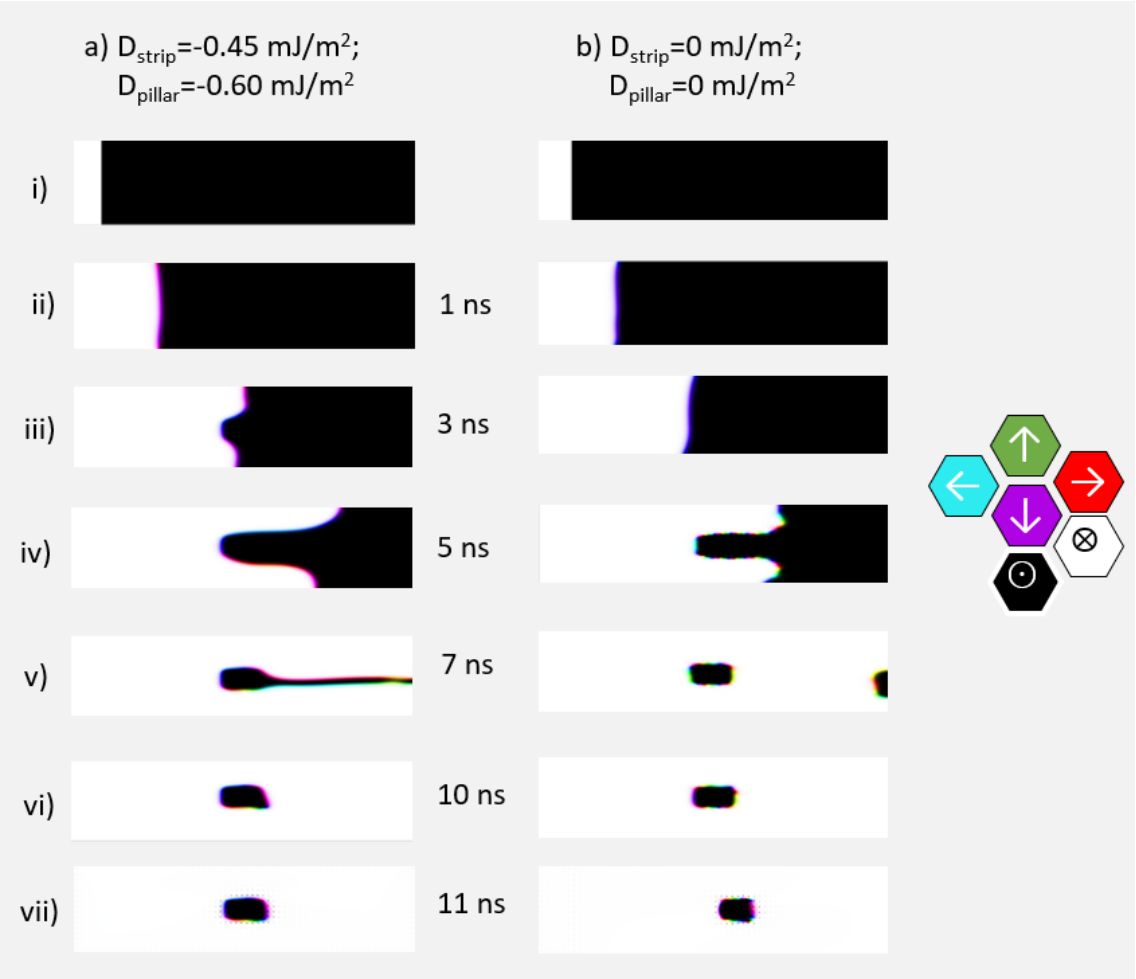

Figure 7.9: Colour representation of m. SOT current-driven domain wall motion. Time-step is displayed in the middle. i)-iv) $J = 3.8 \times 10^{12}$ A/m^2 current applied in the x direction for 6 ns in total. v)-vi) magnetic field pulse of $\mu_0 H = 0.05$ mT during 3 ns and vii) another 1 ns $J = 3.8 \times 10^{12}$ A/m^2 current pulse in the x. a) with $D = 0.6$mJ/m^2 the final configuration after the 3 pulses is the pillar. b) for $D = 0$ mJ/m^2 after vi) the pillar can be observed similar to the DMI case however, after the 1 ns current pulse, the whole structure moved towards the current direction. Colour wheel at the center representing the magnetic moment direction.

First, figure 7.7a) shows the DW motion when applying a current, $J = 5 \times 10^{12}$ A/m^2, along the x direction, which is sufficient to saturate the whole sample including the pillar after a 6 ns pulse, producing an average DW velocity of approximately 180 m/s. This is in the same range of what was found for Fukami *et al.* in perpendicular magnetised nanowires [203]. When the current is decreased from the saturation current to $J = 3.8 \times 10^{12}$ A/m^2 due to the difference in PMA, nucleation can be seen in the strip, however, not in the 250×250 nm^2 pillar as displayed in figure 7.7b). In this case, the dynamics are more complex due to the

pillar not reversing the magnetisation state, the simulation time increased to 12 ns. Furthermore, nucleation in the right-hand side of the pillar presents a more complex dynamic in which switching is not accessible in all the region and leaves a trace of the pillar shape when moving towards the current direction. As a result, the simulation time doubled. In order to have access to the left trace at the right-hand of the pillar [region in black in figure 7.9b)]; first, the pillar dimension are reduced to enhance the reverse contact region and switching and, second, a small magnetic field pulse of 0.005 mT during 3 ns is set after the 6 ns current pulse in the system to help overpass the energy barrier and complete the switching. In the last image of figure 7.7c) shows the pillar with opposite magnetisation from the strip.

One questions that emerges from the final configuration of figure 7.7c) is how the magnetic moment are distributed in the surrounding of the pillar. It is important to recall that the only difference between the pillar region and the rest of the system is the PMA.

7.3 Bubble-skyrmion motion with current

Furthermore, figure 7.9 shows the colour representation of m, where black represents the magnetic moment state pointing down and white the magnetic moment state pointing up. SOT current-driven domain wall motion with the following procedure was performed in the system: i)-iv) $J = 3.8 \times 10^{12}$ A/m^2 current is applied in the x direction for 6 ns. Then, in v)-vi) a magnetic field pulse of $\mu_0 H = 0.05$ mT during 3 ns is applied and finally, in vii) another 1 ns $J = 3.8 \times 10^{12}$A/m^2 current pulse in the x is injected. Figure 7.9a) shows the case with $D = 0.6$ mJ/m^2 which shows the pillar region in the opposite state than the rest of the strip. On the other hand, in the case with zero DMI, after the magnetic field pulse, displayed in figure 7.9b),vi), the final configuration was similar to the non-zero DMI, where the pillar region presents the opposite state from the rest of the strip. However, when applying the final 1 ns current pulse, the entire structure moves to the right towards the current direction.

In this study, to tune the internal structure of the domain wall, a field in the x

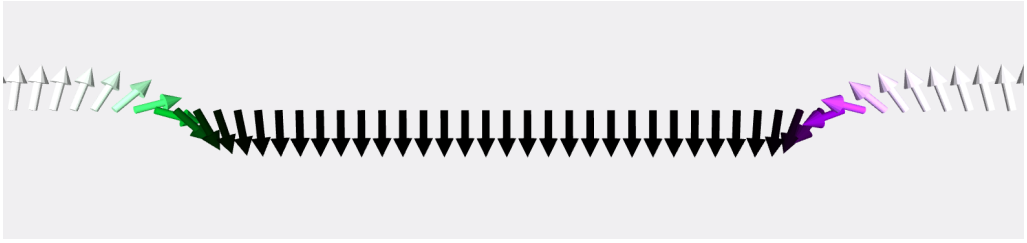

Figure 7.10: x-z plane slice of the pillar. From the left to right the magnetic moment goes from up to down rotating in direction out-of-the-plane. The magnetic moment colourmap is: white (up), black (down), green (right), purple (left), red (coming out of the image) and blue (coming in of the picture).

direction is applied and/or adding DMI to the system. The applied field changes the domain wall from the initial Bloch type to a Néel-type with the centre spin aligned to the field. When the domain wall is of the Néel-type, the spins obtain an x component, thereby breaking the symmetry, which is crucial for the movement of the wall.

In order to check if under the imposed circumstances an artificial bubble-skyrmion structure was created, one can calculate the topological charge or the skyrmion number. This characteristic of skyrmions indicates that they are topologically protected, this means that they possess a non-zero, integer value of the winding number which is the number of times spins wind around the unit sphere. This can also be visualized by wrapping the spin unit vector ($\vec{m}$) around a unit sphere [204]. The skyrmion number can be described mathematically as

$$n = \frac{1}{4\pi} \int \vec{m} \cdot \left(\frac{\partial \vec{m}}{\partial x} \times \frac{\partial \vec{m}}{\partial y} \right) dxdy \tag{7.3.6}$$

where $\vec{m}$ is the normalised magnetic moment within the magnetic thin film. Taking the last configuration in figure 7.9a) it is possible to argue that the PMA protects the configuration and one can check to see if it posses a skyrmion number. Using MuMax^3 to calculate the skyrmion number it was found that for the case of non-zero DMI $n = -0.9983$ (in effect, -1) and also that the domain wall surrounding the pillar was a Néel DW as displayed in figure 7.10. Performing the same calculation for the case with zero DMI, it was found that $n = -0.0045$ (in effect, 0).

Figure 7.11 shows the SOT bubble domain motion from the initial configura-

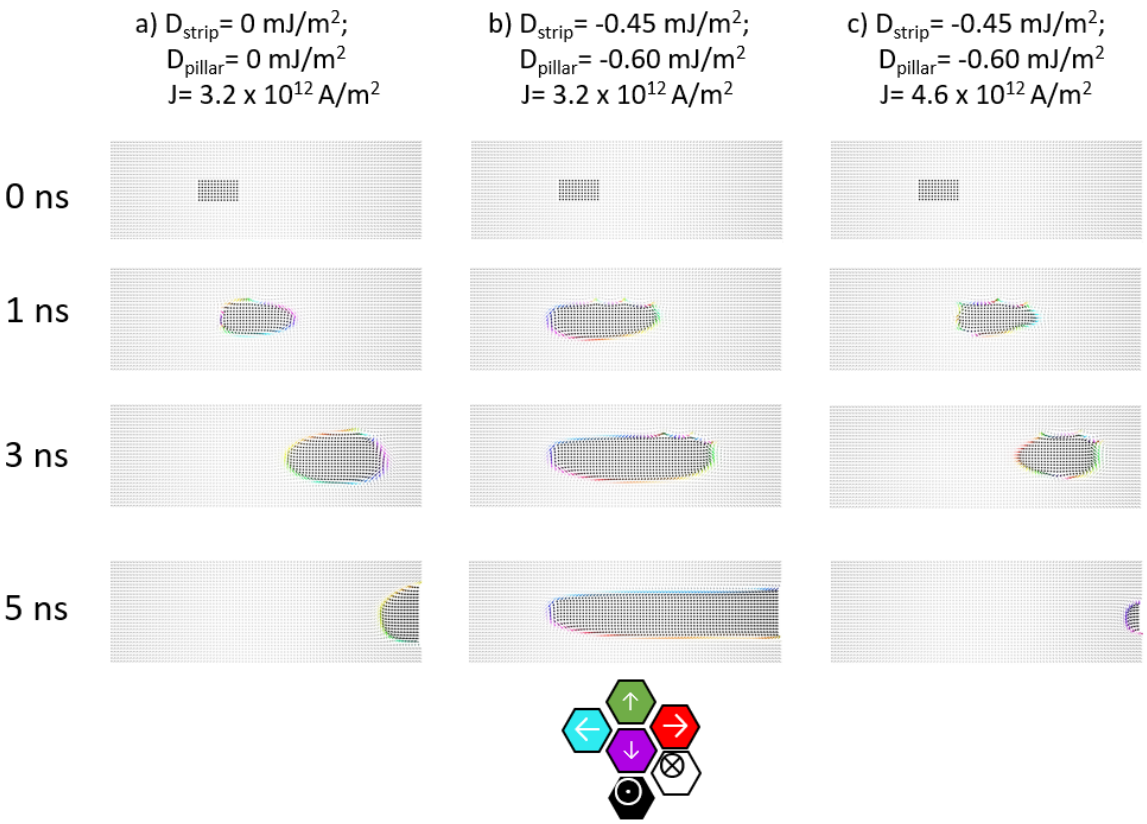

Figure 7.11: The initial configuration is the pillar in the opposite spin state of the rest of the strip. a) The zero DMI case, a current, $J = 3.8 \times 10^{12}$ A/m^2, in the x direction is applied, the pillar region become a bubble-like domain which is depinned in direction of the current. b) $D_2 = 0.6$ mJ/m^2, the pillar region becomes a bubble-skyrmion due to its $n = 1$ and then, it is stretched by the current. c) Increasing the current to $J = 4.6 \times 10^{12}$ A/m^2 depins the structure and move it towards the current direction.

tion when the pillar is in the opposite magnetisation state of the rest of the strip. Hereafter, a current, $J = 3.2 \times 10^{12}$A/m^2, in the x direction was applied for the first two cases. For the zero DMI (both D_{strip} and D_{pillar}) scenario, the pillar region become a bubble-like structure which is moved towards the current direction as displayed in figure 7.11a). Moreover, calculating the topological charge or skyrmion number for this case, it was found $n = -0.0045$, which informs that the structure is just a topologically-trivial bubble domain [204]. In contrast, for the case with $D_{\text{pillar}} = 0.6$ mJ/m^2 (and $D_{\text{strip}} = 0.45$ mJ/m^2), the pillar region stretches towards the current direction as shown in figure 7.11b). Calculating the skyrmion number for bubble-like domain before reaching the right-hand side edge in figure 7.11b) we found that, $n = 1.99$ which means the the structure is a bubble-skyrmion with a

winding number 2, which has not been reported before. When the domain touches the edge the skyrmion number reduces as the DW is no longer continuous. This findings suggest that the topological protected bubble-skyrmion stretches with the current. Increasing the current to $J = 4.6 \times 10^{12}\mathrm{A/m^2}$, the bubble-skyrmion can be depinned as shown in figure 7.11d) after 1 ns current pulse. The structure has a winding number, $n = 1$ and moves in direction of the current with a velocity of 151 m/s.

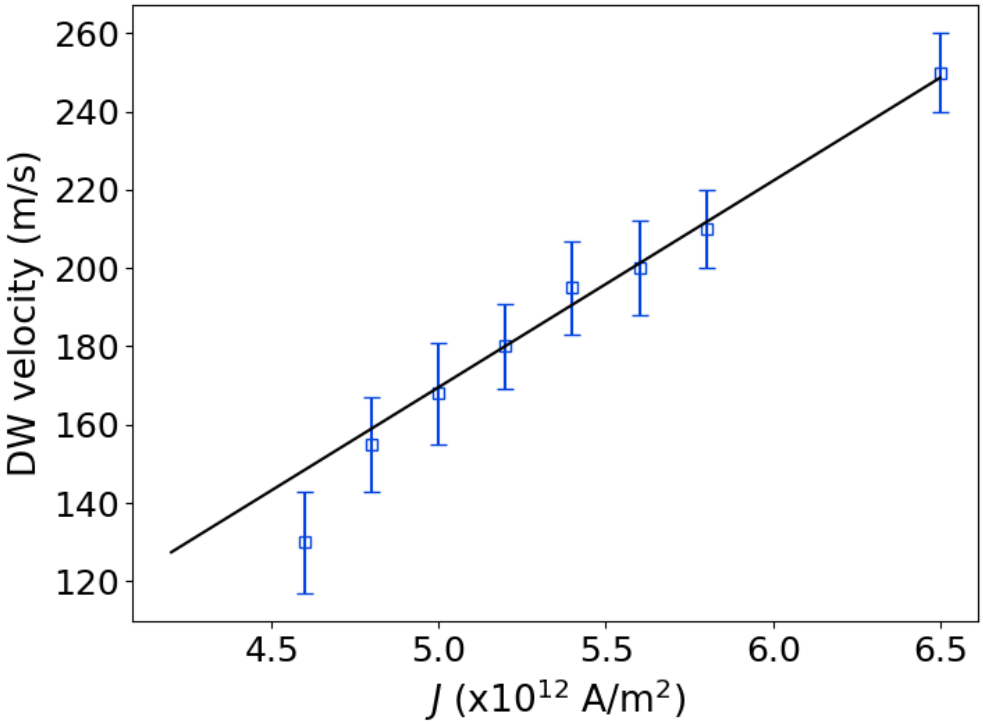

Figure 7.12: Micromagnetic model of DW velocity of a bubble-skyrmion as a function of the injected current.

Furthermore, it is expected that when the current is increased the DW velocity of the bubble-skyrmion will increase as well. Figure 7.12 show the relation DW velocity and the depinning current. This relationship is linear at higher current densities. Fert et al. showed the same behaviour for a MnSi crystal [3]. Also, the DW velocity found here is larger than expected in the standard domains used in the storage devices, which are in the range 140-160 m/s. This demonstrates that these bubble-skyrmions can be driven efficiently along a micro-track by a current induced

SOT in HM/FM/HM asymmetric trilayers. This is also similar to what was found by Jiang *et al.* where they were able to move Néel skyrmions by means of SOT current along a nanotrack within micromagnetic simulations [205]. In this work, both the dimensions of the track and magnetic textures are larger; that is why it requires higher depinning current. However, the results are equivalent. Moreover, Jiang *et al.* presented the relation between J and DW velocity on which they also found a linear relation between the depinning current and the DW velocity [61]. Extrapolating from Jiang's model in the linear regime, to increase the DW velocity by 10 m/s it is required to add $J = 1 \times 10^{14}$ A/m^2 in our model in contrast, it is required to add $J = 2 \times 10^{12}$ A/m^2. This shows that in our model the current required to increased the topological texture velocity by 10 m/s is 50 times lower even though the skyrmion-bubble has to be pulled from the pillar region and also, the bubble velocity is one order of magnitude higher in this work. They presented a maximum DW velocity of 25 μm/s while in our work is nearly 250 m/s. This is a huge 7 order of magnitude difference. Similarly, very recently, magnetic skyrmions of smaller diameter ($\approx$ 200 nm) were also stabilised and driven along a nanoscale racetrack with a velocity up to 120 m/s, at a current density of approximately 5×10^7 A/cm^2 in a multilayer made of Pt/Co/Ta trilayers [13, 206–208]. As a result, this indicates the potential for implementing nanoscale magnetic skyrmions as information carriers in nonvolatile spintronic technology such as skyrmion race-track memory. Similar to the well-known domain wall racetrack memory, the presence or absence of magnetic skyrmions along the racetrack would be used to encode binary bits, 1 and 0, respectively. The memory operation is then enabled by applying a current to move the skyrmions along the racetrack.

As a last note, one of the key issues to use skyrmion in technological applications is to be able to create the structure at a specific position and and, here a potential solution to that problem has been presented.

7.4 Summary

We have modelled the dynamics of the SOT driven domain-wall, bubble, and skyrmion motion in a strip of dimension 1000× 500 nm^2 with a square pillar in the center of 100×100 nm^2 with increased PMA. This analysis was performed numerically using MuMax^3. An appropriate procedure was determined whereby reversal of the strip, without reversal of the pillar, could be driven by SOT - presenting a possible mechanism to write magnetic skyrmions. The case with DMI in the system, the structure present skyrmion-like properties such as a skyrmion number of -1 and Néel DW in the surrounding of the pillar. On the other hand, for the case with zero DMI, the skyrmion number was zero.

Finally, when a current is injected into the system it can move the reversed domain away from the pillar, through the rest of the strip. For the case with DMI, the magnetic structure on the pillar stretched towards the current direction until the edge of the simulation box. Increasing the current depins the bubble-skyrmion making it move faster than the previously reported. The DW velocity of the bubble skyrmion increases linearly with the depinning current. In contrast, the case with zero DMI, the magnetic structure on the pillar became a bubble with $n = 0$ with was moved along the current direction.

Chapter 8

Conclusions and future work

Within spintronics, interfacial effects play a crucial role in magnetism, both in the development of underlying scientific principles and in the many resulting technologies. Many important effects in magnetism are either intrinsically interfacial phenomena or strongly enhanced at interfaces, for example, Dzyaloshinskii-Moriya interaction, the proximity induced magnetisation, chiral domain walls, and spin currents with no accompanying charge current. Interfacial engineering enables potentially novel fundamental behavior by blending and/or competing interactions.

In this thesis, several experimental techniques were employed in the characterisation of interfacial effects in polycrystalline Co_2FeAl and, Co thin films with Pt deposited on Si/SiO_2 substrates by magnetron sputtering. Proximity induced magnetisation (PIM) in both Pt and Ir adjacent to Co_2FeAl and Co layers and the changes with temperature and their relationship with the interfacial Dzyaloshinskii-Moriya interaction has been explored. The Dzyaloshinskii-Moriya interaction in multilayers with engineered interfacial roughness was studied by Brillouin light scattering and the asymmetric bubble expansion. Furthermore, current-driven domain wall motion was studied using micromagnetic simulations on a multilayered square pillar with PMA using SOT with the aim of inducing a chiral domain state at the top of the pillar.

8.1 Thesis conclusions

In chapter 5, Co_2FeAl films were prepared by sputtering on Si/SiO_2 substrates using different buffer and capping layers. There is a consistent and illustrative story told by all three techniques XRR, PNR and XRMR. The annealing process changed the structure of the samples and also modified the magnetic properties both in the layer and at the interfaces. The structural configuration after the thermal process cause a detrimental effect in the magnetism on the Ir samples due to a possible intermixing with the adjacent layers. Moreover, it also induced a decreased in the magnetic moment of the CFA, which in contrast creates an increase in the PIM in the Pt sample. Even though CFA seems to be a promising material for domain-wall devices, careful control of growth, and optimisation of thermal treatments is required for devices containing CFA in order to function optimally. Finally, it was noticed that the magnetisation decreased over time from 1110 $\pm$ 50 emu/cm^3 meaured by VSM to 320 $\pm$ 10 emu/cm^3 in a 3 years lap suggesting that this whole structure will not be able to sustain the properties require to create devices.

It was confirmed that modifying the interface changes the PIM and the DMI. As a result, an intentionally modified interface was engineered to understand the relation DMI and roughness.

Following this, experiments were developed to investigate and quantify the role of the interfacial roughness induced in sputtered Pt(11 nm)/Co(0.6 nm)/Pt(4 nm), Pt(7 nm)/Co(3 nm)/Ta(4 nm) and Pt(4 nm)/Co(3 nm)/Ta(4 nm) deposited onto thermally evaporated Ag layers or sputtered discontinuous SiO_2 layers in order to create an engineered interface roughness in the multilayers were described. Roughness in the range of 0 to 35 Å was obtained.

The asymmetric bubble expansion method was used to estimate the DMI in a Pt/Co/Pt stack, significantly, this analysis showed that the DW travels more slowly with increasing applied in-plane magnetic field, in contrast to the conventional behaviour DMI DW, where the velocity increases.

The BLS spectroscopy for the perpendicularly magnetised Pt/Co/Ta stack presented magnon lines and thus it was possible to determine the DMI. The DMI measurements suggest that the relation between the DMI and the roughness follows a

non-linear behaviour, which does not vary depending on whether the magnetisation is in-plane or out-of-plane.

The results from the asymmetric bubble expansion are yet to be completely understood, but the behaviour observed has similar phenomenological features to the results found by BLS analysis, where the DMI fluctuates when the roughness increases, which tell us that changes in the quality of the interfaces in multilayer modify the interfacial DMI.

Inspired by the idea that patterned roughness underneath a magnetic multilayer could modify the properties of the structure locally, in chapter 7 modelling of the dynamics of the SOT driven domain-wall, bubble, and skyrmion motion in a multilayered thin-film strip of dimension 1000 $\times$ 500 nm^2 with a square pillar in the center of 100 $\times$ 100 nm^2 with increased PMA was reported. This analysis was performed numerically using Mumax^3. An appropriate procedure was determined whereby reversal of the strip, without reversal of the pillar, could be driven by SOT - presenting a possible mechanism to write magnetic bubble-skyrmions. The case with DMI in the system, the structure present skyrmion-like properties such as a skyrmion number of 1 and Néel DW in the surrounding of the pillar. On the other hand, for the case with zero DMI, the skyrmion number was zero.

Finally, when a current is injected into the system it can move the reversed domain away from the pillar, through the strip and in direction of the current. For the case with DMI, the magnetic structure on the pillar stretched along the current direction until the edge of the simulation box. Increasing the current depins the bubble-skyrmion making it move faster than in some previous reports. The velocity of the bubble skyrmion increases linearly with the deppining current. In contrast, the case with zero DMI, the magnetic structure on the pillar became a bubble with $n = 0$ with was moved by the current. The velocity of the bubble-skyrmion found was close to 250 m/s, which is higher that the one reported in the literature (130 m/s) and the bubble-skyrmion creation method gives new insights towards skyrmionic applications.

The work in this thesis has covered the importance of the interfacial magnetism in multilayered thin-films by means of scattering, light and micromagnetic analy-

sis. The main findings indicated that engineering interfacial characteristics imposes changes in the fundamental interaction. Nevertheless, characterising the details of potentially asymmetric interface properties, such as the roughness, degree of intermixing, and density of stacking faults, remains an outstanding materials science challenge.

8.2 Future work

This thesis has demonstrated a systematic study of the effect of annealing on PIM in HMs contacting Heusler alloys as the ferromagnetic layer. Also, the effect of engineered roughness on interfacial DMI and the current-driven DW motion using SOT for the formation of a magnetic skyrmion on an engineered nanopillar were investigated. Further studies are required to test and to find a more suitable heavy metal/ferromagnet interface and/or seed layer for device fabrication and applications. Routes for extending this work in order to obtain a deeper understanding and possible routes to device fabrication are discussed.

The PIM study under annealing process, can be extended to other ferromagnetic materials which can be other Co_2-based Heusler alloy such as Co_2MnSi or the vastly studied CoFeB. Also, change the heavy metal with Pd which is another paramagnetic material within the Stoner region.

For the DMI study, a continuation of this project is required to fully understand the behaviour found in the Pt/Co/Pt structures with the asymmetric bubble expansion method. The simplest step forward is to deposit another set of samples with the same characteristics in order to confirm the trend. Next, to create an asymmetric structure by modifying the top Pt layer by Ir, which will present larger DMI values. This will create a complete picture of the phenomenon and will discard this behaviour as inherent to Pt/Co/Pt. Furthermore, BLS measurements on the same set of samples as for the asymmetric bubble expansion study is required for a direct comparison of the DMI estimation. The BLS setup used in this work was not sensitive enough to resolve the thickness of the ferromagnetic layer in the set of samples with PMA. A theoretical description is required to model the behaviour

found in MOKE microscopy results.

The work in the chapter 7 gave a new method to create a bubble-skyrmion. The main result relies in the creation of skyrmion on the top of the pillar and once the skyrmion is created, one should be able to move at will using current pulses. Confirming experimentally the results would be the natural next step, using structures such as those shown in the MOKE images with a square grid patterned by photolithography shown in the chapter. Additional microfabrication is required to isolate one of the squares pillars and deposit electrical contacts to be able to inject a current.

In terms of micromagnetic simulations, further studies are required to characterise if there is a size restriction in the formation of the bubble-skyrmion or if it is possible to create the structure at any size required. Modifying the pillar size will in principle create a correspondent bubble-skyrmion. Also, use the method suggested here in a nanowire to make it suitable with the racetrack technology. A problem that remains to be solved in domain-wall memory is to pin the domain walls in a controllable manner at the nanometer scale using simple fabrication. Investigation of controllable domain-wall movement using the approach developed in this thesis in nanowires using both magnetic fields an current to pin and depin magnetic textures.

Appendix A

Data fitting procedure for XRR, PNR and XRMR scattering in thin films

This appendix is intended to complement the description of findings in chapter 5 and 6 where fitting is required when having x-ray reflectivity (XRR), polarised neutron reflectivity (PNR) and x-ray resonance magnetic reflectivity (XRMR) using a sodtware called GenX [209]. GenX is an open source software using differential evolution algorithm for fitting, primarily, x-ray and neutron reflectivity data [210]. The differential evolution algorithm is a robust optimization method which is highly effective at avoiding local minima. GenX is written in python and uses the wxPython package for the graphical user interface (GUI) [209]. Information on sample parameters, such as thickness, roughness, density and relative amplitude of magnetic moment in a sample can be extracted from the best fitting simulations of the experimental data.

Although GenX has been used in the fine-tuning of data from several scattering techniques, here specific focus is given to x-ray reflectivity (XRR), polarised neutron reflectivity (PNR) and x-ray resonant magnetic reflectivity (XRMR) data refinement. The refinement process involves optimising a physical reasonable model that simulates the experimental data. The optimisation of the best fitting model to fit the data is not trivial because of the large number of local good fitting mim-

ima [211]. The simulation uses a Gaussian function to describe the finite resolution of the instrument, beam footprint correction and over-illumination at small angle [212, 213]. The deviation of the simulated data from the experimental data is measured through a statistical criterion called the figure of merit (FOM). FOMs are quantitative measure of the conformity of the data and their weights to the simulation independent of the number of degrees of freedom [214]. There are several FOMs in the software, the most recommended measure of the goodness of the fits is the χ^2 function which was used mainly for the PNR, however other FOM were also used in this work. Steps for the proper definition of simulation parameters, models, and possible procedures for tuning these parameters are discussed in the next sections. In some of the FOMs, the errors in the data are considered in the quantification of the goodness of fit giving a weighted fit. A simulation step with a lower FOM from the previous one indicates an improvement in the simulation.

A.1 Setting-up the sample structure in GenX

The sample structure is built using the sample tab [labeled e) on figure A.1] in the GenX software, where the details of the layers and the interfaces of a sample are defined. The thin-film stack is added by pressing the plus button labeled b) in figure A.1. Similarly the layers are added by pressing the plus button c) on figure A.1. Each of the sample layer characteristics is defined in the layer editor dialog where the layer thickness, roughness, number density and magnetic moment are defined, which is shown in figure A.2. The number density, ρ_N, can be calculated following the instruction on the GenX online tutorials (http://genx.sourceforge.net/doc/faq.html) by the expression:

$$\rho = \frac{\rho_N}{1.66 \times 10^3 \times u_{\text{scatt}}} \tag{A.1.1}$$

where ρ_N are the densities in specified units and u_{scatt} is the molecular weight of the layer. For example, to calculate the density, ρ_{Co}, of cobalt the standard volumetric density is $\rho = 890$ kg/m^3 and the u_{scatt}=1$\times$ 58.93 u therefore,

$$\rho_{Co} = \frac{890 \text{ kg/m}^3}{1.66 \times 10^3 \times 58.93u}, \tag{A.1.2}$$

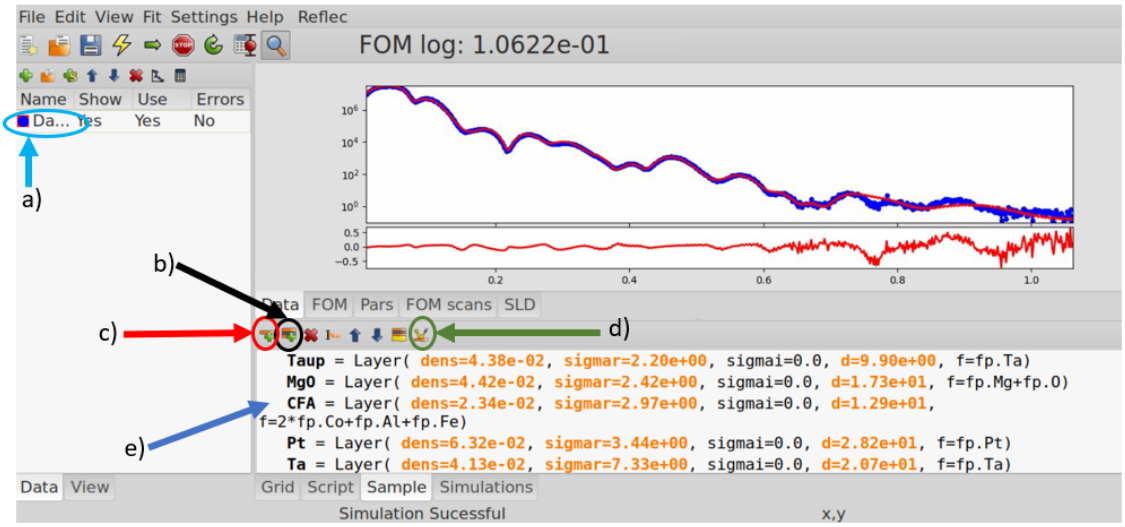

Figure A.1: GenX software interface. a) experimental data upload menu, b) sample stack addition tab, c) sample layer addition tab, d) instrument editor and e) sample tab.

considering that $1u = 1.660 \times 10^{-27}$ kg and 1Å$= 10^{-10}$ m, the density is $\rho_{\text{Co}} = 0.9094\ u/\text{Å}^3$.

The stack with different layers or a combination of many stacks with different layers makes up the sample model. The layer editor for the XRR, PNR and XRMR simulation is displayed in figure A.2 as different parameters that defines the instrument and sample are required. In the simple x-ray scattering used to model the XRR the layer editor has the following parameters: the layer editor composition (f), density (ρ_N), thickness (d) and interfacial roughness (`sigmar`) as shown in figure A.2a). The scattering length density (SLD) factor in the "standard" column is defined as `fp.(element component)`. Here, the SLD is defined by element composition as GenX has a database of all scattering length density factors.

In GenX, for the neutron scattering, used here to model the PNR, the layer editor is divided into the structural (same as in XRR) and the neutron column. Here the magnetic moment (`magn`) is defined on the neutron column as shown in figure A.2b). Similarly to the XRR case, the neutron SLD is defined as `bc.(element component)`.

In the magnetic x-ray scattering layer editor, more parameters are defined, as shown in figure A.2c). The layer editor is divided into four sections: scattering length (`Scatt. len.`), miscellaneous (`Misc.`), magnetism (Magnetism) and inter-

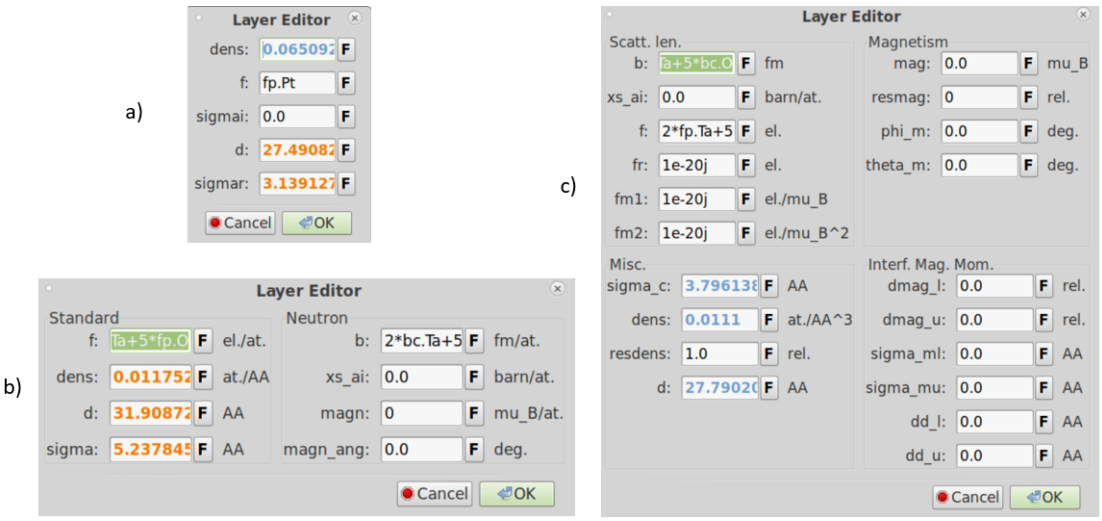

Figure A.2: Layer editor for a) XRR, b) PNR and c) XRMR.

facial magnetic moment (`Interf. Mag. Mom.`). The scattering length section defines the structural SLD factor defined by the element composition of the layer (`f`), which describes the non-resonant x-ray scattering length, the resonant scattering length of the resonant species of atom, which in this case is Pt (`fr`), the magnetic scattering length, related to circular dichoric effect (`fm1`) and the magnetic scattering length, related to linear dichroic effect (`fm2`). These scattering factors describe the refractive index of the medium that the x-ray travels through, as discussed in chapter 3.

The `Misc.` section defines the layer roughness (`sigma_c`), density (ρ_N), relative density of the resonant species (`resdens`=1) and thickness (`d`) of the layer, while the Magnetism section defines the bulk magnetic moment in the layer.

The interfacial magnetic moment section is used to define the magnetism at the interface which is described as an exponential decay with Gaussian roughness around the interface with amplitude (`dmag`), exponential decay length (`dd`) and magnetic roughness (`sigma m`). The upper interface is represented as `_u` while the lower interface as `_l`. Here we have assumed that the structural and magnetic interfaces between the HM and the FM are identical, so the interfacial magnetic roughness and the width are set at zero for the temperature dependent XRMR simulation discussed in chapter 5.

The total magnetic moment is calculated as `mag*(1 + dmag_u)` where `mag` is the magnetic moment per formula unit. Therefore, in order to extract the actual `dmag` value in the simulation, the mag must be made to be very small while `dmag` is made to be large. This helps reduce the possibility of introducing magnetic artefacts into the fitting algorithm.

Finally, within the sample tab is the instrument editor [labeled d) in figure A.1] where the instrument parameters, such as wavelength, incident intensity (I_0), resolution (`res`), beam-width, sample length, probing ray, polarisation and unit of coordinate (θ or q) are defined. The number of simulations (points to include in the resolution calculations) for each individual point is defined using `respoint`.

A.2 Figure of merit (FOM)

In all XRR and PNR simulations, both the `chi2bar` (χ^2) and `NewFOM` were employed as FOM functions for the analysis and comparison of fits. Initially, the `chi2bar` FOM was used to optimise simulations that use χ^2 to extract the χ^2, which was used to compare the goodness of simulations. The χ^2 optimisation function is represented by

$$\mathrm{FOM}_{\mathrm{chi2bar}} = \frac{1}{N-p}\sum_i \left(\frac{Y_i - S_i}{E_i}\right)^2 \tag{A.2.3}$$

where Y_i and S_i represent the experimental and simulated datasets respectively, i indicates individual elements of the dataset, N is the total number of data points, p is the number of fitting parameters and E_i is the uncertainty in the experimental data. This function differs from the Chi-squared in Poisson statistics, described by Hughes & Hase [216], in substituting E_i by S_i. Making this takes into account directly the uncertainty of the experimental data. In the new FOM, the average absolute difference in the data and simulation are still used, but they are now weighted instead by the Poisson counting error on each point ($\sqrt{N_i}$) and a user controlled constant, n. This is then described as [215]

$$\mathrm{FOM}_{\mathrm{new}} = \frac{1}{N-p}\sum_i \frac{|\log_{10}(N_i) - \log_{10}(S_i)|}{\log_{10}(\sqrt{N_i}+n)\times\log_{10}(N_i)} \tag{A.2.4}$$

where n is an additional weighing term which can be used to shift the focus away from the higher angle noisy data. This new FOM not only produced superior fitting in practice, but also has a more thorough grounding in the management of expected errors on counting type errors (i.e. Poisson errors) as described well by Hughes & Hase [216].

Lastly, for XRMR simulation the `diff` was employed as the FOM function, which used the average of the absolute difference between simulation and data.

$$\mathrm{FOM}_{\mathrm{diff}} = \frac{1}{N-p} \times \sum_i |Y_i - S_i| \tag{A.2.5}$$

The $\mathrm{FOM}_{\mathrm{diff}}$ was used because it allows simulation of data even when some of the data values are negative numbers. It represents the average of the absolute difference between the simulated, S and experimental, Y, data. This function was chosen as it is robust enough to capture the variations and nature of data. It does not include error-bars.

A.3 GenX fitting of x-ray reflectivity

For the XRR analysis one XRR dataset was loaded. When selecting the reflectivity simulation plugin and after the sample is created pressing the `run` button enables the simulation tab to dynamically generate a script which can be manually edited in the script tab.

Figure A.3a) shows the first step, which used the `chi2bar` (χ^2) FOM which is very effective for fitting the critical angle and small angles. This FOM relies on the calculation of the residuals which are showed in lowest part of the figure A.3a). The y axis is displayed on a logarithmic scale to represent the fast changing rate. After `q`=0.2 Å there is already four orders of magnitude change in the values which is difficult to keep up for the FOM. Therefore, once the first part of the reflectivity curve is fitted, the next is to proceed using the `newFOM`, to fit the remainder of the data. Figure A.3b) shows the result after using both FOMs to fit the experimental data.

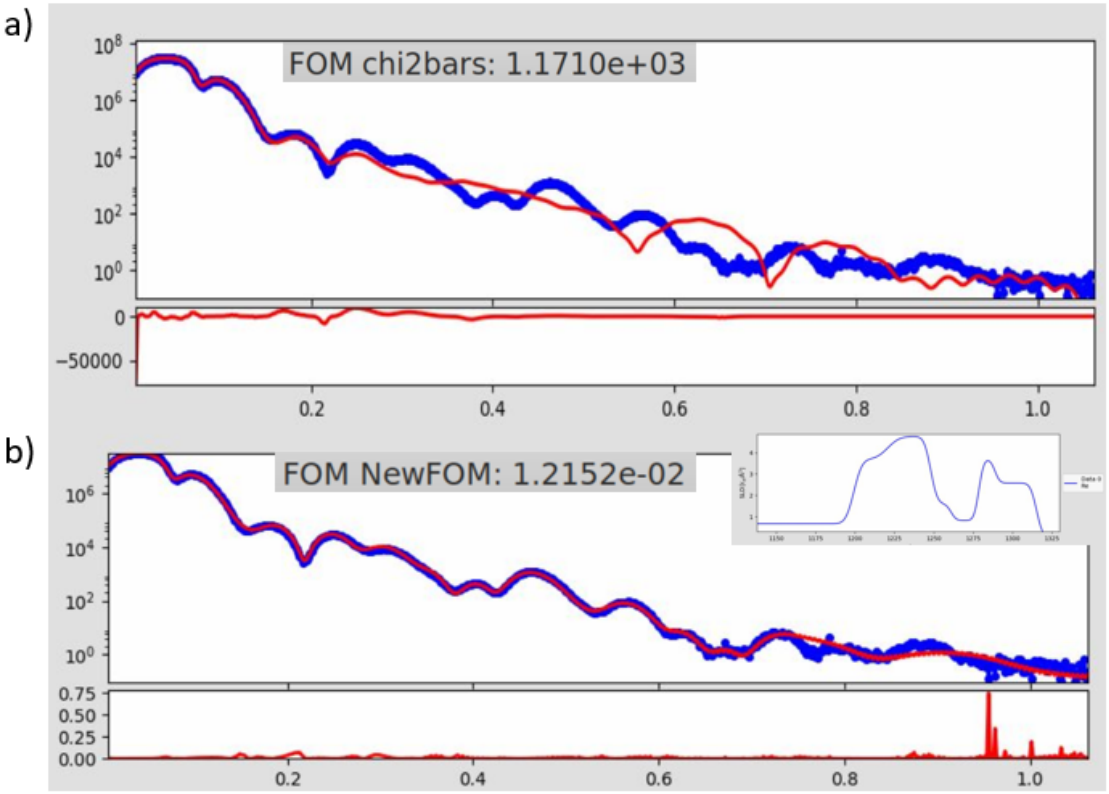

Figure A.3: Screenshot of the data display tab using a) $\mathrm{FOM}_{\mathrm{chi2bars}}$ and b) $\mathrm{FOM}_{\mathrm{new}}$.

A.4 GenX fitting of polarised neutron reflectivity

In the PNR analysis two datasets are loaded, which are the spin-up and spin-down reflectivity data. These two datasets are shown on the simulation tab (indicated by the red arrows in figure A.4a). The simulation parameters for each of these datasets are added by clicking on the + sign on the simulation editor shown in figure A.4b). When clicked, the parameter editor pops up where the instrument polarisation (`setpol`) is set to '`uu`' for spin-up reflectivity, '`dd`' for spin-down reflectivity data. The simulation tab dynamically generates a script which can be manually edited in the script tab. For the PNR data `chi2bar` was used as the FOM. Here, the only parameter defined in the simulations editor is the incident neutron polarisation of each data set.

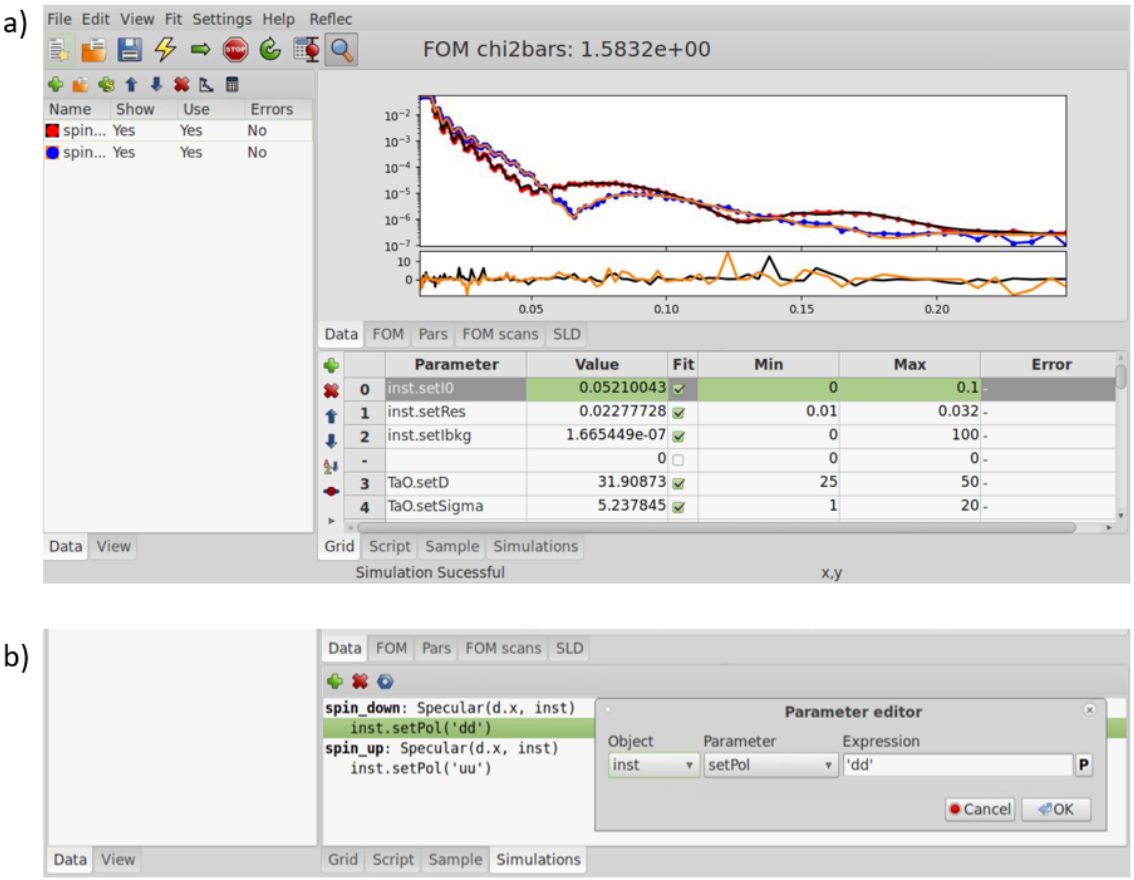

Figure A.4: Screenshot of the software interface a) PNR fitting setup and b) simulation tab.

A.5 GenX fitting of x-ray resonance magnetic reflectivity

Here two datasets (`Data 0` and `Data 1`) are loaded and so two datasets appear on the simulation tab, which represents the reflectivity and the spin asymmetry, R_a, data respectively. The instrument and sample description of each dataset is configured within the simulation tab. Similar to the PNR, the x-ray beam polarisation (`Xpol`) for both datasets is added first. The polarisation for `Data 0` is set as '`tot`' since it is specular x-ray reflectivity data while `Data 1` is set as '`ass`' as it is the SA data [68].

Next, is the definition of the custom variables, this uses the blue nut-shaped button (circled in the figure A.5) where the initial values of the real and imaginary magnetic and structural scattering factors of the resonance species (e.g. Pt) are

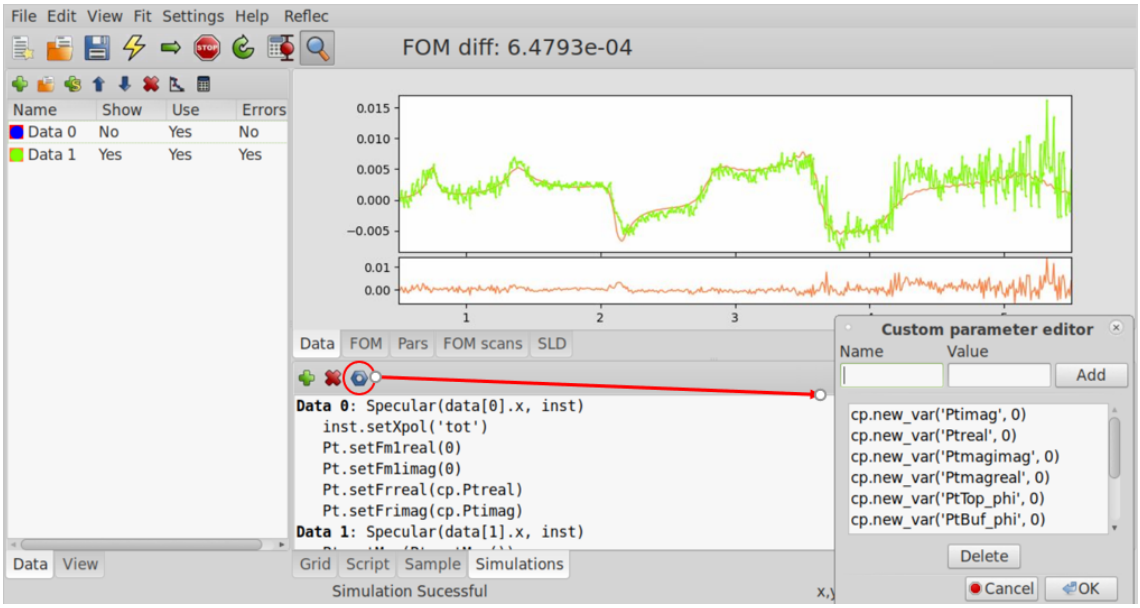

Figure A.5: Screenshot of the software interface XRMR fitting setup the simulation tab where the custom variable are added.

defined. When clicked the custom parameter editor dialog box pops up. The parameters defined are "`Ptreal`, 0", "`Ptimag`, 0", "`Ptmagreal`, 0 ", "`Ptmagimag`, 0" and "`Pt Phi`, 0" which represent the real and imaginary contribution of the charge scattering length factor of Pt, real and imaginary magnetic scattering factor of Pt and the in-plane angle of the magnetic moment relative to the direction of incident x-ray for the Pt layer. These are used to define the respective resonant and non-resonant scattering factors of each dataset.

From chapter 3, the refractive index for resonant magnetic scattering is expressed as

$$n = 1 - \delta - i\beta. \tag{A.5.6}$$

The real and imaginary components, δ and β, describe the dispersive and absorptive aspects of the wave-matter interaction [114],

$$\delta = \left(\frac{r_e\lambda^2}{2\pi}\right) N_0\rho \sum_i x_i(Z_i + f_i'(E))/\sum_i x_i M_i \tag{A.5.7}$$

and

$$\beta = \left(\frac{r_e\lambda^2}{2\pi}\right) N_0\rho \sum_i x_i(Z_i + f_i''(E))/\sum_i x_i M_i, \tag{A.5.8}$$

Since `Data 0` is the specular reflectivity dataset, there is no magnetism. The data and simulation presented in figure A.5 are the XRMR measurement for SiO_2/Ta(2 nm)/ Pt(3 nm)/Co_2FeAl(2 nm)/MgO(2 nm)/Ta(2 nm). Therefore, the real and imaginary component of Fm1 for the buffer Pt layer is defined to be zero while `Frreal` and `Frimag` are configured to extract their values from the custom parameter `Ptreal` and `Ptimag` respectively. This describes the structural profile of the Pt layer. The R_a data, `Data 1`, is configure by setting the magnetic resonant scattering length factor `Fm` to be extracted from `Ptmagreal` and `Ptmagimag` and is defined for the Pt layer. Also, the Pt magnetic moments is set to be estimated using the "`getmag`" command for Pt layer. After the `simulation tab` is set, the parameters are automatically upload into the script. The simulation dataset are now scaled by manually editing `Data 0` using

$$Y = y \times x^4 \times D \tag{A.5.9}$$

where y is the intensity of the reflectivity data obtained from experiment, `x` is the scattering vector and D the scaling factor. This is made by the code

$$I[-1] = (data[0].x^4)/5e^9, \tag{A.5.10}$$

where $D = 1/(5 \times 10^9)$. The R_a data was not scaled as FOM_{diff} was used as the FOM and it allows simulation of negative values without error.

Finally, the instrument and layer parameters such as thickness, roughness, density and magnetic moment are uploaded on the grid tab. The upper and lower limits (priors) of each parameter are adjusted before beginning the simulation. The fitting parameter convergence to the experimental data is monitored from the FOM tab and the fit is judged depending the FOM value (in case of χ^2 to as close to one as possible) to be physically realistic and good. If the fit is not good enough, the parameters are tuned by manually adjusting the priors on the grid tab. A better fit than the previous will have a lower FOM value.

A.6 CFA fittings

A.6.1 XRR

As mentioned in chapter 5, due to the complexity of reflectivity curves it was required to deposit a set of reference samples to build up the final fit of the original samples. For all the reference samples the densities were fixed and the only parameter to fit were the thicknesses and roughnesses.

The first sample consisted in depositing Ta/Pt on the Si/SiO_2 substrate which is shown in figure A.6a). Subsequently, the CFA layer was added and it was capped by Al to avoid oxidation on the ferromagnetic layer. In order to perform the fit, the values for Ta and Pt from the previous sample were taken and during the new fitting process the values were restricted to vary only within 10%. The data and the final fit are shown in figure A.6b). Finally, figure A.6b) shows the data and the fit when the MgO layer was added and then fit using the same procedure described above. Once the information is obtained from fitting the reference samples, the fit for the actual samples was performed. In figure A.7, the fitting process for the Pt unannealed is presented. Initially, the χ^2 figure of merit (FOM) was used to perform the fit. Using the FOM was useful to fit the first section of the reflectivity curve because it is the section with higher intensity with several order of magnitude in comparison with the last section of the curve. The χ^2 procedure relies on the residuals to weight and calculate the next iteration which neglects most of the curve as shown in figure A.7a). By changing to a more equally weighted FOM allows to fit better throughout the curve. The FOM selected calculates the average of the absolute difference between the logarithms (base 10) of the data and the simulation. Figure A.7b) shows the fit using the FOM_{log}. The last fine tuning of the fit was performed by let the densities vary within 10% of the set value for each material– this is shown in figure A.7c). For the Pt annealed fit, the values for the Pt unannealed was taken as the seed values and then the same procedure was taken, the data is presented in figure A.7a). The parameters that do not have error are fixed during the fitting process. The same procedure was performed for the Ir samples. In figure A.7b) and c) the parameters data is shown.

a) Ta/Pt

Layer	Thickness (Å)	Roughness (Å)
Ta	18.04 ± 0.65	3.02 ± 0.31
Pt	32.31 ± 1.12	4.78 ± 0.41

b) Ta/Pt/CFA/Al

Layer	Thickness (Å)	Roughness (Å)
Ta	17.5 ± 0.92	5.07 ± 0.65
Pt	33.1 ± 1.27	3.04 ± 0.51
CFA	19.2 ± 0.82	5.2 ± 0.39
Al_2O_3	37.29 ± 5.23	10.2 ± 2.74

c) Ta/Pt/CFA/MgO/Al

Layer	Thickness (Å)	Roughness (Å)
Ta	17.8 ± 1.32	4.34 ± 0. 54
Pt	34.8 ± 1.73	3.69 ± 0.72
CFA	19.5 ± 0.45	2.87 ± 0.32
MgO	17.13 ± 2.42	2.63 ± 0.83
Al_2O_3	41.28 ± 6.42	11.31 ± 5.32

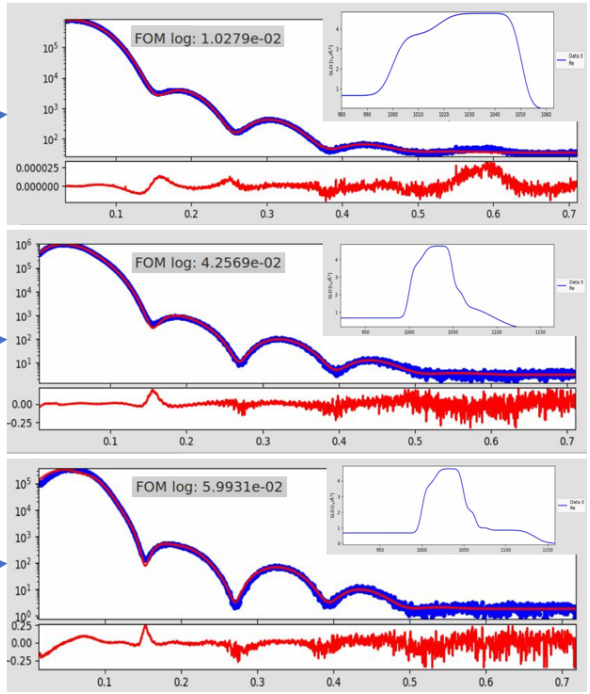

Figure A.6: Fitting process for the reference samples where the data is shown with errors and a screenshot of the fitting software is also displayed. a) Using $FOM_{chi2bars}$ is only useful for the critical angle due to the intensity difference, b) FOM_{log} was used to have first good fit of the curve and c) FOM_{log} was also used but let the densities vary in the fitting process.

a)

Layer	Thickness (Å)	Roughness (Å)
Ta	21.65 ± 0.87	7.80 ± 0.65
Pt	25.40 ± 2.74	2.98 ± 0.51
CFA	14.41 ± 0.96	4.27 ± 0.87
MgO	15.56 ± 2.29	2.07 ± 0.96
Ta	12.3 ± 3.64	4.21 ± 0.75
Ta_2O_5	27.16 ± 5.35	6.42 ± 1.74

b)

Layer	Thickness (Å)	Roughness (Å)
Ta	21.45 ± 1.25	5.79 ± 0.95
Pt	27.49 ± 1.74	3.13 ± 0.78
CFA	14.98 ± 0.82	3.08 ± 0.57
MgO	17.42 ± 2.74	2.48 ± 1.04
Ta	10.10 ± 0.94	2.48 ± 0.84
Ta_2O_5	26.48 ± 3.76	3.12 ± 2.73

c)

Layer	Thickness (Å)	Roughness (Å)	Density (u/Å^3)
Ta	20.73 ± 0.72	7.32 ± 0.85	0.04130 ± 0.00413
Pt	29.20 ± 0.95	3.43 ± 0.67	0.06318 ± 0.00320
CFA	19.32 ± 0.63	2.96 ± 0.53	0.02344 ± 0.00372
MgO	17.27 ± 1.76	2.42 ± 0.65	0.04418 ± 0.00434
Ta	9.90 ± 1.28	2.19 ± 0.85	0.04380 ± 0.00462
Ta_2O_5	26.82 ± 2.41	2.88 ± 1.07	0.01108 ± 0.00223

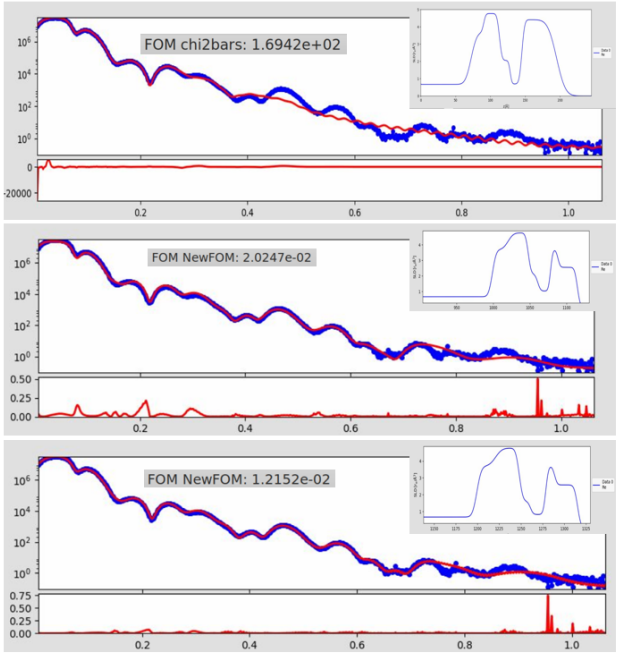

Figure A.7: Fitting process for the Pt unannealed where the data is shown with errors and a screenshot of the fitting software is also displayed. a) Ta/Pt, b) Ta/Pt/CFA/Al and c) Ta/Pt/CFA/MgO/Al.

XRR

a) Pt annealed

Layer	Thickness (Å)	Roughness (Å)	Density (u/Å^3)
Ta	17.93 ± 0.83	4.32 ± 0.85	0.05541
Pt	26.20 ± 1.36	8.43 ± 0.67	0.06566
CFA	20.42 ± 0.57	7.96 ± 0.53	0.01805
MgO	16.29 ± 1.48	7.42 ± 0.65	0.04418 ± 0.00634
Ta	4.30 ± 0.48	1.19 ± 0.63	0.05541
Ta_2O_5	42.82 ± 3.14	11.88 ± 1.07	0.01108 ± 0.00110

b) Ir unannealed

Layer	Thickness (Å)	Roughness (Å)	Density (u/Å^3)
Ta	19.07 ± 0.62	6.34 ± 0.85	0.05130 ± 0.00413
Ir	30.61 ± 0.65	2.55 ± 0.57	0.07189
CFA	15.32 ± 0.53	2.03 ± 0.58	0.02144 ± 0.00372
MgO	19.76 ± 1.54	2.53 ± 0.75	0.05030 ± 0.00434
Ta	17.64 ± 0.88	3.02 ± 0.65	0.04980 ± 0.00662
Ta_2O_5	25.82 ± 2.41	3.75 ± 1.13	0.01184

c) Ir annealed

Layer	Thickness (Å)	Roughness (Å)	Density (u/Å^3)
Ta	25.73 ± 0.81	7.32 ± 0.85	0.05241 ± 0.00215
Ir	21.20 ± 1.03	3.43 ± 0.67	0.07189
Ir-CFA	18.32 ± 0.64	8.46 ± 1.43	0.03440 ± 0.00132
CFA- MgO	20.27 ± 1.52	6.32 ± 1.55	0.05974 ± 0.00244
MgO	8.35 ± 1.46	3.86 ± 1.12	0.05313
Ta	13.12 ± 1.28	2.19 ± 0.85	0.05380 ± 0.00102
Ta_2O_5	23.67 ± 2.41	4.58 ± 1.07	0.01184

Figure A.8: Table of the XRR parameters after fitting a) the Pt annealed sample, b) Ir unannealed and c) Ir annealed.

A.6.2 PNR

For the fitting process of the PNR data the FOM$_{\chi^2}$ was used as shown in figure A.9. The PNR fitting was simpler as the values found by fitting the XRR were used as the seed values for the PNR. Figure A.9a) shows the first attempt where the $\chi^2 = 182.4$. After letting the simulation run, it was possible to get a substantially better fit where $\chi^2 = 2.09$ as shown in figure A.9b). It worth mentioning that the changes in the thickness and roughness of the MgO layer did not impact at all the whole fit – suggesting that the neutrons are not sensitive to the MgO layer. Therefore, it was decided to fix the layer to the value found by x-rays. Finally, after allowing the densities of the CFA and MgO layers vary within 10% of the set value, the fit slightly improved, as shown in figure A.9c). The same procedure was used for the rest of the samples. In figure A.10a) the fit data with its errors are presented. On the other hand, the fit data with its errors for the Ir unannealed and annealed is displayed in figure A.10b) and c).

a)

Layer	Thickness (Å)	Roughness (Å)
Ta	24.99 ± 1.97	3.83 ± 3.89
Pt	25.89 ± 1.43	0.00 ± 2.32
CFA	16.60 ± 1.17	0.00 ± 1.67
MgO	12.59 ± 3.64	0.00 ± 1.56
Ta	10.41 ± 0.87	0.00 ± 1.73
Ta_2O_5	31.70 ± 3.45	5.42 ± 2.51

b)

Layer	Thickness (Å)	Roughness (Å)	μ (μ_B/u)
Ta	10.58 ± 0.73	5.87 ± 0.67	0
Pt	26.10 ± 0.94	0.53 ± 0.86	0
CFA	16.18 ± 0.83	1.04 ± 0.52	4.8 ± 0.73
MgO	12.42 ± 2.68	0.34 ± 0.97	0
Ta	10.62 ± 0.47	0.65 ± 0.76	0
Ta_2O_5	31.91 ± 1.87	5.39 ± 1.56	0

c)

Layer	Thickness (Å)	Roughness (Å)	Density (u/Å³)	μ (μ_B/u)
Ta	20.51 ± 0.54	5.96 ± 0.36	0.05541	0
Pt	27.88 ± 0.43	3.10 ± 0.41	0.06600	0
CFA	18.45 ± 0.39	2.81 ± 0.25	0.02337 ± 0.00413	4.8 ± 0.73
MgO	17.00	3.98 ± 0.37	0.04017 ± 0.00546	0
Ta	7.11 ± 0.47	2.42 ± 0.44	0.05541	0
Ta_2O_5	31.95 ± 1.04	5.39 ± 0.95	0.01184	0

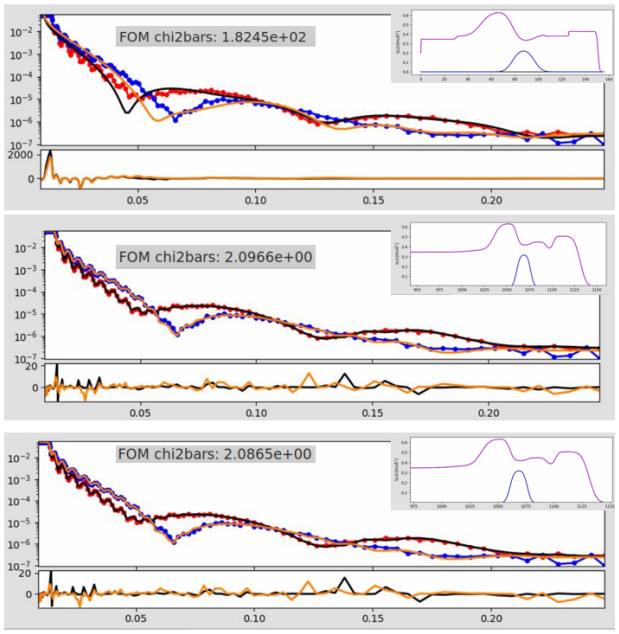

Figure A.9: PNR fitting process using FOM_{χ^2}. a) The first fit attempt, b) second attempt after leaving the simulation run and tweak the parameters. c) Final fine tuning of the fit after allowing the densities of the CFA and MgO vary within 10 %.

PNR

a) Pt annealed

Layer	Thickness (Å)	Roughness (Å)	Density (u/Å³)	μ (μ_B/u)
Ta	20.63 ± 0.83	5.32 ± 0.85	0.05741 ± 0.00342	0
Pt	25.20 ± 1.36	8.02 ± 0.87	0.06566	0
CFA	16.42 ± 0.57	6.56 ± 0.93	0.02265 ± 0.00220	5.4 ± 0.88
MgO	17.00	9.97 ± 1.05	0.05018 ± 0.00235	0
Ta	8.61 ± 0.48	3.87 ± 0.63	0.05541	0
Ta_2O_5	31.02 ± 3.14	4.88 ± 1.07	0.01108 ± 0.00110	0

b) Ir unannealed

Layer	Thickness (Å)	Roughness (Å)	Density (u/Å³)	μ (μ_B/u)
Ta	16.42 ± 0.32	1.34 ± 0.35	0.05203 ± 0.00413	0
Ir	29.5 ± 0.45	2.13 ± 0.47	0.07189	0
CFA	14.52 ± 0.43	5.03 ± 0.48	0.01882 ± 0.00072	5.3 ± 0.85
MgO	17.00	2.15 ± 0.34	0.05130 ± 0.00434	0
Ta	21.24 ± 0.58	3.02 ± 0.35	0.05508	0
Ta_2O_5	26.38 ± 1.21	6.56 ± 0.95	0.01264 ± 0.00034	0

c) Ir annealed

Layer	Thickness (Å)	Roughness (Å)	Density (u/Å³)	μ (μ_B/u)
Ta	21.73 ± 0.81	3.82 ± 0.75	0.05541	0
Ir	21.20 ± 1.03	4.13 ± 0.57	0.07189	0
Ir-CFA	15.92 ± 2.34	2.26 ± 1.43	0.02340 ± 0.00132	0.09 ± 0.03
CFA- MgO	8.02 ± 1.52	5.98 ± 1.55	0.03974 ± 0.00244	0.14 ± 0.06
MgO	8.78 ± 0.56	5.76 ± 1.12	0.05313	0
Ta	12.52 ± 1.28	3.19 ± 0.85	0.05541	0
Ta_2O_5	33.57 ± 2.41	10.58 ± 1.07	0.01584 ± 0.0063	0

Figure A.10: Table of the PNR parameters after fitting a) the Pt annealed sample, b) Ir unannealed and c) Ir annealed.

a)

Layer	Thickness (Å)	Roughness (Å)
Ta	21.46 ± 0.95	2.07 ± 0.56
Pt	25.40 ± 0.87	5.07 ± 0.63
CFA	14.08 ± 0.89	2.45 ± 0.42
MgO	17.34 ± 1.03	2.99 ± 0.48
Ta	11.63 ± 0.58	3.56 ± 0.37
Ta_2O_5	27.69 ± 1.98	4.13 ± 0.77

μ_{Pt}=0.000134 ± 0.000045 μ_B

b)

Layer	Thickness (Å)	Roughness (Å)	Density (u/Å³)
Ta	20.82 ± 0.54	2.83 ± 0.65	0.05540
Pt	28.85 ± 0.56	5.53 ± 0.43	0.06560
CFA	16.76 ± 0.65	2.23 ± 0.57	0.01854
MgO	17.34 ± 1.03	3.77 ± 0.56	0.0530
Ta	11.54 ± 0.67	4.38 ± 0.68	0.05540
Ta_2O_5	28.06 ± 0.94	4.78 ± 0.94	0.010054 ± 0.0032

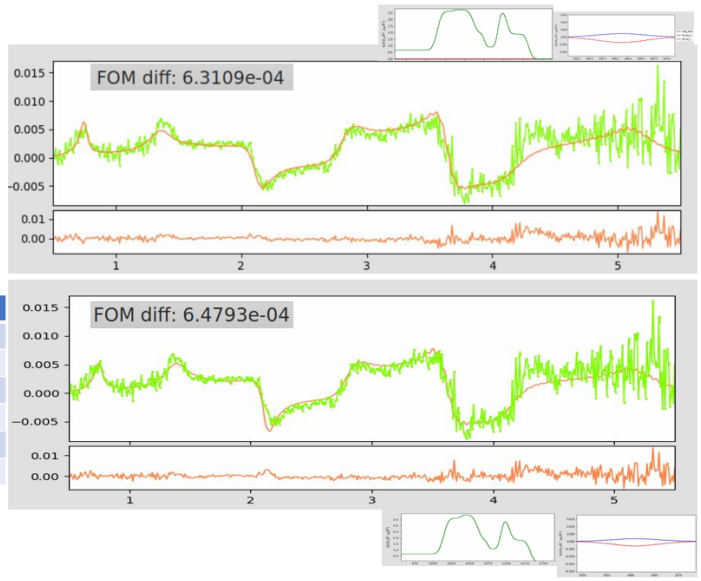

Figure A.11: XRMR fitting procedure. a) Fit allowing the variation of the thicknesses and roughnesses. b) Additionally, the densities are also allow to vary.

A.6.3 XRMR

The fitting process for the XRMR is more time consuming as is substantially more computational extensive. The reason is, during the fitting process it is actually fitting 2 set of data, the structural x-rays reflectivity (with different energy as normal XRR) and the spin asymmetry. The computational time using a personal computer could be a day for a few iterations. Most of the fittings were performed in the supercomputer of the department. Here, the FOM used was FOM_{diff} which was described earlier in the appendix. Figure A.11 shows the both the fit parameters and screenshot of the fitting software displaying the 2-step procedure. In the first instance, only the thicknesses and roughness were allowed to vary which gave a first good fit (figure A.11a). Secondly, the final fine tuning were performed by allowing the Ta_2O_5 layer density to vary as shown in figure A.11b) resulting in the final fit. Hereafter, following the same procedure, the Pt annealed and the Ir unannealed were fit. The fit parameters with their error are displayed in figure A.12a) and b).

XRMR

a) Pt annealed

Layer	Thickness (Å)	Roughness (Å)	Density (u/Å^3)	μ (μ_B)
Ta	22.82 ± 0.44	3.95 ± 0.35	0.05540	0
Pt	28.45 ± 0.58	8.16 ± 0.63	0.06360 ± 0.00342	0.000163 ± 0.000045
CFA	14.96 ± 0.85	3.73 ± 0.47	0.01454 ± 0.00048	0
MgO	18.01 ± 1.23	4.07 ± 0.76	0.04901 ± 0.00423	0
Ta	8.25 ± 0.66	3.25 ± 0.48	0.05940 ± 0.00521	0
Ta_2O_5	29.46 ± 1.34	2.45 ± 0.74	0.01065 ± 0.00685	0

b) Ir unannealed

Layer	Thickness (Å)	Roughness (Å)	Density (u/Å^3)	μ (μ_B)
Ta	18.62 ± 0.56	7.15 ± 0.35	0.05540	0
Ir	30.15 ± 0.78	2.73 ± 0.56	0.7189	0.000158 ± 0.000045
CFA	15.96 ± 0.63	2.89 ± 0.37	0.02304 ± 0.00148	0
MgO	19.61 ± 1.35	2.87 ± 0.74	0.05201 ± 0.00123	0
Ta	21.1 ± 0.88	3.69 ± 0.58	0.05540	0
Ta_2O_5	25.46 ± 2.44	3.72 ± 0.94	0.01045 ± 0.00785	0

Figure A.12: Table of the XRMR parameters after fitting a) the Pt annealed sample, b) Ir unannealed.

A.7 Roughness fittings

The procedure to extract the roughnesses from the roughness-induced samples was performed following the process displayed in figure A.13. As explained in chapter 6, the deposition of the trilayer (Pt/Co/Pt and Pt/Co/Ta) was made simultaneously on all the samples of the set to ensure having the same thicknesses on all the samples. Therefore, using the first sample of the set as a reference as it does not have any Ag layer made the fitting process easier. From fitting the first sample, the thicknesses and roughnesses are extracted as displayed in figure A.13a). The second sample has the same structure of the first sample but with an additional Ag layer of 5 Åunderneath the trilayer therefore, the only parameters to fit are the roughness and during the fit the thicknesses are fixed as shown in figure A.13b). The procedure for the following samples is the same, the Ag layer is increasing the thickness and this will modify all the roughnesses on the sample. Figure A.13c) shows the third

a) d_{Ag}= 0 Å

Layer	Thickness (Å)	Roughness (Å)
Pt	40.42 ± 1.12	4.16 ± 0. 54
Co	4.25 ± 0.53	2.19 ± 0.32
Pt	111.5 ± 3.45	5.87 ± 0.48

b) d_{Ag}= 5 Å

Layer	Thickness (Å)	Roughness (Å)
Pt	40.42	4.85 ± 0. 64
Co	4.25	6.13 ± 0.48
Pt	111.5	5.74 ± 0.63
Ag	4.62 ± 0.36	3.77 ± 1.02

c) d_{Ag}= 10 Å

Layer	Thickness (Å)	Roughness (Å)
Pt	40.42	6.15 ± 0. 74
Co	4.25	8.14 ± 0.62
Pt	111.5	7.24 ± 0.92
Ag	9.42 ± 0.67	4.45 ± 1.45

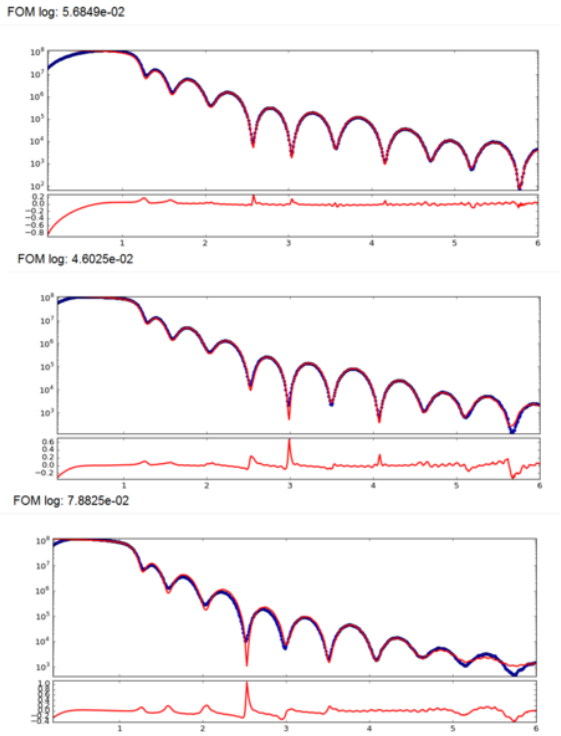

Figure A.13: Fitting procedure for the roughness-induced Pt/Co/Pt. Fit parameters and screenshot of the fitting software displaying the fit. a) Reference sample without Ag underneath the trilayer, with this, the thicknesses were extracted and used in the following steps. b) Second sample, 5 Åof Ag was deposited prior the trilayer, from here only the roughnesses were fit. c)Third sample, 10 Åof Ag was deposited prior the trilayer.

sample, where the Ag layer is 10 Åand again the thicknesses of the trilayer are fixed. The same procedure were followed for rest of the samples. The Ag thicknesses and roughnesss for both trilayer with their error are displayed in figure A.14a) and b).

a) Ag(d_{Ag})/Pt/Co/Pt

d_{Ag}(Å)	Roughness, σ (Å)
0	4.16 ± 0. 54
4.62 ± 0.36	5.73 ± 0.62
9.45 ± 0.57	7.21 ± 0.71
14.36 ± 0.63	12.71 ± 0.78
19.10 ± 0.65	19.23 ± 0.85
23.95 ± 0.85	26.31 ± 0.89
28.85 ± 1.07	26.75 ± 0.95

b) Ag(d_{Ag})/Pt/Co/Ta

d_{Ag}(Å)	Roughness, σ (Å)
0	4.05 ± 0. 74
9.56 ± 0.87	9.14 ± 0.62
19.45 ± 1.24	19.08 ± 0.92
29.10 ± 1.66	26.10 ± 1.45
33.87 ± 2.07	32.23 ± 1.71

Figure A.14: Table of the Ag thicknesses and roughnesses after fitting a) Ag(d_{Ag})/Pt/Co/Pt. b) Ag(d_{Ag})/Pt/Co/Ta.

References

[1] H.-J. Drouhin, 'Chapter 13 - Fundamentals of spin filtering in ferromagnetic metals with application to spin sensors'. Handbook of Infra-red Detection Technologies, Elsevier Science, Amsterdam (2002).

[2] S.S.P. Parkin, M. Hayashi and L. Thomas, Science, vol. 320, p. 190, (2008).

[3] A. Fert, V. Cros, and J. Sampaio. Nature Nanotechnology, vol 8, p 152–156 (2013).

[4] M. Bode, M. Heide, K. von Bergmann, P. Ferriani, S. Heinze, G. Bihlmayer, A. Kubetzka, O. Pietzsch, S. Blügel, and R. Wiesendanger, Nature, vol 447, p 190–193 (2007).

[5] K. Zakeri, Y. Zhang, J. Prokop, T.-H. Chuang, N. Sakr,W. X. Tang, and J. Kirschner, Phys. Rev. Lett. 104, 137203 (2010); Kh. Zakeri, Y. Zhang, T.-H. Chuang, and J. Kirschner, Physical Review Letters, vol 108, p 197205 (2012).

[6] S. Seki, Y. Okamura, K. Kondou, K. Shibata, M. Kubota, R. Takagi, F. Kagawa, M. Kawasaki, G. Tatara, Y. Otani, and Y. Tokura, Physical Review B, vol 93, p 235131 (2016).

[7] Y. Iguchi, S. Uemura, K. Ueno, and Y. Onose, Physical Review B, vol 92, p 184419 (2015).

[8] L. Liu, O. J. Lee, T. J. Gudmundsen, D. C. Ralph, and R. A. Buhrman, Physical Review Letters, vol 109, p 096602 (2012).

[9] J. Sinova, S. O. Valenzuela, J. Wunderlich, C. H. Back, and T. Jungwirth, Review of Modern Physics, vol 87, p 1213 (2015).

[10] M. Heide, G. Bihlmayer, and S. Blügel. Physical Review B, vol 78, p 140403 (2008).

[11] T. A. Moore, I. M. Miron, G. Gaudin, G. Serret, S. Auffret, B. Rodmacq, A. Schuhl, S. Pizzini, J. Vogel, and M. Bonfim, Applied Physics Letters, vol 93, p 262504 (2008).

[12] A. Thiaville, S. Rohart, E. Jué, V. Cros and Albert Fert. Europhysics Letters, vol 100, p 57002 (2012).

[13] S. Emori, U. Bauer, S.-M. Ahn, E. Martinez and G. S. D. Beach. Nature Materials, vol 12, p 611 (2013).

[14] O. Boulle, S. Rohart, L. D. Buda-Prejbeanu, E. Jué, I. M. Miron, S. Pizzini, J. Vogel, G. Gaudin, and A. Thiaville, Physical Review Letters, vol 111, p 217203 (2013).

[15] K.-S. Ryu, L. Thomas, S.-H. Yang and S. Parkin. Nature Nanotechnology, vol 8, p 527 (2013).

[16] J. Torrejon, J. Kim, J. Sinha, S. Mitani, M. Hayashi, M. Yamanouchi, and H. Ohno, Nature Communications, vol 5, p 4655 (2014).

[17] G. Chen, T. Ma, A. T. N'Diaye, H. Kwon, C. Won, Y. Wu, and A. K. Schmid, Nature Communications vol 4, p 2671 (2013).

[18] S. Shimizu, K. S. Takahashi, T. Hatano, M. Kawasaki, Y. Tokura, and Y. Iwasa. Physical Review Letters, vol 111, p 216803 (2013).

[19] M. I. Dyakonov and V. I. Perel, Physical Letters A, vol 35, p 459 (1971).

[20] J. E. Hirsch, Physical Review Letter, vol 83, p 1834 (1999).

[21] Y. K. Kato, R. C. Myers, A. C. Gossard, and D. D. Awschalom, Science. vol 306, p 1910 (2004).

[22] A. Chernyshov, M. Overby, X. Liu, J. K. Furdyna, Y. Lyanda-Geller, and L. P. Rokhinson, Nature Physics, vol 5, p 656 (2009).

[23] Y. Tserkovnyak, A. Brataas, and G. E. W. Bauer. Physical Review Letters, vol 88, p 117601, (2002).

[24] C. W. Sandweg, Y. Kajiwara, A. V. Chumak, A. A. Serga, V. I. Vasyuchka, M. B. Jungfleisch, E. Saitoh, and B. Hillebrands. Physical Review Letters, vol 106, p 216601, (2011).

[25] S. Y. Jang, S. H. Lim and S. R. Lee. Journal of Applied Physics, vol 107, p 09C707 (2010).

[26] R. Rowan-Robinson. Spin-orbit phenomena and interfacial proximity effects in magnetic multilayers. Durham University PhD thesis (2016).

[27] O. Inyang, L. Bouchenoire, B. Nicholson, M. Toka, R. M. Rowan-Robinson, C. J. Kinane, and A. T. Hindmarch, Physical Review B, vol 100, p 174418 (2019).

[28] T. P. A. Hase, M. S. Brewer, U. B. Arnalds, M. Ahlberg, V. Kapaklis, M. Björck, L. Bouchenoire, P. Thompson, D. Haskel, Y. Choi, J. Lang, C. Sánchez-Hanke and B. Hjövarsson. Physical Review B, vol 90, p 104403 (2014).

[29] J. Vogel, A. Fontaine, V. Cros, F. Petroff, J.-P. Kappler, G. Krill, A. Rogalev and J. Goulon. Journal of Magnetism and Magnetic Materials, vol 165, p 96 (1997).

[30] J. Geissler, E. Goering, M. Justen, F. Weigand, G. Schütz, J. Langer, D. Schmitz, H. Maletta, and R. Mattheis. Physical Review B, vol 65, p 020405, (2001).

[31] A. M. Clogston, B. T. Matthias, M. Peter, H. J. Williams, E. Corenzwit, and R. C. Sherwood. Physical Review Letters. vol 125, p 541 (1962).

[32] F. Wilhelm, P. Poulopoulos, H. Wende, A. Scherz, K. Baberschke, M. Angelakeris, N. K. Flevaris, and A. Rogalev. Physical Review Letters, vol 87, p 207202 (2001).

[33] G. Schütz, S. Stähler, M. Knülle, and P. Fischer. Journal of Applied Physics, vol 73, p 6430 (1993).

[34] K. M. Krishnan. Fundamentals and Applications of Magnetic Materials, Oxford University Press, Oxford (2016).

[35] J. Cho, N.-H. Kim, S. Lee, J.-S. Kim, R. Lavrijsen, A. Solignac, Y. Yin, D.-S. Han, Niels J. J. van Hoof, Henk J. M. Swagten, B. Koopmans and C.-Y. You. Nature Communications, vol 6, p 7635 (2015).

[36] A. W. J. Wells, P. M. Shepley, C. H. Marrows, and T. A. Moore. Physical Review B, vol 95, p 054428 (2017).

[37] M. Bode, M. Heide, K. von Bergmann, P. Ferriani, S. Heinze, G. Bihlmayer, A. Kubetzka, O. Pietzsch, S. Blügel and R. Wiesendanger. Nature, vol 447, p 190 (2007).

[38] H. Yang, O. Boulle, V. Cros, A. Fert, and M. Chshiev, Scientific Reports, vol 8, p 12356 (2016).

[39] S. Tacchi, R. E. Troncoso, M. Ahlberg, G. Gubbiotti, M. Madami, J. Akerman, and P. Landeros. Physical Review Letter, vol 118, p 147201 (2017).

[40] A. Ahmad, S. Mitra, S.K. Srivastava, A.K. Das. Journal of Magnetism and Magnetic materials, vol 474, p 599–605 (2019).

[41] H. J. Elmers, S. Wurmehl, G. H. Fecher, G. Jakob, C. Felser, G. Schonhense. Applied Physics A, vol 79, p 557–563 (2004).

[42] R. M. Rowan-Robinson, A. A. Stashkevich, Y. Roussigné, M. Belmeguenai, S.-M. Chérif, A. Thiaville, T. P. A. Hase, A. T. Hindmarch and D. Atkinson. Scientific Reports, vol 7, p 2045-2322 (2017).

[43] A. Fert, V. Cros and João Sampaio. Nature Nanotechnology, vol 8, p 152156 (2013).

[44] X. Z. Yu, N. Kanazawa, Y. Onose, K. Kimoto, W. Z. Zhang, S. Ishiwata, Y. Matsui and Y. Tokura. Nature Materials, vol 10, p 106 (2011).

[45] S. Mühlbauer, B. Binz, F. Jonietz, C. Pfleiderer, A. Rosch, A. Neubauer, R. Georgii, P. Böni. Science vol 323, p 915-919 (2009).

[46] X. Z. Yu, Y. Onose, N. Kanazawa, J. H. Park, J. H. Han, Y. Matsui, N. Nagaosa and Y. Tokura. Nature, vol 465, p 901–904 (2010).

[47] Onose, Y., Okamura, Y., Seki, S., Ishiwata, S. and Tokura, Y. Physsical Review Letters, vol 109, p 037603 (2012).

[48] L.Q. Liu, C.F. Pai, Y. Li, H.W. Tseng, D.C. Ralph, R.A. Buhrman. Science, vol 336, p 555558 (2012).

[49] S. Emori, U. Bauer, S.M. Ahn, E. Martinez, G.S. Beach. Nature materials, vol 12, p 611 (2013).

[50] P. Gambardella, I.M. Miron, Philosophical Transactions of the Royal Society A: Mathematical, Physical and Engineering Sciences, vol 369 p 3175-3197 (2011).

[51] G. Yu, P. Upadhyaya, Y. Fan, J.G. Alzate, W. Jiang, K.L. Wong, S. Takei, S.A. Bender, L.-T. Chang, Y. Jiang, M. Lang, J. Tang, Y. Wang, Y. Tserkovnyak, P.K. Amiri, K.L. Wang. Nature Nanotechnology, vol 9 p 548-554 (2014).

[52] G.Q. Yu, P. Upadhyaya, K.L. Wong, W.J. Jiang, J.G. Alzate, J.S. Tang, P.K. Amiri, K.L. Wang. Physical Review B, vol 89, p 104421 (2014).

[53] G. Yu, P. Upadhyaya, Q. Shao, H. Wu, G. Yin, X. Li, C. He, W. Jiang, X. Han, P.K. Amiri, K.L. Wang. Nano Letters, vol 17, p 261268 (2017).

[54] G.Q. Yu, P. Upadhyaya, X. Li, W.Y. Li, S.K. Kim, Y.B. Fan, K.L. Wong, Y. Tserkovnyak, P.K. Amiri, K.L. Wang. Nano Letters, vol 16, p 19811988 (2016).

[55] M.E. Knoester, J. Sinova, R.A. Duine. Physical Review B, vol 89, p 064425 (2014).

[56] Y. Tchoe, J.H. Han. Physical Review B, vol 85, p 174416 (2012).

[57] J. Iwasaki, M. Mochizuki, N. Nagaosa. Nature Nanotechnology, vol 8, p 742747 (2013).

[58] H.Y. Yuan, X.R. Wang. Scientific Reports, vol 6, p 22638 (2016).

[59] J. Li, A. Tan, K.W. Moon, A. Doran, M.A. Marcus, A.T. Young, E. Arenholz, S. Ma, R.F. Yang, C. Hwang and Z.Q. Qiu. Nature Communications, vol 5, p 4704 (2014).

[60] N. Romming, C. Hanneken, M. Menzel, J. E. Bickel, B. Wolter, K. von Bergmann, A. Kubetzka, R. Wiesendanger. Science, vol 341, p 636639 (2013).

[61] W. Jiang, P. Upadhyaya, W. Zhang, G. Yu, M. B. Jungfleisch, F. Y. Fradin, J. E. Pearson, Y. Tserkovnyak, K. L. Wang, O. Heinonen, S. G. E. te Velthuis, A. Hoffmann. Science, vol 349, p 283286 (2015).

[62] D. Jiles, Introduction to Magnetism and Magnetic Materials. CRC press, 2nd ed., (1998).

[63] S. Blundell. Magnetism in condensed matter. Oxford University Press (2009).

[64] Coey, J.M. D., Magnetism and Magnetic Materials, Cambridge University Press, Cambridge, England (2010).

[65] Charles Kittel. Introduction to Solid State Physics. Wiley eighth edition (2005).

[66] D. Jiles, Introduction to Magnetism and Magnetic Materials. CRC press, 2nd ed., (1998).

[67] E. C. Stoner. The London, Edinburgh, and Dublin Philosophical Magazine and Journal of Science, vol 15, no 101, pp 1018-1034, (1933).

[68] O.-O. Inyang. Magnetic proximity effect and interfacial spin dependent transport in ferromagnet/heavy metal thin films. Durham university thesis (2019).

[69] J. C. Slater. Physical Review, vol 49, no 7, p 537, (1936).

[70] S. Gasiorowicz, Quantum Physics. Massachusetts: John Wiley and sons, 3rd ed., (1974).

[71] J. Geissler, E. Goering, M. Justen, F.Weigand, G. Schütz, J. Langer, D. Schmitz, H. Maletta, and R. Mattheis. Physical Review B, vol 65, no 2, p 020405, (2001).

[72] R. Wienke, G. Schütz, and H. Ebert. Journal of Applied Physics, vol 69, no 8, p 6147-6149, (1991).

[73] Y. Sakamoto, Y. Oba, H. Maki, M. Suda, Y. Einaga, T. Sato, M. Mizumaki, N. Kawamura, and M. Suzuki. Physical Review B, vol 83, no 10, p 104420, (2011).

[74] von Bernd Zimmermann. RWTH Aachen University Thesis. Calculation of the Dzyaloshinskii-Moriya Interaction in ultrathin magnetic Films (2010).

[75] J. Nanayakkara. DMI Interaction and Domain Evolution in Magnetic Heterostructures with Perpendicular Magnetic Anisotropy. Georgia state university PhD Thesis (2018).

[76] L. Néel. Journal Physics Radium, vol 15, p 225-239 (1954).

[77] U. Gradmann, J.M. Physica status solidi (b), vol 27, p 313 (1968).

[78] P.F. Carcia, A.D. Meinhaldt, and A. Suna. Applied Physics Letters, vol 47, p 178–180 (1985).

[79] P.F. Carcia. Journal of Applied Physics, vol 63, p 5066–5073 (1988).

[80] F. J. A. den Broeder, D. Kuiper, A. P. van de Mosselaer and W. Hoving. Physical Review Letters, vol 60, p 2769–2772 (1988).

[81] M. Sakurai, T. Takahata, and I. Moritani. IEEE Translation Journal on Magnetics in Japan, vol 7, p 176–182 (1992).

[82] F.J.A. den Broeder, W. Hoving, and P.J.H. Bloemen. Journal of Magnetism and Magnetic Materials, vol 93, p 562–570 (1991).

[83] M. T. Johnson, P. J. H. Bloemen, F. J. A. den Broeder and J. J. de Vries. Reports on Progress in Physics, vol 59, p 1409 (1996).

[84] J. Stöhr. Journal of Magnetism and Magnetic Materials, vol 200, p 470–497 (1999).

[85] A. P. Mihai, A. L. Whiteside, E. J. Canwell, C. H. Marrows, M. J. Benitez, D. McGrouther, S. McVitie, S. McFadzean, and T. A. Moore. Applied Physics Letters, vol 103, p 262401 (2013).

[86] I. Dsyaloshinskii, Soviet Physics JETP, vol 5, p 1259 (1957).

[87] T. Moriya. Physical Review, vol 120, no 1, p 91, (1960).

[88] https://physics.stackexchange.com/questions/127531/lack-of-inversion-symmetry-in-crystal

[89] J. Chi-Ming, D. Hai-Feng. Chinese Physics B, vol 24, p 128501 (2015).

[90] S. Buhrandt and L. Frits. Physical Review B, vol 88, p 195137 (2013).

[91] Bram van Dijk. Skyrmions and the Dzyaloshinskii-Moriya Interaction. Master Thesis, Utrecht University (2014).

[92] S. Buhrandt, and L. Fritz. Physical Review B, vol 88, p 195137 (2013).

[93] A. Arora. Optical and electric field control of magnetism. PhD Thesis, Universität Potsdam (2018).

[94] B. D. Cullity, C.D.G., Introduction to Magnetic Materials. 2nd Edition. Wiley-IEEE Press (2008).

[95] C. L. Dennis, R. P. Borges, L. D. Buda, U. Ebels, J. F. Gregg, M. Hehn, E. Jouguelet, K. Ounadjela, I. Petej, I. L. Prejbeanu. Journal of Physics Condensed Matter, vol 14, p 1175–1262 (2002).

[96] B.A. Lilley. The London, Edinburgh, and Dublin Philosophical Magazine and Journal of Science: Series 7 (2010).

[97] H. Yang, A. Thiaville, S. Rohart, A. Fert, and M. Chshiev. Physical Review Letters, vol 115, p 267210 (2015).

[98] S.-G. Je, D.-H. Kim, S.-C. Yoo, B.-C. Min, K.-J. Lee, and S.-B. Choe. Physical Review B, vol 88, p 214401 (2013).

[99] A. Hrabec, N. A. Porter, A. Wells, M. J. Benitez, G. Burnell, S. McVitie, D. McGrouther, T. A. Moore, and C. H. Marrows. Physical Review B, vol 90, p 020402 (2014).

[100] O. OzatayT, P. M. Hauet , L. Braganca, W. Mather, M. L. Schneider J.-U. Thiele. Comprehensive Nanoscience and Nanotechnology, Elsevier Science Publishing Co Inc (Second Edition), US (2016).

[101] I. V. Soldatov and R. Schäfer. Journal of Applied Physics, vol 122, p 153906 (2017).

[102] D. Sanz-Hernndez and A. Fernndez-Pacheco. 'Chapter 4 - Fabrication and magneto-optical characterization of 3D-printed permalloy nanowires', Magnetic Nano- and Microwires. Woodhead Publishing, (2015)

[103] J. Hamrle. http://alma.karlov.mff.cuni.cz/hamrle/teaching/lectures/hamrle_moke.pdf

[104] H. Szambolics, J.-Ch. Toussaint, A. Marty, I.M. Miron, L.D. Buda-Prejbeanu. Journal of Magnetism and Magnetic Materials, vol 321, p 1912–1918 (2009).

[105] A.J. Schellekens, A. van den Brink, J.H. Franken, H.J.M. Swagten and B. Koopmans. Nature communications, vol 3, p 847 (2012).

[106] I. M. Miron, T. Moore, H. Szambolics, L. D. Buda-Prejbeanu, S. Auffret, B. Rodmacq, S. Pizzini, J. Vogel, M. Bonfim, A. Schuhl and G. Gaudin. Nature materials, vol 10, p 419 (2011).

[107] L.D. Landau, E.M.L. Physikalische zeitschrift der Sowjetunion, vol 8, p 153 (1935).

[108] J. Chico, S. Keshavarz, Y. Kvashnin, M. Pereiro, I. Di Marco, C. Etz, O. Eriksson, A. Bergman, L. Bergqvist, Physical Review B, vol 93, p214439 (2017).

[109] T.L. Gilbert. IEEE Transactions on Magnetics, vol 40, p 3443–3449 (2004).

[110] A. Mougin, M. Cormier, J. P. Adam, P. J. Metaxas and J. Ferré. Europhysics Letters, vol 78, p 57007 (2007).

[111] P. J. Metaxas, J. P. Jamet, A. Mougin, M. Cormier, J. Ferré, V. Baltz, B. Rodmacq, B. Dieny, and R. L. Stamps. Physical review letters, vol 99, p 217208 (2007).

[112] J. Soong-Geun, K. Duck-Ho, Y. Sang-Cheol, M. Byoung-Chul, L. Kyung-Jin, and C. Sug-Bong. Physical Review B, vol 88, p 214401 (2013).

[113] P. Kelly and R. Arnell. Vacuum, vol 56, p 159 (2000).

[114] Yasaka Miho. The Rigaku Journal Summer, vol 25, no 2 (2010).

[115] W. Hendrickson. Science, vol 254, p 51–58 (1991).

[116] Scattering length database maintained by NIST. http://physics.nist.gov/PhysRefData/FFast/html/form.html.

[117] G. van der Laan, A.I. Figueroa. Coordination Chemistry Reviews, vol 277 p 95-129 (2014).

[118] C. Giles, C. Malgrange, J. Goulon, F. de Bergevin, C. Vettier, E. Dartyge, A. Fontaine, C. Giorgetti and S. Pizzini Journal of Applied Crystallography, vol 27, p 232 (1994).

[119] M. A. Björck. Structural viewpoint of magnetism in Fe and Co based superlattices. PhD thesis, Uppsala (2007).

[120] T. Martin. Faraday's Diary. Volume IV, Nov. 12, 1839 - June 26, 1847. Forgotten Books, UK (2017)

[121] J. Kerr. Philosophical Magazine, vol 4, p 337-348 (1875).

[122] J. Zak, E. R. Moog, C. Liu and S. D. Bader. Journal of Applied Physics, vol 68, p 4203 (1990).

[123] C. J. Kinane, The Interplay of Magnetism and Structure in Patterned Multilayer Thin Films. PhD thesis, University of Leeds, (2008).

[124] https://www.physik.fu-berlin.de/einrichtungen/ag/ag-kuch/research/techniques/fmr/index.html

[125] K. Di, V. L. Zhang, H. S. Lim, S. C. Ng, and M. H. Kuok. Physical Review Letters, vol 114, p 047201 (2015).

[126] J. Hamrle. Magneto-optical determination of the in-depth magnetization profile in magnetic multilayers. PhD Thesis, University of Paris XI in Orsay (2003).

[127] K. Shahbazi, J.-V. Kim, H. T. Nembach, J. M. Shaw, A. Bischof, M. D. Rossell, V. Jeudy, T. A. Moore, and C. H. Marrows. Physical Review B, vol 99, p 094409 (2019).

[128] D.M.F.Hartmann, Domain-Wall Motion in Materials with Perpendicular Magnetic Anisotropy, in Institute for Theoretical Physics. 2014, Utrecht University.

[129] S. Lemerle, J. Ferré, C. Chappert, V. Mathet, T. Giamarchi, P. Le Doussal. Physical Review Letters, vol80, p 849–852 (1998).

[130] R. Lavrijsen, D. M. F. Hartmann, A. van den Brink, Y. Yin, B. Barcones, R. A. Duine, M. A. Verheijen, H. J. M. Swagten, B. Koopmans. Physical Review B, vol 91, p 104414 (2015).

[131] J. Soong-Geun, K. Duck-Ho, Y. Sang-Cheol, M. Byoung-Chul, L. Kyung-Jin and C. Sug-Bong. Physical Review B, vol 88, p 214401 (2013).

[132] K. Duck-Ho, Y. Sang-Cheol, K. Dae-Yun, M. Byoung-Chul and C. Sug-Bong. Scientific Reports, vol 7, p 45498 (2017).

[133] I. V. Soldatov, R. Schäfer. Physical Review B, vol 95, p 014426 (2017).

[134] M. W. Davidson. Configuring a Microscope for Kohler Illumination. Carl Zeiss Microscopy Online Campus Zeiss Logo. http://zeiss-campus.magnet.fsu.edu/articles/basics/kohler.html

[135] https://en.wikipedia.org/wiki/Numerical_aperture

[136] F. Czeschka, L. Dreher, M. Brandt, M. Weiler, M. Althammer, I.-M. Imort, G. Reiss, A. Thomas, W. Schoch, W. Limmer. Physical Review Letters, vol 107, no 4, p 046601, (2011).

[137] A. Hoffmann, IEEE Transactions on Magnetics, vol 49, no. 10, p 5172–5193, (2013).

[138] T. McGuire, R. Potter. IEEE Transactions on Magnetics, vol 11, p 1018-1038 (1975).

[139] G. Bihlmayer, O. Rader, and R. Winkler, New Journal of Physics, vol 17, p 050202 (2015).

[140] M. Belmeguenai, J. P. Adam, Y. Roussigné, S. Eimer, T. Devolder, J. Kim, S. M. Cherif, A. Stashkevich and A. Thiaville. Physical Review B, vol 91, p 180405 (2015).

[141] M. Belmeguenai, Y. Roussigné, H. Bouloussa, S. M. Chérif, A. Stashkevich, M. Nasui, M. S. Gabor, A. Mora-Hernández, B. Nicholson, O.-O. Inyang, A. T. Hindmarch, L. Bouchenoire. Physical Review Applied, vol 9, p 044044 (2018).

[142] G. M. Alonzo-Medina, A. González-González, A. I. Oliva, J. L. Sacedón, and E. Vasco. Journal of Physics D: Applied Physics, vol 45, p 435301 (2012).

[143] S. C. Chen, S. Chen, and P. C. Kuo. Thin Solid films, vol 517, p 5176–5180 (2009).

[144] G. M. Alonzo-Medina, A. González-González, A. I. Oliva, J. L. Sacedón, and E. Vasco. IOP Conference Series: Materials Science and Engineering, vol 1, p 45 (2013).

[145] F. Albertini, L. Nasi, F. Casoli, S. Fabbrici, P. Luches A. Rota, S. Valeri. Journal of Magnetism and Magnetic Materials, vol 2, p 158–161 (2007).

[146] R.C. Taylor and C.C. Tsuei. Solid state communications. vol 41, p 503–506, (1982).

[147] M. von Arx, O. Paul and H. Baltes. Journal of Microelectromechanical Systems, vol 9, p 136–145 (2000).

[148] J. A. Kittl, A. Lauwers, O. Chamirian, M. Van Dal, A. Akheyar, M. De Potter, Microelectronic Engineering, vol 70, p 158–165 (2003).

[149] H. Kappert, N. Kordas, S. Dreiner, U. Paschen and R. Kokozinski. IEEE International Symposium on Circuits and Systems (ISCAS), Lisbon, vol 2 , p 1162–1165 (2015).

[150] Y. Li-Xiu, L. Ching-Ming, S. Jhin-Wei, W. Yi-Rung, L. Kun-Wei, C. Yu-Hsiu. IEEE Transactions on magnetics, vol 44, p 115 (2008).

[151] A. A Knowlton, O. C. Clifford. Transactions of the Faraday Society, vol 8, p 195 (1912).

[152] S. Trudel, O. Gaier, J. Hamrle and B. Hillebrands. Journal of Physics D: Applied Physics, vol 43, p 193001 (2010).

[153] W. Pickett and J. Moodera. Physics Today, vol 54, p 39 (2001)

[154] A. Pagea, P.F.P. Poudeub and C. Uher. Journal of Materiomics, vol 2, p 104–113 (2016).

[155] K. Nawa and Y. Miura. RSC Advances, vol 9, p 30462–30478 (2019).

[156] M. Belmeguenai, H. Tuzcuoglu, M. S. Gabor, T. Petrisor, C. Tiusan, D. Berling, F. Zighem, T. Chauveau, S. M. Chérif, P. Moch. Physical Review B, vol 18, p 1–11 (2013).

[157] M. Björck, The Journal of Applied Crystallography, vol 3, p 1198–1204 (2011).

[158] J. M. Yang, X. Wang, C. Zheng, H. Zhao and Q. Q. Lei, 2013 Annual Report Conference on Electrical Insulation and Dielectric Phenomena, Shenzhen, vol 1, p 719–721 (2013).

[159] Isis Neutron Source. Experiment R1620118. Proximity induced magnetisation in CoFeTaB/Ir thin films (2017).

[160] R. Knut, P. Svedlindh, O. Mryasov, K. Gunnarsson, P. Warnicke, D. A. Arena, M. Björck, A. J. C. Dennison, A. Sahoo, S. Mukherjee, D. D. Sarma, S. Granroth, M. Gorgoi, and O. Karis. Physical Review B, vol 88, p 134407 (2013).

[161] J.F. Ankner, G.P. Felcher. Journal of Magnetism and Magnetic Materials, vol 200, p 741–754 (1999).

[162] K. Nakajima. Quantum Beam Scientific, vol 1, p 9 (2017).

[163] B. P. Toperverg. The Physics of Metals and Metallography, vol 116, p 1337-1375 (2015).

[164] H. C. Kandpal, G. H. Fecher and C. Felser. Journal of Physics D: Applied Physics, vol 40, p 1507-1523 (2007).

[165] M. Kawakami. Hyperfine Interactions, vol 51, p 993-1002 (1989).

[166] H. J. Elmers, S. Wurmehl, G. H. Fecher, G. Jakob, C. Felser and G. Schonhense. Applied Physics A, vol 79, p 557-63 (2004).

[167] E. Wohlfarth. Journal of Physics F: Metal Physics, vol 14, p 155–159 (1984).

[168] J. Friebe and P. Zacharias. IEEE Transactions on magnetics, vol 50, p P.1-P.10 (2014).

[169] P.J. Grundy, Magnetic Layer: Anisotropy, 'Encyclopedia of Materials: Science and Technology', Elsevier (2001).

[170] K. Inomata, N. Ikeda, N. Tezuka, R. Goto, S. Sugimoto, M. Wojcik and E. Jedryka. Science and Technology of Advance Materials, vol 9, p 014101 (2008).

[171] R. Skomski, J. Zhou, R. D. Kirby, and D. J. Sellmyer. Material Materials Research Society Symposium Proceedings, vol 887, p Q07-07.1-Q07-07.7 (2006).

[172] https://www.researchgate.net/publication/317930772_Chiral_Magnetic_Skyrmions_in_Thin_Films

[173] Röler, U.K., A.N. Bogdanov, and C. Pfleiderer. Nature, vol 442, p 797 (2006).

[174] N. Nagaosa, and Y. Tokura. Nature Nanotechnology, vol 8, p 899 (2013).

[175] J. Iwasaki, M. Mochizuki, and N. Nagaosa. Nature Nanotechnology, vol 8, p 742 (2013).

[176] C. C. Cao, Y. G. Wang, L. Zhu, Y. Meng, X. B. Zhai, Y. D. Dai, J. K. Chen, and F. M. Pan. Scientific Reports, vol 8, p 1243 (2018).

[177] S. Lemerle, J. Ferré, C. Chappert, V. Mathet, T. Giamarchi, and P. Le Doussal. Physical Review Letter, vol 80, p 849 (1998).

[178] P. J. Metaxas, J. P. Jamet, A. Mougin, M. Cormier, J. Ferré, V. Baltz, B. Rodmacq, B. Dieny, and R. L. Stamps. Physical Review Letter, vol 99, p 217208 (2007).

[179] S. Lemerle, J. Ferré, C. Chappert, V. Mathet, T. Giamarchi, and P. Le Doussal. Physical Review Letter, vol 80, p 849 (1998).

[180] J.-M. L. Beaujour, W. Chen, J. Z. Sun and A. D. Kent. Journal of applied physics, vol 99, p 08N503 (2006).

[181] A. Hrabec, N. A. Porter, A. Wells, M. J. Benitez, G. Burnell, S. McVitie, D. McGrouther,T. A. Moore,1 and C. H. Marrows1. Physical Review B, vol 90, p 020402(R) (2014).

[182] G. Chen, T. Ma, Alpha T. N., H. Kwon, C. Won, Y. Wu and A. K. Schmid. Nature Communications, vol 4, p 2671 (2013).

[183] L. Berger, Physical Review B, vol 54, p 9353 (1996).

[184] J. C. Slonczewski. Journal of Magnetism and Magnetic Materials, vol 159, p L1-L7 (1996).

[185] S. Bhatti, R. Sbiaa, A. Hirohata, H. Ohno, S. Fukami, S. N. Piramanayagam. Materials Today. vol 20, p 530–548 (2017).

[186] T. Min, Q. Chen, R. Beach, G. Jan, C. Horng, W. Kula, T. Torng, R. Tong, T. Zhong, D. Tang, P. Wang, M. m Chen, J. Z. Sun, J. K. Debrosse, D. C. Worledge, T. M. Maffitt, and W. J. Gallagher, IEEE Transactions on Magnetics, vol 46, p 2322 (2010).

[187] W. S. Zhao, Y. Zhang, T. Devolder, J. O. Klein, D. Ravelosona, C. Chappert, and P. Mazoyer, Microelectrons Reliability, vol 52, p 1848 (2012).

[188] L. Q. Liu, T. Moriyama, D. C. Ralph, and R. A. Buhrman, Physical Review Letters, vol 106, p 036601 (2011).

[189] I. M. Miron, G. Gaudin, S. Auffret, B. Rodmacq, A. Schuhl, S. Pizzini, J. Vogel and P. Gambardella. Nature Materials, vol 9, p. 230-234 (2010).

[190] S. V. Aradhya, G. E. Rowlands, J. Oh, D. C. Ralph, and R. A. Buhrman, Nano Letters, vol 16, p 5987 (2016).

[191] S.-H. Yang, K.-S. Ryu, and S. Parkin, Nature Nanotechnology, vol 10, p 221 (2015).

[192] R. Ramaswamy, J. M. Lee, K. Cai, and H. Yang. Applied Physics Reviews, vol 5, p 031107 (2018).

[193] G. Dresselhaus, Physical Review, vol 100, p 580 (1955).

[194] Yu. A. Bychkov and E. I. Rashba, JETP Letters, vol 39, p 78 (1984).

[195] I. M. Miron, T. Moore, H. Szambolics, L. D. Buda-Prejbeanu, S. Auffret, B. Rodmacq, S. Pizzini, J. Vogel, M. Bonfim, A. Schuhl, and G. Gaudin, Nature Materials, vol 10, p 419 (2011).

[196] A. Manchon and S. Zhang, Physical Review B, vol 79, p 094422 (2009).

[197] S. D. Pollard, J. A. Garlow, J. Yu, Z. Wang, Y. Zhu and Hyunsoo Yang. Nature Communications, vol 8, p 14761 (2017).

[198] Zhang, X., Zhou, Y., Ezawa, M., Zhao, G. and Zhao, W. Scientific Reports, vol 5, p 11369 (2015).

[199] J. Iwasaki, M. Mochizuki and N. Nagaosa. Nature Nanotechnology, vol 8, p 742-747 (2013).

[200] A. Vansteenkiste, J. Leliaert, M. Dvornik, M. Helsen, F. Garcia-Sanchez, and B. Van Waeyenberge, vol 4, p 107133, (2014).

[201] J. Fidler and T. Schrefl. Journal of Physics D: Applied Physics, vol 33, p R135R156 (2000).

[202] P. P. J. Haazen, E. Mure, J. H. Franken, R. Lavrijsen, H. J. M. Swagten and B. Koopmans. Nature materials, vol 12, p 299303 (2013).

[203] S. Fukami, T. Suzuki, N. Ohshima, K. Nagahara, and N. Ishiwata. Journal of Applied Physics, vol 103, p 07E718 (2008).

[204] W. Jiang, G. Chen, K. Liu, J. Zang, S. Velthuis, A. Hoffmann. Physics Reports, vol 704, p 149 (2017).

[205] W. Jiang, W. Zhang, G. Yu, M. B. Jungfleisch, P. Upadhyaya, H. Somaily, J. E. Pearson, Y. Tserkovnyak, K. L. Wang, O. Heinonen, S. Velthuis, and A. Hoffmann. AIP Advances, vol 6, p 055602 (2016).

[206] S. Woo, K. Litzius, B. Kruger, M.Y. Im, L. Caretta, K. Richter, M. Mann, A. Krone, R.M. Reeve, M. Weigand, P. Agrawal, I. Lemesh, M.A. Mawass, P. Fischer, M. Kläui, G.S. Beach. Nature Materials, vol 15, p 501-506 (2016).

[207] S. Woo, M. Mann, A.J. Tan, L. Caretta, G.S.D. Beach. Applied Physics Letters, vol 105, p 212404 (2014).

[208] Jiawei Yu, Xuepeng Qiu, William Legrand, H. Yang. Applied Physics Letters, vol 109, p 096602 (2016).

[209] https://genx.sourceforge.io/

[210] M. Bjrck and G. Andersson. Journal Applied Crystallography, vol 40, p 1174-1178 (2007).

[211] M. Björck, Journal of Applied Crystallography, vol 44, p 1198–1204, (2011).

[212] M. Björck and G. Andersson. Journal of Applied Crystallography, vol 40, p 1174–1178 (2007).

[213] A. Gibaud, G. Vignaud, and S. Sinha. Acta Crystallographica Section A: Foundations of Crystallography, vol 49, p 642–648 (1993).

[214] J. Ihringer. Journal of Applied Crystallography, vol 28, p 618–619, (1995).

[215] J. G. Troughton. On improvements in metal oxide based flexible transistors through systematic evaluation of material properties. PhD thesis, Durham University (2019).

[216] I. G. Hughes, and T. P. A. Hase. Measurements and their Uncertainties: A Practical Guide to Modern Error Analysis. Oxford University Press, Oxford (2009).